Porous Silicon for Light Management in Silicon Solar Cells

by

Josefine Helene Selj

Thesis submitted for the degree of
Philosophiae Doctor

Department of Physics
University of Oslo

December 2010

© Josefine Helene Selj, 2011

Series of dissertations submitted to the
Faculty of Mathematics and Natural Sciences, University of Oslo
No. 1059

ISSN 1501-7710

All rights reserved. No part of this publication may be
reproduced or transmitted, in any form or by any means, without permission.

Cover: Inger Sandved Anfinsen.
Printed in Norway: AIT Oslo AS.

Produced in co-operation with Unipub.
The thesis is produced by Unipub merely in connection with the
thesis defence. Kindly direct all inquiries regarding the thesis to the copyright
holder or the unit which grants the doctorate.

Abstract

In the present work possibilities of utilizing porous silicon (PS) to enhance absorption in silicon solar cells are investigated. Silicon solar cells produce energy by converting the incoming solar radiation to electricity and the efficiency of this technology will naturally depend on the amount of light that can be absorbed by the solar cell. Antireflection coatings are used on the surface of solar cells to increase the fraction of light that enters the cell. In addition texture and rear side reflectors can be used to 'trap' the light within the cell.

PS is a versatile, nanostructured material commonly made by electrochemical etching of silicon. The porosity of PS can be controlled by the etching parameters applied during formation, and because the porosity is closely related to the refractive index, PS is a highly interesting material for optical applications. In this work we show that thin, complex multilayer PS structures can be tailored to give very low reflectances over a broad wavelength range. The versatile optical properties of PS are also utilized to fabricate a variety of colored coatings that retain very low reflectance. Therefore, PS could be an exiting material for use in efficient designer cells, desirable for applications where the visual impression is important. PS can also be used to make highly reflective structures simply by altering the electrochemical etching parameters. Such structures can be used as rear side reflectors in solar cells.

This work also presents detailed investigations of the fabrication process, structure, optical properties, and oxidation of the multilayered PS structures. In particular, spectroscopic ellipsometry is extensively utilized in the characterization of these multilayers, providing accurate in-depth modeling of optical and structural properties. In addition, reflectometry, scanning and transmission electron microscopy, and x-ray photoelectron spectroscopy is utilized in order to unveil the secrets of this complex material.

Acknowledgements

First and foremost, I want to thank my supervisor Erik Stensrud Marstein for introducing me to the fields of solar cells and porous silicon. Your exceptional enthusiasm and positive attitude is contagious and your overview of the field has been much appreciated. Also thanks to my co-supervisor Sean Erik Foss, for fruitful discussions on porous silicon and for introducing me to the treasurous, but treacherous ways of ellipsometry.

I want to thank the department head Arve Holt for believing in me and giving me the opportunity to write a phd thesis on solar cells, even though my astrophysics background left much materials science knowledge to be desired.

During the work with this thesis, Annett Thøgersen has provided highly valued microscope images and careful XPS analysis; both very helful in the quest of disclosing the details and mysteries of porous silicon. Thanks also for always being eager to discuss results and new experiments.

I am also grateful to Morten Kildemo, Paul Bergstrom, Solveig Rørkjær, Krister Mangersnes, Jo Gjessing, Rune Søndenå, Trygve Mongstad, Marie Syre, Birger Rettersdøl Olaisen and Terje Finstad for the collaboration and support through the work with this thesis.

During the time I have spent at IFE, the solar cell research activity has grown from a group of ten to a department of almost thirty. We have gotten to our disposal a brand new lab with state of the art equipment, and I am grateful to be able to utilize this. Thanks to everyone who has taken part in this development. It has made lab work as great a pleasure as its capricious nature allows.

My phd-time at IFE has been enriched by great colleges, entertaining coffee breaks, late solar-beers and unifying seminars and conferences. Thanks to everybody at the solar energy department for making working-days bright. My office-cohabitant and friend over the last three years, Marie, deserves special thanks. What she does not know about my phd-roller coaster trip is

not worth knowing. Probably all that she does know is not worth knowing either. Special thanks also to Krister, Jo, Erik, Ellen, and Annett who have been a vital part of any social event, lunch or extended coffee break, almost since the day I arrived at IFE. I could not have asked for better fellows.

My friends and family have been given undeservedly low priority over the last year, thank you for your understanding and patience. In particular I would like to thank Stine and Marte for their appreciation and invaluable friendship. I know you will still be there when I emerge from the current reclusion.

Throughout my education, my parents have given me exceptional moral support and there have undoubtedly been times when it has been desperately needed. Thank you so much for all encouragement and backing.

Finally, thank you Gorm for your good spirits and for putting up with me these last months. Your support, kindness, and love are, and will always be, inestimable.

Contents

Abstract **i**

Acknowledgements **iii**

1 Introduction **1**
1.1 Motivation for This Work 5
1.2 Thesis Outline 7
1.3 List and Summary of Papers 9

2 Porous Silicon Fundamentals **11**
2.1 History 11
2.2 Anodic Etching of Porous Silicon 12
2.3 Morphology 16
2.4 Influence of Formation Parameters 17
2.5 Formation Models 21
2.6 Optical Properties 27
2.7 Ageing of PS 29

3 Light Management in Silicon Solar Cells **31**
3.1 The Unalterable Source 32
3.2 The Silicon Solar Cell 33
3.3 Theoretical Basis for Light Management 40
3.4 Implementing Light Management 44

4 Fabrication and Characterization of PS **56**
4.1 Fabrication 56
4.2 Porosity and Etch Rate Calculations 58
4.3 Ellipsometry 62

4.4 Complementary Characterization 78

5 Single layer PS and Process Considerations 87

5.1 Substrate 88
5.2 Voltage Transients from Anodic Etching 89
5.3 Inhomogeneity and Repeatability 90
5.4 Electrolyte Aging 95
5.5 Chemical Etching 97
5.6 Pore Nucleation 99
5.7 Porous Silicon Oxidation 106
5.8 Summary 107

6 Porous Silicon Multilayers for Solar Cell Applications 109

6.1 Graded Porous Silicon Antireflection Coatings 110
6.2 Clear Color Porous Silicon Antireflection Coatings 111
6.3 Integration of PS ARCs in Si Solar Cell Processing 116
6.4 Transmission Optimizations 122
6.5 Etching of Multicrystalline Wafers 127
6.6 Porous Silicon Backside Reflector 128

7 Conclusions and Future Work 136

Bibilography 139

Chapter 1

Introduction

Solar cells exploit a virtually infinite source of energy and generate electrical current directly from sunlight in a one-step conversion process. The solar energy that hits the earth's surface in one hour is comparable to the amount consumed by all human activities in a year. No other renewable energy source comes close to such a potential [1]. The need for clean, renewable energy technologies in order to reduce the environmental impact of our increasing energy consumption is by now well documented [2, 3]. The pollution-free operation is the main incentive to promote the use of solar cells over conventional fossil fuels.

Another attractive aspect of solar energy is the global distribution of the resource. Solar energy has an important potential in providing modern energy access to millions of people in developing countries that currently depend on more traditional sources of energy [4]. Already an estimated three million households get power from small solar photovoltaic (PV) systems [4].

One of the main drawbacks of energy conversion by solar cells has been, and still is, high cost.

Cost of Solar Electricity

Grid parity, a long held holy grail in PV, refers to the average cost of energy in a given market. It is therefore an important yardstick for the competitiveness of solar electricity compared to conventional electricity. Significant technological progress with respect to the cost and efficiency of solar cells has been made over the last decade, and only in 2009 the module cost was reduced by almost 40%. As a result, solar electricity has reached grid parity in

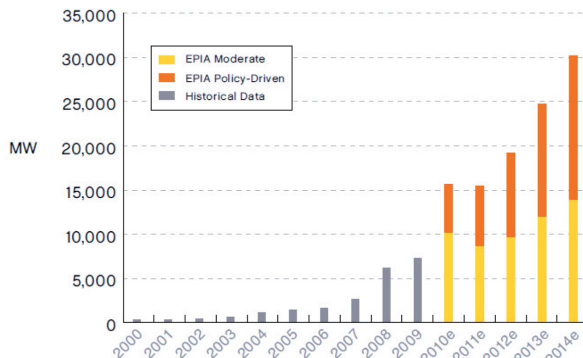

Figure 1.1: Yearly growth of installed PV. Historical data in grey, EPIA forecasts for 2010-2013. Moderate (yellow) and aggressive (orange) estimates are shown. Adapted from [5].

some propitious energy markets, and the use of solar cells is rapidly growing. As of early 2010 almost 23 GW are installed globally, which produce about 25 TWh of electricity on a yearly basis [5]. Figure 1.1 shows historical growth data and the European Photovoltaic Industry Association's (EPIA) forecast for 2010-2013. The historical numbers are remarkable: grid-connected PV has seen an average growth of 60% every year for the past decade, increasing 100-fold since 2000 [4]. This makes PV one of the fastest growing power technologies, and as seen from EPIAs forecast, continued growth is expected.

Another interesting marker of the competitiveness of solar cells for energy production is the energy payback time; i.e. the operation time needed to harvest the amount of energy that was used during the fabrication of the cells. The payback time is not only important for cost reasons; if we want solar cells to create net, zero carbon emission energy, a short energy payback time is clearly extremely important. In 2000 the payback time for a c-Si solar cell module was about five years; today it is approaching one year [6].

Despite module price and payback time reductions and exceptional growth, the total installed PV capacity represents only $\sim 0.1\%$ of the world's energy consumption [7]. The production price of PV is currently around $\$0.15-0.30$ per kilowatt hour; still higher than fossil fuels ($\$0.01-0.05$/kWh) and the

most widespread renewable energy sources, hydro ($0.03 − 0.05/kWh) and wind ($0.10 − 0.14/kWh) [4]. Hence, solar energy must, in most markets, still be subsidised in order to compete with conventional energy sources.

Policy and Framework

Therefore, in addition to continued technological progress, policy incentives are important to secure further utilization of solar energy. By early 2010, more than 100 countries had some type of policy target and/or promotion policy related to renewable energy [4]. The most important solar incentive to date is the feed-in tariff, which offers the producers of renewable energy long-term guaranteed purchase at rates which are generally higher than the production cost [8].

Although not the sunniest country on earth, Germany has by far the greatest installed PV capacity: almost 10 GW, including around 3.8 GW installed in 2009 [5]. This amounts to almost half of the world's total installed PV capacity and is made possible largely due to efficient government incentives. Other major markets are Japan and Spain, but after Spain had a record-breaking year in 2008, installations in 2009 were dramatically reduced due to a cap on subsidies after the national solar target was reached [4]. USA, Italy, Canada, and Australia are other important, emerging markets. While China now manufactures more than a third of the world's PV cells, most Chinese consumers cannot yet afford the technology, and 95% of China's production is exported [8]. However, China and India have huge market potentials and large installations are planned within the next five years [5].

Estimates on when grid parity can be reached in the various markets vary greatly. Some recent reports suggest that solar grid parity in sunnier areas will be reached as early as 2012 [9], while others advocate time horizons of 5 − 10 years [10] or even more [11]. Whether grid parity will be achieved in the near or the somewhat more distant future, there is no lack of optimistic predictions about the effects on the expansion of PV [12]. However, Yang [11] points out that even when/if grid parity is reached, this does not guarantee market penetration of PV because of unfamiliarity with the technology and high upfront costs. Although these barriers are not equally important for PV power plants, Yang [11] argues that dropping costs in solar technology will not automatically resolve our energy problems. Therefore, if policy-makers wish to help distributed solar technologies into commercialization, political

mandates to further encourage their adoption would be necessary [11].

Another question is whether grid parity energy costs truly reflect the cost of fossil fuels. While the need of subsidies for PV is often focused upon, the indirect subsidies of fossil fuels are rarely discussed. To what extent are indirect costs of fossil fuels, such as environmental cleanup, health care costs, and the current and future expenses of adapting to a warmer world, included in the electrical bill? A handful of countries, including Norway, introduced carbon taxes early in the 1990s. Over the next two decades a number of countries followed, but China and the US, who are each responsible for approximately 20% of the world's total energy consumption, have not yet passed any carbon tax laws. Such laws are no guarantee for reduced carbon emissions; Norway's per capita emissions rose by 28% between 1990 and 2009 [13]. However, enforcement of such legislation in China and USA would likely contribute to a levelling of the ground between solar energy and fossil fuels.

Solar Cells in Norway

Although being a global resource, the incoming solar energy is far from *evenly* distributed and Norway is not likely to reach the most-installed-PV lists. Norway is however a considerable *producer* of solar cells. The environment in Norway was well adapted to start production of solar cells, due to a long history of silicon production and favourable energy prices. Elkem has for a long time been one of the world's greatest producers of silicon and as technology director in Elkem in the early 1990s, Alf Bjørseth saw the potential for refining the silicon into silicon wafers for the solar cell industry. He founded Scanwafer 1994, and later three other companies related to solar cell and module production. In 2000 these companies were merged into the company Renewable Energy Corporation (REC), which has become one of the world leaders in the manufacturing of wafers for solar cells. In 2006 Elkem started production of feedstock silicon for the solar industry through a low cost metallurgical route [14]. Recently, REC has opened a large factory in Singapore, following the same trend as several other manufacturers. For the costs of PV to continue to decline, PV analysts anticipate that solar cell manufacturing increasingly will shift to Asia, a track familiar also from other high-volume electronics markets [15].

The Road Ahead

In the International Energy Agency's solar PV roadmap vision, PV is projected to provide 5% of global electricity consumption in 2030, rising to 11% in 2050, avoiding 2.3 gigatonnes of CO_2 emissions per year [7]. Currently, $85 - 90\%$ of solar cells are made of silicon as the active semiconductor material [7, 16] and the cost of the PV module accounts for roughly half of the PV system cost [11]. Acknowledging that grid parity likely is a necessity to secure widespread use of PV, cost reductions of silicon solar cells are of high importance in order to ensure a sustainable expansion of solar, low carbon emission energy in the future. Most solar cell research is therefore aimed towards bringing the cost down and increasing the efficiency of the cells.

1.1 Motivation for This Work

One way to boost efficiency is to increase the fraction of light that is absorbed by the solar cell, a strategy now commonly known as *light trapping*. Here we will use the term light trapping as referring to path length enhancements for the light within the solar cell, hence, enhancement of the absorption probability for a photon *inside* the solar cell. Typical elements used to achieve path length enhancements include textures and backside reflectors. In the wider term *light management*, we also include strategies used to decrease the amount of light reflected from the cell surface using textures and antireflective coatings (ARCs). Since silicon is a relatively weak absorber, light management becomes increasingly important as the thickness of the silicon wafers and solar cells decreases.

The benefit of reduced thickness is of course reduced material expenses. Due to its low absorption, crystalline silicon has traditionally held a much weaker position within thin film solar cells than within the conventional wafer technology. The thin film cells with the highest market share today is Cadmium Telluride (CdTe) cells. Other alternatives are Cadmium Indium Gallium Selenium (CIGS) and amprophous silicon cells. All of the above materials have far higher absorption than crystalline silicon, but all of them also have severe problems of their own. Therefore, within both the aims of improving efficiencies and reducing material cost, the potential benefits of applying efficient light trapping to crystalline silicon cells are significant. Several new technologies are emerging that allow for making crystalline sili-

con wafers with thicknesses well below 50μm, making this a highly relevant topic. This thesis focuses on light management in crystalline silicon solar cells.

Porous silicon (PS) holds great potential to solve several of the light management challenges, offering simplified and affordable processing schemes including PS ARCs, textures and backside reflectors. PS is well known to be a versatile, nanostructured material, which can be made by various etching processes on different crystalline silicon substrates. The porosity is closely related to the refractive index, which again is the key property to control reflection from a surface. Using anodic etching, the porosity can be tuned simply by varying the current density during formation. Consequently, a fast and simple formation process with excellent control of the reflection properties of the resulting PS layer can be obtained.

Anodic etching of PS is performed in hydrofluoric acid which is already present in the standard solar cell process. This means that no new health, safety or environmental issues are expected through its incorporation into an industrial setting. However, use of PS could replace other processes and materials requiring additional concerns, in particular silane. Silane is currently used in the enhanced chemical vapour deposition (PECVD) of silicon nitride ARCs and found in nearly all solar cell factories. Eliminating silane and the required safety precautions from a factory setting could have a large impact both on required capital investments and running costs of process lines.

With all the promising properties described above, it is no surprise that the use of PS in Si solar cells is not a new idea. It *has* been extensively studied, by competent and experienced scientist from a range of different research groups. According to Levy-Clement, one of the scientists that was actively involved in the development of PS ARCs in the late 1990's, they were a hairsbreadth away from commercial implementation [17]. The PS ARC was however beaten on the target string by the new SiN_x ARC, which not only had decent antireflective properties, but also provided excellent passivation.

So, why are we still spending time on investigating implementation of PS for light management in Si solar cells? As discussed in the previous section, the solar cell industry has seen an extraordinary expansion over the last ten to fifteen years, followed by a drastic decrease in cost per watt peak and payback time. Upscaling of the production is of course an important reason for these reductions, but not the only one. The efficiency of both lab scale and commercial large area cells have increased and a range of new cell concepts and manufacturers have emerged. As the market grows, new

unforeseen and foreseen problems, such as securing enough feedstock material have been encountered. Cell thickness is now less than half of what it was 10 years ago [18] and cost has gotten so low that every penny saved in the production process counts.

The point I try to make, is that the solar cell industry is a field of continuous development. Very good solar cells can be made using PS ARCs and although this technique did not win the previous run, demands set for the next run could suit the candidate better. The margins that separate success from failure are not only small, but also intimately intertwined with current status in cell design, production lines and cost. It is always difficult to predict which path takes you all the way and therefore, PS is one out of many paths that should be followed in order to make sure that we don't miss out on any opportunity to reduce the cost of solar cell energy. Renewable energy is one field where we cannot afford to miss out on any viable technology.

Therefore, although the road to commercial implementation may be long and winding, I believe that it is worth continuing research on PS for light management in Si solar cells. The simplicity of the process, without introducing any chemicals or materials that are not already used in the Si solar cell production, in combination with the versatility of PS material is difficult to ignore.

1.2 Thesis Outline

The primary goal of the work carried out towards the completion of this thesis, is to use porous silicon for efficient light management in silicon solar cells. Particularly the use of porous silicon for antireflection coatings is extensively studied. The work is comprised of two intimately intertwined parts; processing of porous silicon and use of these structures in solar cells.

Chapter 2 and 3 take the reader through the theoretical basis which constitutes the framework of this thesis. The theory presented should set out the premises of this thesis and hopefully provide sufficient background information to enable the reader to follow subsequent discussions. An introduction to PS; its properties and the etching process, is given in Chapter 2. Chapter 3 gives some insight into the wily optical finesse needed to obtain sufficient absorption in thin silicon solar cell. Starting with the material and source at our disposal, namely crystalline silicon and the solar spectrum, we look at the challenges and possibilities to maximize the efficiency. This includes a

look at various light trapping schemes and the possibilities of realizing these schemes in a solar cell. Finally, a review of the basic optics is given, providing the framework for subsequent design of optical filters with the desired properties.

Throughout the thesis, much effort has been put down in characterization of PS. For the final antireflection coatings, it is of course the optical properties which are cardinal, and reflectivity is the primary evaluation key. However, in order to control the optical properties, accurate and in depth information about structure is essential, requiring more demanding characterization techniques such as scanning/transmission electron microscopy, x-ray photon spectrometry and spectroscopic ellipsometry. Particularly, structural characterization of complex multilayered PS structures is a demanding task, where spectroscopic ellipsometry has been an indispensible tool and extensively utilized throughout the thesis. Chapter 4 is devoted to describing these characterization techniques and the fabrication setup for the PS structures.

Chapter 5 takes a closer look the process issues which must be considered and, if possible, accounted for in order to achieve accurate control of the etching process during fabrication of PS. Such process issues include electrolyte evaporation, chemical etching, pore seeding, film homogeneity, and repeatability. The main focus of this chapter is to deepen and elaborate on the material, discussions and assumptions made in the published papers. In particular Section 5.1, 5.2, and parts of Section 5.5 present material that is not covered in the articles. Summaries of the published results are included for context and completeness.

With these various process considerations established, Chapter 6 moves on to the design and fabrication of multilayer PS and the integration of these structures into solar cells. The antireflective layers on solar cells are located on top of the emitter and therefore highly doped Si substrates are a reasonable etching substrate. As a starting point, the use of in depth homogeneous substrates, instead of emitters with a certain doping profile, reduces the complexity of the etching process. In reality, the work in Chapter 5 and Chapter 6 is carried out in parallel in a continuous feedback process, increasing the insight in, and control over, the porosification process little by little. Some assumptions and approximations that are made in the multilayer design in Paper V and VI are discussed and refined in Section 6.4. After proving the concept of efficient PS multilayer antireflection coatings and studying the achievable efficiencies, more process realistic etching in emitter structures was attempted. Preliminary results from this work is presented in Section

6.3. Etching of the optimized PS ARC structure on multicrystalline material has been performed and is presented in Section 6.5. Hitherto unpublished results on application of PS structures as backside reflectors are presented in Section 6.6. The software used for ellipsometric modelling also constitutes the platform for modeling and optimization of the PS multilayers.

1.3 List and Summary of Papers

Papers included in this thesis are:

Paper I: J. H. Selj, E. S. Marstein, A. Thøgersen, S. E. Foss. *Porous silicon multilayer antireflection coating for solar cells; process considerations* Accepted for publication in Physica Status Solidi (c).[1]

Paper II: J. H. Selj, S. E. Foss, E. S. Marstein *Ellipsometric study of the influence of chemical etching on porous silicon* Accepted for publication in Thin Solid Films.[2]

Paper III: J. H. Selj, A. Thøgersen, P. Bergstrom, S. E. Foss, E. S Marstein. *Thin porous silicon films displaying a near-surface dip in porosity* Accepted for publication in The Electrochemical Society Transactions.

Paper IV: J. H. Selj, A. Thøgersen, S. E. Foss, E. S Marstein. *Ellipsometry and XPS comparative studies of oxidation effects on graded Porous Silicon antireflective coatings* Accepted for publication in The Electrochemical Society Transactions.

Paper V: J. H. Selj, S. E. Foss, A. Thøgersen and E. S. Marstein. *Optimization of multilayer PS antireflection coatings for silicon solar cells* Journal of Applied Physics 107 (2010).

Paper VI: J. H. Selj, R. Søndenå, T. T. Mongstad and E. S Marstein. *Reduction of optical losses in colored solar cells with multilayer antireflection coatings* Accepted for publication in Solar Energy Materials and Solar Cells.

[1] PSST 2010 proceedings issue
[2] ICSE-V proceedings issue

Paper I deals with the repeatability and homogeneity of the porous silicon etching process. Selective electrolyte evaporation is found to cause relatively large variations in etch rate and porosity over time. Sample homogeneity and process repeatability is studied and the effects on graded antireflection coatings for solar cells are assessed.
Paper II presents a study of the effect of chemical etching on the processing of graded ARCs. As the etching time necessary to fabricate these multilayers is so short, no adjustments of the current density needs to be adopted to correct for this chemical etching.
Paper III discusses the porosity profile of single layer PS films as determined by spectroscopic ellipsometry. Specifically, a dip in porosity close to the surface of the layers is discussed in detail.
Paper IV considers possible effects on the reflection properties of the antireflection coatings due to oxidation of PS. Results obtained by ellipsometry is compared to chemical analysis performed by XPS.
Paper V presents the modelling and fabrication of a porous silicon ARC structure optimized for use in solar cells. Weighting of the reflection spectrum is performed with respect to angle of incidence and the solar spectrum. Scenarios with and without module glass is explored. An integrated reflectance of $\sim 3\%$ is achieved.
Paper VI presents a comparative study of colored antireflection coatings made by SiN_x and PS. It is shown that a range of different colors can be obtained, while retaining excellent antireflection properties. This is interesting to increase the use of building integrated photovoltaic systems.

Chapter 2

Porous Silicon Fundamentals

This chapter gives a short review of the fundamental concepts behind the formation and resulting structure of porous silicon (PS). The center of attention will be the aspects of PS which are directly relevant for the solar cell applications explored in this thesis. The chapter facilitates the basis for discussions around the presented results. We also seek to highlight both fundamental and practical, application specific limitations which define the accessible PS structures.

As a proper commencement, Section 2.1 places PS in a historical setting. This is followed by an introduction to the most traditional means of studying PS formation, namely the I-V curves. From here we sketch a framework consisting of the basic electrochemical reactions and the morphology of the resulting structures. Weight is put on how the anodization conditions and substrate properties affect the PS structure. We touch upon some of the numerous, and so far incomplete, formation models developed to describe the physical and chemical mechanisms that link the etching parameters to the resulting morphology. In Section 2.6 the optical properties of PS relevant for this work are briefly reviewed. Finally, in Section 2.7 the effect of ageing on PS is discussed.

2.1 History

As so many discoveries before, that of PS was an accidental one. In 1955 Arthur Uhlir Jr. and Ingeborg Uhlir worked at the Bell laboratories in the US developing a technique for polishing and shaping the surfaces of silicon

and germanium. Under certain conditions a thick colored film was formed on the silicon surface [19]. As this did not provide the smooth polish desired, the results were reported in the Bell labs technical note, but otherwise pretty much ignored [20]. Some early important papers did appear in the 1960s to 1980s [21–25] and one of the first reports on PS for solar cell applications was published as early as 1982 [26].

However, it was the discovery of PS luminescence [27, 28] which really spurred PS research in the late 1980s. In the mid nineties the material's low luminosity and stability problems led to a waning interest for its use in optoelectronic applications. In the same time period, the large surface area and controllable pore sizes of PS began to inspire research on other applications. The earliest application of PS in solar cells was as antireflection coating on a p^+ emitter [26], an application that is still actively researched today. The application of PS as an antireflective coating in silicon solar cells will be the main focus of this thesis, but a few other applications will also be touched upon. Several other potential advantages of using PS in solar cells were also discussed early on [29, 30]. Since then some of the old application ideas have been rejected and many new ideas have emerged. In particular, several concepts have arisen from the need to cut down on silicon consumption; PS as surface conditioning for layer transfer [31] and PS for epitaxial free layer transfer [32]. PS used as rear side reflector is not a new idea, but has received renewed attention due to the evolution towards thinner cells [33–35]. Before we pursue the applications any further, a closer look at the formation and properties of PS is in order.

2.2 Anodic Etching of Porous Silicon

There are two well known techniques commonly used to fabricate PS; stain-etching [36] and anodization [19]. In the stain-etching method, hydrofluoric (HF) acid is mixed with a strong oxidizing agent such as nitric acid, and no external bias is needed. This is a simple method which can give very thin layers, but it has poor control over reaction parameters compared to the anodization technique. Anodization under galvanostatic conditions is generally the preferred approach for reproducibility, attaining wide ranges of porosity and thickness.

For electrochemical etching of PS, the Si wafer is placed in an externally biased etching cell with platina electrodes and an electrolyte consisting of

HF, water and/or ethanol plus possible additives. A platinum electrode constitutes the cathode, while the Si wafer constitutes the anode. Alternatively, both cathode and anode are platina electrodes and the wafer forms a seal separating the front and rear half cells. When a potential is applied, a measurable external current is induced to flow through the system. Holes from the sample move towards the electrolyte-substrate interface where they react with F^- ions from the electrolyte. Under appropriate potentials, this reaction results in PS formation on the side of the wafer which faces the cathode electrode. The anodization technique has been used for fabrication of all PS layers in this thesis and we shall therefore elaborate on this technique in the following sections.

2.2.1 I-V Characteristics

The traditional way of studying PS formation has been by characterization of the evolution of the I-V curve during electrochemical etching [37]. Figure 2.1 shows a typical plot of an I-V curve of p-type Si in an electrolyte containing HF. Two characteristic current peaks, J_1 and J_2 are displayed in the figure. At small anodic overpotentials, the current increases exponentially with the electrode potential, this is where PS is formed. After the exponential increase, the current reaches a peak, J_1. For potentials, V, higher than $V(J_1)$, formation and dissolution of a surface oxide film result in a smooth surface. This is the electropolishing regime. At potentials higher than the second peak, $V(J_2)$, current oscillation may occur. The values of these characteristic currents are a function of electrolyte composition, but are largely independent of doping [38].

Figure 2.1 also shows that illumination of the sample during etching has very little effect for p-type Si under anodic overpotential. As holes are already the majority carrier, the relative contribution of the photo-induced holes is very small. For n-type Si, illumination is known to have a large effect. For p-type Si and a cathodic overpotential, there is no dissolution of Si, but a high hydrogen overpotential and H_2 gas evolution. Illumination in this regime will result in a photogenerated current proportional to the light intensity. The I-V curve of n-type Si will be somewhat different, but as etching in p-type Si is the focus of this thesis, we concentrate on the I-V curve for p-type Si.

The I-V curve resembles that of a Schottky diode, with a few important differences. Most notably the two peaks, J_1 and J_2 seen in the I-V curve under forward bias are not found for a normal Schottky diode. The reason

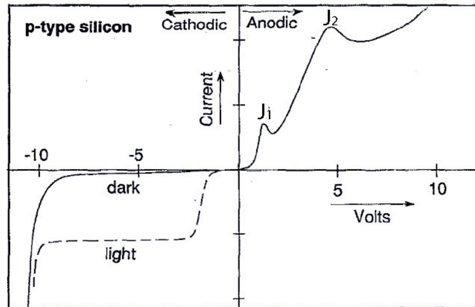

Figure 2.1: I-V curve for electrochemical etching of p-type Si under cathodic and anodic potential. Adapted from Smith and Collins [37].

for the similarities lies in the resemblance of the Si/electrolyte barrier system to that of the metal/semiconductor barrier system of a Schottky junction [37, 39]. The energy levels of electrons in the electrolyte are characterized by the redox potential, E_{redox}. This potential describes the tendency of the species to give up or accept electrons and can be considered the effective Fermi level of the solution. Equilibrium between the semiconductor and the electrolyte is attained when the Fermi levels in the two phases become equal, resembling a Schottky contact. A Schottky diode models the Si electrolyte interface accurately only as long as the charge transfer is limited by the electrode [39, Chap. 3].

The resulting excess charge in the solid semiconductor is distributed in a region near the surface called the space charge region or depletion region because it is devoid of carriers. On the electrolyte side, there exists an ionic layer which can be further subdivided into a Helmholtz layer and a Gouy-Chapman layer [40–43]. The actual thickness of these three depends on doping level, electrolyte concentration and bias [44]. Lehmann [39, Chap. 3] and Zhang [38, Chap. 2] provide extensive descriptions of the Si/electrolyte interface.

2.2.2 Electrochemistry

Although there is still controversy regarding the exact nature of the reaction kinetics of PS formation, many aspects of the process are known. Any

complete and successful model must account for all these findings.

For any current to pass the Si/electrolyte interface it must first change from electronic to ionic charge carriers. This conversion is always accomplished by means of a specific chemical redox reaction at the Si interface. The surface of Si in a HF solution will be hydrogen terminated. This was discovered in the late 1980s/early 1990s [38, Chap. 5] and led to modifications of the early models. For a hydrogen terminated Si surface, the first step in the dissolution of Si involves a replacement of a surface hydrogen atom with a negatively charged fluorine ion, F^-. The released hydrogen gives the characteristic H_2 bubbles, observed already by Memming and Schwandt [21] in 1966. The absorption of fluorine also polarizes the Si-Si back bonds, making them an easy target for chemical attack by HF and H_2O molecules [45].

In the so called direct dissolution path, leading to a porous structure, the Si-SiF bond is broken by reacting with HF. The Si surface is again hydrogen terminated while the fluorine terminated Si atoms are dissolved into the solution where the Si complex is further hydrolyzed. In the process, one electron from the broken Si-Si bond is transferred to the hydrogen of the new Si-H bond, i.e. a hydrogen ion is reduced by an electron from the Si-Si bond [46].

For higher potentials, the fluorine terminated Si atoms react with H_2O (instead of HF) to form Si-O-Si bonds which are not stable in HF. This is the onset of indirect dissolution of Si through formation and dissolution of oxide and corresponds to electropolishing [46].

Regardless of whether pore formation or electropolishing occurs, the final, stable end product for Si in HF is H_2SiF_6 [37]. An illustration of the reactions is given in Fig. 2.2.

In the pore formation regime, it is found that $2 - 2.8$ electrons are dissolved per Si atom [47, 48]. As seen from Fig. 2.2, the valence resulting from the suggested pore formation model is exactly two. This reflects the shortcomings of the model used and the complexity of the reaction. During electropolishing, four electrons are dissolved per Si atom removed, as seen from the lower path in Fig. 2.2.

It is clear that the choice of reaction path depends on the potential [39, Chap. 4]. The coverage of the surface Si-O-Si bonds increases with increasing potential (increasing hole density) and the surface becomes increasingly less active until it is passivated when the bonds completely covers the surface [46]. However, the interplay between oxide formation and removal rates also makes

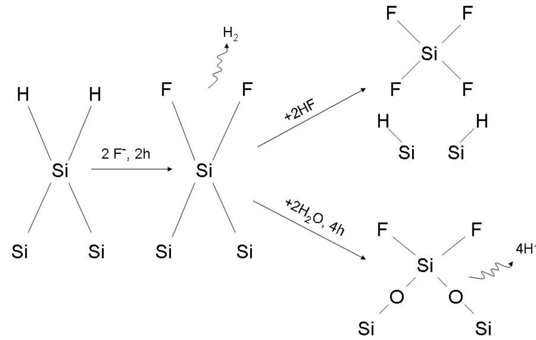

Figure 2.2: The two possible reaction paths during anodic etching of Si. The upper path shows direct dissolution leading to porousification. The lower path shows indirect dissolution via an oxide, leading to electropolishing.

the processing of PS sensitive to the HF concentration in the electrolyte. Low HF concentrations give low oxide removal rates favoring electropolishing [44]. Note that the reaction process is determined by the chemical nature of Si and the electrolyte, but is independent of the electronic nature of Si [38].

The reaction path described above explains the removal of Si, but it does not explain the selectivity which leads to pore formation. Therefore, additional models are used to explain pore formation and the final geometry of PS. All of these models start with a Si surface where small pits or pores are already formed. In Section 2.5, a few of the most influential formation models are presented. However, let us first take a look at the shapes and structures that, together with the electrochemical reactions, have been the starting point for constructing theories regarding the underlying formation mechanisms.

2.3 Morphology

Morphology is the study of shape, size, texture, and phase distribution of physical objects. The morphology of PS is therefore a broad term, em-

bracing all physical features which describe the dimensions of the material. Properties such as pore size, porosity and structure are often used to attempt to quantify the morphology. One can further look at the orientation of the pores, the sort of branching they reveal, their shape and how they vary with depth. In PS all these properties show great variation depending on the etching conditions. A schematic summary and a thorough description of different pore structures found in literature are given by Zhang [38].

Following the definitions set by the International Union of Pure and Applied Chemistry (IUPAC), three pore size regimes exists. Pore sizes less than 2 nm are denoted nanoporous, between 2 and 50 nm are mesoporous and above 50 nm are macroporous. The pore size is defined as the distance between two opposite walls of the pore and covers four orders of magnitude in the case of PS. Although it is the different pore formation mechanisms and pore morphologies that are fundamental, pore size is a classical way of classifying PS.

PS porosity is simply a measure of the amount of Si etched away during the formation. The porosity range available to different pore regimes does vary, but porosity is principally dependent on the current density passed and the HF concentration in the electrolyte during etching.

2.4 Influence of Formation Parameters

A wide parameter space is available for variations under anodic formation of PS. Table 2.1 provides a simplified summary of the influence of various parameters. We will take a more nuanced look at each of the listed parameters in the following section.

Table 2.1: Parameter influence on PS etching

Parameter (increasing)	Porosity	Etch rate	Electropolish	Pore diameter
HF concentration	decrease	increase	increase	decrease
Current density	increase	increase	-	increase
Time	increase	-	-	-
Temperature	-	-	increase	-
Resistivity (p-type)	increase	decrease	decrease	decrease
Resistivity (n-type)	decrease	decrease	-	increase

2.4.1 Wafer Doping

We have seen that the doping concentration does not affect the nature of the electrochemical reactions. However, it is a principal factor in determining the morphology of PS. Therefore, one way of grouping the PS morphology is by type and concentration of substrate doping: i) lowly doped p-Si, ii) moderately doped p-Si, iii) lowly/moderately doped n-Si, and iv) highly doped n- and p-Si. As a general rule, the size of the pores typically increases with increasing doping concentrations for p-Si, while it decreases with doping concentration for n-Si [46]. In lowly doped p-Si, two distinctive pore diameter distributions can result: large pores in the order of micrometers and small pores in the order of nanometers. In moderately doped p-Si the pores are rather small, typically ranging from $1-10$ nm and generally highly interconnected. Low/moderately doped n-type Si results in a very complex morphology, showing a wide range of pore diameters, from 10 nm - 10μm. Clearly separated, smooth pores with large aspect ratios have been obtained for these doping levels [49]. High doping densities typically produce mesopores and little morphological differences are expected between n-type and p-type material. Adding large formation current densities on these substrates results in pore dimensions approaching the macroporous regime with typical pore size ranging from $10-100$ nm. The pores show clear orientation and less interconnection than those formed on moderately doped p-Si.

The etch rate of nano and macro PS shows little dependence on doping concentration, while that of mesoporous PS shows a strong dependence. The dependence of pore size on doping is summarized in Table 2.2 [46]. The

Table 2.2: Influence of doping and resistivity on pore diameter.

Substrate type	Doping (cm^{-3})	Res (Ωcm)	Resulting pore size
	$< 10^{15}$	< 13.5	$1-10$ nm and $> 1\mu$m
p-type	$10^{15}-10^{18}$	$13.5-0.04$	$1-10$ nm
	$> 10^{19}$	0.009	$10-100$ nm
	$< 10^{18}$	0.02	10 nm - 10μm
n-type	$> 10^{19}$	0.005	$10-100$ nm
	illumination	...	$1-10$nm and 50nm - 10μm

dopant distribution in Si wafers is usually slightly inhomogeneous. This can result in corresponding local inhomogeneities in etch rate and porosity. These

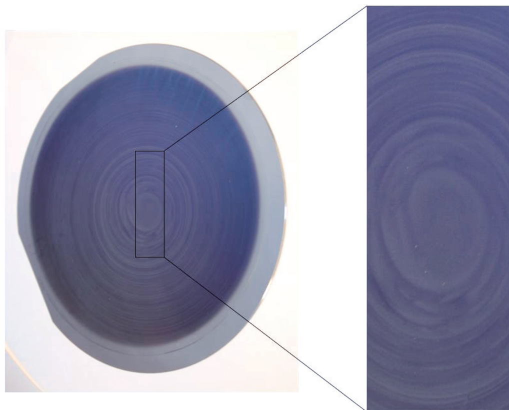

Figure 2.3: Striations are clearly visible in this PS layer. The wafer has a diameter of 4 inches.

inhomogeneities are visible on the surface of some of the porous structures fabricated for this thesis, as small deviations in color. They can best be described as concentric circles with origin roughly in the center of the wafer.

This type of doping inhomogeneity is recognized as striations, a well known issue in Si-technology [50]. Figure 2.3 shows visible striations on a thin sample etched at constant current density.

2.4.2 Current Density

The current density affects the porosity, etch rate and pore diameter. In general, increased current density leads to an increase in all of these parameters. When other parameters are held constant, the current density governs whether the Si wafer will be etched or electropolished, high current densities giving electropolishing, lower current densities leading to PS formation.

2.4.3 Electrolyte Properties

The basic constituents of the electrolyte used for PS etching is HF and solvent. The nature of this solvent determines whether the electrolyte is termed

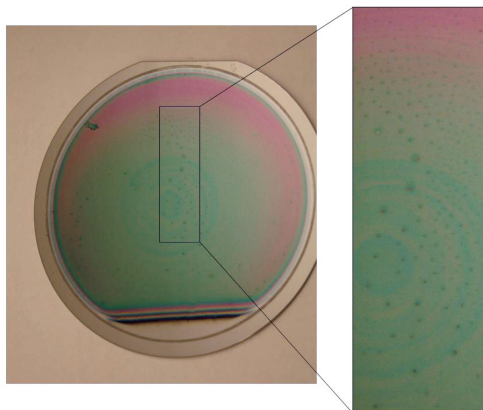

Figure 2.4: The small dots seen in the middle of the sample are likely inhomogeneities produced by H_2 bubbles during formation of the layer. The visible color difference springs from larger scale thickness inhomogeneities. The wafer diameter is 4 inches.

aqueous electrolyte, for solvents comprised mainly of water, or *organic electrolyte*. For all samples etched in this thesis, electrolytes consisting of water and ethanol are used. The term aqueous electrolyte is used also when ethanol is added [49]. The ethanol serve to reduce surface tension, and thereby improve the removal of hydrogen bubbles formed during etching. Reduced surface tension will also improve the infiltration of the electrolyte in the nanometer sized pores. Concentration of HF in the electrolyte has a large impact on the resulting porous structure. If other parameters are fixed, increased concentration of HF results in decreased porosity and increased etch rate. HF concentration is also important for determining the onset of electropolishing. Local variation in HF concentration can cause roughness on the millimeter scale and may be caused by inhomogeneous electrolyte convection at the electrolyte-electrode interface or by bubbles that stick to the electrode surface. Marks on the PS layer likely resulting from H_2 bubbles are clearly displayed in Fig. 2.4.

2.4.4 Illumination

Illumination is essential for supplying the required holes for electrochemical etching of n-type Si. It also plays a major role in determining the resulting morphology. The I-V curve of p-type Si (Fig. 2.1) does not show any dependence on illumination in the anodic regime. However, illumination may be used to produce smaller structures in p-type material. For p-type samples a depletion of holes in the porous layer passivates the PS from further dissolution. Light-assisted generation of holes allows a further attack of the porous structure and results in a reduction of the size of nanocrystals according to the quantum model [51].

2.4.5 Drying

When air drying PS, a meniscus will form in the pores, giving rise to capillary stress on the pore walls. The mechanical stability of highly porous films may not be sufficient to withstand this stress [52], resulting in cracking, peeling and shrinkage of the film. Visible inhomogeneities, like small speckles, were indeed observed on the surface of high porosity PS layer after cleaning in water (with a surface tension of 72 mJ/m^2). The stress on the pore walls can be reduced by choosing a liquid with low surface tension for cleaning the layers prior to drying. We therefore exchanged the cleaning substance to ethanol because of its lower surface tension (22 mJ/m^2). Cleaning substances with even lower surface tension and other drying techniques do exist [52], but cleaning in ethanol seems satisfactory for the samples fabricated for this work.

2.5 Formation Models

Different concepts are invoked when explaining the formation of different pore types. To a certain extent this is a natural development because of the wide range of pore dimensions. Quantum confinement for instance, is important for the small scale displayed in nanoporous material, while it is not relevant for macropores. Many aspects of the formation process are known, but a single theory which can provide a globally coherent description of the nature of the reactions and the resulting PS morphology is still sought for. However, several models are suggested and we will take a look at a few of them. Although a few pages will be spent on the formation theories of PS,

this is far from a comprehensive review and the reader is referred to Smith and Collins [37], Zhang [38, 46], and Föll et al. [49] for further reading.

Three important formation models for PS are the Beale model, the diffusion-limited model and the quantum confinement model, each explaining certain aspects of PS formation. The Beale model [25] was one of the first models to arise and many of the concepts proposed in this model have been adopted and further developed in later models. The diffusion-limited model [53] explains pore structure in terms of diffusion instead of electric fields, but is really equivalent to the Beale model [37]. The quantum model [28] explains pore formation in terms of increasing band gaps due to quantum charge confinement within the small dimensions of the Si wires formed in PS.

It is experimentally observed that the resistivity of p-type PS is similar to that of undoped Si, indicating that the pore walls are depleted of free carriers [25]. In all three models, this lack of carriers leads to preferential etching at the pore tips. It is the reason for the carrier depletion which is different, the Beale model explaining it by overlapping depletion regions, the diffusion-limited model describing it by random walk, and the quantum confinement model accounting for it by, exactly, quantum confinement. Different depletion mechanisms are typically invoked to describe different pore sizes, and this led Lehmann et al. [54] to an attempt to unify the theories on the formation mechanism of all types of PS. Figure 2.5 shows the organization chart put forward by Lehmann et al. [54]. We see that the depletion mechanism for nanopores is quantum confinement, while for larger pores the space charge layer formation is responsible. This depletion by the space charge layer is further divided into groups. Although this organization of the models seems to cover the whole range of pore formation mechanisms, it does not constitute a coherent theory [38]. The final model discussed, the current burst model, may have potential to constitute a more general model. The model is still qualitative in nature, but already it supplies explanations of observed phenomena not obtainable in other models [49].

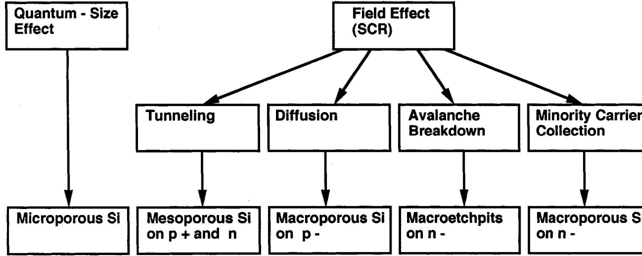

Figure 2.5: Top row - effects proposed to be responsible for pore wall passivation. Middle row - effects responsible for passivation breakdown at the pore tip. Bottom row - resulting kind of PS structure. Note that the term microporous is equivalent to nanoporous. Adapted from Lehmann et al. [54].

2.5.1 The Beale Model

Beale et al. [25] suggested that the high resistivity of PS was due to overlapping depletion regions in the pore walls. As a result of this lack of mobile carriers in the inter-pore regions, current is selectively directed to the pore tips. The model rests on the premise that the large surface state density of the Si surface in the PS film results in pinning of the Fermi level [25]. The pinning of the Fermi level is necessary to obtain sufficient carrier depletion under anodization potentials.

Let us now take a look at how doping affects the system. With increasing doping density the electric field strength increases and the width of the depletion region decreases. A narrow depletion region enables charge carriers to pass through the depletion region by tunneling. The width is at a minimum at the pore tips because of the electric field distribution, so maximum current flow will occur here [25]. For planar Si, tunneling will dominate the charge transfer for doping densities in excess of $2 \cdot 10^{19}$ cm^{-3} [25]. For lower doping densities, we see a difference between p-type and n-type Si. P-type Si will be under forward bias, while n-type Si will be under reverse bias under the anodization potential. For lightly doped p-type Si, a forward bias will reduce the majority carrier barrier and thermionic emission will dominate the charge transfer. In this case the barrier height, rather than its width, determines the current flow. For n-type doping, the reverse bias permits avalanche breakdown at sufficiently high potentials. Theunissen [23] first

proposed that PS formation in n-type Si results from reverse bias breakdown because of high fields concentrated at the pore tips.

We have now seen how the doping affects the charge transfer process responsible for the pore growth. Doping also affects the morphology. The depletion of the pore wall is assumed to be the reason for preferential etch at the pore tips. If the distance between the pores then becomes significantly larger than twice the depletion width, the pore walls are no longer depleted. Branching of the pores is then possible and these branches would penetrate this region until depletion is again established. As a consequence, pores tend to space themselves at distances below two times the width of the depletion region. We then see that the spacing of the pores is related to the depletion width and thereby the doping. The pore diameter is also related to the depletion width, W. For highly doped p-type or n-type Si, the pore diameter is comparable to W. For low doped n-type Si the pore diameter is much smaller than W.

The Beale model explains pore formation using well known solid-state terminology. It is however somewhat questionable whether the classic Schottky junction analogy actually applies to the Si/HF system and whether the Fermi level is actually pinned [37].

2.5.2 Diffusive Transport

The diffusion limited model describes the formation of PS in terms of a stochastic random walk. The basis of the model is diffusion limited annihilation proposed by Meakin and Deutch [55]. The diffusion limited annihilation model is based on the older diffusion limited aggregation model [56]; particles undergoing a random walk, due to Brownian motion, cluster together and form aggregates. When applying the diffusion model to PS, diffusion limited annihilation is used to acknowledge that PS is a dissolution process and not a growth phenomenon [57]. For PS it is the diffusion limited rate of hole transfer from the bulk of the Si to the pore surface that is the primary factor responsible for the formation [53]. The preferential etch of the pore tips is explained by the shorter diffusion distance for the holes coming from the other side of the wafer. It is then simply the nature of the random walk which explains why the pore generation preferably happens at the pore tips. The different pore morphologies are controlled by a characteristic diffusion length which again depends on experimental parameters such as dopant concentration and voltage [37, 53]. Figure 2.6 shows the two formation regimes,

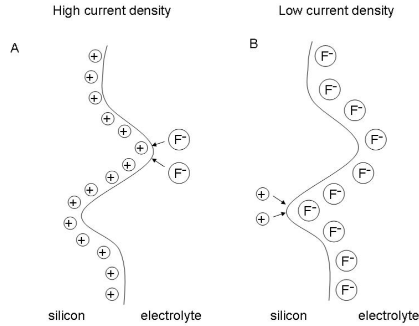

Figure 2.6: Two formation regimes. Electropolishing results for high current densities where the mobility of the flour ions in the electrolyte are limiting. PS films results for low current densities where the hole concentration at the surface is limiting.

porosification and electropolishing, illustrated within the frame of the diffusion model. For high hole densities, when the mobility of the fluorine ions is the limiting factor, random walk leads to a selective etching of peaks on the Si sample, giving a polished result. When the hole concentration is the limiting factor, selective etching at the pore tips results. As discussed by Smith and Collins [37], the main advantage of the diffusion limited model is that it can be generally applied to all systems, because of its construction in terms of standard diffusional physics. Therefore the diffusion model avoids some of the debated issues related to the Beale-model; neither Fermi level pinning nor Schottky barrier needs to be assumed. The Beale model and the diffusion limited model are in fact two sides of the same story. According to Smith and Collins [37] a fundamental equivalence between the two models arise from a mathematical equivalence between the spatial electric and diffusional field distributions.

2.5.3 Quantum Confinement

The quantum confinement theory was first proposed by Lehmann and Gösele [28] to explain the low absorption of visible light in PS etched on moderately doped p-type Si. A lowered absorption in the visible is equivalent to an increased band gap compared to bulk Si. This is reasonable as moderately doped p-type Si typically produces nanoporous material, consisting of interconnected crystallites of a few hundred Si atoms. In structures of such small dimensions the motion of the particle is restricted and this quantum confinement gives an increased band gap. For PS formation, this is interesting because an increased band gap would also lead to fewer carriers in the pore walls. The increased energy in the pore-walls produces an energy barrier, making it energetically more favorable for the holes to travel directly via the pore tip than through the porous, quantum confined structure. If a higher current density is applied, the holes cross the barrier more easily. The porous skeleton will then be etched thinner and thinner until the now stronger quantum confinement again dominates. The same is true for illumination; the photogenerated holes initiate dissolution of the pore walls, this reduces their size and thereby increases their bandgap energy until it is higher than the photon energy, which establishes passivation again [39].

Quantum confinement was put forward as a formation mechanism for PS etched on moderately p-type Si. It is unlikely that quantum effects regulate pore formation in p^+ Si, or especially in n-Si where the inter-pore dimensions can be as large as several micrometers [37]. It might however seem like the lower limit for the pore dimensions is governed by the quantum aspects of charge confinement. The quantum confinement model has been extended to include tunneling probabilities between the walls and the bulk. It is, however, still qualitative in character, and a quantitative correlation between the anodization parameters and the morphology and properties of the porous structure is not determined [39].

2.5.4 The Current Burst Model

A complete model of the electrochemistry of Si should explain the wide range of pores, the I-V characteristics and also accommodate results which have been used to validate the models described above [49]. The current burst model assumes that current flow is spatially and temporally inhomogeneous [58]. This starting point is a key concept in the model and separates the

model from other electrochemical considerations of Si where the current flow generally (and incorrectly according to Föll et al. [49]) is assumed homogeneous. An electrochemical process that dissolves Si involves four different net chemical reactions; direct dissolution, oxidation, oxide dissolution, and hydrogen coverage. The current burst model postulates that there are definite correlations between the four basic processes. The event sequence starts with direct dissolution, followed by oxidation, oxide dissolution and finally hydrogen passivation if there is no immediate new current bursts [49]. This is a potentially promising model, but there is still a long way to a global and quantitative description of PS formation.

2.6 Optical Properties

As mentioned introductorily, the PS research really gathered headway when its luminescent properties were discovered. However, due to low and unstable luminosity, in time focus shifted to other qualities of PS. Although luminescence is an important and thoroughly studied aspect of PS, this section will leave it be, as it is not utilized in the applications addressed in this work. Instead attention is drawn to optical aspects of PS which are more relevant for the setting of this thesis, such as optical anisotropy and absorption. The possibilities of light management in solar cells that arise due to the controllable refractive index of PS will be thoroughly explored in Chapter 3 and 6.

2.6.1 Anisotropy

Optical anisotropy, or birefringence, is experienced in media where the speed of light is different in different directions. This means that the optical constants are directionally dependent. If all three directions are different, the material is biaxially anisotropic. If only one axis is different, the material is uniaxially anisotropic.

It is well known that PS may exhibit significant optical anisotropy [52, 59–64]. This is not introduced by Si itself, as the diamond lattice structure of c-Si is highly symmetric and exhibits very little birefringence [65]. It is also known that formation of pores does not seem to destroy the short-range order in the Si crystal and the material between the voids retains its crystalline structure [61]. Two reasons have therefore been invoked to explain

this dielectric anisotropy in PS: (i) The stress present in the PS films, (ii) an anisotropic morphology of the PS skeleton. Given that the PS nanostructure retains the diamond structure, the estimation performed by Mihalcescu et al. [62] showed that the birefringence caused by lattice distortion is much too small to be responsible for the anisotropy of the porous layers. Therefore, the observed birefringence is due to shape anisotropy in the porous structure which induces distinct boundary conditions to the electrical and magnetic fields in the material.

As the optical anisotropy is induced by the shape of the pores, it is not surprising that the amount of birefringence in PS is closely related to the etching conditions, doping level, and crystallographic direction of the substrate. For highly doped ($> 10^{18}$ cm^{-3}), (100) oriented, p- and n-type substrates, interconnected, elongated pores are expected, leading to pronounced anisotropy. For PS layers grown on lightly doped ($< 10^{16}$ cm^{-3}) p-type substrates the anisotropy is less severe [66].

A dependence on porosity is also found; PS layers etched on heavily doped Si experience an increase in the birefringence with porosity, while layers grown on moderately doped substrates will experience a decrease in birefringence with porosity [66]. This is probably due to the less ordered position of pores in the PS layer formed on moderately doped Si [61].

One way of assessing the degree of anisotropy is by the optical anisotropy parameter, β. It is defined by

$$\beta = 100\%(n_e - n_0)/n_e, \tag{2.1}$$

where n_e is the extraordinary refractive index, while n_0 is the ordinary refractive index. $n_e > n_0$ corresponds to positive birefringence, while $n_e < n_0$ corresponds to negative birefringence. In Section 4.3.5 an alternative terminology for optical anisotropy, which is more conveniently used during ellipsometric modeling, is introduced.

2.6.2 Absorption

Optical transmission measurements of PS have traditionally been a way to disclose information about the mechanisms behind PS luminescence and a number of papers have been published on the subject.

Absorption in PS is really the sum of absorption from a high number of individual nanocrystals of different band gaps. The absorption therefore, is

an average characteristic of the sample [67]. The deviation of this integral absorption of PS from that of crystalline Si has two sources. First, during anodization a significant amount of Si material is removed. The remaining material consists of Si nanocrystals and pores of air. When the wavelength of the absorbing light is much larger than the typical dimension of the nanocrystals, an effective medium approximation can be used to solve the problem of a local field inside a nanocrystal. This is further discussed in Section 4.3. Second, the effect of reduced density of states must be accounted for [28]. At small scales, the energy spectrum becomes discrete, the number of electronic states is reduced and the bandgap therefore is size dependent. If quantum confinement effects are present, this leads to a significantly increased optical transmission below the direct gap ($\sim$ 3 eV) [67]. This is commonly referred to as a blueshift.

For large crystallites (tens of nm), the traditional understanding has been that the bandgap remains at its original energy due to continuous energy states. The change in absorption should then be purely due to depolarization field effects and be well approximated by effective medium approximations [67–69]. However, several more recent papers seems to complicate this picture somewhat. Lerondel et al. [70], and Diesinger et al. [71] both report that their observed absorption spectra cannot be explained by a shift of the absorption simply due to an increase of the Si gap, as would be expected in quantum confined structures. Instead, the effect of the large distribution of crystallite sizes and large scale disorder is suggested as possible reasons for the irregular deviation from the Si absorption spectrum.

2.7 Ageing of PS

PS films are significantly more chemically reactive than bulk Si. This is largely due to their very high internal surface area, varying from $200 - 600$ m^2/cm^3, depending on formation conditions [72]. Freshly etched PS films react slowly with ambient air and consequently both the structural and optoelectronic properties can continuously evolve with storage time from minutes to months.

Fresh, as-prepared PS is initially covered by hydride species (SiH, SiH_2, SiH_3) [73]. After only hours in air ambient, a rapid, but partial, oxidation takes place through oxidation of Si (Si-O bonds). The compounds Si_2O, SiO, Si_2O_3, and SiO_2 are commonly found in oxidized Si samples and are

also expected in PS [74, 75]. A further, somewhat slower, oxidation continues through the formation of Si-O-Si groups, but also formation of O-Si-H and O_3-Si-H groups that do not modify the hydrogen passivation [76]. In addition, amorphous Si (Si:H) [75] and various forms of fluorine [77] and carbon impurities [76] have been repeatedly detected.

For practical application of PS structures, the ageing effects of the material must be known and preferably be possible to control. A number of options exists, such as oxidizing the material in a controlled manner, impregnate the pores or cap the surface. Alternatively, the storage time and conditions can be optimized for the given application requirements [52].

It is important to emphasize that the oxidation effects vary greatly with respect to the porosity, morphology and thickness of the PS structures. Even for nominally very similar samples, the differences are surprisingly large [78]. What is clear is that after weeks of ambient air exposure, oxygen and carbon levels of several tens of percent are commonly observed [78].

Experiments to study the effect of oxidation on the optical properties of PS, and on the multilayer PS antireflection coatings specifically, is carried out. Procedures and results are described in Paper IV and also discussed in Chapter 5 of this thesis.

Chapter 3

Light Management in Silicon Solar Cells

A solar cell, or more generally a photovoltaic device, employs the photovoltaic effect to generate electric current directly from sunlight. The principle was observed by Edmund Bequerel already in 1839 and Charles Fritts is credited for preparing the first solar cell in 1894. A major contribution to understanding the photovoltaic effect was Einstein's explanation of the photoelectric effect in 1905. However, it took almost a century before research on using photovoltaic devices for power production were initiated. The first Si solar cell was reported by Chapin, Fuller and Pearson in 1954 [79] and converted sunlight with an efficiency of 6%. The efficiency rose significantly over the following years, but with estimated production costs of $200 per Watt, power production by solar cells seemed highly improbable. The 1970's oil crisis led to an increased interest in alternative sources of energy, and a range of different photovoltaic devices were explored. Still, little commercial development resulted. During the 1990's an awareness of the need to secure alternative, and preferably 'green', sources of electricity grew, and the interest in photovoltaics expanded. Since then, large cost reductions and significant efficiency increases have made photovoltaic energy a tangible supplement to conventional energy sources. For this trend to continue, further advances in the cost-efficiency is essential.

The three primary factors that determine the generated current in the solar cell is the incident light, the cells ability to absorb the light, and the cells ability to separate and transport the charge carriers. This chapter deals primarily with the interplay between the two first factors. Although the

effect of the alternative processing steps on electrical properties of the cell is very important, the separation and transportation of the charge carriers are not the focus of this work.

The first two sections (3.1 and 3.2.1) in this chapter presents the starting points; the incident solar spectrum and the properties of silicon as a solar cell material. Although, solar cells today are made from a range of different materials, silicon retains a market share of almost 90% [16]. The typical processing steps in the fabrication of a silicon solar cell are briefly addressed in Section 3.2.2. A comparison of the incident solar spectrum and the optical response of silicon clearly illustrates both some of the fundamental - and some of the more practical - difficulties of exploiting all incident radiation. The scope of this thesis is restricted to the 'practical' challenges; trapping the energy that is within the inherent absorption range of silicon. Section 3.3 provides a theoretical description of the optical concepts relevant for manipulation of light into and within the cell. Section 3.4 elaborates on the more concrete paths to improve light collection and how they can be implemented in a silicon solar cell. Both conventional light trapping structures and possible PS structures are discussed. Section 3.2.2, where the processing steps were described, now facilitates a basis for assessing the feasibility of implementing various optical structures in practice. The structures must not only be cost effective, but also be compatible with preceding and subsequent processing steps.

3.1 The Unalterable Source

The fundamental starting point which cannot be circumvented for any earth based solar cells is the spectrum of photons received on earth. Sure, you can up convert, down convert, and concentrate, and indeed, there are large variations with regard to latitude, longitude, altitude, and local topography. But the available incident energy will, inevitably, be distributed more or less like that of a $\sim$ 5800 K blackbody, notably with some distinct atmospheric absorption bands. The atmosphere not only attenuates the incoming radiation, it also scatters. The fraction of diffuse light will vary according to weather and latitude. Due to these varying atmospheric and geographical conditions a standardized terrestrial solar spectrum is defined, with a global air mass of AM1.5 and a spectrally integrated energy flux of 1000 W m^{-2}. The air mass quantifies the amount of atmospheric attenuation experienced by the radia-

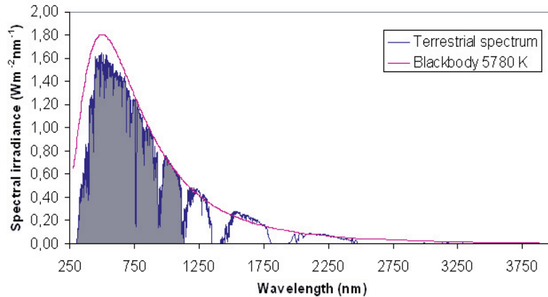

Figure 3.1: The spectral irradiance of the terrestrial solar spectrum and for a blackbody at a temperature of 5780 K and a diameter the size of the sun seen from earth. The part of the solar spectrum that can be exploited by a Si solar cell is shaded. Data for the standardized AM1.5 terrestrial spectrum adopted from Gueymard et al. [80].

tion. An air mass of 1.5 corresponds to the sun being at an altitude of 42°. The numbers are chosen because they are close to an average of the actual values and because they are easy to work with. A standardized spectrum is important also to provide an absolute reference for cell efficiencies. Figure 3.1 shows the resemblance of the solar spectrum to that of a black body with a temperature of 5780 K. The deviations are mainly due to absorption in the earths atmosphere at certain wavelengths. The terrestrial spectrum shown is the standardized AM1.5 spectrum adopted by the American Society for Testing and Materials (ASTM) [80]. Figure 3.2 shows the terrestrial spectral photon flux derived from the standardized AM1.5 spectrum. This spectrum is generally used for all weighting performed on transmission, reflection and absorption spectra with respect to the number of incoming photons at each wavelength.

3.2 The Silicon Solar Cell

Si solar cells have a theoretical upper efficiency limit of $\sim$ 29% which is largely due Si's inability to fully exploit the energy in the terrestrial solar spectrum [81]. Long wavelength photons pass through Si unabsorbed, while only a fraction of the energy is exploited for the short wavelength photons.

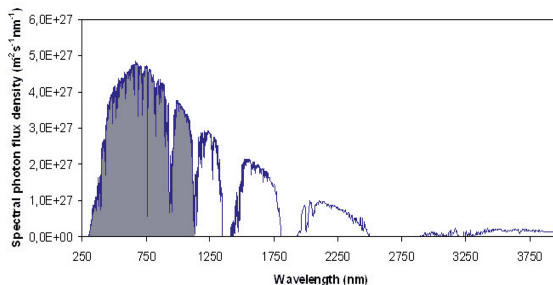

Figure 3.2: The spectral photon flux of the terrestrial solar spectrum. The part of the solar spectrum that can be exploited by a Si solar cell is shaded. Data for the standardized AM1.5 terrestrial spectrum adopted from Gueymard et al. [80].

Large efforts are laid down to improve these fundamental incompatibilities, for instance by up- and down conversion of photons or by combining Si with materials of different band gaps in multi-junction cells. In the following, we will focus on efforts made to improve the plain, single Si cell.

The world record efficiency for a full scale Si solar cell is currently 24.2% and held by Sun Power [82]. On lab scale, the PERL cell, made at the University of New South Wales (UNSW), holds the record at $25.0 \pm 0.5\%$ [83]. However, the PERL cell uses floatzone Si and complex processes, such as lithography and double layer antireflection coatings, that make it prohibitively expensive to manufacture in volume. The PERL cell is also a thick cell, $\sim 400\mu$m, and internal light trapping will only have a very small impact on the current density. For multicrystalline Si cells, the lab scale record is significantly less; $20.4 \pm 0.5\%$ [84].

Continuous cost reductions have driven Si cells to reduced thicknesses. Although 28% of the earths crust is Si, the recovery and purification processes are expensive [85]. As a result, the material cost makes up a significant part of the total production expenses and a reduction in Si consumption will contribute to lower cost. High efficient thin film Si cells have been made; Sanyo's HIT cell has delivered high efficiencies at thicknesses well below 100μm [86] and a 47μm thick monocrystalline Si PERL cell [87] has achieved 21.5%. This cell is ten times thinner than the conventional PERL cell, but still gen-

erates $\sim 90\%$ of the current density of the thicker device. The light trapping employed is 'inverted pyramids' at the front and a planar rear reflector. Although this is an excellent example for demonstrating efficient light trapping, it is made by thinning a thick float-zone Si substrate and does not represent a cost reduction compared to conventional cells. In addition, the processing steps are, as for the thick PERL cell, too complex and expensive for commercial use. The official thin film cell record efficiency is currently $16.7 \pm 0.4\%$ [88, 89] and applies to cells made by thin film transfer, where, assumably, material costs really are reduced. However, the thin film transfer process in itself introduces new challenges for instance with respect to material quality, in addition to the light trapping challenges.

3.2.1 Optical Response of Silicon

The efficiency of a solar cell is, naturally, very closely linked to the absorption of incoming light. The efficiency can be expressed as

$$\eta = \frac{P_{out}}{P_{in}} = \frac{J_{sc} V_{oc} FF}{P_{sun}} \tag{3.1}$$

where, P_{out} and P_{in} are the out and incoming power densities, J_{sc} is the short circuit current density and V_{oc} is the open circuit voltage. FF is the fill factor which is defined as the ratio of the current (J_m) and voltage (V_m) at the operating point of the cell to that of open circuit voltage and short circuit current density, $FF = J_m V_m / J_{sc} V_{oc}$. Let us then see how the optical response of Si affects the short circuit current density and the open circuit voltage.

If we disregard recombination losses, i.e. the collection efficiency is set to unity, the short circuit current density is given by the absorption and incident spectrum:

$$j_{sc} = \frac{q}{hc} \int \lambda a(W_{\text{eff}}, \lambda)[1 - R(\lambda)] I_{\text{AM1.5}}(\lambda) d\lambda. \tag{3.2}$$

$I_{\text{AM1.5}}$ is the standardized incident spectrum and $a(W_{\text{eff}}, \lambda)$ is the probability of absorption as a function of wavelength and effective thickness. From this equation it is evident that an increased absorption leads to increased current density. As seen from Fig. 3.1, the incident radiation has a broad spectrum with significant irradiance also at long wavelengths, Si, however, is an indirect semiconductor with a band gap of $E_g = 1.12$ eV, corresponding to a

wavelength of $\lambda = hc/E_g = 1108$ nm. Due to Urbach absorption below the band gap, the onset of absorption at the gap energy is not completely abrupt, but from $1100 - 1200$ nm the absorption is reduced by more than two orders of magnitude. The Si solar cell, therefore, is in practice not able to absorb the light with wavelengths longer than ~ 1100 nm. Clearly, the number of absorbed photons would increase if the band gap was lowered. A band gap of $E_g = 0.5$ eV would correspond to absorption of wavelengths shorter than ~ 2600 nm, and give a significantly larger short circuit current density.

Eq. 3.1 shows that the efficiency also depends on the open circuit voltage. For homojunction photovoltaic systems, the open circuit voltage, V_{oc}, can never exceed the band gap of the solar cell material, $V_{oc} < E_g/q$. Photons with $E > E_g$ are absorbed, but can only deliver an electric energy less than qV_{oc}. A large fraction of the energy of the short wavelength photons is therefore not utilized for energy production. The smaller the band gap, the larger this 'wasted' energy fraction becomes. Consequently, there is a trade-off between short circuit current density and open circuit voltage. For a given spectrum, there is an optimal band gap where the efficiency is maximized. For the standardized AM1.5 solar spectrum this is about 33% at a band gap of approximately 1.4 eV, i.e. somewhat higher than the band gap of Si [90].

To achieve the 'available' 29% efficiency for a Si solar cell, all incident photons with $\lambda < 1108$ nm should be absorbed and collected. Si, as an indirect semiconductor, is a rather poor absorber. The irradiance of a wave is reduced by $1/e$ after travelling a distance $\lambda/(4\pi k)$, called the optical absorption length. The inverse of this is defined as the absorption coefficient, α

$$\alpha = \frac{4\pi k}{\lambda_0}, \tag{3.3}$$

where k is the imaginary part of the refractive index and λ_0 is the wavelength in free space. Transmittance through a medium can then be expressed by Beer-Lambert's law as

$$I(x) = I(0) \exp(-\alpha x) \tag{3.4}$$

$$T = \frac{I(x)}{I(0)} = \exp(-\alpha x). \tag{3.5}$$

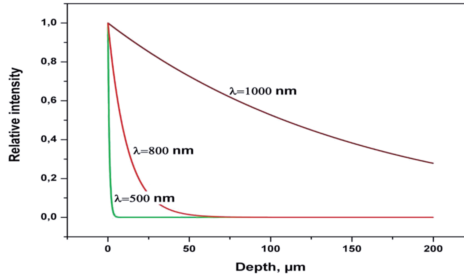

Figure 3.3: Photon absorption in Si. Long wavlengths require a long optical path to be absorbed. **Source: courtesy of Sean Erik Foss.**

At the median wavelength of the solar spectrum, around 1000 nm corresponding to a photon energy of 1.24 eV, Si has an optical absorption length of 156 μm. Figure 3.3 illustrates the absorption lengths of Si for three different wavelengths. With a thick Si substrate (i.e. $400-500$ μm), the great majority of light is absorbed during its first pass and only a good antireflection coating is required for light management. The continuous cost reductions drive Si cells toward reduced thicknesses and today the standard wafer thickness is already down to $\sim$ 250 μm. Further reductions down to at least $\sim$ 150 μm are expected. At these thicknesses a significant amount of the light in the long wavelength end is lost. For thin film Si solar cells, defined as thinner than 50 μm, the losses are severe. Light trapping is applied to reduce the absorption losses by imposing a path length for the light that is longer than the thickness of the substrate.

3.2.2 The Silicon Solar Cell Process in a Very Small Nutshell

The process steps necessary to produce a finished Si solar cell are not unique; each producer have their own secret - or patented - ingredients. With the large range of cell concepts that have emerged, including epitaxial cells, backside contacted cells, and emitter wrap through cells, just to name a few, the processing steps may not even resemble the ‘standard’ process line anymore. Still, the ‘standard line’ is used as a reference here, to remind the reader of the most basic steps necessary to produce a wafer based Si solar cell. The

section is largely based on textbooks by Markvart and Castaner [91] and Luque and Hegedus [92]. How the Si is refined and becomes the familiar thin multi or mono crystalline 'starting blocks' of solar cell production is another story that will not be retold here.

Damage Etch and Texturing

The first treatment of the wafers is usually an etch to remove damage from the sawing process. Typically, heated, aqueous KOH is used for this purpose. The damage etch is followed by an etch used to texture the surface of the wafers. Etching in a mix of weak alkaline solution and an organic solvent results in a preferential etch since the etch rate for the (111) crystal planes of the Si crystal is smaller by one to two orders of magnitude than the etch rate of any other crystal plane [93]. The resulting structure is a surface of random pyramid structures defined by (111) planes. The preferential etching is very effective on monocrystalline wafers, but on multicrystalline wafers the varying crystal orientation degrades the resulting structure. A range of alternative etching methods has been suggested, such as isotropic etches, inverted pyramids, mechanical grooving, and PS texture [94–96].

Diffusion

The key element of a standard Si solar cell, the charge separator, is the p-n junction. It is made by in-diffusion of phosphorous in the case of a p-type wafer or in-diffusion of boron in the case of a n-type wafer. There are several ways of performing in-diffusion, but the one most commonly used in industry is in-diffusion from a $POCl_3$ source. The wafers are loaded into a quartz tube which is pumped to vacuum and heated to around 900°. The wafers are then exposed to a flow of $POCl_3$ and phosphorous atoms diffuse into the Si. Depending on diffusion time and temperature the doping typically diffuses $0.1 - 1$ μm into the wafer. This layer, called the emitter, has a relatively high doping compared to the substrate. It is usually considered a 'dead' layer, i.e. the photons absorbed here do not lead to collected charge carriers. Therefore, a thin emitter is beneficial. On the other hand, industrial techniques used for front contacting require a deep junction to obtain acceptable contact resistance.

Simultaneous with the in-diffusion of the dopant, mobile impurities are trapped, or gettered, at cites that are less critical in the operation of the cell.

During the diffusion process a layer of insulating P-silicate glass is formed, which must be removed in HF. The in-diffusion occurs also at the back and at the edges of the wafer. Therefore, edge isolation is required to prevent short circuiting the cell. This can for example be done by laser grooving.

Antireflection Coating and Surface Passivation

An antireflection coating (ARC) is deposited to reduce the large reflection from a bare silicon wafer surface. Often a single layer of silicon nitride (SiN_x:H), deposited by plasma enhanced chemical vapor deposition (PECVD), is used for this purpose. The reflectance is routinely reduced to below 10% with this treatment. Alternatives to silicon nitride coatings exists, double and triple layer ARCs such as MgF_2/ZnS, SiO_2/TiO_2, MgF_2/CeO_2, and MgF_2 /Al_2O_3/ZnS may be used to reduce the reflectance further. However a corresponding number of processing steps are required. In addition, silicon nitride provides very good surface passivation without additional processing steps. Therefore, double and triple layer ARCs are used in systems where higher cost of the cell can be justified.

Contact Formation

Finally, metal contacts are required to extract the current generated in the solar cell. Contacts are most commonly formed by screen printing. The solar cell is placed under a mask that defines the pattern of the contacts and metal paste is applied through the mask. The aluminium contacts fully cover the backside of the cell, only broken by silver bus bars. The front side contacts consist of a fine silver metal grid. The process requires separate deposition through three masks, each deposition followed by a drying step. The coverage of the front silver grid is a compromise between increased series resistance due to large distances between the metal fingers and light-shadowing effects. The light hitting the metal grid is reflected from the cell. As a result of this difficult trade-off, cells contacted solely on the backside are becoming more common. Front shadowing from the contacts is avoided and more photons can be collected. However, backside contacted cells have severe challenges of their own, such as throughput and complex formation processes [97].

The last step in the contact formation is a quick anneal to allow the paste on the front to etch through the insulating antireflection layer and into the emitter while the paste at the rear similarly etch into the Si to form

near ohmic contacts. The anneal must be long enough to allow the paste to etch through the ARC at the front side and into the Si at the backside in order to make good contacts. However, the anneal must also be swift enough to prevent the front paste to etch through the ARC and emitter and thereby short circuit the cell. This requires a relatively deep emitter. A thick emitter is also necessary in order to prevent metallic impurities to penetrate to the junction region. To achieve a low contact resistance a high surface concentration of carriers is needed. The sum of these requirements; a deep and highly doped emitter, will generally result in a decrease of the short circuit current and the fill factor. One solution is to form emitters with two distinct regions: a highly doped and deep region under the fingers and a lowly doped and thin one under between the fingers. Such structures are called selective emitters.

3.3 Theoretical Basis for Light Management

The history of optical coatings is a long one, with important contributions from among others Newton, Fraunhofer, Fresnel, and Lord Rayleigh. In 1936 John Strong were able to produce an antireflection coating reducing the reflectance of glass to visible light by 89% [98]. However, the subject did not catch much industrial attention until it was triggered by World War II. By the end of the war, optical coatings were an established part of optical components. Today the areas of application of thin films are countless and great progress is still being made within the field [99].

In this work, calculations of the optical properties of thin films are utilized to relate reflectance, absorption, and transmittance to the presumably known, optical constants of the material. Perhaps to an even greater extent, the reverse problem is posed; relation of the desired reflection to the corresponding optical constants (and thickness). The following section summarizes the theory and equations most relevant for these applications.

Basic Theory

When a beam is reflected from the upper and the lower surfaces of a thin film, interference will occur - destructively if the phase shift is a multiplum of 180° and constructively when there is no phase shift (or a multiple of 360°). When reflectance takes place in a medium of lower refractive index than the

adjoining medium, a phase shift of 180° will occur, while if the refractive index is higher than the adjoining the phase shift of the reflected light is zero.

A film is said to be thin when interference effects can be detected in the reflected or transmitted light, that is, when the path difference between the beams is less than the coherence length of the light. A film can appear thin or thick depending on the illumination conditions.

Single Boundary

Let us start with a definition of transmittance and reflectance that is rather intuitive. The reflectance, R, is defined as the ratio of the reflected irradiance, I_r to the incident irradiance, I_i:

$$R = \frac{I_r}{I_i}. \tag{3.6}$$

The transmittance, T, is the ratio of the transmitted irradiance, I_t to the incident irradiance, I_i:

$$T = \frac{I_t}{I_i}. \tag{3.7}$$

Note that these relations can also be formally derived, see MacLeod [100].

Recall that the irradiance is usually defined as the (scalar) time averaged value of an electromagnetic wave's energy flux or Poynting vector, $\mathbf{S} = \mathbf{E} \times \mathbf{H}$. The irradiance therefore is related to the electric and magnetic field of an harmonic wave by

$$I = \frac{1}{2}\mathrm{Re}(\mathrm{EH}^*), \tag{3.8}$$

where E and H are scalar magnitudes and * denotes the complex conjugate. For a homogeneous, plane, plane-polarized, harmonic wave, the electric field **E** and magnetic field, **H**, are given by

$$\mathbf{E} = \mathcal{E} \exp\left(i[\omega t - (2\pi N/\lambda)x + \psi]\right), \tag{3.9}$$

$$\mathbf{H} = \mathcal{H} \exp\left(i[\omega t - (2\pi N/\lambda)x + \psi']\right), \tag{3.10}$$

where x is the distance along the direction of propagation, $(2\pi N/\lambda)$ is the wavenumber, $\mathcal{E}$ is the electric amplitude, $\mathcal{H}$ is the magnetic amplitude, and ψ and ψ' are arbitrary phases. The ratio of the electric and magnetic fields gives the complex optical admittance, y, of the material; $y = H/E$. In free space,

y is denoted by $\mathcal{Y}$ and has a value, $\mathcal{Y} = 2.65 \times 10^{-3}$ S. At optical frequencies the optical admittance is connected to the refractive index by $y = N\mathcal{Y}$. We see that through these equations we have a means of relating the refractive index to the definitions of reflection and transmittance in Eq. 3.6 and 3.7. To actually calculate the reflectance and transmittance, boundary conditions for the electric and magnetic vector and Snell's law must be applied. For non-absorbing incident material, i.e. incident material with real refractive index (N_0) and real optical admittance (y_0) it can be shown that:

$$R = \left(\frac{y_0 - y_1}{y_0 + y_1}\right)\left(\frac{y_0 - y_1}{y_0 + y_1}\right)^* \tag{3.11}$$

and

$$T = \frac{4y_0 \operatorname{Re}(y_1)}{(y_0 + y_1)(y_0 + y_1)^*}. \tag{3.12}$$

For an absorbing incident medium, fundamental difficulties arise which are not addressed here. Generally, air can be approximated as a non-absorbing incident medium. For derivation of these equations, see MacLeod [99].

The expressions above hold for absorption free emergent media as well, but can then be simplified to

$$R = \left(\frac{y_0 - y_1}{y_0 + y_1}\right)^2 = \left(\frac{n_0 - n_1}{n_0 + n_1}\right)^2 \tag{3.13}$$

and

$$T = \frac{4y_0 y_1}{(y_0 + y_1)^2} = \frac{4n_0 n_1}{(n_0 + n_1)^2}. \tag{3.14}$$

To generalize this result to be valid also for oblique incidence, the wave is split into p and s polarization (parallel and perpendicular to plane of incidence, respectively). Tilted optical admittances η_p,

$$\eta_p = \frac{N\mathcal{Y}}{\cos\phi}, \tag{3.15}$$

and η_s,

$$\eta_s = N\mathcal{Y}\cos\phi, \tag{3.16}$$

are introduced and replace the optical admittance, y, in the equations above. Since sunlight is unpolarized, the total reflectance will be half from R_p and half from R_s.

Successive Interfaces

When the structure consists of several planar interfaces, a number of beams will be produced by successive reflections and the optical properties of the film will be determined by the summation of these beams. We concentrate on thin films, meaning that interference effects can be detected in the reflected or transmitted light. The tangential components of **E** and **H** are continuous across a boundary, and at the last interface, the waves in the film can be summed into one resultant positive-going (transmitted) and one resultant negative-going (reflected) wave. The tangential components of the **E** and **H** field at one interface are connected to the previous interface by a simple alteration of the phase factors, allowing for a shift in the z coordinate from 0 to $-d$, where d is the distance between the interfaces. The phase factor of the positive-going wave will be multiplied by $\exp(i\delta)$, where δ is given by

$$\delta = 2\pi N_1 d \cos\theta_1/\lambda. \tag{3.17}$$

A negative-going wave will be multiplied with $\exp(-i\delta)$. In this way, the field at the first interface can be expressed as a function of the field at the second interface. For the simplest case of successive interfaces, a single thin film, the relation between the tangential components of the electric and magnetic field at the two interfaces can be expressed in matrix notation by

$$\begin{bmatrix} E_a \\ H_a \end{bmatrix} = \begin{bmatrix} \cos\delta & (i\sin\delta)/\eta_1 \\ i\eta_1\sin\delta & \cos\delta \end{bmatrix} \begin{bmatrix} E_b \\ H_b \end{bmatrix}, \tag{3.18}$$

where subscript a denotes the first boarder (between the incident medium and the thin film) and subscript b denotes the second boarder (between the thin film and the substrate). The reader is referred to MacLeod [100] for a derivation of this expression. We now have a connection between the tangential components of **E** and **H** at the incident interface with those transmitted through the final interface. The input optical admittance of the assembly is defined by $Y = H_a/E_a$. Normalizing Eq. 3.18 by dividing through by E_b gives

$$\begin{bmatrix} E_a/E_b \\ H_a/E_b \end{bmatrix} = \begin{bmatrix} B \\ C \end{bmatrix} = \begin{bmatrix} \cos\delta & (i\sin\delta)/\eta_1 \\ i\eta_1\sin\delta & \cos\delta \end{bmatrix} \begin{bmatrix} 1 \\ \eta_2 \end{bmatrix} \tag{3.19}$$

We can then find the optical admittance of the assembly from

$$Y = \frac{H_a}{E_a} = \frac{C}{B} = \frac{\eta_2\cos\delta + i\eta_1\sin\delta}{\cos\delta + i(\eta_2/\eta_1)\sin\delta} \tag{3.20}$$

The optical admittance of the thin film replaces the optical admittance of the exit medium for a single boundary in the equations of transmittance and reflectance. The result can easily be generalized to apply for any number of interfaces (q):

$$\begin{bmatrix} B \\ C \end{bmatrix} = \left\{ \prod_{r=1}^{q} \begin{bmatrix} \cos\delta_r & (i\sin\delta_r)/\eta_r \\ i\eta_r \sin\delta_r & \cos\delta_r \end{bmatrix} \right\} \begin{bmatrix} 1 \\ \eta_m \end{bmatrix}. \tag{3.21}$$

The multiplication must be done in the right order, starting with the layer closest to the incident medium. Inserting the optical admittance of the assembly in the equations for reflectance, transmittance, and absorption yields for a non-absorbing incident medium

$$R = \left(\frac{\eta_0 B - C}{\eta_0 B + C}\right)\left(\frac{\eta_0 B - C}{\eta_0 B + C}\right)^* = \left(\frac{\eta_0 - Y}{\eta_0 + Y}\right)\left(\frac{\eta_0 - Y}{\eta_0 + Y}\right)^*, \tag{3.22}$$

$$T = \frac{4\eta_0 \,\mathrm{Re}\,(\eta_m)}{(\eta_0 B + C)\,(\eta_0 B + C)^*} = \frac{4\eta_0 \,\mathrm{Re}\,(\eta_m)}{(\eta_0 + Y)\,(\eta_0 + Y)^*}, \tag{3.23}$$

$$A = \frac{4\eta_0 \,\mathrm{Re}\,(BC^* - \eta_m)}{(\eta_0 B + C)\,(\eta_0 B + C)^*}. \tag{3.24}$$

3.4 Implementing Light Management

The previous sections of this chapter have presented a dilemma; a solar cell should be thin to save Si material costs, but it must be thick enough to absorb the photons from the solar spectrum. So, how can we decrease the thickness of the Si substrate without reducing the photon absorption? An oblique path through the substrate would increase the thickness of the Si substrate as seen by the photon. If the photon also was reflected from the rear side of the substrate, this would effectively double the thickness. The term commonly used to describe the measures taken to elongate the light path through the media is light trapping. Textures and backside reflectors are the most commonly used means. Although not strictly included by this definition of light trapping, antireflection coatings are another aspect of the same story. Antireflection coatings are essential to couple the light into the cell and thereby ensure that there actually is a substantial amount of light

to trap. Light management is important for all solar cells, but become indispensable for thin Si solar cells. Antireflection coatings are equally important for all solar cells.

3.4.1 Texture

This section takes a closer look at the absorption enhancement which may be obtained by texturing the cell surface. Texture has two functions. One is to reduce reflection by giving the cell surface steep angles of incidence with respect to the incoming light to allow the light at least a double bounce at the surface. The other is to increase the path length once the photon is inside the cell. The path length is increased due to the photon's oblique angle through the substrate, but also because the probability of total internal reflection is increased. Total internal reflection is particularly important at the front surface, where mirrors cannot be used. From Snell's law it can be seen that a light ray going from media n_0 towards the interface to media with a lower refractive index, n_1, will be internally reflected if the angle of incidence is greater than a critical angle $\theta_c = sin^{-1}(n_1/n_0)$. For a transition from Si to air the critical angle is $\theta_{cSi} \approx 17°$. An added benefit of the oblique path is that photogeneration takes place closer to the junction and thereby enhance the collection efficiency for medium- to long wavelengths. A drawback is that textured surfaces present higher surface recombination velocities.

A good standard to measure a texture by is the Lambertian surface. A Lambertian surface is defined as a surface which fully randomizes the reflected and transmitted light for all wavelengths. The degree of intensity enhancement to be expected from such perfect randomization was first derived by Yablonovitch and Cody [101]. Unity backside reflection is assumed here, but the result can be generalized to non-unity backside reflection. The path length resulting from a Lambertian surface was found to be

$$l = 4n_s^2 W_{\text{eff}}, \tag{3.25}$$

where W_{eff} is the effective thickness of the cell. W_{eff} is used instead of just W to include wafers which are not planar. The origin of this path length enhancement is threefold. A factor of two comes from the unity backside reflection, another factor of two comes from oblique transmission angles. For

fully randomized light the average path length for one traversal is

$$2\pi \int_0^{\pi/2} \frac{W_{\text{eff}}}{\cos\theta} \cos\theta \sin\theta \; d\theta \; / \; 2\pi \int_0^{\pi/2} \cos\theta \sin\theta \; d\theta = 2W_{\text{eff}}. \tag{3.26}$$

Finally, only rays with $\theta_s < \theta_c$ can escape and so only $1/n_s^2$ of the rays striking the front surface will leave the cell.

Under normal incidence it has been demonstrated that certain geometrical surface textures can outperform Lambertian surfaces [102], but normal incidence is not very representative for non-tracking solar module systems. Under isotropic illumination it is shown that the average path length of Lambertian light trapping schemes equals the theoretical maximum of the average path length for any geometrical light trapping scheme. However, the theoretical optimum absorption is reached for a texture with all of the isotropically incident rays having a path length, l, equal to the theoretical maximum. This is called optimum geometrical light trapping. Whether there exists a structure which can provide optimum geometrical light trapping is not known [31].

Porous Silicon Texture

Light scattering from PS is repeatedly observed in a range of different structures [e.g. 103, 104]. In principle, there are three possible origins of this scattering: the air/PS interface, the volume or inner surface of PS, and the PS/Si interface.

For efficient light diffusion, the size of the texture should be on the same scale as the wavelength. Macroporous Si can be made on a scale suitable for light diffusion and is therefore considered the most interesting pore regime for texture applications. Because of these diffusing properties and the simplicity of fabrication, it has been suggested that macroporous Si can replace conventional texturing in Si solar cells. The etching should ideally combine both saw damage removal and texturing. These processing steps are performed in the beginning of the cell process and therefore it is the substrate, not the emitter that is etched. Macropores of the right dimensions are most easily obtained in n-type Si material, which would lead to a n/p$^+$ solar cell structure. Several papers have reported that PS structures with the right dimensions can be made and that improved light trapping results [94–96]. Macroporous Si withstands heat treatment fairly well, but removal of the P-silicate glass that forms during diffusion may pose a problem. The glass

is typically removed in HF and it has been reported that the PS texture is also partly removed in this process [95].

For nano/meso PS, studies on thick PS layers show that there is no scattering from the volume and the first interface [105]. This means that for nano/meso PS the scattering originates from the second interface. Internal light trapping provided by scattering from nano/meso PS is an additional benefit from implementation of PS ARCs. This structure is typically made after emitter diffusion. We will look at the PS ARC more closely in Section 3.4.3, but let us here take a look at the nature of the scattering from the PS/Si interface.

The roughness of the PS/Si interface increases linearly with increasing film thickness before saturating [103]. Therefore, the light diffusing property of nano/meso PS layers has been found to depend on the PS layer thickness. For the thin PS layers optimal for solar cell ARCs the light diffusion is less pronounced than for thicker films. However, even for relatively thin films, significant scattering has been observed. Bilyalov et al. [104] finds an effective entrance angle of 60° for light entering a cell structure after passing through a PS layer thickness of 160 nm. According to Bilyalov et al. [104] this means that the light is fully randomized due to the scattering behavior of the random PS medium. Figure 3.4 shows a TEM image of a 300 nm thick PS film etched in a p^+ Si substrate. Since $n = v/c$, a medium with higher refractive index than air (or vacuum to be precise) results in a reduced phase speed v. The frequency remains unchanged while the wavelength is reduced. Therefore, the roughness scale that will produce scattering is also smaller than in air.

A model for light propagation in PS, based on the random-medium theory, enables the specular and the diffuse part of the light to be determined and treated separately [106]. This analysis indicates a scattering behavior which is stronger in the forward direction (transmission) than in the reverse way (reflection). This model is therefore consistent with the experimental observation of a rather specular reflectance behavior in combination with diffused transmitted light [104].

3.4.2 Backside Reflector

An ideal back surface reflector would of course reflect all photons that reached it. In many conventional, ‘thick’ ($200 - 300\mu$m) silicon solar cells, the backside contact, typically Al, also serve as optical reflector. A metal surface is however not totally reflective. Typical reflectance from an air/Al interface

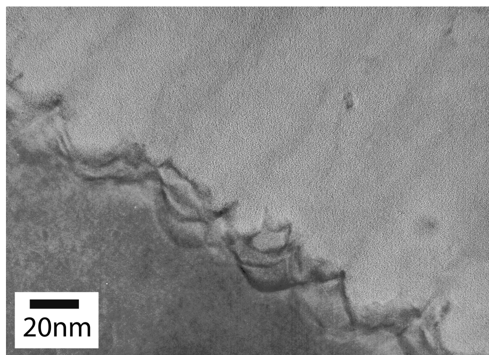

Figure 3.4: TEM image of the PS/Si interface of a 300 nm thick, meso PS film. The roughness is of a scale $30 - 40$ nm.

may be $\sim 90\%$, but the reflectance from a Si/Al interface will be lower [107]. For conventional 'thick' cells, the short wavelengths are absorbed during the first pass and only photons with wavelengths longer than $\sim 900 - 1000$ nm reaches the backside. When the thickness of the cell decreases, photons of shorter wavelengths will also reach the backside reflector and the long wavelength photons may experience repeated reflections. For thin cells the photon loss due to insufficient backside reflection therefore becomes a severe problem [107]. Figure 3.5 shows how the transmittance through a slab of Si varies with thickness and wavelength.

Wire cut Si wafers are now approaching thicknesses where improved backside reflection becomes important [35]. Dielectric layers are often, and fairly successfully, used in conjunction with metal backside reflectors to improve the reflectivity and reduce contact recombination [108]. By using double-sided texture, silicon oxide passivation and Ag as metal, a nearly perfect rear mirror can be realized, although the electrical performance of such a rear side is not optimum.

Many of the thin film cell structures differ from a conventional cell and the reflector will typically be situated between the active solar cell and the substrate. Alternative reflectors are therefore sought after.

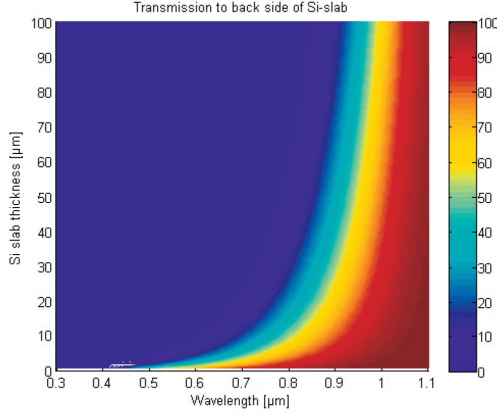

Figure 3.5: Transmission of light through Si as a function of wavelength and thickness of the Si slab. **Source: courtesy of Jo Gjessing.**

Dielectric Multilayer Reflectors

A classical high-efficiency reflector is a dielectric multi-layer stack which exhibit a maximum reflectance at its design wavelength. A distributed Bragg reflector (DBR) is a structure which consists of alternating high and low refractive index layers. The most frequently used design is that of a quarter-wave mirror, where each layer has an optical thickness corresponding to one quarter of the wavelength for which the mirror is designed. When light propagates in a medium with refractive index n_1 and reaches an interface to a medium with refractive index n_2, there is a 180° phase shift if $n_1 < n_2$. If $n_1 > n_2$, there is no phase shift. The quarter wave layer DBR design therefore results in constructive interference of the reflected waves from all interfaces and a correspondingly high reflectivity. Implementation of such reflectors in silicon solar cells have been shown [109]. The main drawback of a DBR is that the high reflectance is obtained over a limited range of wavelengths.

The admittance of a stack of quarter wave layers with alternating high index (n_H) and low index (n_L) and where the high index layer is outermost

on both sides, is given by

$$Y = \left(\frac{n_H}{n_L}\right)^{2N} \frac{n_H^2}{n_m}. \tag{3.27}$$

$(2N + 1)$ is the number of layers in the stack and n_m is the refractive index of the substrate. The reflectance in a non-absorbing incident medium with refractive index n_0 is then

$$R = \left(\frac{n_0 - (n_H/n_L)^{2N}(n_H^2/n_m)}{n_0 + (n_H/n_L)^{2N}(n_H^2/n_m)}\right)^2. \tag{3.28}$$

The bandwidth of the photonic stop band, W_b, can be calculated by

$$W_b = \frac{4}{\pi} \sin^{-1}\left(\frac{n_H - n_L}{n_H + n_L}\right). \tag{3.29}$$

We see that the width of the reflection band only depends on the indices of the two materials in the stack. The greater the difference in refractive indices, the greater the width of the reflection zone. A more complete derivation of this result can be found in MacLeod [99].

Porous Silicon Reflectors

The simplest PS back reflector would be a single layer of PS with very high porosity and an optical thickness of 1/2 of the design wavelength λ_0. Such a layer would enhance the reflectance significantly, although only one maximum would be obtained. The larger the porosity of the PS layer, the larger the refractive index difference between PS and bulk, and the higher the reflectance. However, the range of accessible porosity values has an upper bound, because highly porous layers are mechanically unstable.

A DBR consisting of PS with alternating high and low porosity would not require as high porosities as the single layer, but could still be fabricated in a single process step [108]. Further benefits of using PS reflectors are the compatibility with the existing silicon solar cell technology and low fabrication costs. Implementation of such layers in lab scale solar cells have been performed [33, 34, 110, 111]. The structures are particularly interesting for thin film epitaxial cells, where the mirror must be situated between the active Si region, making conventional mirrors unsuitable. Kuzma-Filipek et al. [33] estimates that the fabrication costs of such PS reflectors can be as low as

$0.07 - 0.04$ Euro/W_{peak}, assuming a high throughput porousification system of 1200 wafers/h.

For target wavelengths in the infrared, parasitic absorption in the PS multilayered reflector structures is relatively low.

3.4.3 Antireflection Coatings

Even if a great internal light trapping scheme is accomplished, it will be in vain if the light never enters the cell. Antireflection coatings supplement the internal light trapping schemes, but in contrast to the other light trapping features, ARCs are equally important for all cells, thick or thin.

Silicon is a typical high index substrate, meaning that it has a refractive index sufficiently higher than the available thin-film material to enable the design of antireflection coatings consisting entirely of layers with indices lower than that of the substrate.

The ARC depends on the more or less complete cancellation of the light reflected from the air/ARC interface and the ARC/Si interface. For complete cancellation of the reflected light, the reflected amplitudes from the two interfaces must be equal. This implies that

$$\frac{y_0 - y_1}{y_0 + y_1} = \frac{y_1 - y_m}{y_1 + y_m}, \tag{3.30}$$

where y_0, y_1, and y_m is the optical admittances of air, the film (ARC) and the emergent medium, respectively. This infers that the ratio of refractive indices at each boundary should be equal;

$$y_0/y_1 = y_1/y_m \tag{3.31}$$

$$y_1 = (y_0 y_m)^{1/2}. \tag{3.32}$$

We see that the optical admittance (and refractive index) of the thin film should be intermediate between the indices of air and that of the substrate. To ensure a relative phase shift of 180° for complete destructive interference, the thickness of the film should be one quarter wavelength. The reflectance is given by

$$R = \left(\frac{y_0 - Y}{y_0 + Y}\right)^2 = \left(\frac{y_0 - y_1^2/y_m}{y_0 + y_1^2/y_m}\right)^2, \tag{3.33}$$

Clearly, if y_1 is given by Eq. 3.32 the reflectance is zero.

At oblique incidences, the tilted values of the optical admittance, from Eq. 3.15 and 3.16 must be used. This angular dependence is then also introduced in Eq. 3.30. The disadvantage with a single layer ARC is that reflection only can be optimized at one wavelength. Better ARCs can be constructed from two or more layers, often being a quarter wavelength each.

It is seldom possible to find material of exactly the refractive index which is required. If there is a small error, ε, in y_1 such that

$$y_1 = (1+\varepsilon)(y_0 y_m)^{1/2} \tag{3.34}$$

then the minimum reflectance for this coating is given by

$$R = \left(\frac{-2\varepsilon - \varepsilon^2}{2 + 2\varepsilon + \varepsilon^2}\right)^2 \approx \varepsilon^2 \tag{3.35}$$

for small ε.

Porous Silicon Antireflection Coatings

The first attempts of PS ARCs for solar cells were made in the early eighties [26]. Since then extensive work has been performed. There is little controversy in claiming that formation of a PS layer decreases the reflectance from a Si wafer; all results point to an improvement of the optical characteristics due to the reduced reflectance losses of a PS surface [104, 112–115]. All possible refractive indices of PS are intermediate between that of air and Si, thereby reducing the reflection from the interface. In addition, the rough surface provides a certain amount of texture, further reducing reflection.

However, low reflection is not reason enough to integrate a new ARC material in the solar cell process. Antireflection coatings with excellent broadband properties are known, the most efficient system is the ZnS/MgF_2 double layer, with an integrated reflectance of $\sim 3.3\%$. However, these materials are typically deposited by high vacuum evaporation techniques and separate processing steps are necessary for each layer. Such ARCs will therefore contribute to raise expenses in the production of solar cells. It is the combination of excellent antireflective properties and inexpensive production that make PS relevant as solar cell ARC material. Additional requirements that should be met is that the PS fabrication must integrate well into the solar cell process, the PS layer must be able to withstand subsequent processing steps, and it must not degrade the electrical properties of the cell.

Reducing the number of steps in the solar cell process gives cost savings. Therefore, simplified processing schemes are always sought for. The PS ARC has been suggested to fulfill a number of functions. One of the most common combinations is a simplified process where PS replaces the texture, surface passivation and ARC [104]. Solar cells with this simplified processing scheme have indeed been fabricated with a resulting efficiency of 14.1% for a 5×5 cm^2 mc-Si cell [116]. The PS ARC formation is typically performed at the end of the process because PS reorganizes and oxidizes if exposed to high temperatures. A selective emitter is then formed without any alignment, as the area below the contacts are protected from etching. The two main challenges in this processing scheme is the inadequate surface passivation provided by PS and a potential degradation of the Ag contacts during etching in HF.

Table 3.1 shows an extensive, but not exhaustive, overview of what has been done in the history of PS ARCs for solar cells. Many groups have contributed to the development and solar cell efficiencies of $12 - 14\%$ have been obtained by several groups. Mostly this is through a simplified processing scheme where a single PS layer is etched in the n$^+$ emitter after metallization. Generally, screen printed contacts are used and no texture, surface passivation or additional ARC applied. Both stain etched and electrochemically etched PS layers are utilized with similar efficiencies. The highest reported conversion efficiency is 16.8%, obtained by Yuan et al. [131]. This is obtained using Au nanoparticles as catalysers for the etching process and is, judging from the results, clearly an interesting approach. The highest efficiency obtained with pure anodic etching is 14.1%, obtained by Bilyalov et al. [116], using evaporated contacts instead of screen printed ones. The best efficiency of cells with screen printed contacts from the same author was 13.2%.

It is difficult to directly compare the reported results as a range of parameters, which cannot easily fit into a table, will greatly affect the obtained results. Some of the ARCs are too thick for implementation in a conventional silicon solar cell [112, 117], some use non-standard contacting to avoid contact degradation during etching.

The best, in terms of low reflection, reported PS ARC has a reflection of 2.7% over the wavelength range $400 - 1000$ nm [126]. The ARC was formed in an n$^+$ emitter structure. The etching time was however > 100 s, which would very likely lead to a significant degradation of the contacts.

In the great majority of the PS ARC studies, homogeneous single or, in a few cases, double layer ARCs are fabricated. Uehara et al. [112] first

Table 3.1: Reflectance and cell efficiencies obtained with PS ARCs

Reference	Layer type	Refl.[1]	λ range (nm)	$\eta(\%)^2$
Tsuo et al. [117]	SL, pc-p	$\sim 10\%$	$350 - 850$	–
Menna et al. [29]	SL, pc-p	4.7%	$350 - 1120$	–
Vazsonyi et al. [118]	SL, mc, n^+/p	–	–	11.5%
Coles et al. [119]	SL, mono-p	12.0%	$400 - 1100$	–
Strehlke et al. [120]	SL, mc, n^+/p	–	–	13.2%
Schirone et al. [121]	SL, mc, n^+/p	3%	$400 - 800$	12%
Stalmans et al. [122]	SL, mc, n^+/p	–	–	12.7%
Bilyalov et al. [116]	SL, mc, n^+/p	$5 - 6\%$	$300 - 1000$	14.1%
Strehlke et al. [123]	SL, c, n^+/p	7.3%	$400 - 1150$	–
Panek et al. [124]	SL, c, n^+/p	–	–	9.5%
Panek et al. [124]	SL, mc, n^+/p	–	–	9.5%
Lipinski et al. [125]	SL, c, n^+/p	9.7%	$400 - 1000$	12%
Uehara et al. [112]	Grad., p sub.	$< 2\%$	$400 - 1000$	–
Strehlke et al. [126]	DL, c, n^+/p	2.7%	$400 - 1000$	–
Yerokhov et al. [127]	SL, c, n^+/p	7.6%	$400 - 1000$	13.5%
Martin-Palma et al. [128]	SL, mc, n^+/p	–	–	9.6%
Lipinski et al. [113]	SL, mc, n^+/p	13%	$400 - 1100$	13.3%
Lipinski et al. [114]	DL[3], mc, n^+/p	5.8%	$400 - 1100$	–
Striemer and Fauchet [129]	Grad.,sr[4]	3.7%	$350 - 1000$	–
Striemer and Fauchet [129]	Grad.,p+ sub	8.1%	$350 - 1000$	–
Kwon et al. [115]	SL, mc, n^+/p	4.7%	$400 - 1000$	13.2%
Chaoui and Messaoud [130]	SL, c, n^+/p	9.5%	$400 - 1100$	12.5%
Yuan et al. [131]	Grad.[5], n^+/p	$< 3\%$	$350 - 1000$	16.8%
Remache et al. [132]	SL, c, $n^+/p+SiO_x$	3.8%	$400 - 1100$	–

[1]The reflectance is the effective reflectance over the wavelength range given in column four. [2]η is the cell efficiency. [3]macroPS + nanoPS in n^+. [4]Fabricated on string ribbon solar cells. [5]Nanocatalyzed formation method. Abbriviations used in the Table: SL - single layer, DL - double layer, Grad. - graded layer, c refers to monocrystalline silicon.

reported a graded index PS ARC formed by a gradual change in the porosity. Excellent broad band reflectivity of less than 3% in the visible spectrum was achieved, but the thickness of these stacks ($> 1\mu$m) are not suitable for solar cell ARCs. In addition to a degradation of the electrical characteristics, parasitic absorption in the ARC would be rather high. Striemer and Fauchet [129] fabricated thin (~ 100 nm) gradient index PS layers with a reflectance of 8.1% on a polished 0.01 Ω cm p-type Si wafer over the spectral range $350 - 1000$ nm. The etching process took only 5 seconds.

The gold-catalyzed PS emitter fabricated by Yuan et al. [131] requires an etching time of 3 minutes and is 500 nm thick. However, the broadband reflectance is low ($< 3\%$) and the excellent cell efficiency are obtained, despite the relatively thick dead PS layer.

A few reports exists where PS ARCs are used in different cell concepts. One example is a thin film polycrystalline cell where separate PS layers are used as ARC and buffer layer between the substrate and the active cell [133]. Another concept that is included in Table 3.1 is a double layer structure where macropores are etched in the substrate before diffusion to provide texture and a nanoporous layer is etched in the emitter after diffusion to provide an ARC [114].

Chapter 4

Fabrication and Characterization of PS

In this chapter, the methods used to fabricate and characterize the PS samples in this work are presented. Firstly, the fabrication setup we have for electrochemical etching of PS at IFE is described. The setup is used for all PS samples presented in this work. To obtain all desired information about the structures, several characterization techniques have been used. In particular spectroscopic ellipsometry (SE) has been extensively utilized for characterization and is described in some detail, both practically and theoretically. Complementary characterization techniques used to probe the optical, structural, and chemical properties include spectroscopic reflectometry, gravimetry, scanning electron microscopy (SEM), transmission electron microscopy (TEM), and X-ray photoelectron spectroscopy (XPS). Each of these characterization techniques are briefly review towards the end of this chapter.

4.1 Fabrication

In this section we will describe the constituent parts of the etching setup. The electrochemical cell and the current source are both bought from Advanced Micromachining Tools (AMMT) and are designed especially for the purpose of making PS.

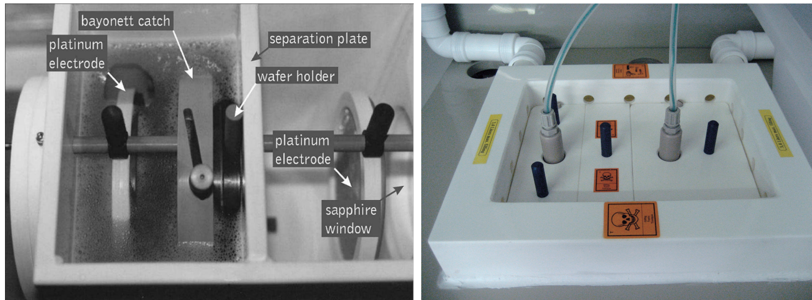

Figure 4.1: The etching cell. Left: the wafer is in place, dividing the two chambers so that the current has to pass through the wafer. Right: Etching cell with the lids on.

4.1.1 Etching Setup

The electrochemical etching cell is a double cell, meaning that the Si substrate is vertically placed between two separate reservoirs. Each reservoir contains the same electrolyte and one Pt-electrode, working as anode in one reservoir and as cathode in the other. Figure 4.1 shows the inside and outside of the cell. The system has sapphire windows to allow for the possibility of illumination during etching. Window covers are supplied to enable etching in complete darkness. The cell requires 3.4 l electrolyte per filling.

An advantage of the electrochemical double cell is that the frequently used metal contacts can be replaced by an electrolytic contact. This will avoid a potential source of contamination and establish a transparent contact. However, the potential of the wafer will not be known [39]. The fixation arrangement for the sample allows easy access and fast removal of the sample after etching.

The PS2 current source from AMMT has two operation modes; constant voltage (potentiostatic) and constant current (galvanostatic). The current range is $0 - 12$ A, while the voltage range is $0 - 36$ V. The PS layers in this work are generally processed in the constant current operation mode. This means that the current source is controlled to adjust for possible changes in resistivity during etching (by adjusting the voltage). In the galvanostatic operation mode, current is generally kept constant to within ± 2 mA. For the 4 cm^2 sample holder this corresponds to a variation in current density

of ±0.5 mA. The resolution of the output data is quite low and given with irregular time intervals. The potentiostat allows programming of current density profiles with a time resolution down to 50 ms, but in this so called fast mode, current and voltage data are not available for readout.

The electrolytes used consist of different ratios of 49% wt. HF and ethanol. In the mixing of these two constituents, volume ratios are used. When we state that the electrolyte has an HF concentration of 10%, this corresponds to a ratio of 1 : 4 and the % wt. consentration of HF will therefore be somewhat higher (about 12% wt.) since the density of HF is 1.15 g/mL and the density of ethanol is 0.79 g/mL.

4.1.2 Substrates

For most of the work in this thesis, monocrystalline, (100)-oriented, p-type Si wafers from Siltronix are used as substrates. The wafers have a doping of ∼ 0.01 Ωcm and are single or double side polished; the side used for PS formation is polished in all experiments. Considerations leading to the choice of this etching substrate are discussed in Section 5.1.

Also p-type multicrystalline wafers, c-Si n-type wafers with p-type emitters (p^+/n structures), c-Si p-type wafers with n-type emitters (n^+/p structures), and p/p^+ structures are used for some experiments. Different emitter profiles are made by in-diffusion in a horizontal tube furnace from Tempress. These emitter profiles, and the electrochemical etching of such substrates, will be discussed in Section 6.3.1.

4.2 Porosity and Etch Rate Calculations

To achieve an effective graded PS ARC, access to a wide range of porosities, by variation of the current density only, is highly desirable. It is well known that increased HF concentration leads to decreased porosity. With a wish to keep HF concentrations as low as possible for safety reasons, a starting concentration of 10% was adopted. We early established that this gave access only to the high porosity range. The HF concentrations were therefore increased to 15% and eventually 20%, where we found the available porosity range satisfactory. Table 4.1 [Paper V] summarizes the accessible porosity range for the different HF concentrations for a moderately doped p-type substrate, etched in dark and in an electrolyte containing solely HF,

Table 4.1: Porosity limits

Current density J	10% HF	15% HF	20%HF
1 mA/cm^2	···	38	26
5 mA/cm^2	76	49	40
max mA/cm^2	90	80	76

ethanol and water in our setup.

In order to accurately control the fabrication of complex samples the relation between current density and porosity and between current density and etch rate must be known with some accuracy. SE has been the primary characterization tool used to obtain porosity and thickness in this work. However, to confirm the validity of the ellipsometric results, gravimetry and SEM were also used in the initial characterization phase.

The gravimetric procedure is described in Section 4.4.1. The gravimetric results are shown in Table 4.2, where m_0 and m_1 are the masses of the wafer before and after PS formation, respectively and m_2 is the mass of the wafer after removal of the PS layer. $\delta_1 = (m_0 - m_1)$ is then the mass change due to anodic etching and $\delta_2 = (m_1 - m_2)$ is the mass change due to KOH etching. The accuracy of the weight used is 0.0001 g and from Table 4.2 it is evident that the relative uncertainty in some of these measurements is very large. In addition to the large measurement uncertainty, there are also other sources of uncertainty, such as the size of the area on which PS is formed, possible removal of small amounts of Si during the KOH etch, and changes in weight of the PS sample due to oxidation. A clear ring is visible around the sample and this ring likely has a different thickness and porosity than the rest of the sample.

Most of these uncertainties will be reduced by increasing the thickness and area of the PS layer, and only the layers where both δ_1 and δ_2 have a mass much larger than the accuracy limit of the weight are expected to provide reasonably accurate results. Unfortunately, the thickest samples, which gives the most accurate gravimetry results, are the most difficult to characterize by ellipsometry. Therefore, the number of layers that can be accurately characterized by both ellipsometry and gravimetry is rather few. A comparison of the results obtained by ellipsometry, gravimetry and SEM are shown in Table 4.3. The correspondence between porosity values obtained by gravimetry and SE is fairly good, while the deviations in thickness is

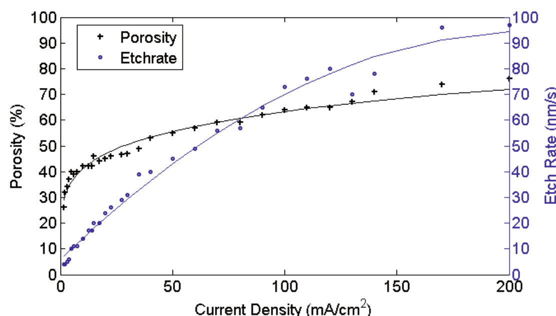

Figure 4.2: Porosity and etch rate versus applied current density. The trend line added for the porosity curve is a power curve, the trend line added for the etch rate is a second order polynomial. The lines are primarily a guide to the eye [Paper V].

somewhat larger. We were unable to fit satisfactory ellipsometry models to Sample 33, 43, and 44, but the etch rate and porosity determined from gravimetry is in correspondence with values found by ellipsometry for thinner layers etched at the same current density.

The most valuable outcome of the gravimetric results is an independent assessment of the approximate thickness and porosity of the PS structures. Although deviations exist, we regard the gravimetry results as a general support to the sense and validity of the ellipsometric model used. Thicknesses measured by SEM is generally in good accordance with ellipsometry results. In the few cases where TEM investigations are also performed, thicknesses obtained by this method is also in agreement with that obtained from ellipsometry. In conclusion we regard SE as a reliable technique for accurate determination of the PS structure parameters, dependable enough to be used as sole characterization technique in further work.

Figure 4.2 shows the experimentally determined dependence of porosity and etch rate on current density for a p^+ substrate in an electrolyte consisting of 20% HF. The relation between current density and porosity appears nonlinear, with the steepest gradient occurring at low current densities. For further discussion on this, see Paper V where the data was originally presented.

Table 4.2: Gravimetry results

Sample	m_0 (g)	m_1 (g)	δ_1 (g)	m_2 (g)	δ_2 (g)	t (nm)	P (%)
13c	2.7629	2.7467	0.0162	2.7445	0.0022	1579	88
14b	1.6531	1.6367	0.0164	1.6350	0.0017	1553	91
18f	1.4699	1.4673	0.0026	1.4669	0.0004	2861	87
25	9.3990	9.3941	0.0049	9.3880	0.0061	833	45
33	9.4003	9.3995	0.0008	9.3977	0.0018	189	32
34	9.3599	9.3443	0.0156	9.3391	0.0052	1574	75
42	5.0244	5.0200	0.0044	5.0155	0.0045	674	49
43	4.9307	4.9044	0.0263	4.8966	0.0078	2580	77
44	4.8796	4.8494	0.0302	4.8420	0.0073	2850	80

Table 4.3: Results obtained by different characterization techniques

	Thickness (nm)			Porosity (%)	
Sample	Ellipsometry	Gravimetry	SEM	Ellipsometry	Gravimetry
15a	262	...	258 − 268	79	...
15b	321	...	320 − 339	81	...
15c	426	...	370 − 424	83	...
15d	486	...	464 − 475	87	...
25	860	833	...	44	45
33	243	189	...	34	32
42	630	674	...	52	49

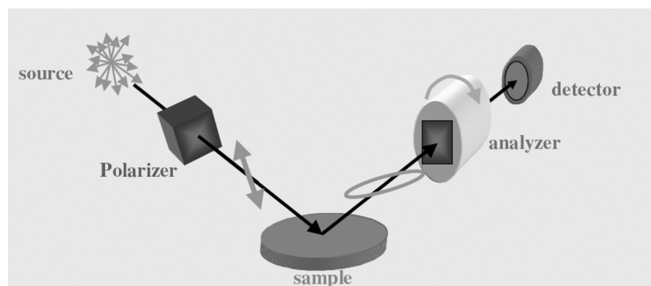

Figure 4.3: Schematic sketch of a typical ellipsometry setup. Adapted from the VASE Manual, Woollam Co. [136].

4.3 Ellipsometry

SE measurements and modeling have been central for much of the work presented in this thesis. In the following pages, we will therefore look at this technique in some detail. A brief introduction to ellipsometry is followed by a review of the most important underlying physical concepts. The ellipsometry equipment, hardware and software, used in this thesis is described. A discussion of the models applied in analysis of thin PS layers rounds off the section. Readers requiring a more in-depth description of ellipsometric modeling are suggested to read Tompkins and McGahan [134] and Fujiwara [135].

4.3.1 A Brief Introduction

Ellipsometry is the study of changes in the polarization states of light after reflection (or transmission) from a surface. A polarized light probe interacts with the sample and this interaction changes the state of polarization of the wave. By controlling the initial polarization state and measuring the final state, optical and compositional properties of the sample can be deduced, including the optical constants, thickness, composition, and anisotropy. The technique has been used in scientific laboratories for over a century and for about 50 years in the industry [134]. Ellipsometry is a well known technique, supported by a complete theoretical description.

The components typically found in an ellipsometer are depicted in Fig.

4.3. They include a light source, a polarizer, a compensator, an analyzer, and a detector.

The two most common light sources for ellipsometers are lasers and arc lamps. Lasers have high output intensity and well collimated, Gaussian beams. This is an advantage when the beam is focused and for angle measurements close to the Brewster angle where the intensity of the p-polarized reflectance is very small [134]. However, a laser typically only has one wavelength, hence arc lamps are generally used for spectroscopic measurements. Such sources have a significant output over a very broad wavelength range, but they are more difficult to focus and less intense.

The polarizer (or a combination of a polarizer and a compensator) is used to set the state of polarization of the incident beam. It does this by converting a light beam of any polarization state (unpolarized, partially polarized or elliptically polarized) into a known polarization state - in most cases a linearly polarized state. A linear polarizer works by letting through light with **E**-field directed along the optical axis, while extinguishing light with **E**-field perpendicular to the optical axis.

The analyzer is nothing but a polarizer set to do a different task, namely to resolve the polarization state of the light beam *after* it is reflected from the sample.

The compensator of the system is optional. Whether it is necessary or not depends on the desired measurement. Compensators are also referred to as retarders, phase retarders or quarter-wave plates. Their function is to alter the phase of one polarization component with respect to the other. If information about the depolarization of the sample is desired, a compensator will be needed.

Semiconductor photodiodes are often used as detectors in the ellipsometer. They are inexpensive, very linear over a broad range of intensity levels and reasonably sensitive over a broad spectral range.

4.3.2 Physical Principles

The theory in the following section is largely based on textbooks by Fujiwara [135] and Tompkins and McGahan [134].

Polarization

An electromagnetic wave requires four basic field vectors for a complete description: the electric field strength **E**, the electric displacement density **D**, the magnetic field strength **H** and the magnetic flux density **B**. The state of polarization is defined by the electric field strength. This choice springs from the nature of the interaction between electromagnetic waves and matter. The force exerted on an electron by the electric field is much stronger that the force exerted by the magnetic field.

In general photons are emitted with electric fields in all different directions, resulting in unpolarized light. If the photons instead have **E** fields oriented in a given direction, the light is referred to as polarized. A linearly polarized wave is confined to a given plane along the direction of propagation, in other words, the tip of a linearly polarized wave will trace out a line in the plane. This happens when adding two waves that are in phase and have the same frequency. The direction of the line depends on the amplitudes of the two components. If the two waves are exactly out of phase and have the same amplitude, a circular polarization results. The most general form of polarization is elliptical, which results for random phases and amplitudes.

When looking at light incident on a surface, it is convenient to specify two orthogonal polarization directions termed p and s. P is by definition parallel to the plane of incidence while s by definition is perpendicular to the plane of incidence. The directions are illustrated in Fig. 4.4.

Jones-matrix Formalism

A concise and convenient notation is needed to make polarization calculations as simple as possible. One such representation is the Jones formalism, which will be introduced in this section.

Assume that the incoming wave is time harmonic, monochromatic, uniform transverse-electric (TE) and plane.[1] Recall that the state of polarization of a wave can be generalized from linear to elliptic by superposition of two linearly polarized waves. The electromagnetic field vector was given in Eq. 3.9. We have a xyz orthogonal, right-handed, Cartesian coordinate system

[1] A time harmonic wave is periodic, repeating itself in time and space. Monochromatic refers to the single frequency of the wave. Uniform transverse electric means that the fields have no dependence on the transverse coordinates x, y and are functions only of z, t. A plane wave has wavefronts that are infinite parallel planes of constant amplitude normal to the direction of propagation.

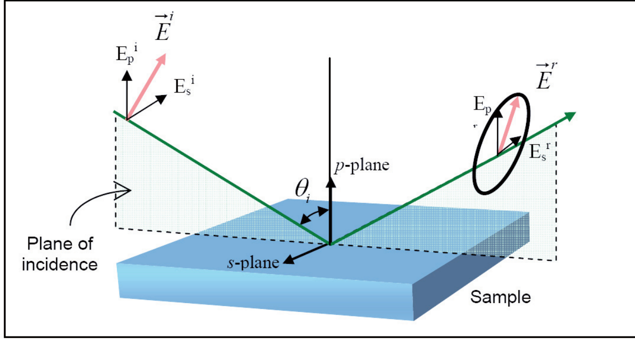

Figure 4.4: Illustration of the p and s directions relative to the plane of incidence. Adapted from the VASE Manual, Woollam Co. [136].

with unit vectors parallel to the positive directions of the x and y axis. If the wave is propagating along the positive z direction, the electromagnetic field vector for an elliptically polarized wave is given by

$$\mathbf{E} = \mathcal{E}_x \exp\left(i[\omega t - (2\pi N/\lambda)z + \psi_x]\right)\tilde{\mathbf{x}} + \mathcal{E}_y \exp\left(i[\omega t - (2\pi N/\lambda)z + \psi_y]\right)\tilde{\mathbf{y}}. \tag{4.1}$$

Because the electric field is transverse-electric there is no field-component in the direction of propagation, z. To construct a convenient notation for use in ellipsometry, we want to remove all unnecessary information. By writing the expression using matrix formalism we can dispose of the fixed unit vectors

$$\mathbf{E} = \begin{pmatrix} \mathcal{E}_x \exp\left(i[\omega t - (2\pi N/\lambda)z + \psi_x]\right) \\ \mathcal{E}_y \exp\left(i[\omega t - (2\pi N/\lambda)z + \psi_y]\right) \end{pmatrix}. \tag{4.2}$$

The spatial information about the wave can be dropped by considering the field over one fixed transverse plane, substituting $z = 0$. The temporal information can be suppressed because it is known that the wave oscillates sinusoidally with time at the same frequency. We are then left with the expression below

$$E(0) = \begin{vmatrix} \mathcal{E}_x \exp(i\psi_x) \\ \mathcal{E}_y \exp(i\psi_y) \end{vmatrix} = \begin{vmatrix} E_{0x} \\ E_{0y} \end{vmatrix}. \tag{4.3}$$

The last equality is simply a short notation, E_{0x} is by definition equal to $\mathcal{E}_x \exp(i\psi_x)$. This vector is the desired concise representation of a single

plane wave which is known to be monochromatic, uniform and transverse-electric. It is called the Jones vector and provides full information about the amplitudes and phases of the field components, and hence about the polarization of the wave.

Next step is to extend this notation to include the influence of a sample upon the light. When a light wave is reflected at an interface between two optically dissimilar media, the state of polarization is changed. In the Jones formalism this can be expressed as

$$\begin{vmatrix} E_{ox} \\ E_{oy} \end{vmatrix} = \begin{vmatrix} T_{11} & T_{12} \\ T_{21} & T_{22} \end{vmatrix} \begin{vmatrix} E_{ix} \\ E_{iy} \end{vmatrix}. \tag{4.4}$$

The 2×2 transformation matrix, $\mathbf{T}$, is called the Jones matrix of the optical system and its elements are in general complex. Taking a closer look at the elements of the matrix reveals that the diagonal elements map the input-to-output of the same linear polarizations (**E**-field along the same axis), while the off-diagonal elements map the polarization that switches between p and s. The Jones matrix therefore relates the p and s modes of the incident and reflected waves, and in the case of reflection ellipsometry it is defined as

$$J = \begin{vmatrix} r_{pp} & r_{sp} \\ r_{ps} & r_{ss} \end{vmatrix}. \tag{4.5}$$

A diagonal Jones matrix results when light is reflected at the interface between two isotropic and non-optically active media. The linear polarizations are then reflected with no change in polarization. These two diagonal elements, which are simply the amplitude ratio of the electric field before and after interaction, $r_{pp} = E_{ip}/E_{rp}$ and $r_{ss} = E_{is}/E_{rs}$, are refereed to as Fresnel coefficients. To avoid any confusion with the reflection coefficient, R, calculated in Section 3.3, which is the ration of the *irradiances*, lower case letters are used. It is the ratio of the Fresnel coefficients which leads us to the common ellipsometric variables Ψ and Δ through the relation

$$\frac{r_{pp}}{r_{ss}} = \tan\Psi \exp i\Delta. \tag{4.6}$$

The form of this equation immediately reveals that Ψ is related to the amplitude ratio while Δ is related to the phase shift. The Fresnel coefficients are directly related to the optical constants of the material. This can be seen by considering the boundary conditions for electric and magnetic fields.

The boundary conditions require that the **E** component *parallel to an interface* is continuous at the interface. The **E**-field component *tangential to the plane of incidence*, $E_\perp$, is therefore continuous over the boundary (as it is parallel to the interface), while the **E**-field component perpendicular to the plane of incidence, $E_{||}$ is discontinuous. For the **B** field, it is the component *normal to the interface* that is continuous. However, $\mathbf{B} = \mu\mathbf{H}$ and the **H** field is similar as the **E** field in that the component parallel to the interface is continuous. Therefore, we use the ratio $\mathbf{B}/\mu$, which has a continuous component tangential to the plane of incidence, in the equations below. The boundary conditions can be derived from Maxwell's equations.

When deriving the Fresnel equations it is convenient to look at the p and s polarizations separately. Let us look first at s-polarized light at a boundary. The **E**-field is then by definition parallel to the boundary and therefore continuous

$$E_i + E_r = E_t, \tag{4.7}$$

where E_i, E_r, and E_t are the electric field of the incoming, reflected, and transmitted waves, respectively. The tangential part of the product $\mathbf{B}/\mu$ is also continuous and given by

$$-\frac{B_i}{\mu_i}\cos\theta_i + \frac{B_r}{\mu_r}\cos\theta_r = -\frac{B_t}{\mu_t}\cos\theta_t. \tag{4.8}$$

Recall that the **B**-field changes direction from incoming to reflected. We now assume that $\mu = \mu_0$ and use $B = nE/c$ and Snell's law, $\theta_i = \theta_r$ to rearrange the equations. Only the amplitude of the waves at the boundary is considered. We find that

$$n_i(E_{0r} - E_{0i})\cos\theta_i = -n_t(E_{0r} + E_{0i})\cos\theta_t. \tag{4.9}$$

The reflectance can be given by the ratio E_{0r}/E_{0i}. Rearranging gives

$$r_{ss} = \frac{E_{0r}}{E_{0i}} = \left(\frac{n_i\cos\theta_i - n_t\cos\theta_t}{n_i\cos\theta_i + n_t\cos\theta_t}\right). \tag{4.10}$$

The same procedure is used for p-polarized light. The **B**-field is then completely parallel to the surface. Thus the continuous tangential **E**-field and **B**-field are given by

$$E_i\cos\theta_i + E_r\cos\theta_r = E_t\cos\theta_t \tag{4.11}$$

$$-B_i + B_r = -B_t. \tag{4.12}$$

Rearranging using the same conditions as for s-polarization we get

$$n_t(E_{0r} + E_{0i})\cos\theta_i = n_i(E_{0r} + E_{0i})\cos\theta_t \tag{4.13}$$

$$r_{pp} = \frac{E_{0r}}{E_{0i}} = \left(\frac{n_t\cos\theta_i - n_i\cos\theta_t}{n_t\cos\theta_i + n_i\cos\theta_t}\right) \tag{4.14}$$

For a critical angle, r_{pp} will become 0. This is called the Brewster angle and as ellipsometry measures the ratio of r_{ss}/r_{pp}, the measurement will be very sensitive around this angle. Note that we here used the real refractive index, i.e. we assume non-absorbing media. The Fresnel equations still hold for complex refractive indices. In this case we get complex amplitude coefficients.

We see that the equations derived here (Eq. 4.10 and 4.14) bear resemblance to the equations derived for the reflectance in Section 3.3, Eq. 3.6. For isotropic media and absorption free incident medium the Fresnel coefficients and the reflection has the simple relation:

$$R_s = r_{ss}r_{ss}^* \tag{4.15}$$

$$R_p = r_{pp}r_{pp}^*, \tag{4.16}$$

where * denotes the complex conjugate.

If the sample is anisotropic, the off-diagonal elements in the Jones matrix may become nonzero. This regime is called generalized ellipsometry and in this case we get two additional ratios to deal with. However, if the material is uniaxial anisotropic (anisotropy in only one direction) and the axis of anisotropy is aligned either perpendicular to or parallel with the incident light, the off-diagonal elements in the Jones matrix will remain zero and generalized ellipsometry is not needed.

Stokes Vectors and Mueller-matrix Formalism

The Jones formalism introduced is convenient for a wide range of ellipsometric studies. However, the Jones-matrix formalism cannot handle depolarization, i.e. that a sample decreases the degree of polarization of the transmitted light. In such cases we have to resort to the more powerful Mueller matrix formalism. This formalism is based upon the representation of the state of polarization of the electromagnetic wave by a so called Stokes vector and

a representation of the optical system by a Mueller matrix. The different possible polarization states of transverse-electric (TE) plane waves can be represented by the four Stokes parameters. The Stokes parameters are defined by

$$S_0 = |E_x(t)|^2 + |E_y(t)|^2 \tag{4.17}$$
$$S_1 = |E_x(t)|^2 - |E_y(t)|^2 \tag{4.18}$$
$$S_2 = 2\text{Re}(E_x E_y^*) \tag{4.19}$$
$$S_3 = 2\text{Im}(E_x E_y^*). \tag{4.20}$$

The Stokes parameters of a wave can be grouped into a 4×1 column vector

$$\mathbf{S} = \begin{vmatrix} S_0 \\ S_1 \\ S_2 \\ S_3 \end{vmatrix}, \tag{4.21}$$

called the Stokes vector. For unpolarized light the Stokes vector assumes the simple form $S = S_0, 0, 0, 0$. An important feature of the Stokes vector is that it easily quantifies the degree of polarization as the ratio of the intensity of the totally polarized component to the total intensity of the wave

$$P = (S_1^2 + S_2^2 + S_3^2)^{1/2}/S_0. \tag{4.22}$$

Although the Mueller-matrix formalism also is valid in the cases when the optical system is non-depolarizing and the incident light is totally polarized, it cannot give information about the absolute phase of the wave. This absolute-phase information is suppressed in the definitions of the Stokes vector and therefore the Jones matrix formulation should be used in this case.

4.3.3 The VASE Ellipsometer

All ellipsometric characterizations performed in this work have been carried out employing a J. A. Woollam Variable Angle Spectroscopic Ellipsometer (VASE).

The incident light is provided by an arc lamp, glowing from xenon discharges, mounted within the monochromator lamp housing. The monochromator sort out the unwanted wavelengths. For the VASE systems a Czerny-Turner Scanning Monochromator is used.

The ellipsometer is equipped with a rotating analyzer (RAE) which generally produces very accurate data when detecting circularly polarized light. It is however less accurate when the detected light is linearly polarized. In addition it cannot determine the handedness of the reflected beam polarization ellipse [136, pp 2-17]. Adding a compensator, in this case Woollams AutoRetarder, alleviates these drawbacks and enables generalized ellipsometry and depolarization data to be collected. Depolarization of the light beam can be caused by a non-uniform or patterned film, backside reflections from a transparent substrate, or from the spectral resolution [137]. For the majority of samples depolarization data is acquired, while generalized ellipsometry is not needed as the samples are satisfactorily modeled with off-diagonal elements being zero. This will be discussed in more detail in Section 4.3.5.

Incident angles have been varied from 55° to 80°. Inserting the refractive index of Si into Eq. 4.14, the Brewster angle for Si can be calculated to be approximately 75° (but wavelength dependent). This is where the measurements are most sensitive.

The wavelength range of the ellipsometer extends from $300 - 2500$ nm, but with focus probes mounted the range is restricted to $400 - 1000$ nm. The resolution used has been either 50 Å or 100 Å, depending on the expected thickness - and therefore complexity - of the given sample. Several of the data sets are taken with focus probes present. This reduces the spot size from 4 mm to 0.2 mm and leaves the data less prone to errors due to inhomogeneities on the sample. With the focus probes installed the maximum angle of incidence is 75°.

4.3.4 The WVASE32 Software

For modeling the ellipsometric data, the special purpose WVASE32 software from Woollam is used. The software provides a wide variety of modeling options and an extensive database of optical constants. In the program, you build an initial model, based on your best guesses. The program can then generate ellipsometric data from this guessed model and an algorithm is used to reduce the deviation between experimental data and model data. For modeling of PS in this thesis, tabulated constants of Si [138] and p-doped poly Si [139] are extensively used. Other optical constants from the database, including a-Si [140] and SiO_2 [141], are also made use of on occasion.

Numerical algorithms are used to vary the unknown parameters and minimize the difference between simulated and experimental data. In WVASE32,

the Levenberg-Marquardt minimization routine is used to measures the quality of the fit by a mean square error (MSE):

$$MSE = \frac{1}{2N - M} \sum_{i=1}^{N} \left[\left(\frac{\Psi_i^{mod} - \Psi_i^{exp}}{\sigma_{\Psi,i}^{exp}} \right)^2 + \left(\frac{\Delta_i^{mod} - \Delta_i^{exp}}{\sigma_{\Delta,i}^{exp}} \right)^2 \right]. \quad (4.23)$$

N is the number of measured sets, M is the number of variable parameters in the model, Ψ^{mod} and Δ^{mod} are the modeled ellipsometric values, Ψ^{exp} and Δ^{exp} are the experimentally determined ellipsometric values, and σ denotes the standard deviations of the measurement at each data point. For measurements with larger fluctuations in measurement values, the standard deviations will be larger causing such measurements to be less weighted in the fit [59, 142, 143].

The WVASE32 software provides a range of statistics regarding the fit quality; the MSE value, the 90% confidence intervals in the model parameters, and a parameter correlation table. These features serve as the basis for estimating the quality of the match between the data calculated from the model and the experimental data as well as for judging the validity of the model employed.

4.3.5 Ellipsometric Modeling of PS

All information about physical parameters extracted from ellipsometry depends critically on the modeling of the measured data. The cornerstone in the modeling of the PS samples in this thesis is the use of the Bruggeman effective medium approximation (BEMA) [144]. Some special attention will therefore be directed to the nature of effective medium approximations (EMA), including how to implement grading and optical anisotropy in these models. Finally, we look at the construction of the model step by step.

Effective Medium Models

The essence of the EMA is that the macroscopic properties of a medium is described based on the properties and the relative fractions of its components. The property under consideration is usually the dielectric constant of the medium, and so an ensemble of nanoclusters is considered as some

new medium with an effective permittivity or refractive index [61]. An immense advantage of the EMA is that within this approximation the analysis of light propagation in nanostructured material does not require solving the Maxwell equations at each point in space [61]. The EMA relies on the size of the nanoparticles and the distance between them to be very small compared with the optical wavelength of light in the medium. The structural dimensions in meso and nano PS are of a scale that allows us to treat them in the framework of the effective medium concept. In literature the EMA is commonly utilized for PS and the optical properties are typically modeled as a mix of crystalline Si and air ("void") [145–147].

EMAs available in the WVASE32 software are Maxwell Garnett [148], Bruggeman [144], and linear. All the EMAs uses the same equation but with different "host" material. For a two component system, the approximation is given by

$$\frac{N_{\text{eff}}^2 - N_h^2}{N_{\text{eff}}^2 + 2N_h^2} = f_A \left(\frac{N_A^2 - N_h^2}{N_A^2 + 2N_h^2} \right) + f_B \left(\frac{N_B^2 - N_h^2}{N_B^2 + 2N_h^2} \right), \tag{4.24}$$

where f_A and f_B are the volume fractions of the two components and therefore $f_A + f_B = 1$. N_A and N_B are the already known refractive indices of the two components and N_h is the refractive index of the host. In the BEMA the host is the effective medium, in Maxwell-Garnett the host is air. For the BEMA it can easily be seen that the left hand side of the above equation reduces to zero as $N_{\text{eff}} = N_h$.

It is, in principle, possible to extend the analysis to three constituents and thereby include SiO_2 in the EMA layers. However, with a few notable exceptions [149, 150], it is rather common to neglect oxidation when performing ellipsometric characterization of PS [151, 152]. This is likely because SE appears to be rather insensitive to moderate oxidation in the PS structures. Partly, the inclusion of oxide is complicated by the number of different oxidation states; from XPS measurements it is clear that Si_2O, SiO, Si_2O_3, and SiO_2 all can be present [Paper IV]. But, regardless of this, the difference in Ψ and Δ is marginal, and consequently it is a challenge to determine oxidation of PS with SE. Whether neglecting SiO_2 is a viable approach or not depends, of course on the amount of oxide, but also on the information sought. Clearly, information about the chemical composition of the material is lost, while changes in the effective refractive index of the material are marginal. This is further discussed in Paper IV.

Grading of the Effective Medium

The PS layer is not necessarily homogeneous. For instance, the interfaces between PS/Si and PS/air are not expected to be abrupt, but rather display a certain roughness. The existence of such roughness layers has previously been reported in several papers [59, 153, 154]. The main section of the PS layer may not be homogeneous either. Even if etching is performed at constant current density, small porosity gradings can occur, either due to chemical etching or changes in HF concentration with depth [155]. There are different ways of accommodating these layer inhomogeneities into an ellipsometric model. The transition between the Si substrate and PS is often modeled by adding a separate intermix layer consisting of the substrate and the PS film mixed together. Similarly the transition between PS and air is commonly modeled by adding a BEMA layer with 50% void and 50% PS at the surface of the PS layer. The main section may be approximated as homogeneous, it can be divided into separate EMA layers or it can be modeled by the addition of a porosity gradient.

In the models used in this work, all the interface layers and possible inhomogeneities in the main layer are incorporated into a grading of the PS layer. In the graded model, independent porosities are fitted at three to six positions in the layer (depending on the exact model). Between these positions the porosity varies linearly with a chosen number of steps. Two of the positions are fixed, one at the surface and one at the PS/Si interface.

Figure 4.5 shows the modeled porosity profile for three samples etched at three different current densities. Some grading is seen within the main layers. A steep increase in porosity close to the Si interface (0% depth) and close to the surface (100% depth) is also clearly displayed. The small dip in porosity seen in Fig. 4.5 is a feature visible in the majority of the modeled porosity profiles. It has a relatively large impact on the fit, and is particularly evident in the models of lower porosity samples. The dip has a physical origin and the feature is thoroughly discussed in Paper III.

Anisotropy

A short introduction to the concept of optical anisotropy was given in Section 2.6.1. Ellipsometry allows characterization of both uniaxially and biaxially anisotropic materials. Anisotropy induces cross-polarization and characterization of birefringent materials requires generalized ellipsometry. However,

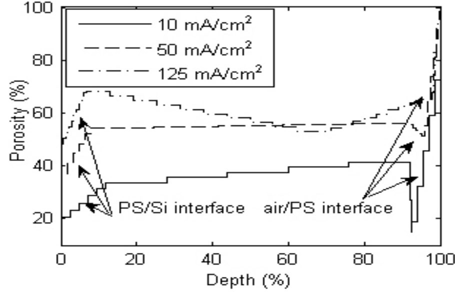

Figure 4.5: Porosity with depth in the PS layer.

in the special case of uniaxially anisotropic material with axis normal to or parallel with the plane of incidence (sample surface), standard ellipsometry is sufficient.

As ellipsometric measurements are extensively utilized for characterization of the fabricated PS films, it is convenient to adopt an terminology which is in accordance with that used during modeling. In addition, this anisotropy terminology relates directly to the shape of the inclusions causing the anisotropy. This is convenient as it eases the visualization of the effect of the different pore morphologies.

The shape anisotropy of the pores introduces distinct boundary conditions for the electric and magnetic fields in the medium. This can be described by a charge screening parameter, κ, or equivalently, the depolarization factors q_x, q_y and q_z, related to κ by

$$\kappa = \frac{1 - q_i}{q_i}. \tag{4.25}$$

The depolarization factor is again directly related to the geometry of the medium or, more specifically, the eccentricity of the inclusions, ζ. For a prolate spheroid, the depolarization component along its major axis is given by

$$q_i = \frac{1-\zeta^2}{\zeta^2}\left[\frac{1}{2\zeta}\ln\left(\frac{1+\zeta}{1-\zeta}\right) - 1\right]. \tag{4.26}$$

The sum of the depolarization factors is always 1, so for an isotropic material, $q_x = q_y = q_z = 0.33$. $q_z = 0$ corresponds to a completely columnar structure, while $q_z = 1$ corresponds to a horizontally layered structure.

Although the pores of the PS samples investigated here grow predominantly in the (100) direction, substantial branching could introduce anisotropy that is not normal to the surface. Generalized ellipsometry was therefore performed on a representative sample. As the generalized ellipsometry did not show any sign of in-plane anisotropy, in all further work (on the same substrate) we assume uniaxial anisotropy with axis normal to the sample surface and that standard ellipsometry therefore is sufficient. It is also previously reported that PS has a uniaxial anisotropic nature [59, 60].

In the BEMA, anisotropy can be modeled by introducing one depolarization parameter in each direction (q_x, q_y, and q_z). In the most general model, the three depolarization factors are allowed to vary in three arbitrary directions. However, for the samples presented here, we now know that the anisotropy is uniaxial and perpendicular to the sample surface. The x and y directions can then be set equal, while the value of the depolarization factor in the z-direction is allowed to vary.

For all the ellipsometric models of PS layers employed in the work of this thesis, the anisotropy is modeled by an ungraded depolarization factor. The depolarization factor has been reported to depend on porosity [66] and could therefore exhibit a grading corresponding to that of the porosity. However, experimentally we find that the depolarization factor varies relatively little between samples of different porosity. Only minor improvements in MSE ($5-8\%$) is found when graded depolarization is introduced and it leads to significantly increased parameter correlation. As a consequence, an ungraded depolarization factor is used.

The Model - Step by Step

We will now take a closer look at some of the features invoked in the models. In Fig. 4.7, 4.8, 4.9, 4.10, and 4.11 the evolution of an ellipsometry fit, from the simplest model (a) to the more complex model (e) is shown. All samples are modeled on an isotropic Si substrate, and Ψ and Δ values for three angles are shown in each plot. The parameters resulting from each model are shown in Table 4.4.

Model a) is the very simplest model consisting of a BEMA layer with two components; crystalline Si and void (air). The thickness of the layer is also fitted. The fit is very poor and it is evident that the model does not represent the ellipsometric data very well. By adding a porosity grading in the BEMA a large improvement in MSE is achieved (model b). This is

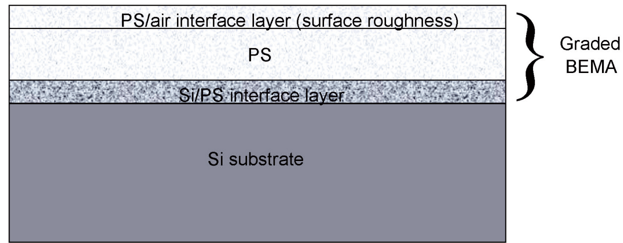

Figure 4.6: An illustration of the general ellipsometric model required to describe the obtained data. The illustration is not to scale.

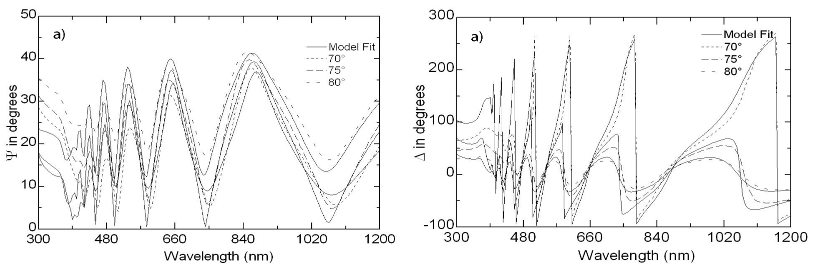

Figure 4.7: Experimental and fitted ellipsometric variables ψ and Δ for a model of a PS layer etched at constant current density. Model a) consists of BEMA with Si and void.

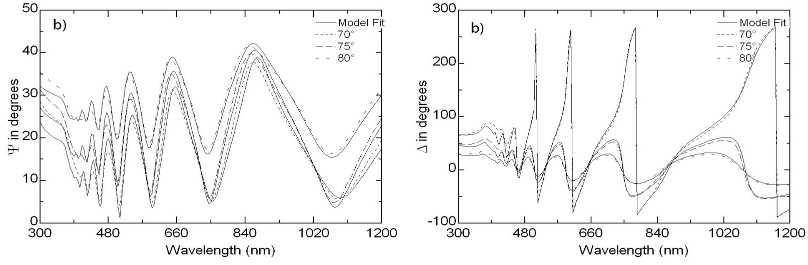

Figure 4.8: Model b) consists of BEMA with Si and a graded void fraction.

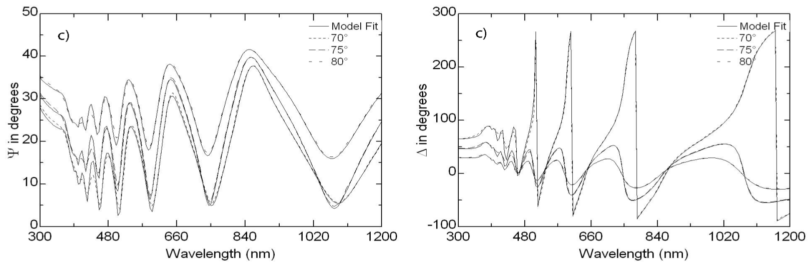

Figure 4.9: Model c) consists of a uniaxially anisotropic BEMA with Si and a graded void fraction.

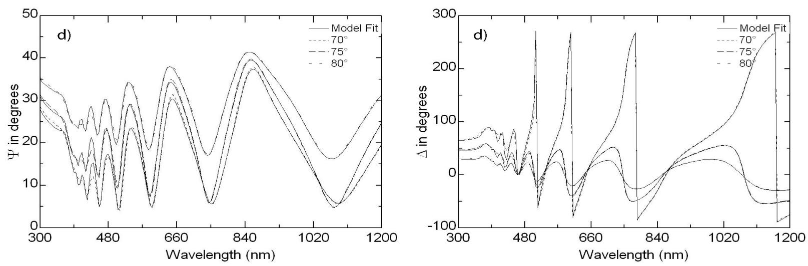

Figure 4.10: Model d) consists of a uniaxially anisotropic BEMA with Si and a graded void fraction, depolarization and non-uniform sample thickness

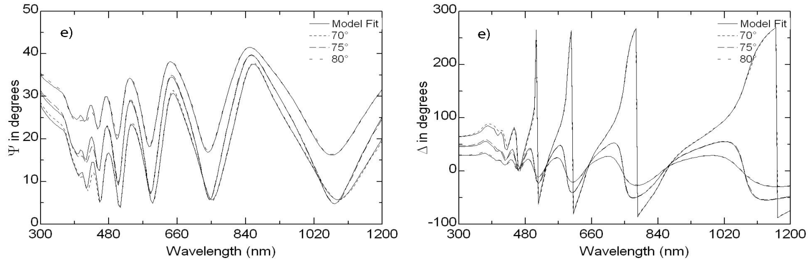

Figure 4.11: Model e) consists of uniaxially anisotropic BEMA with Si, p-doped poly-Si and a graded void fraction, depolarization and non-uniform thickness.

probably due to a better accommodation of the interface regions between Si/PS and PS/air. The next step is to add anisotropy in the model (model c). This is done by introducing a depolarization parameter, q_z. This model provides a relatively good fit to the data, and for some datasets, this is the best model. For other datasets, further improvements can be made. In model d) the possibility of non-uniform thickness of the sample is added. This is not necessary for all samples and the parameter is only added if it results in significant improvement of the MSE. The last model introduces a third constituent in the effective medium. In addition to c-Si and void, a fraction of p-doped poly-Si is fitted. Although the crystallinity is retained, the small dimensions of the PS pore walls may result in modified refractive indices compared to bulk Si. The poly-Si component is used to model the enhanced absorption at the boundaries of the nanocrystals. The poly-Si constituent is not used in all models. In general models d) and e) are used, but variations between the samples do exist.

4.4 Complementary Characterization

4.4.1 Gravimetry

Gravimetry provides an independent measure of the porosity and thickness of the PS samples. The weight used to measure samples is a Sartorius balance (CP 224s) with a readability of 0.0001 g. The wafer is weighted before and after the PS layer is formed. The PS layer is then etched away and the wafer

Table 4.4: Ellipsometry models

Model	T (nm)	P (%)	q_z	NUT[1]	pc-Si (%)	MSE	MC[2]
a)	601	55.4	0.333	0	0	84.2	0.916
b)	664	graded ($\sim$ 59)	0.333	0	0	31.3	0.906
c)	648	graded ($\sim$ 57)	0.274	0	0	14.0	0.916
d)	648	graded ($\sim$ 57)	0.273	3.5	0	11.8	0.919
e)	604	graded ($\sim$ 57)	0.267	3.4	12.7	9.2	0.918

[1]Non Uniform Thickness, [2]Maximum parameter Correlation. The stated porosities are the average porosities for each PS layer.

is weighted again. For the samples presented here, a few minutes in 2% KOH, the time depending somewhat on the thickness of the PS layer, is used to etch the PS layer.

The mass of the bare wafer is given by:

$$m_0 = A_w \cdot t_w \cdot \rho_{Si}, \tag{4.27}$$

where A_w is the area of the wafer, t_W is the wafer thickness, and ρ_{Si} is the density of Si, known to be 2.33 g/cm^3. The mass of the wafer after PS formation, m_1 is given by:

$$m_1 = m_0 - (A_{PS} \cdot t_{PS} \cdot P \cdot \rho_{Si}), \tag{4.28}$$

where P is porosity in percentage, A_{PS} is the area of the PS layer and t_{PS} is the thickness of the PS layer. The mass of the wafer after preferential PS etch, m_2, is given by

$$m_2 = m_0 - (A_{PS} \cdot t_{PS} \cdot \rho_{PS}). \tag{4.29}$$

A_{PS} is known from the area of the sample holder in the PS etching system and m_0, m_1, and m_2 are all measured. Therefore the last two equations for m_1 and m_2 gives us the porosity, P_{PS} and the thickness, t_{PS} of the PS layer.

4.4.2 Reflectance Measurements

While many of the previous characterization techniques have primarily been used to determine the structure and physical properties of the PS films, it is the optical properties, and in particular reflectance measurements, that is the final yardstick. Low reflectance is a relatively important property for an

antireflection coating. Three different setups have been used for reflectance measurements, two located at IFE and one at REC in Sandvika. The reason for using three different setups is split. Firstly, the availability of the setups has varied. Secondly, the setups are complementary to each other with respect to wavelength and spot size. Thirdly, we desire quite accurate absolute measurements and it is advantageous to have checks on calibration and equipment.

The setup that was in place at IFE from the start is a Stanford Research System setup, consisting of a CVI AS220 light source, a lock-in amplifier from Stanford Research Systems and a preamplifier from EG&G. The incident light is focused on the sample using two successive lenses and a mirror. The spot size is adjustable in width ($0 - 1.5$ cm) but not in height (1.5 cm). The operational wavelength range of the Stanford system is $400 - 1200$ nm. The incident angle is adjustable, but $11°$ (which is the lowest possible) was used for all reflectance measurements unless otherwise stated. A new setup from Ocean Optics was installed at IFE in 2010. It consists of two separate spectrometers, in principle allowing for a broader wavelength range. However, problems with the near IR spectrometer reduced the use of this setup. The incident angle of the Ocean Optics setup is $8°$. The setup at REC in Sandvika is a Varian Cary 5000 Spectrophotometer set to an incident angle of $8°$. All three setups are equipped with an integrating sphere and it is the total reflectance that is measured. A weighted average with respect to the solar spectrum is then calculated from the measured spectral reflectance. The angle of incident is very similar between the setups and should not significantly affect the resulting reflectances. The reason for not using $0°$ incident angle is that specularly reflected light would escape through the same opening in the integrated sphere as it entered.

4.4.3 Scanning Electron Microscopy

A scanning electron microscope (SEM) uses electrons instead of light to image the sample surface. A high energy electron beam is scanned over the sample surface. The electrons interact with the sample and produce information about the samples surface topography and composition. Several types of signals result from the deceleration of the electrons in the sample. The two signals most commonly used to produce SEM images are secondary electrons and backscattered electrons [156].

SEM has a large depth of field, allowing portions of the sample with

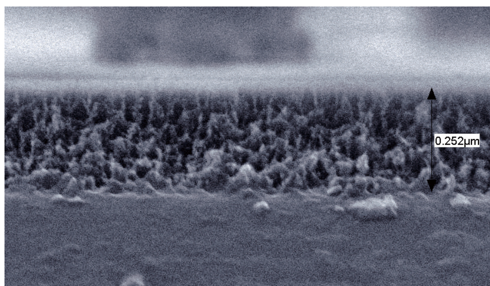

Figure 4.12: Cross sectional SEM image of a homogeneous PS layer.

significant height differences to be simultaneously in focus. This results in a characteristic three dimensional appearance useful for understanding the surface structure of a sample. The resolution is set by the diameter of the incident beam and the operation mode, and can be as high as ~ 1 nm.

The SEM utilized for the characterization presented in this work is a Hitachi S4800 localized at IFE. The resolution is specified down to 1 nm for an accelerating voltage of 15 kV.

Sample preparation is usually relatively straight forward, as SEM only requires the sample to be conductive. We eventually adopted a procedure of simply fracturing the samples (to display the cross section) and place a piece directly into the SEM. This worked quite well, and is the only preparation done for the SEM sample images presented in this thesis.

For macro PS, SEM can be used to determine size and shape of the pores. Due to the small scale of nanopores determination of pore structure grows harder for such layers. A cross sectional SEM image of a homogeneous PS layer is shown in Fig. 4.12. Here, the pores and pore walls are discernible and some impression of the pore structure can be obtained. However, the primary goal when using SEM for the PS samples is to find an independent measure of their thickness.

4.4.4 Transmission Electron Microscopy

TEM is a collection of microscopy based techniques, widely used to obtain detailed structure information of various materials. For PS, TEM provides detailed structural information and valuable visual impressions of the pore

morphology. Not only are these images much more expressive than verbal descriptions, they are also the basis of the schematic layouts we use to (attempt) to classify PS structures.

The microscope used to study the PS layers was a 200 keV JEOL 2010F microscope equipped with a Gatan imaging filter and detector, located at the University of Oslo. The energy resolution at 200 keV can be about 0.8 eV. The majority of the PS TEM images included in this work have been taken by Dr. Annett Thøgersen, a few have been taken by Foerste Amenuensis Anette Gunnæs.

The instrument works by firing a high energy beam of electrons in vacuum through a thin, electron-transparent region of the sample. The electron beam is produced by accelerating the electrons through a potential drop, before focusing the beam onto the sample by electromagnetic lenses. The resolution of any imaging microscope is ultimately limited by the wavelength of the image-forming wave. For a 300 keV electron, the De Broglie wavelength, $\lambda = h/p$, is almost a hundred thousand times smaller than the wavelength of light. A higher accelerating voltage means a larger momentum and a smaller electron wavelength. Although today's TEMs are far from approaching this wavelength limit of resolution (due to imperfect electron lenses [157]) the resolution limit of conventional electron microscopes is about a thousand times smaller than that of the best light microscope [158]. Therefore TEM provides some of the most detailed information on the internal structure of materials.

Electrons interact strongly with the sample, producing diffracted electron beams, energy loss electrons, back-scattered electrons, secondary electrons, and X-rays. Different TEM techniques exploit the different reaction products. According to the techniques used TEM can give images related to the local thickness of the material, the phase-contrast (reveal the atomic lattice) and diffraction-contrast (reveal crystallographic defects). I will briefly touch upon the techniques used on the PS images in this work.

The directly transmitted electrons are focused by electromagnetic lenses and imaged onto a fluorescent screen. A "shadow image" of the sample, with the structure showing up as variations of darkness according to the sample density variations, results. An example is showed in Fig. 4.13. The structure is very similar to that shown in the cross sectional SEM image in Fig. 4.12. Electrolyte, substrate and etching time is identical, the current density is increased from 5 mA/cm^2 (SEM sample) to 7 mA/cm^2 (TEM sample).

High resolution transmission electron microscopy (HRTEM) is a phase-

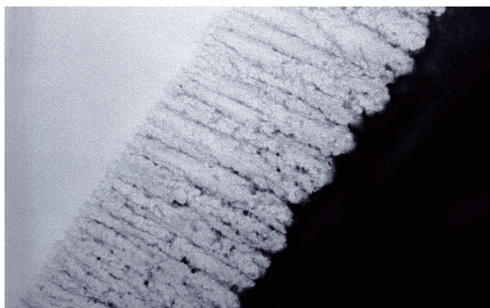

Figure 4.13: Cross sectional TEM image of a homogeneous PS layer.

contrast imaging mode of the TEM that allows imaging of crystal structure. HRTEM produces an image based on several electron beams, while conventional TEM uses only one beam. It is dubbed phase contrast imaging because the contrast arises from the interference of the direct beam with the diffracted electron wave instead of arising from absorption by the sample. Different materials give rise to small phase changes in the diffracted wave function and this is how the contrast between different areas of the image is produced. Figure 4.14 shows a HRTEM image of the interface between pores and Si at the bottom of the porous layer. The pores are filled with epoxy from the sample preparation.

Selected area diffraction (SAD) is a diffraction-contrast imaging mode. Here the atoms act as a diffraction grating to the electrons and the scattering angles are determined by the crystal structure of the sample. The resulting image on the TEM screen will be a series of spots in the case of a single crystal, while polycrystalline or amorphous material will give series of rings. This method is used on a selection of the PS samples to determine whether they have retained their crystallinity. Figure 4.15 shows that the Si walls of the PS structure retains their crystalline structure.

Figure 4.16 shows some examples of energy filtered TEM (EFTEM) images. In B), electron energy corresponding to Si is imaged, while in C) the filter is switched to an electron energy corresponding to SiO_2.

The way in which the preparation of thin specimens is carried out for TEM often controls the quality of the final data obtained. Ion milling is used in the TEM specimen preparation process to obtain a centre region

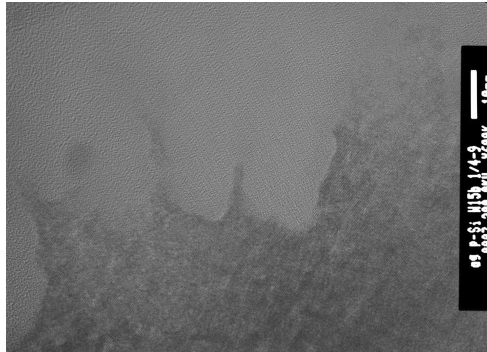

Figure 4.14: HRTEM image of pore bottoms in a PS layer.

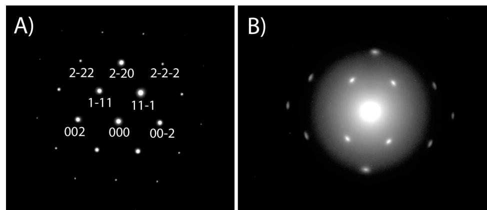

Figure 4.15: SAD patterns from the Si substrate and from the central area of the porous layer showing that the crystalline walls in the porous region remain as a single crystal. Only a slight variation in orientation is seen inside the porous region. The diffuse rings in the pattern from the porous region are identical to the rings observed for the epoxy used in the sample preparation.

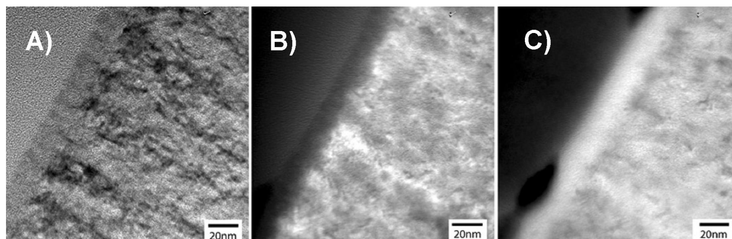

Figure 4.16: TEM images of a PS layer etched at a constant current density of 50 mA/cm^2 for 15 s. A) Non filtered, B) EFTEM image, filtered at 16.8 eV (Si) and C) EFTEM image, filtered at 23 eV (SiO_2).

that is electron transparent (usually 250 − 500 nanometers, depending on material) It accomplishes this by firing a beam of argon ions at the specimen, sputtering away material until the desired thickness is achieved [157]. For Si it is vital that the specimen preparation technique does not introduce significant atomic-scale damage such as amorphization. Such damage is avoided by using low energy ions or using the natural tendency of the material to split in certain direction (cleavage).

4.4.5 X-ray Photoelectron Spectroscopy

X-ray Photoelectron Spectroscopy (XPS) is a surface analysis technique to characterize chemical states in a material. The sample is irradiated by X-rays, causing electrons to be ejected from their atomic shells. These electrons are called photoelectrons and their kinetic energy depends on their original binding energy. The number of electrons that escape and their kinetic energy is detected by a spectrometer and plotted. Each binding energy corresponds to a specific state (or chemical shift) of a specific element, and by peak fitting the spectra the atomic percentage of each state can be extracted. However, peaks can lie so close that they are superimposed and detailed and careful analysis must be performed in order to separate them.

The XPS characterizations presented in this thesis was performed using a KRATOS AXIS ULTRA^{DLD} with monochromated Al Kα radiation and zero angle of emission. For the escaped electrons to actually reach the detector without being absorbed, or loose kinetic energy on the way, XPS must be performed under ultra-high vacuum conditions. The XPS measurements

performed on PS samples for this thesis have been carried out by Martin Sunding. The peak fitting of the spectra has been performed by Annett Thøgersen using the software Casa XPS [159]. A Shirley type background was subtracted before peak fitting.

Only those electrons that have actually escaped into the vacuum of the instrument are detected, and therefore only shallow depths of the material are probed. The mean free path of Si-2p electrons in Si, d, is 3.18 nm. Commonly, the sampling depth is taken to be $3d$ (corresponding to 95% detection) [160]. This means that the photoelectron escape depth in Si is $3 \cos \psi = 9.65$ nm, as the emission angle (ψ) is zero. The escape depth must be adjusted according to the porosity of the PS sample under investigation.

If it is desired to probe deeper parts of the material, ion beam etching can be used prior to XPS. This is done in Paper IV where the oxidation on the surface of the PS films is expected to vary from the oxidation at some depth. In this work, XPS was used to study ageing of the PS structures. A change in the chemical environment of an atom leads to shifts in the electronic binding energy, called chemical shifts. Oxidation of the Si structure can therefore be detected by studying shifts in the Si-2p peak position. In a high resolution spectrum, all oxidation states of Si, from pure Si (Si^0) to Si_2O (Si^{+1}), SiO (Si^{2+}), Si_2O_3 (Si^{3+}), and SiO_2 (Si^{4+}) can be resolved. Chemical shifts due to Si in other compounds can also be detected.

Chapter 5

Single layer PS and Process Considerations

To manage controlled production of complex PS structures, accurate understanding of and control over the etching process is essential. As discussed in Chapter 2, electrochemical etching of PS is a many-faceted process, with a very large number of factors affecting the result. A range of etching-cell-specific factors have influence; the size of the etching chamber, positioning of the electrodes, whether the setup is a double cell or single cell with horizontal or vertical configuration. In addition, electrolyte evaporation, chemical etching, electrolyte stirring, temperature fluctuations, and pore seeding effects should ideally be controlled or accounted for in order to optimally tailor the resulting PS structures. Little literature is found on many of these issues and some are quite system-specific. In addition to all the above factors influencing the PS structure during etching, drying and storage conditions will also affect the structures. Oxidation of PS structures *is* extensively discussed in literature, but there are large variations in reported results.

Homogeneity, electrolyte evaporation, chemical etching, pore seeding, and oxidation of PS are studied and discussed in Paper I - IV. The main focus of this chapter is on material that is supplementary to the published papers. However, summaries of the published results are included for the sake of completeness and to put the supplementary material in context. When a summary of a published paper is presented, this is clearly marked by a subheading. Work and discussions which are not included in the paper, but deals with the same subject are presented under a subheading labeled 'Further Work and Discussions'.

5.1 Substrate

To achieve results easily applicable to solar cells, the etching substrates should preferably have doping densities relevant for the solar cell process, i.e. corresponding to that of the bulk or the emitter doping. A bulk doping of $\sim 10^{16}$ cm^{-3}, corresponding to base resistivities of $1 - 3\ \Omega$ cm, is used for the majority of commercial cells produced, although recent reports suggest that the optimal resistivity is lower than this [161]. The optimal emitter doping density has repeatedly been subject for discussions [162, 163], but a doping between $10^{18} - 10^{20}$ cm^{-3} is frequently used. The optimal bulk and emitter doping in solar cells will depend on the cell design, metallization process, impurity level in the substrate, and cell thickness.

Initially, p-type substrates were chosen as a starting point to avoid additional complications and equipment demands due to illumination, as would generally be required for n-type substrates. With the double cell electrochemical setup, etching of samples with bulk-like doping densities requires additional doping on the cathodic side of the substrate (the 'backside' where PS is not formed) in order to achieve sufficiently good contact between the electrolyte and the wafer. Experiments were performed on p-type substrates with resistivities of $1-3\ \Omega$ cm and in-diffused p$^+$ backside doping. This provided a clear illustration of the inhomogeneity of the boron doping process available to us at the time and resulted in inhomogeneous current density distribution during etching and hence inhomogeneous PS layers.

Etching in emitter structures, i.e. after diffusion, is the most utilized procedure in the literature for integration of PS ARCs in the solar cell process. This is partly due to rearrangements taking place in the PS structure during high temperature processing steps, but also because moderately/highly doped substrates are suitable to produce nano- or meso PS. As previously discussed, in this size regime the light sees an effective refractive index, intermediate of that of Si and air, and reflection is reduced. A highly to moderately doped substrate would remove the need for additional backside doping and also provide a fair approximation to the emitter doping density.

The most common solar cell processing uses p-type substrate with n$^+$ emitter (currently about 85% of commercial Si cells [164]), but there is a rising interest in n-type Si for solar cell applications [163, 165–167]. A structure with n-type substrate benefits from a higher tolerance to common impurities such as Fe or O due to the lower capture cross section of holes by these impurities [161, 168]. On the industry side Sanyo [169] and SunPower [170] have

demonstrated cells with efficiencies well above 20% produced on large-area n-type Czochralski and solar-grade float-zone wafers. It seems that n-type Si wafers have potential for larger commercial utilization.

The largest challenges connected with using n-type Si substrates are found in the metallization and diffusion process [165]. Boron diffusion is more difficult than phosphorous diffusion, in addition SiN_x does not give adequate passivation for p^+ emitters [167]. For p-type Si cells, it is the combination of antireflective and passivating properties offered by SiN_x that makes it difficult to outdo. The use of PS ARCs on the p-type emitters in n-type Si solar cells is therefore particularly interesting.

Due to these considerations and the initial problems with the homogeneity of the in-house boron doping, the substrate chosen for the following experiments was homogeneous, moderately p-doped ($\sim 5 \cdot 10^{18}$ cm^{-3}) Si.

5.2 Voltage Transients from Anodic Etching

The etching is generally performed in the galvanostatic mode, so any resistivity variations during etching will result in changes in the applied voltage. The voltage transient therefore can be a valuable source of information about possible changes in the etching conditions. A selection of voltage transients, representative for the etching of homogeneous PS layers etched in p^+ substrates, are shown in Fig. 5.1. The initially very low voltages seen in a few of the voltage transients in Fig. 5.1 can be attributed to that these transients have their first read out data point closer to zero than the other voltage transients. By close inspection this can also be seen from the figure.

Detailed analysis of PS voltage transients with very high time resolution has been performed by Ronkel and Schultze [171]. According to these authors the voltage transients show formation of the double layer at a time $t < 1-30$ μs, followed by silicon surface passivation for $t < 10^{-2}$ s. After that a small decrease in voltage appears in the time period $t \sim 1 - 10$ s, corresponding to pore nucleation. These times correspond to experiments performed in an aqueous electrolyte and in the current density region $5 - 30$ mA/cm^2.

Unfortunately, the time resolution of our output data is too low to observe the shortest of these voltage variations. The slight reduction in voltage around $1 - 10$ s, interpreted as due to pore nucleation, is seen in many, but not all, of the voltage transients from our PS etching experiments. As the time periods of the different stages in the voltage transients are closely con-

nected to current density [172], it is not surprising that the voltage transients obtained from etching at low current densities generally are better resolved i.e. show more features. Figure 5.1c shows some early voltage variation during PS etching at 15 mA/cm^2. The shape does resemble that observed by Ronkel and Schultze [171] for their highly resolved voltage transients; first a steep initial increased, and after about a second a region of slightly decreased potential possibly associated with pore nucleation follows.

After the early variations, a slow voltage increase with increasing etching time can be seen for the majority of the voltage transients, see Fig. 5.1. For low current densities, the increase is small. For the sample etched at 10 mA/cm^2 for 30 s in Fig. 5.1a the voltage increase is 0.05 V, for the 50 mA/cm^2 sample the voltage increase is 0.27 V after 15 s, and for the 125 mA/cm^2 sample the increase is 0.66 V after 15 s. According to Ronkel and Schultze [171] the voltage increases because the pores are sufficiently deep that the complete surface is no longer used for silicon oxidation. The absolute spread in voltage between samples etched under nominally identical conditions, exampled in Fig. 5.1b, increase with increasing current density. However, the percentual voltage spread is approximately 20%, independent of current density.

However, even for PS samples etched on the same substrate under nominally identical conditions, the shape and features in the voltage transients vary significantly between the different etches. Combined with the low time resolution, this makes it difficult to draw conclusions from this data.

5.3 Inhomogeneity and Repeatability

Studies on the homogeneity and repeatability of the PS etching process are presented in Paper I and II. Here we provide some more detailed information about how these uncertainty assessments were performed.

5.3.1 Sample inhomogeneities

Summary from Paper I

In Paper I, a study of the lateral homogeneity of 4 cm^2 PS samples were undertaken. The porosity and thickness at 32 different spots over the sample were assessed by spectroscopic ellipsometry (SE). The measurement was

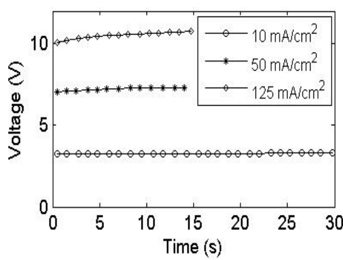

(a) Voltage transients for etching at three different current densities.

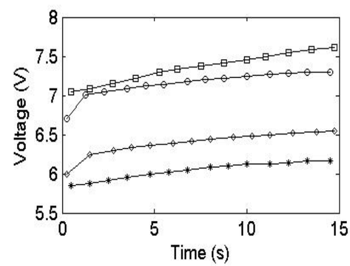

(b) Voltage transients for samples etched under nominally identical conditions at a current density of 50 mA/cm^2.

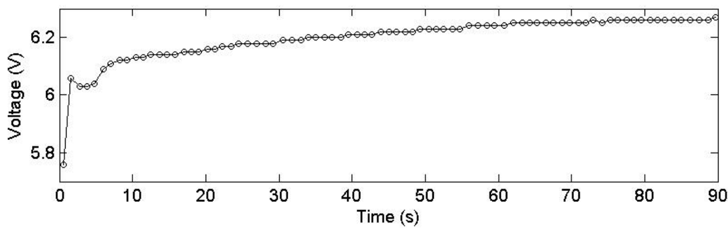

(c) Voltage transient for sample etched at 15 mA/cm^2 for 90 s.

Figure 5.1: Changes in voltage over time during etching in galvanostatic mode.

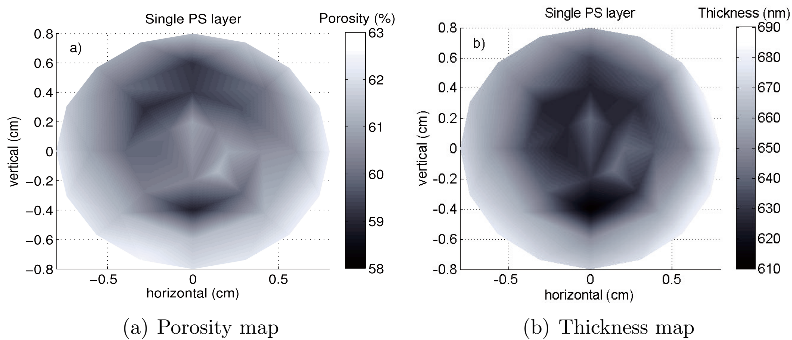

(a) Porosity map

(b) Thickness map

Figure 5.2: PS sample etched at constant current density [Paper I, Fig. 3a and b].

performed on one single PS layer etched at 50 mA/cm^2 and on a multi-layer sample optimized as solar cell ARC.

A correlation between variations in thickness and porosity over the samples is found, indicating that local differences in current density are responsible for the inhomogeneities. In the single layer, the relative porosity and thickness variations are 5.4% and 10.2%, respectively. For the graded layer, the average porosity of each layer is used, and we find a variation of 2.2% absolute for the porosity and 7.1% for the thickness. Note that these values are the largest difference between the measured values, it is not the standard deviation. The thickness and porosity map of the single PS layer is shown in Fig. 5.2 [Paper I, Fig. 3a and b]. A corresponding map for the multilayer PS sample (PS ARC) is shown in Paper I.

Further Discussions

From the thickness and porosity map, a trend of higher values toward the lower end of the sample can be discerned. This may be due to the design of the etching set up. The electrode mesh is approximately 10 cm in diameter, designed to cover the full wafer when a large sample holder is used. Most of the samples etched in this work are etched with the small sample holder, approximately 2.5 cm in diameter. In the small sample holder, the sample opening is situated in line with the upper part of the electrode mesh. The current flow towards the bottom of the small sample may therefore be en-

larged compared to the flow towards the upper part of the wafer. Similarly, the 'edge-effect' with higher porosities and thicknesses along the edges may be due to crowding of the current at the edges, since the electrode mesh is much larger than the sample.

Why we find a greater variation in the parameters of the single layers than the graded layers is not clear. We have observed that samples etched at low current densities are more homogeneous than samples etched at high current densities. The multi-layer have a lower time averaged current density than the single layer studied here. This may therefore contribute to the observed difference between the single and the multi-layers. In addition the ellipsometry model of the multi-layer samples is significantly more complex than that of the single layers. The model might therefore be less sensitive to small changes in the multi-layers than in the single layers.

Assessment of parameter variations over the samples is important in order to evaluate whether the PS etching technique can provide sufficient homogeneity over large area. The homogeneity is also important in order to know the uncertainty related to where on the sample the measurements are made. If we make one measurement on each of two samples etched under nominally identical conditions and get deviating results; how much of this deviation can be due to sample inhomogeneity? We consider that a full measurement of the whole wafer is not necessary in order to obtain and estimate of this. Since we can say that we will always measure relatively close to the center of the sample, four measurements, made at a radial distance of 2 mm from the center of the sample at angles 0°, 90°, 180°, and 270°, should provide sufficient information. An average of these values can then be used to minimize the effect of a randomly picked measurement spot (which differes from another spot due to sample inhomogeneities) on the results obtained by ellipsometry.

A standard deviation in porosity and thickness for each sample is calculated based on data from the four measured points. The calculated standard deviation depends on the current density during etching of the sample. Looking at samples in the porosity range 40-60% and thicknesses around $400 - 700$ nm, the standard deviation is typically less than 1% (relative) for both porosity and thickness. In a 90% confidence interval, this corresponds to inhomogeneity uncertainty of less than 2% (relative) in porosity and thickness.

5.3.2 Repeatability

Summary from Paper I

In Paper I, the process uncertainty or repeatability uncertainty, η_R is studied by looking at differences between eight samples etched under nominally identical etching condition, i.e. the same electrolyte, the same day, the same wafer batch and equal, constant, current density and etching time. The etching parameters used were a current density of 50 mA/cm^2 and an etching time of 15 s. The thickness and porosity of the samples are modeled using ellipsometry.

To try to separate the effects related to the repeatability of the etching process from the inhomogeneity uncertainty, we make four measurements close to the center of the sample. We estimate the sample center by eye and perform the measurements at a radial distance of 2 mm from the center of the sample, at angles 0°, 90°, 180°, and 270°. The average porosity and thickness of each sample are used to calculate the standard deviation between the eight samples. For these samples, the uncertainty, with a 90% confidence interval, becomes:

$$P = 58.4 \pm 0.9\% \tag{5.1}$$

$$T = 619.3 \pm 9.5 \text{ nm} \tag{5.2}$$

The relative values are for porosity $0.9/58.4 \approx 0.015$ and for thickness $9.5/619.3 \approx 0.015$.

The differences between these 8 nominally identical samples are interpreted as the uncertainty related to the etching process itself and give an estimate of how large variations that can be expected between samples etched under nominally identical conditions. The relative uncertainty values calculated above are therefore used as a measure of repeatability-, or process uncertainty in all further uncertainty assessments.

The repeatability experiment is only performed at one single porosity and thickness. It may be discussed whether the resulting uncertainty, acquired at a specific current density and etching time, is representable for the PS layers in general. The parameters used are, however, rather typical for many of the layers made in this thesis. Separate repeatability experiments for each parameter set would be too time consuming in the context of this work.

5.3.3 Uncertainty Assessment

A reasonable assessment of the total uncertainty in thickness and porosity of the PS layers can be made by combining the inhomogeneity uncertainty with the process uncertainty determined in Paper I, and the modeling uncertainty given by WVASE32. The total uncertainty, η_{total}, is then given by:

$$\eta_{total} = \sqrt{\eta_H^2 + \eta_R^2 + \eta_M^2}. \tag{5.3}$$

Here η_H is the uncertainty resulting from sample inhomogeneity/arbitrary measurement-point (Section 5.3.1), η_R is the process uncertainty or repeatability uncertainty (Section 5.3.2), and η_M is the uncertainty assessment obtained from the WVASE32 modeling software.

Typically, 90 % confidence limits (cl.) for porosity gives values around 2 % relative, and the porosity is generally stated to the first decimal place. For thickness, the uncertainty is typically between $2 - 3$ % (90 % cl.), and the thickness is stated without decimals. We regard the uncertainties as sufficiently small to allow reasonable control over the etched PS structures.

5.4 Electrolyte Aging

Throughout the work with this thesis, the electrolyte in the etching cell has been changed more or less regularly, every third or fourth week. This rather infrequent change is done due to practical, economical and safety considerations. After experiencing a noticeable decay in the electrolyte level in the cell, we performed a study of how electrolyte ageing affects the resulting PS structure. The results are presented in Paper I. Here a short summary and a few additional remarks are included.

Summary from Paper I

Twelve PS samples taken from three nominally identical wafers were etched at a current density of 50 mA/cm^2 for 15 s over a time span of six weeks, without changing the electrolyte. Changes in PS porosity, thickness and PS/Si interface width of the single layers over time were assessed by SE.

Electrolyte ageing clearly displays itself in a decreasing porosity and increasing etch rate of the PS samples, as shown in Fig. 5.3. These are the

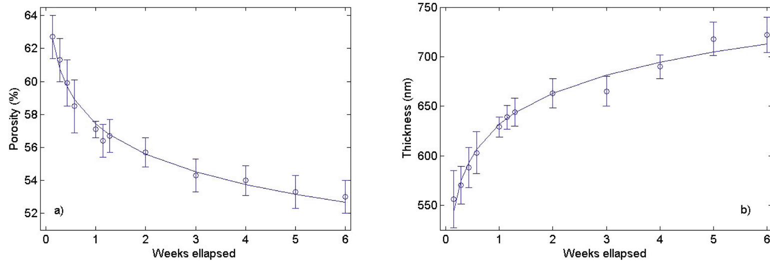

Figure 5.3: Evolution of a) porosity and b) thickness with ageing of the electrolyte [Paper I, Fig. 5a and b].

same changes in PS properties as are expected for an increased HF concentration in the electrolyte. The differences in PS properties with ageing of the electrolyte are therefore attributed to an increasing HF concentration due to differences of the evaporation rate of the electrolyte constituents (water, ethanol and, HF) as they have different vapor pressures. The effect is demonstrated to be significant, even over the duration of a few days.

Further work and Discussions

Master student Solveig Rørkjær carried out similar ageing experiments on our PS distributed Bragg Reflectors. Figure 5.4 shows how the reflectance from a PS DBR reflector changes depending on the 'age' of the electrolyte in which it is etched. A significant wavelength shift of the reflectance peak is evident. The difference is larger between the two structures etched in 3 and 15 days old electrolytes than between the structures etched in 15 and 29 days old electrolytes. This is in accordance with the results in Fig. 5.3 where the largest changes occur during the first two weeks.

To verify that the HF concentration is indeed responsible for the observed variations in PS properties, direct measurements of the HF concentration are necessary. This would also give additional information about possible changes in the rate of evaporation. Is the variation in HF with ageing linear or does it resemble the curves for porosity and thickness? If the variation in HF is "only" linear, the logarithmic shape of variation in porosity and thickness would need alternative or supplementary explanation. Experimental results from Penczek and Smith [174] imply that porosity is more sensitive to changes

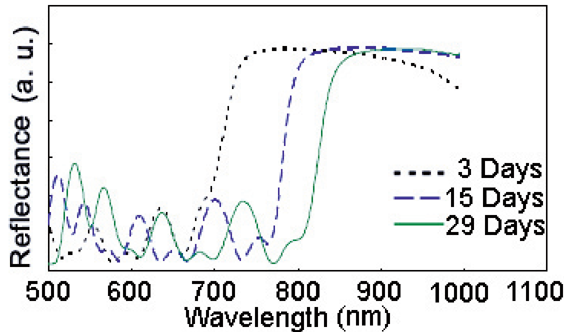

Figure 5.4: Evolution of the reflectance from a PS distributed Bragg reflector with ageing of the electrolyte. Printed with permission from Rørkjær [173, Rørkjær's master thesis].

in HF concentration if the HF concentration is low. Hence, as the relative HF concentration increases with ageing, larger effects on PS properties could be expected in the start of the experiment. Whether this could account for the observed non-linearity remains uncertain. For the time being, we unfortunately do not have at our disposal any equipment to accurately and quantitatively measure HF concentration.

5.5 Chemical Etching

The main results from the experiments related to chemical etching of PS are presented in Paper II. However, some elaborate discussions and figures that were rationalized away from the final paper due to length restrictions are presented here.

Summary of Paper II

Si is relatively resistant to etching in HF but, due to its large surface area ($200-600$ m^2/cm^3 [72]), PS can be attacked more rapidly than bulk Si. This type of etching of the PS structure is independent of the applied current density during PS formation and is called chemical etching [175]. Such etching can result in challenges for accurate control of electrochemically etched PS

structures, since the obtained porosity profiles after chemical etching can differ from the desired and designed current-controlled profiles. The experiments performed to study chemical etching are presented in Paper II and consisted of three sample series. The first set was etched at a current density of 10 mA/cm^2 for 30 s, the second set etched at 50 mA/cm^2 for 15 s and the third set etched at 125 mA/cm^2 for 15 s. After the current was switched off, the samples were left in the electrolyte and subjected to chemical etching for $\sim$ 0 s, 10 s, 30 s, 60 s, 180 s, 600 s, 1200 s, and 3600 s (+ the anodic etching time), before the samples were rinsed and air dried.

SE was carried out on all wafers according to the model presented in Section 4.3. The main effects of chemical etching on porosity, thickness and PS/Si interface thickness are presented in Fig. 5.5 [Paper II, Fig. 4]. See Paper II for further discussions of the displayed trends.

Further Work and Discussions

Figure 5.6 shows the ellipsometric data and corresponding fits, represented by Ψ, for all three series. The model shows an excellent fit to the ellipsometric data when applied to the low porosity samples. For the highest porosities, somewhat larger MSE values result.

The evolution of the depolarization factor with chemical etching time is shown in Fig. 5.7. The samples here are etched at 50 mA/cm^2 and 125 mA/cm^2 for 15 seconds. Note first that the depolarization parameters obtained for the highest porosity samples (etched at 125 mA/cm^2) are slightly higher than for the lower porosity samples (etched at 50 mA/cm^2). According to Künzner et al. [66] such a trend can be expected since increased porosity tends to lead to more anisotropy for highly doped substrates. The substrates used here are however in the limit between moderately and highly doped. Since the depolarization factor for the series etched at 10 mA/cm^2 is fixed (in order to avoid parameter correlation), and the difference between the series etched at 50 and 125 mA/cm^2 is small, it is not completely clear whether the trend observed by Künzner et al. [66] really applies to the samples presented here.

We now look at the evolution of the depolarization parameter in time. Although the spread is quite large, there seems to be a trend of increasing depolarization factors, i.e. the depolarization factor is getting closer to 0.33 with increasing chemical etching. This corresponds to a *reduced* anisotropy with *increasing* porosity (since increased chemical etching results in increased

porosity). This might reflect the different nature of the chemical and electrochemical etch. The chemical etch is isotropic, and could work to smooth out the anisotropic structures resulting from the preferential etching of pore tips during electrochemical etching.

Figure 5.8 shows a comparison of the porosity profiles of the samples etched at 10 mA/cm^2 after chemical etching. P_{diff} is the difference in porosity before chemical etching and after 3600 s of chemical etching. Closest to the surface, the porosity has increased by 8.4 % absolute after 3600 s, at the deepest part of the PS layer, the porosity increase is only 5.8% absolute. The trend is similar for the series etched at 50 mA/cm^2 and 125 mA/cm^2. This means that the increase in porosity due to chemical etching is not isotropic through the layer. The upper part of the layer has a higher increase in absolute porosity than the deeper part. We have seen that the chemical etching does not attack the PS structure significantly the first few minutes. Therefore the initial gradients in porosity are due to pure electrochemical etching. Since the chemical etching will depend on the exposed surface area, it is not surprising that the porosity gradients existing after the electrochemical etch are amplified by the chemical etch, as indicated in Fig. 5.8. The net effect is a larger grading and likely wider interface layers. This is in accordance with Fig. 5.5c, which shows an increase in the width of the PS/Si interface with increased chemical etching time.

5.6 Pore Nucleation

Relatively little literature exists on the field of pore nucleation and early PS growth. We will briefly mention a few notable contributions to the field that is relevant for the work presented in Paper III.

Without proposing a complete formation model, Brumhead et al. [176] made an effort to relate the preparation parameters to some intrinsic characteristics of the pore growth kinetics. They reported a non-linear growth of PS at short anodisation times, before a linear, stable pore growth was reached after about 1 minute. This general growth development is now relatively well established [172, 177, 178]. According to Brumhead, if the valence of a reaction remains the same, the total mass loss rate will, according to Faradays law, be constant. Consequently, at low porosity, initial pore growth is fast before a balanced, slower growth with larger porosities, take over. Three possible explanations for this initial faster pore growth were proposed by

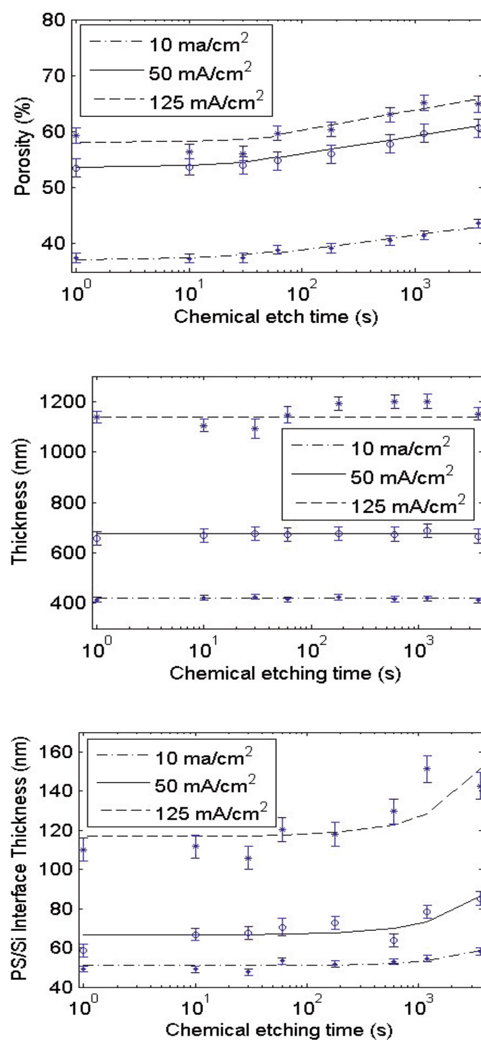

Figure 5.5: Results of chemical etching on porosity, thickness and Si/PS interface thickness. Three series of PS samples are exposed to chemical etching in HF for 0 s - 3600 s [Paper II, Fig. 4]

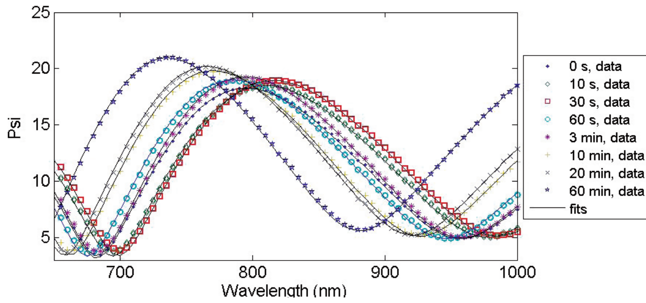

(a) Samples etched at 10 mA/cm^2 for 30 s.

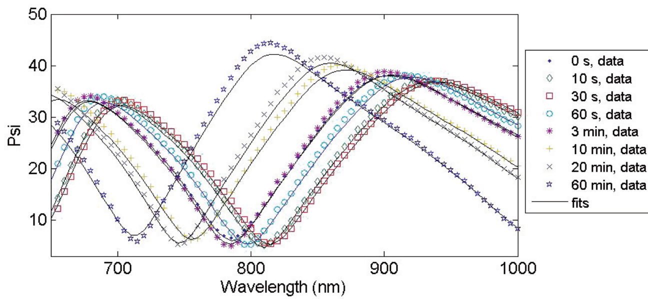

(b) Samples etched at 50 mA/cm^2 for 15 s.

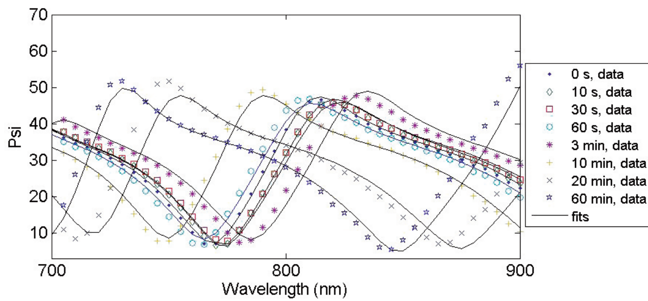

(c) Samples etched at 125 mA/cm^2 for 15 s.

Figure 5.6: Changes in the ellipsometric variable Ψ due to chemical etching. Three series of PS samples are exposed to chemical etching in HF for 0 s - 3600 s. Fits to the ellipsometric data are shown for all samples. The best fits are obtained for the low porosity samples.

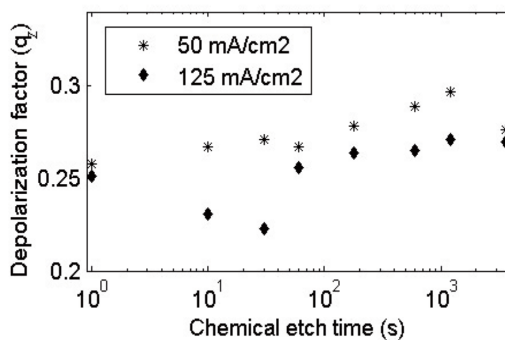

Figure 5.7: Evolution of the depolarization parameter of PS samples with chemical etching time.

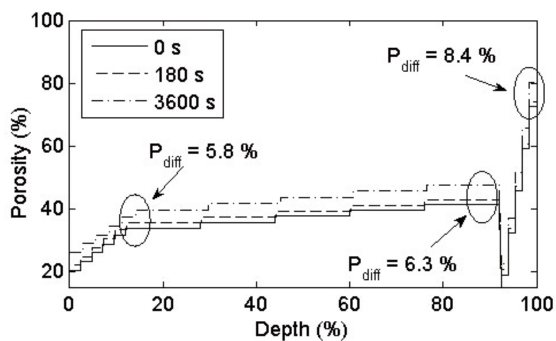

Figure 5.8: Comparison of the porosity profiles of the samples etched at 10 mA/cm^2 after chemical etching. P_{diff} is the difference in absolute porosity before chemical etching and after 3600 s of chemical etching.

Brumhead et al. [176]; (i) each individual pore could be initiated at $t = 0$ with a small cross section, and expand as it grows into the substrate, (ii) the number of pores initiated at $t = 0$ could be small but multiply quickly by branching, (iii) at $t = 0$ a few pores are generated, and their number increase steadily by further continuous generation at the surface until they are close enough together for carrier depletion to prevent any more pores being formed. By this argumentation, in model (iii) the porosity of the pore initiation region would in time be the same as for the bulk PS layer. Model (i) and (ii) are believed by Brumhead et al. to inhibit flow of chemicals into the pores, thereby preventing continued growth, and model (iii) was therefore proposed as the most likely mechanism. The formation time necessary to complete the PS nucleation process is proposed to last from a few seconds [171] to $2.5 - 3$ minutes [172, 176]. The proposal of a pore nucleation period of only a few seconds is based on features in the current and potential transients which are interpreted as due to pore nucleation [171].

Summary of Paper III

In Paper III, we showed the existence of a near-surface PS region with lower porosity then the bulk PS and discuss possible origins of this dip in porosity (dense PS region). The indications of this porosity dip first appeared in the best fit ellipsometry models of the PS samples etched in p^+ substrates where a significant lowering of the porosity in a thin region just below the surface was displayed. The feature improved the quality of the fit for all measured samples of low and intermediate porosity. In TEM images of the same samples a thin, slightly darker region of the PS layer can be seen towards the PS/air interface. The darker areas corresponds to more Si, hence the darker line is a region of lowered porosity. In Fig. 5.9 [Paper III, Fig. 2] it can be seen that the depth of these denser regions roughly corresponds with the depth of the lower porosity region detected in the ellipsometry porosity profiles.

The dense PS region does not seem to be affected by etching time. Figure 5.10 [Paper III, Fig. 4] shows the first 80 nm of the porosity profile for four samples etched under nominally identical conditions, but for different etching times. No significant changes can be seen between the profiles, except a slight increase in average porosity of the full profiles, which is likely due to chemical etching. As there is no evolution of the porosity dip in time, it is natural to assume that the region is related to the initial stages of PS growth. Since the

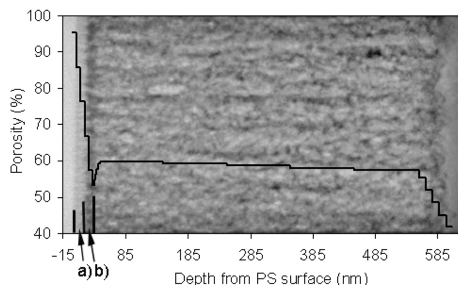

Figure 5.9: Ellipsometry porosity profile overlaid TEM image of the same sample. a) points towards the surface oxide, b) points towards the dense PS region. A rough correspondance exists between the densee PS region in the TEM image and the dip in porosity in the ellipsometry porosity profile [Paper III, Fig. 2].

initial pore nucleation in PS has been suggested to take from a few seconds to $2-3$ minutes, the pore growth and propagation cannot likely be explained by continuous nucleation (model (iii) as suggested by Brumhead et al. [176]). Instead, pore widening and/or porosity increase by branching may be the responsible mechanisms.

Experiments have been performed in different HF concentrations, for different current densities and etching times. The existence of the dense PS region is sensitive both to HF concentration and current density, and the common denominator appears to be variation in porosity. Both reduced HF concentration and increased current density leads to high porosity and a PS structure without a densified region close to the surface.

Further Work and Discussions

To further study the origin of the dense PS region, etch stop - etch start experiments were performed. In samples where the etch was aborted after 2 s and then restarted, the best fitted ellipsometry model displays an increased thickness of the densified region. In the porosity profile determined by ellipsometry the constant porosity layer starts at a depth of $60-70$ nm, while in the TEM images the dense PS regions seems to end at a depth of around 50 nm. The experiments performed so far are therefore not conclusive with

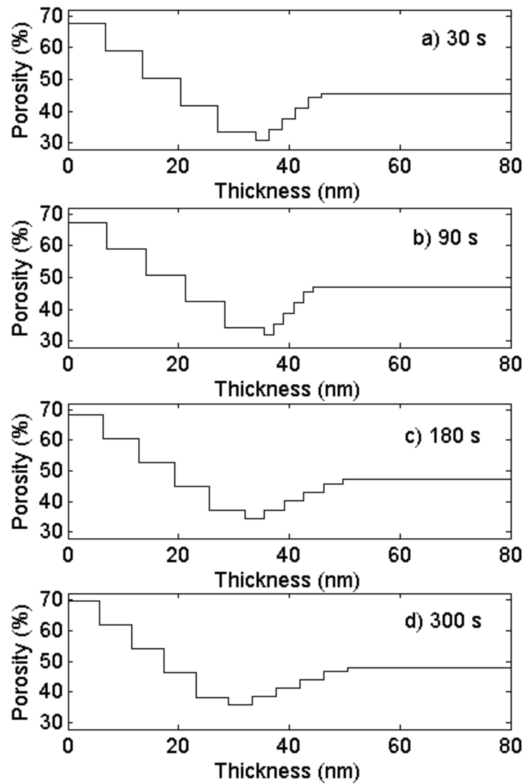

Figure 5.10: Evolution of the porosity dip in time. Porosity profiles from best fit ellipsometry model on samples etched at 15 mA/cm^2 in 20% HF for different times; a) 30 s, b) 90 s, c) 180 s, and d) 300 s [Paper III, Fig. 4].

respect to the effect of an etch restart on the dense PS region.

5.7 Porous Silicon Oxidation

In Paper IV, the effect of ageing of PS layers stored in ambient air and room temperature, studied by use of XPS, SE, and spectroscopic reflectometry, is presented. Here the complete fitted XPS spectra are presented, in addition to a summary of Paper IV.

Summary

Due to the small binding energy shifts in the Si 2p core level (covering a range of only 4 eV), and large number of observed compounds, resolving distinct features by curve-fitting the Si 2p core level can be difficult [179]. The high resolution in our spectra enables a quite detailed fitting of the spectra, and the evolution of pure Si (Si^0) and the intermediate oxide states Si_2O (Si^{+1}), SiO (Si^{+2}), Si_2O_3 (Si^{+3}), and SiO_2 (Si^{+4}) can be followed over time. The complete fitted XPS spectra for the Si-2p peaks from the PS surface and PS bulk is shown in Fig. 5.12.

We observe that a relatively rapid but partial oxidation, covering a few percent of the inner surface of the PS by oxide, takes place in the early stages of ageing. A gradual increase in oxidation, through the intermediate oxidation states, is observed. Detection of Si^+ (Si_2O), is followed by detection of $Si2^+$ (SiO) and Si^3+ (Si_3O_2), before SiO_2 is formed after about one week. This evolution is plotted in Paper IV, Fig. 4.

Comparing the XPS results with SE, it is clear that SE is rather insensitive to oxidation in the PS structures. Partly, the inclusion of oxide is complicated by the number of different oxidation states; for most of the samples only a small fraction of the oxidized species is SiO_2. It is also possible that an alternative model could give larger deflections with respect to oxygen content. However, when this is said, the marginal difference in Ψ and Δ, and consequently in refractive index between day 1 and day 42 indicates that it is a challenge to determine oxidation of PS with SE. It is also rather common to neglect oxidation when performing ellipsometric characterization of PS [151, 152]. Since the difference in Ψ and Δ and also in effective refractive index is so small, the effect of the oxidation on the reflectance of the PS ARCs is very small. Measurements performed over a time period of 11

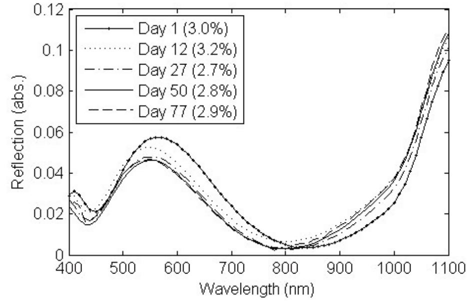

Figure 5.11: Evolution of the reflectance from a PS ARC in time [Paper IV, Fig. 5].

weeks is shown in Fig. 5.11 [Paper IV, Fig. 5].

5.8 Summary

The studies performed and described in this chapter show that the PS etching process, carried out on p^+-type substrates in our double PS etching cell, gives relatively good control over the etching parameters. It is clear that for short etches, chemical etching does not alter the original PS structure. However, inevitable interface regions and pore seeding effects can be possible challenges. Still, in conclusion, tailoring of multilayer PS structures seems feasible. The evolution of the PS structures with storage time does not appear to be a hindrance for the optical performance of the PS structures.

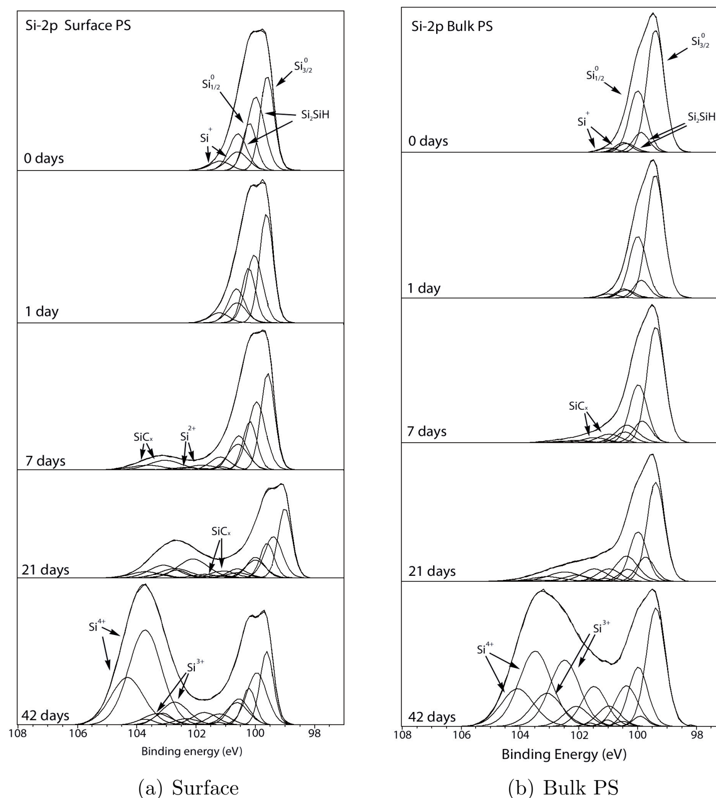

(a) Surface (b) Bulk PS

Figure 5.12: Peak fitted XPS spectra for the Si-2p core level from homogeneous PS layers aged for different time periods. a) Spectra obtained from the PS surface. b) Spectra obtained after ion sputtering at a depth of approximately 100 nm.

Chapter 6

Design and Fabrication of Porous Silicon Multilayers for Solar Cell Applications

There are many reasons why multilayered PS is an attractive alternative for use in Si solar cells. Obviously, the Si is already there. The fabrication expenses are moderate, and with electrochemical etching, multilayers are barely more demanding to make than single layers. From an optical point of view, this creates a well of opportunities to tailor the optical properties exactly as you wish. However, major challenges remain before these benefits can be exploited in commercial Si solar cell. As in Chapter 5, the focus here is on the material that is complementary to the published articles. A brief summary and some additional considerations to the work published in Paper V and VI constitutes Section 6.1 and 6.2. Section 6.3 is devoted to initial experiments and considerations with respect to implementing the PS ARC in an emitter structure. In Section 6.4, we take a closer look at the optimal thickness of the PS ARCs from an optical point of view. Section 6.5 shows the results of forming the graded PS ARCs on multicrystalline substrates. Finally, in Section 6.6, the work on PS rear reflectors, performed in collaboration with master student Solveig Rørkjær, is presented.

6.1 Graded Porous Silicon Antireflection Coatings

Most of the work performed in order to model and fabricate minimum reflectance PS ARCs is presented in Paper V and only a short summary is given here.

Summary Paper V

In this work, multilayered refractive index stacks optimized for antireflection, in bare air and within modules, were modeled and fabricated. Simulations of PS antireflective layers were performed in the WVASE32 software. "Ideal structures" without imposed limitations on thickness and available porosity range were modeled to show the potential of these structures. Confinements with respect to efficient implementation in Si solar cells, i.e. limited porosity range and thickness, were then examined and applied. An angular distribution of the incoming light (as the sun moves over the sky) was also accounted for. Optimizations were conducted for cell operation both in air and under module glass.

An experimentally determined relationship between porosity and current density and etch rate and current density was established using SE, gravimetry, and SEM. The porosity profile of the optimized models were then translated into current density profiles using these experimentally determined relations. The resulting multilayers were characterized with SE, SEM, XPS, reflectometry and TEM.

Figure 6.1 [Paper V, Fig. 10] shows how the porosity profiles obtained by ellipsometric modeling of the sample compare to the designed porosity profiles. For the profile optimized for operation under module glass (a), the design and model porosity profiles have the same shape, but deviates from each other towards the interfaces. For the profile optimized for air ambient (b), the fabricated PS ARC structure follows the general trend of the designed porosity profile, but cannot follow the fine structures. Figure 6.2 [Paper V, Fig. 11] shows the reflectance of the design and modeled porosity profiles, in addition to the measured reflectance for both ARC structures. Wavelength shifts between the reflectance generated by the designed and modeled porosity profiles are evident for both ARCs, but the shapes of the modeled reflectance profiles match the designed profils quite well. Fig. 6.2 also shows that there is a very good correspondence between the modeled

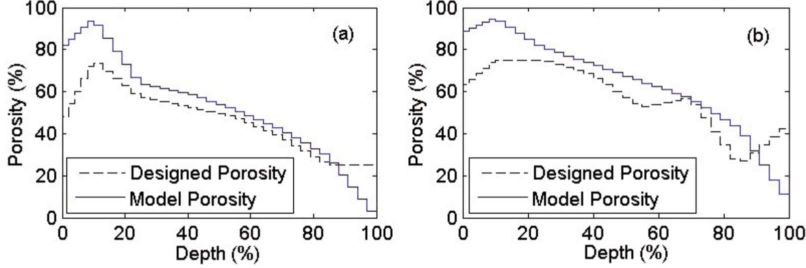

Figure 6.1: The designed porosity profiles plotted together with the porosity profile which best fit the ellipsometric data [Paper V, Fig. 10]. Interface between PS and air/glass at 0%, interface between PS and Si at 100%. a) Optimized for operation with module glass. b) Optimized for operation without module glass.

and the measured reflectances. The measured integrated reflectances (at an incidence angle of $\sim 10°$) of the structures were $\sim 3\%$ in air and 1.4% under glass (not including reflection from the glass) in the wavelength range 400-1100 nm.

6.2 Clear Color Porous Silicon Antireflection Coatings

Summary Paper VI

So far, the installation of solar modules has typically been performed without aesthetic concerns as common locations have been rooftops or solar power plants. However, exciting new products that incorporate PV modules into actual building materials such as curtain walls, windows, and roofing shingles are now available, increasing the focus on the visual impression of solar modules. Building integrated photovoltaic (BIPV) systems represent an interesting, alternative approach for increasing the available area for electricity production and potentially for further reducing the cost of solar electricity.

The color of a solar module is primarily determined by the color of the cells in the module, which is given by the antireflection coating (ARC). The most commonly used ARC for Si solar cells today is SiN_x, which gives the modules

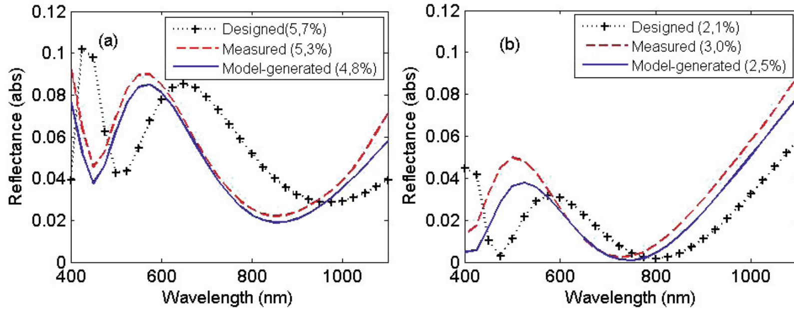

Figure 6.2: The designed, fabricated and modeled (by ellipsometry after fabrication) reflectance spectrum of the PS ARCs [Paper V, Fig. 11]. a) Optimized for operation with use of module glass, reflectance data taken without module glass. b) Optimized for operation without use of module glass.

a dark blue appearance. The color of the ARC is of course very intimately connected to its antireflective properties, and changes in the appearance will therefore easily be made at the expense of the cell's efficiency. Although more than 85% of architects in one survey stated that aesthetic concerns would allow for the installation of solar energy systems with reduced efficiency [180], the optimal scenario is freedom in design *and* competitive efficiency.

In Paper VI the impact of varying the color of SiN_x- and PS ARCs upon the optical characteristics and efficiency of a solar cell was investigated. The overall transmission and reflection of a set of differently colored single layer SiN_x ARCs is compared with triple layer dielectric stack ARCs, all made using PECVD. These are again compared with PS ARCs. Although the reflection from single layer SiN_x ARCs is generally low, the colors available by simple thickness variations are limited. Using triple layer dielectric ARCs, a broader range of colors can be achieved, at the expense of a modest increase in reflection. For the PS ARCs, control over both thickness and refractive index results in a large freedom of tailoring the reflection spectra of the films. The layers can then be optimized for low reflection in addition to specific color. Solar cells able to absorb in excess of 90% of the incoming light is shown to be accessible with PS ARCs, demonstrated by green, red, purple and orange structures.

Table 6.1: Simulated parameters for 'standard' solar cell with different ARCs.

Sample	Efficiency	J_{sc}	V_{oc}	J_{sc}/J_{sc}(black)
"Black"[1]	19.8	38.5	620.1	100.0%
Single layer SiN - green	16.6	32.5	615.8	84.4%
Single layer SiN - red	17.6	34.5	617.4	89.6%
Single layer SiN - blue	17.5	34.1	617.1	88.6%
Dielectric stack - green	15.2	29.8	613.5	77.4%
Dielectric stack - red	13.0	25.7	609.7	66.8%
Dielectric stack - blue	16.6	32.5	615.7	84.4%
PS multilayer - green	16.9	33.0	616.2	85.7%
PS multilayer - red	17.5	34.3	617.2	89.0%
PS multilayer - purple	17.8	34.8	617.7	90.4%
PS multilayer - orange	18.1	35.4	618.0	91.9%

[1] "Black" refers to perfect transmission through the ARC; no reflection, no absorption.
Simulated values for efficiencies, short circuit current density (J_{sc}), and open circuit voltage (V_{oc}) obtained when each fabricated ARC is used on a standardized solar cell.

In addition to a comparison of the optical characteristics of such solar cells, the effect of using colored ARCs on solar cell efficiency is quantified using the solar cell modeling tool PC1D. A solar cell model producing fairly representative solar cell characteristics is used as basis for the modeling. The experimentally determined transmission spectra of the various ARC structures were used as input to the modeling. The results are shown in Table 6.1 [Paper VI, Table 2].

Further Work

Figure 6.3, 6.4, 6.5, and 6.6 show (from the top) i) the current density recipe used for etching the respective structures, ii) the designed and model porosity profiles, iii) the design, model and measured reflectance of the ARCs, and iv) an image of each ARC. From the current density recipes, we see that all etches are very swift, the recipe of the green ARC is the longest at 9 s. Comparing the designed porosity profile with the porosity profile obtained from ellipsometry measurements, a rough correspondence is found for all samples. The porosity profiles of the purple and red ARCs are closer to their design than the green and orange. The largest deviations between the design and model are found at the interfaces between Si/PS and PS/air.

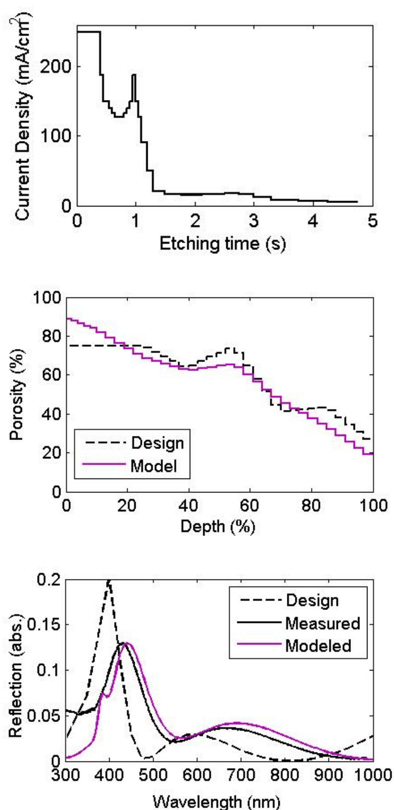

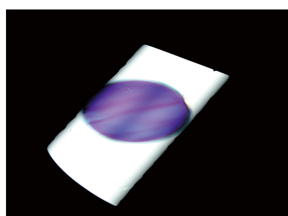

Figure 6.3: From the top: Current density recipe, porosity profile, reflectance, and image of the purple PS ARC.

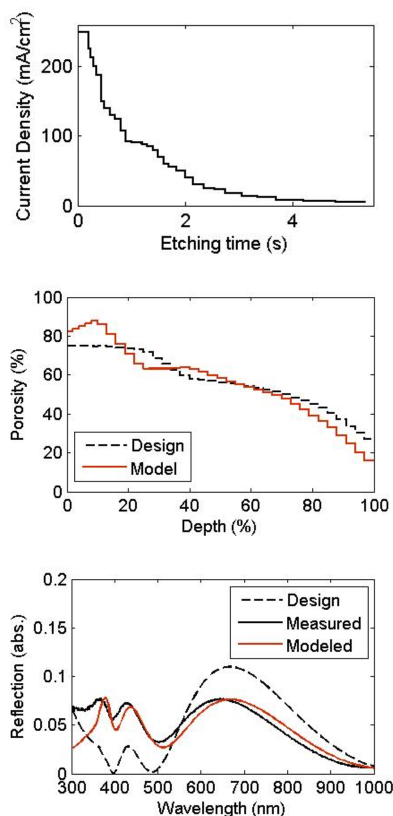

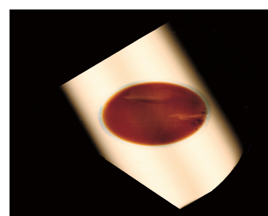

Figure 6.4: From the top: Current density recipe, porosity profile, reflectance, and image of the red PS ARC.

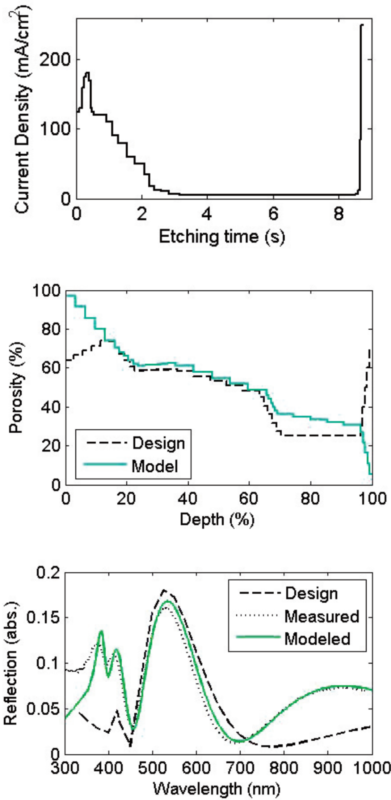

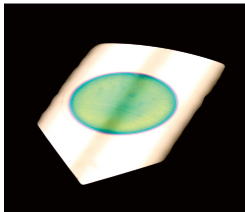

Figure 6.5: From the top: Current density recipe, porosity profile, reflectance, and image of the green PS ARC.

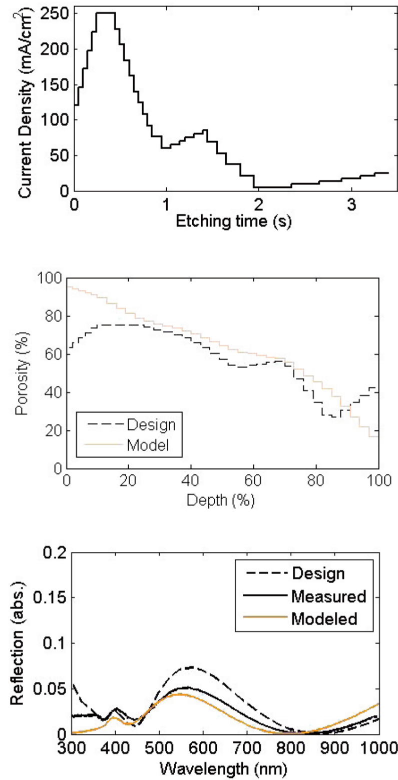

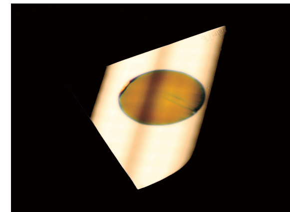

Figure 6.6: From the top: Current density recipe, porosity profile, reflectance, and image of the orange PS ARC.

The same appearance of a rough correspondence is seen between the designed and modeled reflectance. The shapes of the reflectance curves are similar, although a perfect match is not obtained. The purple ARC has a clear wavelength shift in the reflectance spectrum, the other ARCs have the reflectance peak at the same wavelength as the design and show mainly amplitude differences. An excellent correspondence is found between the measured and model reflectances for all the ARCs, although there are some deviations in the short wavelength end. This is possibly because these wavelengths are approaching the nanostructure size ($\lambda_{\text{air}} = 300$ nm $\rightarrow$ Si ~ 70 nm) and hence also the end of the applicability range of the static effective medium theory [61]. The model reflectance is generated from the best fit ellipsometry profile for each ARC and the good fit to the measured data is therefore remarkable.

The image and the modeled and measured reflectance of each ARC were also shown in Paper VI, while the design reflectance, the current density recipe and the porosity profiles are only presented here.

6.3 Integration of Porous Silicon Antireflection Coatings in Si Solar Cell Processing

In Chapter 2 we discussed the impact of substrate doping on the resulting PS structure. In the previous work presented in this thesis, a highly doped p-type substrate is used. The high doping is convenient to achieve good contact with the electrolyte in addition to imitate the high doping of the emitter. However, so far we have not etched in actual emitter structures. A diffused emitter will have a doping density profile in depth. In addition, it is to be expected that electrochemical etching of PS in a pn junction will complicate the formation. In this section we look at the possibilities of integrating the PS ARCs described in Section 6.1 and 6.2 into a realistic solar cell structure. The PS etching may be performed before or after emitter diffusion, each process presenting different opportunities and challenges.

6.3.1 Porous Silicon Etching in Emitter Structure

There are a few important differences between etching in a homogeneous p^+ substrate and an n/p^+ structure; (i) the emitter is not homogeneously doped and (ii) a junction is introduced. In fact two junctions are introduced in

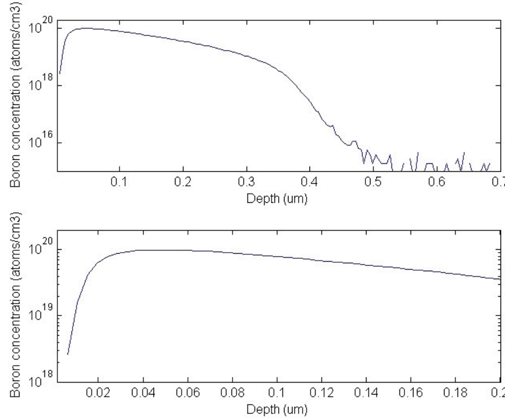

Figure 6.7: The doping profile obtained with SIMS showing the standard boron emitter used in the cell process at IFE. The bottom figure is simply a section of the upper to display the topmost 200 μm in some detail. **Source: courtesy of Krister Mangersnes [181].**

the study performed here, as the wafer is doped on both sides. Two sided doping is standard in IFE's solar cell process and, as discussed in Section 5.1, backside doping also provides good contact between the electrolyte and the wafer during electrochemical etching.

The preliminary results from PS etching in an n-type substrate with a p^+ emitter is presented in the following section (really a $p^+/n/p^+$ structure). For comparison, experiments with etching in $p^+/p/p^+$ structures are also performed. Two different boron doping profiles have been used, one 'standard' profile used in solar cell processes at IFE and one where in-diffusion is performed under the same temperature and deposition time as the 'standard' profile, but with a longer drive in (i.e. deeper). The doping profile of the standard emitter is studied by SIMS and is plotted in Fig. 6.7. From a depth of approximately 20 nm and down to 200 nm, the doping profile is relatively flat, varying from $\sim 9 \cdot 10^{19}$ to $\sim 3 \cdot 10^{19}$.

Other possible effects of the backside doping are resistivity variations if the doping is inhomogeneous. Such resistivity variations could easily be reflected in the homogeneity of the PS layer on the opposite side of the wafer.

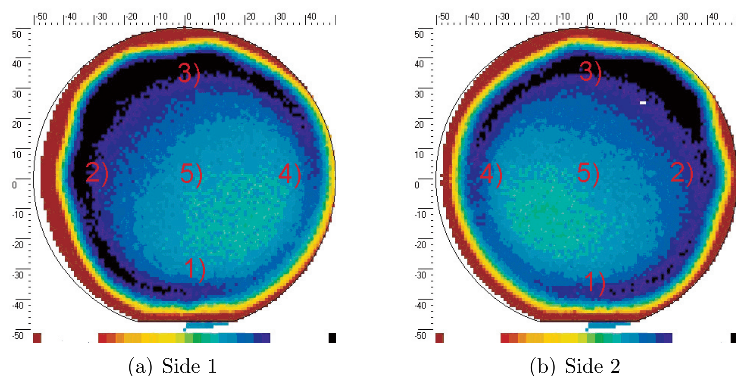

(a) Side 1 (b) Side 2

Figure 6.8: Sheet resistance maps of wafers with the standard IFE boron emitter profile. Only relative values can be seen from this sheet resistance map, due to inadequate calibration of the equipment. Corresponding values for the marked spots are shown in Table 6.2. The marking of where the measurement is made is only indicative.

A sheet resistance map showing the lateral doping homogeneity is displayed in Fig. 6.8. Both sides of the wafer are shown. Only relative values can be seen from this sheet resistance map, due to inadequate calibration of the equipment. The sheet resistance has therefore also been measured by four point probe as shown in Table 6.2. As the four point probe is unfit to measure at the sample edges a quantitative measure of the sheet resistance outer rim of the wafer is not obtained.

A schematic of the band structure in the substrate, in equilibrium and under applied bias, is shown in Fig. 6.9. The front side (PS etching side) junction does not present a barrier to the holes. The backside n/p^+ structure, however, will present a barrier towards holes before they reach the formation site. During PS formation, this n/p^+ junction will be forward biased, hence increasing the voltage drives the current through. In addition to the junctions within the substrate, one anodic and one cathodic Si-electrolyte junction exists.

Figure 6.10 shows the voltage versus etching time for layers etched at a constant current density of 40 mA/cm^2. The etch rate at this current density has been measured to be approximately 9 nm/s. During the first 10

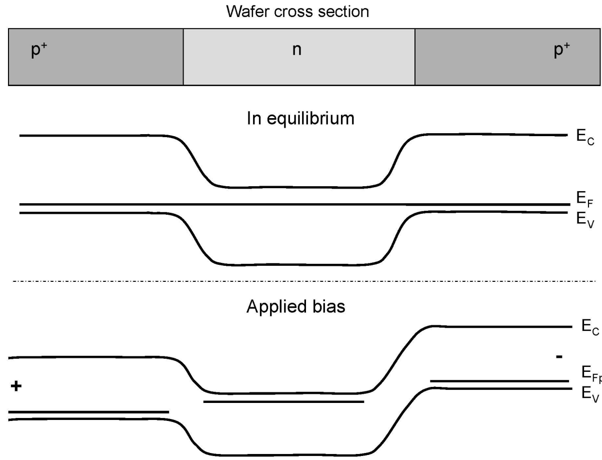

Figure 6.9: Schematic overview of the band bending at the junctions within the etching substrate in equilibrium and under applied bias. The drawing is not to scale.

Table 6.2: Sheet Resistance

	Spot 1	Spot 2	Spot 3	Spot 4	Spot 5
Side 1	11.70Ω/sq	12.00Ω/sq	12.30Ω/sq	11.70Ω/sq	11.69Ω/sq
Side 2	11.90Ω/sq	11.80Ω/sq	12.19Ω/sq	11.79Ω/sq	11.44Ω/sq

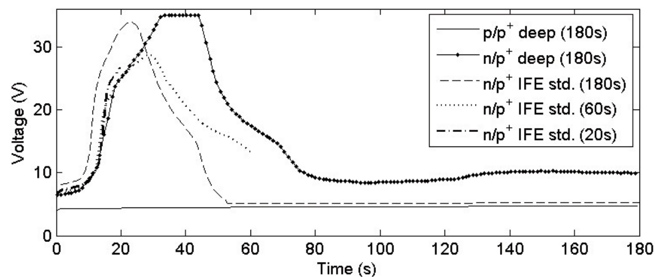

Figure 6.10: Voltage data from PS layers etched in $p^+/n/p^+$ structures at a constant current density of 40 mA/cm^2. The voltage data from a PS layer etched at the same current density in a $p^+/p/p^+$ structure is also included.

seconds, the increase in voltage is moderate, but still significant compared to the $p^+/p/p^+$ structures (as shown in Fig. 6.10). As the change in the doping profile at this depth is marginal (except for possibly the first 20 nm), the increase in voltage should not be due doping variations at the etch sites.

After ten seconds, we expect the pore tips to have reached a depth of approximately 90 nm. From Fig. 6.7 it is clear that the doping profile around this depth shows a gentle decline in doping density, with no specific features. Still, the voltage for all etches performed in $p^+/n/p^+$ structures increase strongly between approximately $10 - 20$ seconds. The following $10 - 15$ seconds the voltage increases less rapidly, before it starts to decrease and finally is reduced to approximately the starting voltage. The voltage decrease seems to occur at a deeper depth for the sample with a deep boron diffusion profile.

Experiments with illumination were also performed. Figure 6.11 shows the voltage data for three identical samples etched at the same, constant current density of 50 mA/cm^2. The PS layer etched with backside illumination displays a significant increase in etch rate (14.3%) and a small increase in porosity (4.2% relative) compared to the sample etched without illumination. Both increased etch rate and porosity would be expected from a higher current density. The illumination will ease the current flow through the barrier at the backside junction and this could explain the observed results. For the etching performed without illumination or with front side illumination, the voltage limit of the potentiostat is reached (36 V), and the set constant

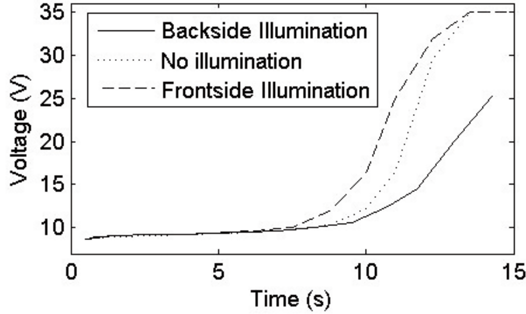

Figure 6.11: Transient voltage during etching of PS in three emitters under identical constant current density, with varying illumination conditions. All the samples are ~ 4 cm^2.

Table 6.3: Changes in PS structure due to Illumination

Sample	Thickness	Ave. porosity
Dark	137 nm	67 %
Backside illumination	160 nm	70 %
Frontside illumination	140 nm	67 %

current density is not supplied for the complete duration of the etch.

The results presented in this section are preliminary and sufficient control over porosity and etch rate during etching in $p^+/n/p^+$ emitter structures have not yet been demonstrated. The subject will receive continued attention in upcoming projects. Specifically, alternatives to the p^+ backside doping to achieve good contact between the electrolyte and wafer will be tested in order to avoid the hole barrier formed by the rear side n/p^+ junction.

6.3.2 Porous Silicon Etching Before Emitter Doping

Etching the PS ARC directly into the Si substrate before emitter doping would avoid the problems associated with doping variations in depth and etching in junction structures. However, it would introduce quite a few problems of its own. Emitter diffusion necessitates very high temperatures for extensive periods of time. This would likely lead to a significant reorga-

nization of the porous structure. In addition solar cell substrates are usually doped to a resistivity of $1 - 3\ \Omega$ cm. This is not sufficient to achieve a good contact with the electrolyte and an additional backside doping would have to precede the PS etching. Indeed, a back surface field is often introduced in the solar cell process to reduce the surface recombination velocity, since a p/p^+ junction presents a potential barrier for the minority electrons. A back surface field therefore reflects electrons and reduces the effective rear surface recombination velocity [90].

Another issue is that the obtainable porosity span of a $1-3\ \Omega$ cm substrate would also be different from the one assumed in all optimizations in this thesis, so the designed structures might not be obtainable.

6.4 Transmission Optimizations

An ARC with practically zero reflection could easily be made from thick PS layers with a continuously graded refractive index, see Paper V for an extensive discussion on this. Uehara et al. [112] have made very low reflection (2%) PS stacks with a thickness of $1 - 5\ \mu$m. Such stacks are however much too thick for solar cell applications, both because of interference with the solar cell junction and absorption in the PS layer. Even for much thinner PS layers, relevant for solar cell ARC applications, absorption is an issue which must be addressed. While the reflection improves with thickness this is counterbalanced by increased absorption. The highest transmission is therefore subject to an optimization between these two. In Paper V an optimal thickness of ~ 150 nm was assumed. Here, we aim to refine this assumption.

6.4.1 Modeling and Ellipsometry

We use the same basic ARC structure as that used in Paper V and IV; porosities are set to $25 - 75\%$ and a maximum of 36 steps in each ARC. However, instead of using only one thickness, the reflectance is minimized for a range of thicknesses. The optical constants of each BEMA model are used to calculate the absorption through the structure as a fraction of the incoming light

$$I = I_0 \cdot \exp(-t \cdot \alpha), \tag{6.1}$$

where I_0 is the initial intensity minus reflected light, I is the intensity after one EMA sublayer, t is the thickness of the sublayer and α is the

absorption coefficient of this layer. This calculation is performed for each wavelength and each subsequent layer. The total intensity loss is the difference between incoming and transmitted intensity for each wavelength and finally this intensity loss for each wavelength is weighted by the solar flux at this wavelength and an average absorption calculated.

In Paper V, the PS structure was assumed to consist of c-Si and void. In later ellipsometric studies of PS, an improvement in the models was found by adding a small amount of poly-Si. In the thickness optimizations performed here, both models with pure c-Si walls and models with a mix of c-Si and poly-Si (5% absolute) are used.

Figure 6.12 shows the transmission (a), absorption (b) and reflectance (c) of the PS ARCs for increasing thicknesses. We see that for an ARC optimized for use without module glass the optimal thickness in the range $160 - 180$ nm. If the PS structure is solely monocrystalline, the highest achievable transmission is approximately 93 %. If 5 % (abs.) polycrystalline Si is added, the absorption increases somewhat, while the reflection remains the same. The best achievable transmission therefore decreases by almost 1 % when poly-Si is included in the model. For an ARC optimized for performance in a module glass environment, the maximal transmission is higher, $\sim 93.5\%$, and peaks at an ARC thickness of approximately 110 nm. The shift towards lower transmission when including poly-Si is seen here as well. Compared to the ARCs optimized for air ambient, the ARCs optimized for module glass have a larger average apsorption coefficient due to a lower average porosity. Hence, the ARCs optimized for module glass have a thinner optimal thickness. In addition the reflectance of the ARCs optimized for module glass does not increase as rapidly as the reflectance of the ARCs optimized for air when the ARC thickness decreases. This optimization is only valid to the extent that the ellipsometric model built in WVASE32 actually is representable for the given structure. We have previously shown good correspondence between macroscopic properties, such as thickness and porosity, obtained from ellipsometry and other techniques (SEM, TEM, and gravimetry). However, for the absorption to be correct, the model must also give accurate optical constants. Although we know that the material is predominantly crystalline Si and air, changes in the extinction coefficient of Si may occur due to size effects. To assess the accuracy of the optical constants given by the ellipsometry model, it would be beneficial to compare absorption calculated with the BEMA with measured absorption.

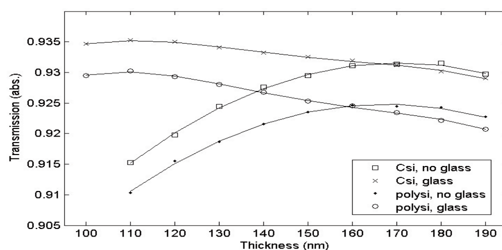

(a) Transmission of PS ARCs. Broad peaks of optimal thickness are visible for all models.

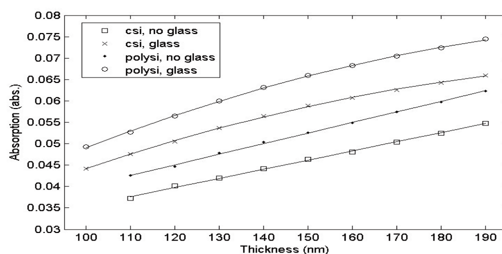

(b) Absorption of PS ARCs. It is evident that films modeled with a mix of c-Si and poly-Si have a higher absorption than films modeled with only c-Si.

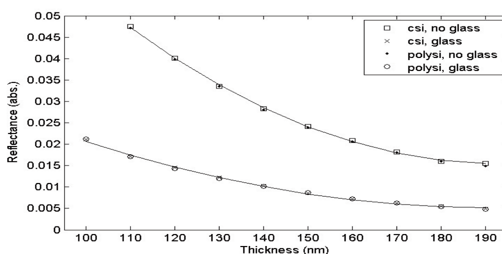

(c) Reflectance of PS ARCs of increasing thickness

Figure 6.12: Optimization of transmission of PS ARCs with respect to thickness showing different optimal thickness for ARCs designed to be used in glass/air ambient. The difference in optimal thickness found between models including poly-Si and c-Si and models using solely c-Si is marginal.

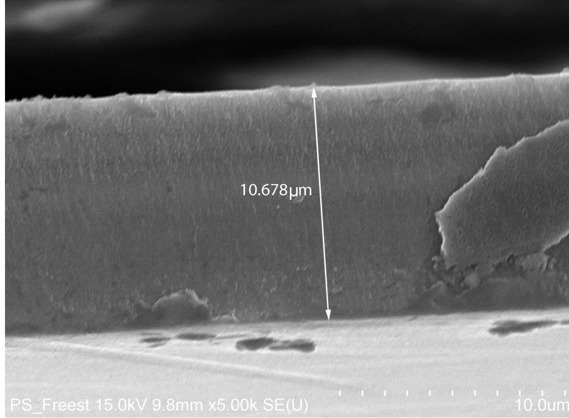

Figure 6.13: SEM image of a freestanding PS film.

6.4.2 Direct Optical Measurement

To study the accordance between absorption in the BEMA model and in an actual structure, freestanding PS films are produced. A freestanding film is etched at 50 mA/cm^2 for 8 minutes, followed by and electropolishing at a current density of 250 mA/cm^2 for 1 minute. The film is attached to a carbon tape which works as conducting substrate in the SEM. From SEM images the thickness can then be determined to be approximately 10.7 μm, see Fig. 6.13.

Reflection, R, and transmittance, T, are measured on a freestanding film etched under identical conditions to the one above. The PS film is attached to a glass substrate with a hole in the middel to allow direct transmission measurements of the PS film. Absorption is then given by $A = 1-T-R$, or to exclude reflection, $A_{nr} = A/(1-R)$. In previous experiments performed in this thesis, it is found that a current density of 50 mA/cm^2 in 20% HF corresponds a film porosity of approximately 55%. We did not manage to perform ellipsometry measurements on the thick freestanding film.

Results from the comparisons between the measured absorption and the absorption generated from a PS layer of 10.7 μm thickness and 55 % porosity can be seen in Fig. 6.14. To illustrate the effect of changes in the model, with respect to crystallinity, porosity and thickness, four slightly different

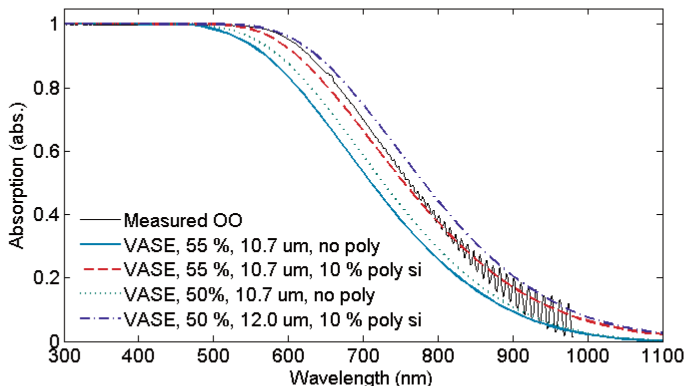

Figure 6.14: Absorption obtained from reflectance and transmission measurements compared with absorption generated from a model of the structure.

WVASE32 models are shown. An initial model consists of solely c-Si and void, the thickness-value obtained from SEM, and a porosity based on the previously obtained value of 55 % ('VASE 55 %, 10.7 μm, no poly'). We see that this model underestimates the absorption somewhat. In the second model ('VASE 55 %, 10.7 μm, poly'), 10 % poly crystalline Si is included. This shows a reasonable fit to the measured data. In the third model ('VASE 50 %, 10.7 μm, no poly') we reduce the porosity instead of including poly-Si. We see that a model without poly Si underestimates the absorption even after this porosity reduction. The last model ('VASE 50 %, 12 μm, poly') we increase the thickness, use the reduced porosity and 10 % poly Si. Not surprisingly these factors add up to overestimate the absorption compared to the measured.

6.4.3 Summary

The model based on the thickness measured by SEM, the porosity determined from measurements on a sample etched under the same current density as the freestanding film, and an addition of 10 % poly Si give an absorption relatively close to the measured absorption. However, there are four relatively large uncertainty factors; i) the porosity estimation, ii) the amount of poly-Si, iii)

possible thickness inhomogeneities over the sample, and iv) the measurement accuracy.

Therefore, the performed freestanding PS layer experiment provides only an estimate of the correspondence between actual optical constants and modeled optical constants, and we can only conclude that the measured absorption is in rough correspondence with the values obtained from the utilized WVASE32 models. The thickness optimizations performed earlier in this section should therefore be a good pointer to the optimal ARC thickness from an optical point of view. For optimal ARC thicknesses, the loss due to absorption in the PS structure is greater than the reflection loss. It should be stressed that the electrical properties of the PS ARC as a solar cell component is not taken into account in the thickness optimizations performed here.

6.5 Etching of Multicrystalline Wafers

For multicrystalline wafers the etch rate dependence upon grain orientation results in non-optimal surface textures when etching in KOH. PS can provide an alternative to the alkaline texturing. The electrochemical etching also depends on crystallinity but to a much smaller extent than alkaline etches. Therefore PS is particularly interesting for multicrystalline wafers. For the optimized PS ARC structures, we have seen that no pretexturing is necessary.

Homogeneously doped multicrystalline wafers with a resistivity of $\sim$0.02 Ω cm were etched in an electrolyte containing 20 % HF. Multicrystalline samples with both homogeneous PS layers and PS multilayers optimized for antireflection were fabricated.

Figure 6.15 shows a comparison of the reflectance spectrum obtained using identical current density profiles during etching of a monocrystalline and a multicrystalline substrate. The substrates have similar (but not identical) resistivities. The spot used for measuring reflectance was rather large ($\sim$1 cm^2) compared to the grain size of the multiwafer. Therefore, the obtained reflection is an effective reflection from a group of randomly selected grains. The differences in the reflectance spectra between the mono and multiwafers are significant, but the multicrystalline Si wafer also displays very low reflectivity and and has fairly homogeneous appearance. The increase in reflection above $\sim$1000 nm is due to reflection from the backside of the wafer, i.e. light that escapes after a double pass through the substrate.

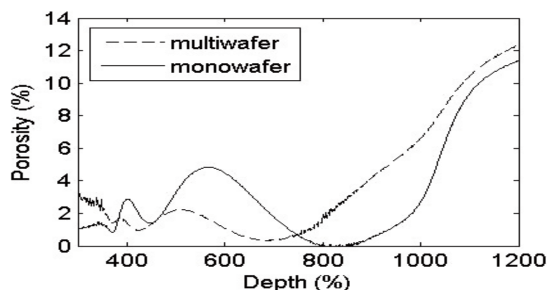

Figure 6.15: Comparison of the reflectance spectra of the PS ARC optimized for air ambient etched on one monocrystalline and one multicrystalline substrate.

The only highly doped, multicrystalline wafers we had access to were unpolished. This makes characterization by ellipsometry very difficult and does not provide an optimal comparison with the polished monolayers. Initial attempts to polish the multicrystalline wafers were unsuccessful. Therefore only spectroscopic reflectometry is used to characterize the samples. More information would be gained by coupling the variations in reflectance with grain orientation.

6.6 Porous Silicon Backside Reflector

The objective of the work presented in this section was to produce a PS rear side reflector for thin Si solar cells. The structure of the reflector was a multilayer stack of quarter wave layers of alternating high and low porosity layers, i.e. a PS distributed Bragg reflector (DBR). The work performed was conducted in collaboration with master student Solveig Rørkjær, whom the author - together with Dr. Erik Stensrud Marstein - was supervising during spring 2010. Much of the work is presented in Rørkjær's master thesis "Porous Silicon as Rear Side Reflectors for Very Thin Silicon Solar Cells" [173]. The fabrication and the majority of characterization were conducted by Rørkjær. The model on which simulations of the optimal PS reflector profiles prior to fabrication was based was made by the author. Also, modeling of the ellipsometric data after processing was done by the author. The results to be

presented here again illustrate the capabilities of ellipsometry to characterize multilayer structures well. Analysis and discussions of results was performed by collaboration between Rørkjær, the author and Erik Stensrud Marstein. A relatively short summary of the work performed will be presented in the following.

6.6.1 Designing the reflector structure

As discussed in Section 3.4.2, the refractive index of the high and low porosity layers is decisive for the performance of the reflector. For optimal performance the refractive index difference should be as large as possible. For a given refractive index span, higher porosities may be a benefit as this gives less parasitic absorption and higher internal reflection.

For the chosen set of parameters, the highest available porosity is 76% and is limited by the onset of electropolishing at higher current densities. Higher porosities are achievable with a reduced HF concentration in the electrolyte, but mechanical stability may become a problem for very high porosities. More importantly, the highest achievable refractive index is decreased if lower HF concentrations are utilized, and the net refractive index span is reduced. Therefore no improvement of the reflectance is expected from lowering the HF concentration. The lowest available porosity at the time this work was performed was 40%. Porosities as low as 25% has previously been achieved using the same setup, substrate and electrolyte composition as what was used for the PS reflector experiments. However, a fault on the potentiostat (it fails to reach the lowest current densities) prevented us from reaching this low porosities for the samples prepared as rear side reflectors. Initially a design wavelength of 950 nm was chosen, based on reported literature values [34]. At this wavelength, the utilized porosities of 40% and 76% correspond to refractive indices of 2.5 and 1.4 respectively.

As the sun is not stationary, it is desirable with a reflector that is efficient for a broader range of incident angles. As light with incident angles larger than a critical angle will be reflected due to total internal reflection, the PS DBR should take care of the light with incident angles smaller than the critical angle. The critical angle depends on the porosity used, but will typically be around 20°.

For normal incidence, the construction of the stack follows very simple rules and hardly needs simulation (only calculation). However, a simulation tool is beneficial when the angular dependence of incoming light is included.

Simulation also enables us to assess the effect of increasing the number of layers in the DBR.

The ellipsometric software WVASE32 was used for modeling and optimizing the reflector prior to fabrication. In the simulations, the low porosity layers were fixed to have the same porosity, and similarly, the high porosity layers were fixed. Also the ratio of the thickness of the high and low porosity layers were fixed to 1.76 (the ratio of their refractive indices) to ensure that both type of layers fulfill the quarter wavelength rule for the same wavelength.

Using an odd number of layers, starting and ending with the low refractive index (high porosity) layer, improves the reflectance. The critical angle for total internal reflection between Si and a layer with refractive index of 1.4 is $\sim 23°$. If the front texture effectively randomizes the light entering the cell, the majority of photons reaching the back reflector will in fact be totally internally reflected rather than reflected by the DBR structure as such.

For angles of incidence approaching 20°, the simulations showed that the reflector no longer produced a well defined region/plateau of high reflectance. As a compromise, the optimization was therefore performed for angles of incidence from $0 - 15°$.

6.6.2 Results

SEM images of the fabricated PS DBR structures with five and fifteen layers are shown in Fig. 6.16 and 6.17 respectively. The layer structure is clearly displayed in both images. Superimposed on the SEM image in Fig. 6.16 is the ellipsometric model of this layer. Very good correspondence between the SEM image and the rather complex ellipsometric model is found. The thickness obtained from ellipsometry is in excellent accordance with the thickness seen in the SEM image, and the layer structure with graded interface regions between the alternating layers match the visual impression quite well. This is regarded as a strong confirmation of the accuracy and physical validity of the ellipsometric model employed.

The ellipsometric model for this structure is composed of five anisotropic BEMA layers. Each layer has four nodes (point where the porosity gradient changes), where the first node in each layer is set equal to the ending node of the previous layer, as seen by counting the nodes in Fig. 6.16. The model structure is illustrated in Fig. 6.18a and the corresponding refractive index profile in Fig. 6.18b. As the PS layers are uniaxially anisotropic, the optical

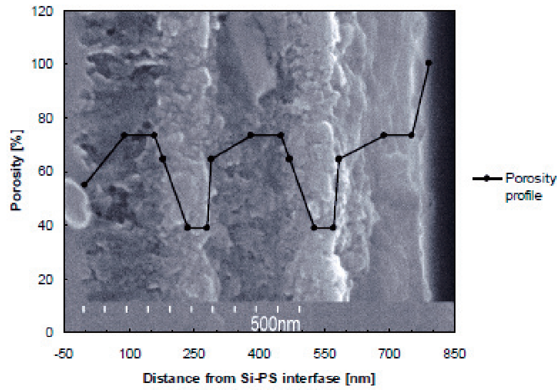

Figure 6.16: A superposition of the porosity profile determined from ellipsometry and a SEM image of a five layer PS DBR structure. SEM image taken by Rørkjær, superimposed ellipsometric profile modeled by the author.

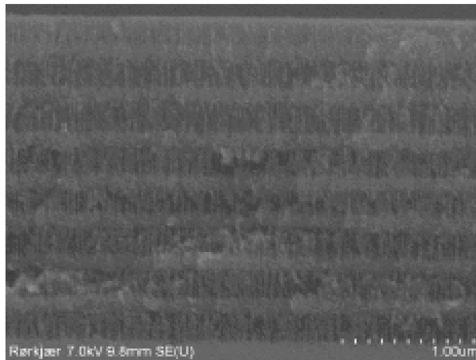

Figure 6.17: SEM image of a 15 layer PS DBR structure [173, Rørkjær's master thesis].

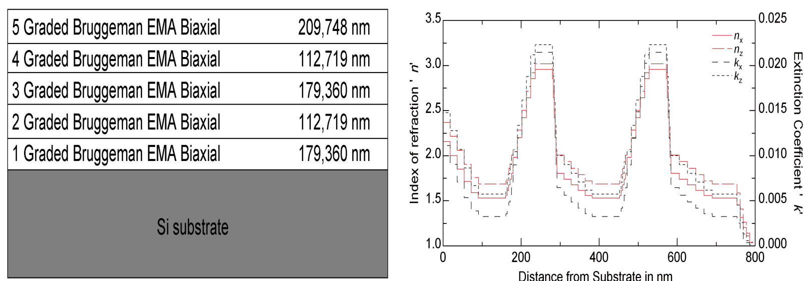

(a) Layer structure of the ellipsometric model.

(b) Refractive index and extinction coefficient of the ellipsometric model as function of depth in the layer.

Figure 6.18: Ellipsometry model structure and best fit refractive index profile of the five layer PS DBR structure.

constants in x and z directions are different. The goodness of the model, measured by the mean square error (MSE) is 27.5. This is relatively high, but acceptable for such a complex structure.

Note that when the reflectance is measured experimentally, we are unable to measure the reflectance at the PS/Si surface directly. Instead, the reflectance is measured on the PS/air interface. To study whether the fabricated structures are in conformity with the design, the experimental reflectance measurements are compared with the designed structures response in air ambient (instead of Si ambient). Figure 6.19 shows the modeled reflectance of the 5 layer PS DBR with air and Si as ambient. A clear plateau is visible in the reflectance from both interfaces. A study of the evolution of the reflectance with increasing number of layers in the DBR was also performed. For a 15 layer PS DBR, the reflectance of the plateau was about 98%. Further increase therefore was found to give little gain in reflectance. The high reflection plateau covered the wavelength region $\sim 700 - 950$ nm.

6.6.3 Considerations on implementation of PS backside reflectors

As we have shown in the previous section, from an optical point of view the PS DBR is a promising and very flexible technology which can easily

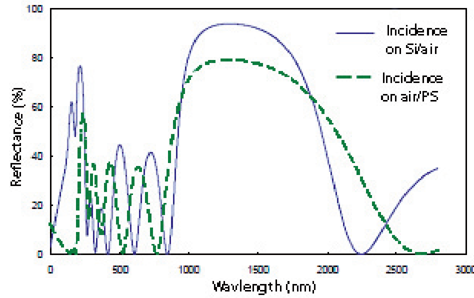

Figure 6.19: A comparison of the reflectance of a 5 layer PS DBR in air and Si ambient.

be optimized for different cell designs. In our work we did not get as far as implementing the PS DBR in an actual solar cell structure since work to find a suitable cell structure and surface passivation is not (yet) carried out.

Some reported efficiencies of solar cells with PS rear side reflectors can be found in literature. In the most common implementation, PS is used as combined backside reflector and seeding layer for epitaxial Si growth [33, 34, 108, 111]. There are several potential challenges associated with this cell structure: i) during growth of the Si epitaxial cell the PS structure is expected to reorganize, potentially changing the fabricated reflector structure, ii) the roughness of the PS surface will be important for the quality of the epitaxial Si layer, iii) for thick PS DBR situated between the cell and the backside contact, PS must provide sufficient conductance, and iv) recombination losses due to insufficient surface passivation of PS could result in reduced cell efficiency. In the following, each of these issues will be given some consideration.

Duerinckx et al. [34] report that although a reorganization of the PS layers take place, the original distribution of alternating layers is preserved. However, the voids in the original high porosity PS layer are reported to grow to a diameter of $\sim$ 150 nm [34]. For these dimensions, one is approaching the validity limit of the effective medium approximation. The structure is designed mainly for infrared wavelengths, but the wavelength in these PS layers is more than halved compared to the corresponding air wavelength (reported refractive index of 2.3 [34]). Zettner et al. [108] report a rather

poor agreement between simulation and measurements of the PS reflector structure after epitaxial Si growth. Abouelsaood et al. [106] report that high porosity layers (60%) experience a drastic reduction in porosity (to $20-30\%$) under normal CVD growth. Clearly, reorganization of the PS layers is an issue that should be considered and addressed when implementing PS rear side reflectors within this cell design.

A method to close the top surface and reduce the surface roughness in order to improve epitaxial Si quality of the PS layers has been presented by Kuzma-Filipek et al. [33]. They use a 30 min heat treatment in hydrogen before epitaxial Si growth. A cell efficiency of 15.2% is achieved for an epitaxial Si cell with this method.

Kuzma-Filipek et al. [111] have investigated the specific resistivity of the PS layers to determine the conductivity of the PS reflector. They conclude that there is no significant increase in resistance with increasing number of PS layers.

It is known that adequate surface passivation of PS can be a challenge. For these PS backside structures, the importance of surface passivation is greater than for front side PS ARC structures fabricated in the dead emitter layer. Little is written that specifically address the surface passivation of the PS rear side reflector structures, but an improved surface passivation of PS would likely give an enhanced efficiency for this type of cells.

We see that the challenges with respect to surface roughness and conductivity can be overcome, while better solutions are still sought to prevent or account for pore reorganization and improve surface passivation. Even so, the obtained efficiencies are promising, and a PS rear side structure could benefit from many of the same advantages as the front side PS structure; low cost, no new materials introduced and great optical flexibility.

Alternative implementation regimes may of course be possible. Dedicated rear side reflectors have traditionally not been necessary in thick Si wafer based solar cells. As the thickness of the wafer based cells are now continuously decreasing the need for efficient rear side reflectors will become evident. The rear side reflector could be etched in the substrate before diffusion, but will then suffer from reorganization during emitter diffusion, or the PS etch may be performed in the back surface field after diffusion. Diffusion on both sides is commonly performed as it simplifies the processing and can have a positive effect on the gettering. A challenge with this scenario is the depth of the PS rear side reflector structure, typically significantly thicker than a standard emitter profile. Another challenge is again PS etching in a

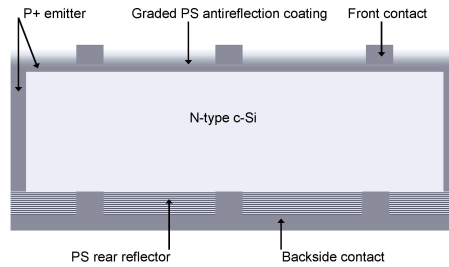

Figure 6.20: Schematic design of n-type Si solar cell with PS rear reflector and PS ARC.

$p^+/n/p^+$ junction structure. Figure 6.20 shows a schematic drawing of an n-type Si solar cell with PS rear reflector and PS ARC.

Chapter 7

Conclusions and Future Work

Through the work with this thesis, it has been demonstrated that the PS formation process can be controlled with sufficienct accuracy to allow precise tailoring of very thin multilayer PS structures. As the porosity of PS is tightly and relatively predictivly tied to the optical properties of the material, a great diversity of optical coatings can be produced. In this work, the focus has been on fabrication of efficient PS antireflection coatings (ARCs) for implementation in silicon solar cells. The reflection from such thin PS ARCs can be made very low without any additional texture. Integrated reflectances of less than 3% have been obtained for PS films thinner than 200 nm, using rapid and inexpensive electrochemical fabrication.

The PS ARCs are also interesting for building integrated photovoltaic (BIPV) applications as they can be fabricated in a range of colors with minimal increase in reflectance. In my opinion, BIPV is a very exiting application that has only begun to gain momentum. Although some products already are available, hopefully a great variety of designs and innovative solutions will emerge and make BIPV an economically viable techonology.

In addition to excellent *antireflective* films, very good *reflectors* can also be fabricated from PS. We have fabricated PS distributed Bragg reflectors (DBR) with plateau reflectance of $\sim 98\%$, suitable for use as rear side reflectors in thin silicon solar cells.

Increased knowledge about the properties of PS is valuable in order to implement PS in solar cells, but also as general puzzle pieces to contribute to a more complete understanding of this complex material. Through the work with PS multilayers we have observed a dense PS surface layer which likely originates in the pore nucleation process. We have also measured a gradual

oxidation of the PS structures with aging in room temperature and air ambient; from pure Si via intermediate oxidation states, and finally SiO_2. The oxidation of the PS ARC structures does not seem to degrade their antireflective qualities. Thorough investigations have been performed with respect to the processing and control of the PS layers, assessing the homogeneity of the produced structures, effects of chemical etching and electrolyte evaporation. Hopefully, these studies have made a small contribution towards an improved understanding of and control over this extraordinary material.

Future Work

Considering the promising optical properties of PS, I believe it would be worthwhile to make a serious effort to implement our multilayer PS ARC structures in a finished solar cell. The first important milestone toward efficient implementation would be to achieve sufficient control over the etching process in an emitter structure. Efforts to fabricate the optimized PS ARCs in the p^+ emitter of our n-type solar cells will be continued and work on etching PS ARCs in n^+ emitters has also recently been initiated. If satisfactory reflectance from PS ARCs etched in emitter structures is obtained, the next step is naturally to optimize the remaining cell structure, including work on the surface passivation and metallization, to the new ARC.

While continuing the investigations of the well known possibilities for PS application in solar cells, one should also keep watch for new and inventive ways of implementing PS to improve the cost efficiency of silicon solar cells.

With respect to the more fundamental studies of the PS structure, the dense PS surface layer calls for further investigations and exploration of the parameter space resulting in such structures. Follow-up studies of this dense region could provide further information about the initial growth phase of PS, which is not fully understood today.

Bibliography

[1] M. Antal, G. Concas, E. Despotou, A. El Gammal, D. F. Montoro, M. Latour, P. Llamas, S. L. G. Masson, P. Vanbuggenhout, S. Teske, S. Rolland, and R. Short. *Solar Generation 6 Exceutive Summary*. European Photovoltaic Industry Association and Greenpeace, 2010.

[2] R. K. Pachauri and A. Reisinger, editors. *Climate Change 2007: Synthesis Report*. Intergovernmental Panel on Climate Change, 2008.

[3] United Nations Environmental Programme. Climate change. 2010.

[4] J. L. Sawin and E. Martinot. *Renewables 2010 Global Status Report*. REN21 Secretariat and Deutsche Gesellschaft fur Technische Zusammenarbeith (GTZ) GmbH, 2010.

[5] E. Despotou, A. El Gammal, B. Fontaine, D. F. Montoro, M. Latour, S. Lenoir, G. Masson, P. Philbin, and P. Van Buggenhout. *Global Market Outlook for Photovoltaics Until 2014*. European Photovoltaic Industry Association, 2010.

[6] Renewable Energy Corporation. http://rec-group.com, November 2010.

[7] N. Tanaka, editor. *Technology Roadmap Solar Photovolatic Energy*. International Energy Agency, 2010.

[8] J. M. Roney. Solar cell production climbs to another record in 2009. *Earth Policy Institute, Eco-Economy Indicators. http://www.earth-policy.org/index.php?/indicators/C47/*, 2010.

[9] A. Hutchinson. Solar panel drops to $1 per watt: Is this a milestone or the bottom for silicon-based panels? *Popular Mechanics*, 2009.

[10] K. Macwilliams, J. Shu, A. Moretto, and F. Ahmad. Towards grid parity: advances in c-si pv manufacturing technology. *Applied Materials*, 2010.

[11] C. Yang. Reconsidering solar grid parity. *Energy Policy*, 38(7):3270 – 3273, 2010.

[12] Ch. Breyer, A. Gerlach, J. Mueller, H. Behacker, and A. Milner. Grid-parity analysis for eu and us regions and market segments - dynamics of grid-parity and dependence on solar irradiance, local electricity prices and pv progress ratio. In *EUPVSEC proceedings*, 2008.

[13] Statistisk Sentralbyra Statistics Norway. Large reduction in greenhouse gas emissions. 2010.

[14] Elkem. http://www.elkem.no, November 2010.

[15] B. Stuart. Research: Module production increasingly moving to asia. *PV Magzine*, November 2010.

[16] M. Schmela. *Photon International*, 3:176 – 199, 2010.

[17] C. Levy-Clement. Personal communication. *Electrochemical Society Conference, Las Vegas*, 2010.

[18] R. M. Swanson. Developments in silicon solar cells. In *Electron Devices Meeting. IEEE International*, pages 359 – 362, 2007.

[19] A. Uhlir Jr. Electrolytic shaping of germanium and silicon. *The Bell System Technical Journal*, pages 333 – 347, 1956.

[20] A. Uhlir Jr. and I. (Williams) Uhlir. Historical perspective on the discovery of porous silicon. *physica status solidi (c)*, 2:3185 – 3187, 2005.

[21] R. Memming and G. Schwandt. Anodic dissolution of silicon in hydrofluoric acid solutions. *Surface Science*, 4(2):109 – 124, 1966.

[22] S. Watanabe. Application of a thick anode film to semiconductor devices. *Rev. Elec. Commun. Lab*, 1971.

[23] M. J. J. Theunissen. Etch channel formation during anodic dissolution of n-type silicon in aqueous hydrofluoric acid. *Journal of The Electrochemical Society*, 119(3):351 – 360, 1972.

[24] C. Pickering, M. I. J. Beale, D. J. Robbins, P. J. Pearson, and R. Greef. Optical studies of the structure of porous silicon films formed in p-type degenerate and non-degenerate silicon. *Journal of Physics C: Solid State Physics*, 17(35):6535–6552, 1984.

[25] M. I. J. Beale, J. D. Benjamin, M. J. Uren, N. G. Chew, and A. G. Cullis. An experimental and theoretical study of the formation and microstructure of porous silicon. *Journal of Crystal Growth*, 73(3):622 – 636, 1985.

[26] A. Prasad, S. Balakrishnan, S. K. Jain, and G. C. Jain. Porous silicon oxide anti-reflection coating for solar cells. *Journal of the Electrochemical Society*, 129:596–599, 1982.

[27] L. T. Canham. Silicon quantum wire array fabrication by electrochemical and chemical dissolution of wafers. *Applied Physics Letters*, 57(10): 1046 – 1048, 1990.

[28] V. Lehmann and U. Gösele. Porous silicon formation: A quantum wire effect. *Applied Physics Letters*, 58(8):856 – 858, 1991.

[29] P. Menna, G. Di Francia, and V. La Ferrara. Porous silicon in solar cells: A review and a description of its application as an ar coating. *Solar Energy Materials and Solar Cells*, 37(1):13 – 24, 1995.

[30] Y. S. Tsuo, Y. Xiao, M. J. Heben, X. Wu, F. J. Pern, and S. K. Deb. Potential applications of porous silicon in photovoltaics. *IEEE*, pages 287 – 293, 1993.

[31] R. Brendel. *Thin-film crystalline silicon solar cells*. Wiley-VCH Verlag GmbH & Co. KGaA, Weinheim, 2003.

[32] V. Depauw, I. Gordon, G. Beaucarne, J. Poortmans, R. Mertens, and J.-P. Celis. Proof of concept of an epitaxy-free layer-transfer process for silicon solar cells based on the reorganisation of macropores upon annealing. *Materials Science and Engineering: B*, 159-160:286 – 290, 2009. ISSN 0921-5107. EMRS 2008 Spring Conference Symposium K:

Advanced Silicon Materials Research for Electronic and Photovoltaic Applications.

[33] I. Kuzma-Filipek, K. V. Nieuwenhuysen, J. V. Hoeymissen, M. R. Payo, E.V. Kerschaver, J. Poortmans, R. Mertens, G. Beaucarne, E. Schmich, S. Lindekugel, and S. Reber. Efficiency (> 15) for thin-film epitaxial silicon solar cells on 70 cm^2 area offspec silicon substrate using porous silicon segmented mirrors. *Progress in Photovoltaics: Research and Applications*, 18:137 – 143, 2010.

[34] F. Duerinckx, I. Kuzma-Filipek, G. Beaucarne K. Nieuwenhuysen, and J. Poortmans. Stimulatino and implementation of a porous silicon reflector for epitaxial silicon solar cells. *Progress in Photovoltaics: Research and Applications*, 16:399 – 407, 2008.

[35] D. Kray, M. Hermle, and S. W. Glunz. Theory and experiments on the back side reflectance of silicon wafer solar cells. *Progress in Photovoltaics: Research and Applications*, 16:1–15, 2008.

[36] R. J. Archer. Stain films on silicon. *Journal of Physics and Chemistry of Solids*, 14:104 – 110, 1960.

[37] R. L. Smith and S. D. Collins. Porous silicon formation mechanisms. *Journal of Applied Physics*, 71:1, 1992.

[38] G. Zhang. *Electrochemiestry of silicon and its oxide*. Kluwer Academic/Plenum Publishers, 2001.

[39] V. Lehmann. *Electrochemistry of Silicon: Instrumentation, Science, Materials and Applications*. Exploration of Space: Issues and Status, 2002.

[40] L. G. Gouy. Sur la constitution de la charge électrique à la surface d'un électrolyte. *Comptes rendus hebdomadaires des séances de l'Académie des sciences*, 149, 1909.

[41] L. G. Gouy. Sur la constitution de la charge électrique à la surface d'un électrolyte. *Journal de Physique Théorique et Appliquée*, 9, 1910.

[42] D. L. Chapman. Sur la constitution de la charge électrique à la surface d'un électrolyte. *The London, Edinburgh, and Dublin Philosophical Magazine and Journal of Science*, 25, 1913.

[43] O. Z. Stern. Zur theorie der elektrolytischen doppelschicht. *Electrochemestry*, 30, 1924.

[44] B. Hamilton. Porous silicon. *Semiconductor Science and Technology*, 9:1187, 1995.

[45] H. Ubara, T. Imura, and A. Hiraki. Formation of si-h bonds on the surface of microcrystalline silicon covered with siox by hf treatment. *Solid State Communications*, 50(7):673 – 675, 1984.

[46] X. G. Zhang. Morphology and formation mechanisms of porous silicon. *Journal of The Electrochemical Society*, 151(1):C69 – C80, 2004.

[47] Y. Arita. Formation and oxidation of porous silicon by anodic reaction. *Journal of Crystal Growth*, 45:383 – 392, 1978.

[48] T. Unagami. Formation mechanism of porous silicon layer by anodization in hf solution. *Journal of the electrochemical Society*, 127:476 – 483, 1980.

[49] H. Föll, M. Christophersen, J. Carstensen, and Hasse G. Formation and application of porous silicon. *Materials Science and Engineering: R: Reports*, 39:93 – 141, 2002.

[50] D. T. J. Hurle and P. Rudolph. A brief history of defect formation, segregation, faceting, and twinning in melt-grown semiconductors. *Journal of Crystal Growth*, 264(4):550 – 564, 2004. Proceedings of the Symposium - Progress in Crystal Growth.

[51] M. Thönissen, M. G. Berger, R. Arens-Fischer, O. Gluck, M. Kruger, and H. Luth. Illumination-assisted formation of porous silicon. *Thin Solid Films*, 276, 1996.

[52] A. G. Cullis, L. T. Canham, and P. D. J. Calcott. The structural and luminescence properties of porous silicon. *Journal of Applied Physics*, 82(3):909 – 965, 1997.

[53] R. L. Smith, S.-F. Chuang, and S. D. Collins. A theoretical model of the formation morphologies of porous silicon. *Journal of Electronic Materials*, 17:533–541, November 1988.

[54] V. Lehmann, R. Stengl, and A. Luigart. On the morphology and the electrochemical formation mechanism of mesoporous silicon. *Materials Science and Engineering B*, 69-70:11 – 22, 2000. ISSN 0921-5107.

[55] P. Meakin and J. M. Deutch. The formation of surfaces by diffusion limited annihilation. *The Journal of Chemical Physics*, 85(4):2320 – 2325, 1986.

[56] T. A. Witten and L. M. Sander. Diffusion-limited aggregation, a kinetic critical phenomenon. *Physical Review Letters*, 47(19):1400 – 1403, 1981.

[57] G. C. John and V. A. Singh. Diffusion-induced nucleation model for the formation of porous silicon. *Physical Reveiw B*, 52(15):11125 – 11131, 1995.

[58] J. Carstensen, M. Christophersen, and H. Föll. Pore formation mechanisms for the si-hf system. *Materials Science and Engineering B*, 69-70: 23 – 28, 2000.

[59] S. Zangooie, R. Jansson, and H. Arwin. Ellipsometric characterization of anisotropic porous silicon fabry-perot filters and investigation of temperature effects on capillary condensation efficiency. *Journal of Applied Physics*, 86(2):850 – 858, 1999.

[60] H. Krzyzanowska, M. Kulik, and J. Zuk. Ellipsometric study of refractive index anisotropy in porous silicon. *Journal of Luminescence*, 80: 183 – 186, 1999.

[61] L. A. Golovan', P. K. Kashkarov, and V. Y. Timoshenko. Form birefringence in porous semiconductors and dielectrics: A review. *Crystallography Reports*, 52:z, 2007.

[62] I. Mihalcescu, G. Lerondel, and R. Romestain. Porous silicon anisotropy investigated by guided light,. *Thin Solid Films,*, 297:245–249, 1997.

[63] L. H. Qin, Y. D. Zheng, R. Zhang, S. L. Gu, H. T. Shi, and D. Feng. Ellipsometric studies of porous silicon. *Applied Physics A: Materials Science & Processing*, 58:163–165, 1994.

[64] D. Kovalev, G. Polisski, J. Diener, H. Heckler, N. Künzner, V. Yu. Timoshenko, and F. Koch. Strong in-plane birefringence of spatially nanostructured silicon. *Applied Physics Letters*, 78(7):916 – 918, 2001.

[65] J. Pastrnak and K. Vedam. Optical Anisotropy of Silicon Single Crystals. *Physical Review B*, 3:2567–2571, 1971.

[66] N. Künzner, J. Diener, E. Gross, D. Kovalev, V. Y. Timoshenko, and M. Fujii. Form birefringence of anisotropically nanostructured silicon. *Physical Review B*, 71(19):195304, 2005.

[67] D. Kovalev, H. Heckler, G. Polisski, and F. Koch. Optical properties of si nanocrystals. *Physica status solidi(b)*, 215:871, 1999.

[68] I. Sagnes, A. Halimaoui, G. Vincent, and P. A. Badoz. Optical absorption evidence of a quantum size effect in porous silicon. *Applied Physics Letters*, 62:1155 – 1157, 1993.

[69] J. von Behren, L. Tsybeskov, and P. M. Fauchet. Preparation and characterization of ultrathin porous silicon films. *Applied Physics Letters*, 66:1662, 1995.

[70] G. Lerondel, F. Madeore, R. Romestain, and F. Muller. Direct determination of the absorption of porous silicon by photocurrent measurements at low temperature. *Thin Solid Films*, 366:216 – 224, 2000.

[71] H. Diesinger, A. Bsiesy, R. Hérino, and B. Gelloz. Effect of the quantum confinement on the optical absorption of porous silicon, investigated by a new in-situ method. *Materials Science and Engineering B*, B69-70: 167 – 170, 2000.

[72] R. Herino, G. Bomchil, K. Barla, C. Bertrand, and J. L. Ginoux. Porosity and pore size distributions of porous silicon layers. *Journal of The Electrochemical Society*, 134(8):1994 – 2000, 1987.

[73] Y. Kato, T. Ito, and A. Hiraki. Initial oxidation process of anodized porous silicon with hydrogen atoms chemisorbed on the inner surface. *Japanese Journal of Applied Physics*, 27:L1406 – L1409, 1988.

[74] F. J. Himpsel, F. R. McFeely, A. Taleb-Ibrahimi, J. A. Yarmoff, and G. Hollinger. Microscopic structure of the sio_2/si interface. *Physical Review B*, 38(9):6084 – 6096, 1988.

[75] E. P. Domashevskaya, V. M. Kashkarov, E. Yu. Manukovskii, A. V. Shchukarev, and V. A. Terekhov. Xps, usxs and pls investigations of porous silicon. *Journal of Electron Spectroscopy and Related Phenomena*, 88-91:969 – 972, 1998. Proceedings of the Seventh International Conference on Electron Spectroscopy.

[76] A. Grosman and C. Ortega. Chemical composition of 'fresh' porous silicon. In L. Canham, editor, *Properties of Porous Silicon*. The institution of Electrical Engineers, 1997.

[77] T. Sunada, T. Yasaka, M. Takakura, T. Sugiyama, S. Miyazaki, and M. Hirose. The Role of Fluorine Termination in the Chemical Stability of HF-Treated Si Surfaces. *Japanese Journal of Applied Physics*, 29: L2408 – L2410, 1990.

[78] L. Canham. Chemical composition of 'aged' porous silicon. In L. Canham, editor, *Properties of Porous Silicon*. The institution of Electrical Engineers, 1997.

[79] D. M. Chapin, C. S. Fuller, and G. L. Pearson. A new silicon p-n junction photocell for converting solar radiation into electrical power. *Journal of Applied Physics*, 25:676 – 677, May 1954.

[80] C. Gueymard, D. Myers, and K. Emery. Proposed reference irradiance spectra for solar energy systems testing. *Solar Energy*, 73:443 – 467, December 2002.

[81] T. Tiedje, E. Yablonovitch, G. Cody, and B. Brooks. Limiting efficiency of silicon solar cells. *IEEE Transactions on electron devices*, ED-31(5), 1984.

[82] *www.renewableenergyworld.com*, 2010.

[83] J. Zhao, A. Wang, M. A. Green, and F. Ferrazza. Novel 19.8% efficient "honeycomb" textured multicrystalline and 24.4% monocrystalline silicon solar cells. *Applied Physics Letters*, 73:1991 – 1993, 1998.

[84] O. Schultz, S. W. Glunz, and G. P Willeke. Multicrystalline silicon solar cells exceeding 20% efficiency. *Progress in Photovoltaics: Research and Applications*, 12:553 – 558, 2004.

[85] A. Müller, M. Ghosh, R. Sonnenschein, and P. Woditsch. Silicon for photovoltaic applications. *Materials Science and Engineering: B*, 134 (2-3):257 – 262, 2006. EMRS 2006, Symposium V; Advanced Silicon for the 21st Century.

[86] Y. Tsunomura, Y. Yoshimine, M. Taguchi, T. Baba, T. Kinoshita, H. Kanno, H. Sakata, E. Maruyama, and M. Tanaka. Twenty-two percent efficiencty hit solar cell. *Solar Energy Materials and Solar Cells*, 93:670 – 673, 2009.

[87] A. Wang, J. Zhao, S. R. Wenham, and M. A. Green. 21.5% eficient thin silicon solar cell. *Progress in Photovoltaics: Research and Applications*, 4:55 – 58, 1996.

[88] M. A. Green, K. Emery, Y. Hishikawa, and W. Warta. Solar cell efficiency tables (version 35). *Progress in Photovoltaics: Research and Applications*, 18:144 – 150, 2010.

[89] R. B. Bergmann, C. Berge, T. J. Rinke, J. Schmidt, and J. H. Werner. Advances in monocrystalline si thin film solar cells by layer transfer. *Solar Energy Materials and Solar Cells*, 74:213 – 118, 2002.

[90] J. Nelson. *The Physics of Solar Cells*. Imperial College Press, 2003.

[91] T. Markvart and L. Castaner, editors. *Solar Cells: Materials, Manufacture and Operation*. Elsevier Advanced Technology, 2005.

[92] E. Luque and S. Hegedus, editors. *Handbook of Photovoltaic Science and Engineering*. John Wiley & Sons, 2003.

[93] H. Seidel. The mechanism of anisotropic, electrochemical silicon etching i n alkaline solutions. In *IEEE*, pages 86 – 91, 1990.

[94] V. Pačebutas, K. Grigoras, and A. Krotkus. Porous silicon applications in solar cell technology. *Physica Scripta Volume T*, 69:255, 1997.

[95] R. Ludemann, B. M. Damiani, and A. Rohatgi. Novel processing of solar cells with porous silicon texturing. *Photovoltaic Specialists Conference, 2000. Conference Record of the Twenty-Eighth IEEE*, pages 299–302, 2000.

[96] V. Yerokhov, R. Hezel, M. Lipinski, R. Ciach, H. Nagel, A. Mylyanych, and P. Panek. Cost-effective methods of texturing for silicon solar cells. *Solar Energy Materials & Solar Cells*, 72:291 – 298, 2002.

[97] E. Van Kerschaver and G. Beaucarne. Back-contact solar cells: A review. *Progress in Photovoltaics: Research and Applications*, 14:107 – 123, 2006.

[98] H. A. MacLeod. The early days of optical coatings. *Journal of Optics A: Pure and Applied Optics*, 1, 1999.

[99] H. A. MacLeod. *Thin-Film Optical Filters*. Thin-Film Optical Filters by H A Macleod London, GB: Institute of PHysics Publishing, 1986, 1986.

[100] A. MacLeod. *The Essential MacLeod, Version 8.9.55 (ie), ©Thin Film Center Inc.*, 2000, 2001, 2002.

[101] E. Yablonovitch and G. D. Cody. Intensity enhancement in textured optical sheets for solar cells. *Electron Devices, IEEE Transactions on*, 29(2):300 – 305, 1982.

[102] P. Campbell and M. A. Green. Light trapping properties of pyramidally textured surfaces. *Journal of Applied Physics*, 62(1):243 – 249, 1987.

[103] G. Lerondel, R. Romestain, F. MadEore, and F. Muller. Light scattering from porous silicon. *Thin Solid Films*, 273:80 – 83, 1996.

[104] R. Bilyalov, R. Ludemann, W. Wettling, L. Staalmans, J. Poortmans, J. Nijs, L. Schirone, G. Sotgiu, Strehlke S., and C. Levy-Clemet. Multicrystalline silicon solar cells with porous silicon emitter. *Solar Energy Materials and Solar Cells*, 60:391 – 420, 2000.

[105] C. Liang-Yao, H. Xiao-Yuan, H. A-Ming, Z. Fu-Long, F. Ing we YI, A. In, S. Yi, Q. You-Hua, and W. Xun. Study of photon-trapping phenomenon in porous silicon layer. *ACTA PHYSICA SINICA*, 3, 1994.

[106] A. A. Abouelsaood, M. Y. Ghannam, L. Stalmans, J. Poortmans, and J. F. Nijs. Experimental testing of a random meidum optical model of porous silicon for photovoltaic applications. *Progress in Photovoltaics: Research and Applications*, 9, 2001.

[107] B. Sopori. Thin-film silicon solar cells. In E. Luque and S. Hegedus, editors, *Handbook of Photovoltaic Science and Engineering*, pages 307 – 357. John Wiley & Sons, 2003.

[108] J. Zettner, M. Thoenissen, T. Hierl, R. Brendel, and M. Schulz. Novel porous silicon backside light reflector for thin silicon solar cells. *Progres in Photovoltaics*, 6(6):423 – 432, 1998.

[109] P. Vitanov, G. Agostinelli, A. Harizanova, T. Ivanova, M. Vukadinovic, N. Le Quang, and G. Beaucarne. Low cost surface passivation for p-type mc-si based on pseudobinary alloys (al2o3)x(tio2)1-x. *Solar Energy Materials and Solar Cells*, 90(15):2489 – 2495, 2006. ISSN 0927-0248. Selected Papers from the Solar Cells and Solar Energy Materials Symposium -IMRC 2005.

[110] R. Bilyalov, C. S. Solanki, J. Poortmans, A. Richard, H. Bender, M. Kummer, and H. von Kanel. Crystalline silicon thin films with porous si backside reflector. *Thin Solid Films*, 403-404:170 – 174, 2002.

[111] I. Kuzma-Filipek, F. Duerinckx, K. Van Nieuwenhuysen, G. Beaucarne, J. Poortmans, and R. Mertens. Porous silicon as an internal reflector in thin epitaxial solar cells. *Physica status solidi (a)*, 204:1340 – 1345, 2007.

[112] S. Uehara, K. Kurose, and T. Matsubara. Wide bandwidth porous silicon coatings for silicon. *Physica status solidi (a)*, 182:461 – 464, 2000.

[113] M. Lipinski, S. Bastide, P. Panek, and C. Levy-Clement. Porous silicon antireflection coating by electrochemical and chemical etching for silicon solar cell manufacturing. *Physica status solidi(a)*, 197:512 – 517, 2003.

[114] M. Lipinski, P. Panek, E. Beltowska, and H. Czternastek. Reduction of surface reflectivity by using double porous silicon layers. *Materials Science and Engineering B*, 101(1-3):297 – 299, 2003. EMRS 2002 Symposium S: Micro- and Nano-structured Semiconductors.

[115] J.-H. Kwon, S.-H. Lee, and B.-K. Ju. Screen-printed multicrystalline silicon solar cells with porous silicon antireflective layer formed by electrochemical etching. *Journal of Applied Physics*, 101:4515, 2007.

[116] R. Bilyalov, L. Stalmans, and L. Schirone. Use of porous silicon antireflection coating in multicrystalline silicon solar cell processing. *IEEE Transactions on electron devices*, 46, 1999.

[117] Y. S. Tsuo, Y. Xiao, M. J. Heben, X. Wu, F. J. Pern, and S. K. Deb. Potential applications of porous silicon in photovolatics. In *IEEE*, 1993.

[118] E. Vazsonyi, M. Fried, T. Lohner, M. Adan, T. Mohacsy, and I. Barsony. High efficiency silicon pv cells with surface treatment by anodic etching. In *Conf. Rec. 13th EC PVSEC*, pages 37 – 40, 1995.

[119] A. X. Coles, R. A. Gerhardt, and A. Rohatgi. Optimization of porous silicon reflectance for solar cell applications. In *Material Research Society Symposium Proceedings*, volume 426, pages 557 – 562, 1996.

[120] S. Strehlke, D. Sarti, A. Krotkus, K. Grigoras, and C. Levy-Clement. The porous silicon emitter concept applied to multicrystalline silicon solar cells. *Thin Solid Films*, 297:291 – 295, 1997.

[121] L. Schirone, G. Sotgiu, and F. P. Califano. Chemically etched porous silicon as an anti-reflection coating for high efficiency solar cells. *Thin Solid Films*, pages 296 – 298, 1997.

[122] L. Stalmans, J. Poortmans, H. Bender, M. Caymax, K. Said, E. Vazsonyi, J. Nijs, and R. Mertens. Porous silicon in crystalline silicon solar cells: a review and the effect on the internal quantum efficiency. *Progress in Photovoltaics: Research and Applications*, 6:233 – 246, 1998.

[123] S. Strehlke, S. Bastide, and C. Levy-Clement. Optimization of porous silicon reflectance for silicon photovoltaic cells. *Solar Energy Materials and Solar Cells*, 58:399 – 409, 1999.

[124] P. Panek, M. Lipinski, and H. Szternastek. Porous silicon layer as antireflection coating in solar cells. *Opto-electronics review*, 8:57 – 59, 2000.

[125] M. Lipinski, P. Panek, E. Bielanska, J. Weglowska, and H. Czternastek. Influence of porous silicon on parameters of silicon solar cells. *Opto-electronics review*, 8:418 – 420, 2000.

[126] S. Strehlke, S. Bastide, J. Guillet, and C. Levy-Clement. Design of porous silicon antireflection coatings for silicon solar cells. *Materials Science and Engineering: B*, 69:81 – 86, 2000.

[127] V. Yerokhov, I. Melnyk, A. Tsisaruk, and I. Semochko. Porous silicon in solar cell structures. *Opto-electronics review*, 8:414 – 417, 2000.

[128] R. J. Martin-Palma, L. Vazquez, P. Herrero, J. M. Martinez-Duart, M. Schnell, and S. Schaefer. Morphological, optical and electrical characterization of antireflective porous silicon coatings for solar-cells. *Optical Materials*, 17:75 – 78, 2001.

[129] C. C. Striemer and P. M. F Fauchet. Dynamic etching of silicon for solar cell application. *Physica status solidi*, 197:502 – 506, 2003.

[130] R. Chaoui and A. Messaoud. Screen-printed solar cells with simultaneous formation of porous silicon selective emitter and antireflection coating. *The Ninth Arab International Conference on Solar Energy (AICSE-9)*, 209:118 – 121, 2007.

[131] H.-C. Yuan, V. E. Yost, M. R. Page, P. Stradins, D. L. Meier, and H. Branz. Efficient black silicon solar cell with a density-graded nanoporous surface: Optical properties, performance limitations, and design rules. *Applied physics letters*, 95:123501, 2009.

[132] L. Remache, E. Fourmond, A. Mahdjoub, J. Dupuis, and M. Lemiti. Design of porous silicon/pecvd sio$_x$ antireflection coatings for silicon solar cells. *Materials Science and Engineering: B*, In Press, Uncorrected Proof, 2010.

[133] V. Skryshevsky. Thin film PV module. *Thin Solid Films*, 368:125 – 129, 2000.

[134] H. G. Tompkins and W. A. McGahan. *Spectroscopoc Ellipsometry and Reflectometry*. John Wiley & Sons, Inc., 1999.

[135] H. Fujiwara. *Spectroscopic Ellipsometry: Principles and Applications*. Wiley, 2007.

[136] J. A. Woollam Co. *User Manual: Guide to Using WVASE32. A Short Course in Ellipsometry*, 2001.

[137] T. Wagner, J. N. Hilfiker, T. E. Tiwald, C. L. Bungay, and S. Zollner. Materials characterization in the vacuum ultraviolet with variable angle spectroscopic ellipsometry. *Physica status solidi (a)*, 188:1553 – 1562, 2001.

[138] C. M. Herzinger, B. Johs, W. A. McGahan, J. A. Woollam, and W. Paulson. Ellipsometric determination of optical constants for silicon and thermally grown silicon dioxide via a multi-sample, multi-wavelength, multi-angle investigation. *Journal of Applied Physics*, 83 (6):3323 – 3336, 1998.

[139] J. A. Woollam. Optical constants provided by the wvase32 software under the layer name 'polysi-p'. Technical report, Woollam Co.

[140] E. D. Palik, editor. *Handbook of Optical Constants of Solids, I.* Academic Press, 1985.

[141] E. D. Palik, editor. *Handbook of Optical Constants of Solids, II.* Academic Press, 1991.

[142] M. Schubert. Polarization-dependent optical parameters of arbitrarily anisotropic homogeneous layered systems. *Physical Review B*, 53(8): 4265 – 4274, 1996.

[143] P. Petrik, É. Vázsonyi, M. Fried, J. Volk, G. T. Andrews, A. L. Tóth, Cs. S. Daróczi, I. Bársony, and J. Gyulai. Optical models for the ellipsometric characterisation of porous silicon structures. *Physica status solidi*, 2:3319 – 3323, 2005.

[144] D. A. G. Bruggeman. Berechnung verschiedener physikalischer konstanten von heterogenen substanzen. i. dielektrizitätskonstanten und leitfähigkeiten der mischkörper aus isotropen substanzen. *Annalen der Physik*, 416:665 – 679, 1935.

[145] L. A. A. Pettersson, L. Hultman, and H. Arwin. Porosity Depth Profiling of Thin Porous Silicon Layers by use of Variable-Angle Spectroscopic Ellipsometry: A Porosity Graded-Layer Model. *Applied Optics*, 37:4130 – 4136, 1998.

[146] U. Rossow, U. Frotscher, M. Thönissen, M. G. Berger, S. Frohnhoff, H. Munder, and W. Richter. Influence of the formation conditions

on the microstructure of porous silicon layers studied by spectroscopic ellipsometry. *Thin Solid Films*, 255:5 – 8, 1995.

[147] P. Petrik, M. Fried, E. Vazsonyi, T. Lohner, E. Horvath, O. Polgar, P. Basa, I. Barsony, and J. Gyulai. Ellipsometric characterization of nanocrystals in porous silicon. *Applied Surface Science*, 253:200–203, 2006.

[148] J. C. Maxwell Garnett. Colours in metal glasses and in metallic films. *Philosophical Transactions of the Royal Society A*, 203:385 – 420, 1904.

[149] M. Fried, O. Polgár, T. Lohner, S. Strehlke, and C. Levy-Clement. Comparative study of the oxidation of thin porous silicon layers studied by reflectometry, spectroscopic ellipsometry and secondary ion mass spectroscopy. *Journal of Luminescence*, 80(1-4):147 – 152, 1999.

[150] U. Frotscher, U. Rossow, M. Ebert, C. Pietryga, W. Richter, M.G. Berger, R. Arens-Fischer, and H. Mtinder. Investigation of different oxidation processes for porous silicon studied by spectroscopic ellipsometr. *Thin Solid Films*, 276:36 – 39, 1996.

[151] C. Wongmanerod, S. Zangooie, and H. Arwin. Determination of pore size distribution and surface area of thin porous silicon layers by spectroscopic ellipsometry. *Applied Surface Science*, 172(1-2):117 – 125, 2001.

[152] M. Fried, T. Lohner, O. Polgár, P. Petrik, É. Vázsonyi, I. Bársony, J. P. Piel, and J. L. Stehle. Characterization of different porous silicon structures by spectroscopic ellipsometry. *Thin Solid Films*, 276 (1-2):223 – 227, 1996. Papers presented at the European Materials Research Society 1995 Spring Conference, Symposium I: Porous Silicon: Material, Technology and Devices.

[153] M. G. Berger, S. Frohnhoff, R. Arens-Fischer, M. Thoenissen, C. Dieker, H. Muender, H. Lueth, W. Theiss, and M. Arntzen. Fabrication and properties of multilayer porous silicon filters. In F. Abeles, editor, *Society of Photo-Optical Instrumentation Engineers (SPIE) Proceedings*, volume 2253 of *Presented at the Society of Photo-Optical Instrumentation Engineers (SPIE) Conference*, pages 865 – 871, 1994.

[154] M. G. Berger, R. Arens-Fischer, M. Thönissen, M. Kruger, S. Billat, H. Luth, S. Hilbrich, W. Theiss, and Grosse P. Dielectric filters made of ps: advanced performance by oxidation and new layer structures. *Thin Solid Films*, 297:237 – 240, 1997.

[155] S. Billat. Influence of etch stops on the microstructure of porous silicon layers. *Thin Solid Films*, 297:22 – 25, 1997.

[156] J. Goldstein, D. E. Newbury, and D. C. Joy. *Scanning electron microscopy and x-ray microanalysis*. Springer, 2003.

[157] D. B. Williams and C. B. Carter. *Transmission electron microscopy: a textbook for materials science*. Springer, 1996.

[158] H. H. Rose. Optics of high-performance electron microscopes. *Science and Technology of Advanced Materials*, 9(1):014107, 2008.

[159] http://www.casaxps.com. *Casa XPS*, 2010.

[160] D. Briggs. *Surface analysis of polymers by XPS and static SIMS*. Cambridge University Press, 1998.

[161] L. J. Geerligs and D. Macdonald. Base doping and recombination activity of impurities in crystalline silicon solar cells. *Progress in Photovoltaics: Research and Applications*, 12(4), 2004.

[162] N. Stem and M. Cid. Studies of phosphorus Gaussian profile emitter silicon solar cells. *Materials Research*, 4:143 – 148, 2001.

[163] M. C. Sanchez and S. Nair. Phosphorus emitter and metal - grid optimization for homogeneous (n+p) and double-diffused (n++n+p) emitter silicon solar cells. *Materials Research*, 12:57 – 62, 2009.

[164] V. D. Mihailetchi, Y. Komatsu, G. Coletti, R. Kvande, L. Arnberg, C. Knopf, K. Wambach, and L. J. Geerligs. High efficiency industrial screen printed n-type solar cells with front boron emitter. In *Photovoltaic Specialists Conference, 33rd IEEE*, pages 1 – 5, 2008.

[165] J. E. Cotter, J. H. Guo, P. J. Cousins, M. D. Abbott, F. W. Chen, and K. C. Fisher. P-type versus n-type silicon wafers: Prospects for high-efficiency commercial silicon solar cells. *Electron Devices, IEEE Transactions on*, 53(8):1893 –1901, 2006.

[166] R. Kopecek, T. Buck, J. Libal, I. Rover, K. Wambach, L. J. Geerligs, P. Sanchez-Friera, J. Alonso, E. Wefringhaus, and P. Fath. Large area screen printed n-type silicon solar cells with rear aluminium emitter: Efficiencies exceeding 16%. In *Conference Record of the 2006 IEEE 4th World Conference on Photovoltaic Energy Conversion*, volume 1, pages 1044 – 1047, 2006.

[167] V. D. Mihailetchi, Y. Komatsu, and L. J. Geerligs. Nitric acid pretreatment for the passivation of boron emitters for n-type base silicon solar cells. *Applied Physics Letters*, 92(6):063510, 2008.

[168] T. Buck, R. Kopecek, J. Libal, A. Herguth, K. Peter, I. Röver, K. Wambach, and B. Geerligs. Industrial screen printed n-type silicon solar cells with front boron emitter and efficiencies exceeding 17%.

[169] H. Sakata, T. Nakai, T. Baba, M. Taguchi, S. Tsuge, K. Uchihashi, and S. Kiyama. 20.7% highest efficiency large area (100.5 cm^2) hit cell. In *Photovoltaic Specialists Conference, 2000. Conference Record of the Twenty-Eighth IEEE*, pages 7 – 12, 2000.

[170] W. P. Mulligan, D. H. Rose, M. J. Cudzinovic, and D. M. De Ceuster. Manufacture of solar cells with 21% efficiency. In *Proc. 19th EUPVSEC*, pages 387 – 390, 2004.

[171] F. Ronkel and J. W. Schultze. Electrochemical aspects of porous silicon formation. *Journal of Porous Materials*, 7:11 – 16, 2000.

[172] A. Pascual, J. F. Fernandez, and C. R. Sanchez. Nucleation and growth of pores and photoluminescence in p-type porous silicon. *Journal of Applied Physics*, 92(2):866, 2002.

[173] S. Rørkjær. *Porous Silicon Backside Reflectors for Very Thin Silicon Solar Cells*. The Norwegian University of Tehcnology and Natural Sciences (NTNU), 2010.

[174] J. Penczek and R. L. Smith. The relationship of porous silicon film morphology to the photoluminescence spectra. In *Materials Research Society Symposium Proceeding*, volume 298, 1993.

[175] D. Navarro-Urrios, C. Pérez-Padróna, E. Lorenzoa, N. E. Capuja, Z. Gaburrob, C. J. Otonb, and L. Pavesi. Chemical etching effects in porous silicon layers. In *Proceedings of SPIE*, volume 5118, 2003.

[176] D. Brumhead, L. T. Canham, D. M. Seekings, and P. J. Tufton. Gravimetric analysis of pore nucleation and propagation in anodised silicon. *Electrochimica Acta*, 38:191 – 197, 1992.

[177] D. Buttard, D. Bellet, G. Dolino, and T. Baumbach. Thin layers and multilayers of porous silicon: X-ray diffraction investigation. *Journal of Applied Physics*, 83(11):5814 – 5822, 1998.

[178] P. Granitzer and K. Rumpf. Review porous silicon - a versatile host material. *Materials*, 3:943 – 998, 2010.

[179] L.-A. O'Hare, B. Parbhoo, and S. R. Leadley. Development of a methodology for xps curve-fitting of the si 2p core level of siloxane materials. *Surface and Interface Analysis*, 36:1427 – 1434, 2004.

[180] W. Weiss and I. Stadler. Façade integration, a new and promising opportunity for thermal solar collectors. In *Proceedings of the Industry Workshop of the IEA Solar Heating and Cooling Programme*, 2001.

[181] K. Mangersnes. *Back-contacted back-junction silicon solar cells*. PhD thesis, University of Oslo, 2010.

I

II

III

Thin porous silicon films displaying a near-surface dip in porosity

J. H. Selj[a], A. Thøgersen[a], P. L. Bergstrom[b], S. E. Foss[a] and E. S. Marstein[a]

[a] Solar Energy Department, Institute for Energy Technology, 2003 Kjeller, Norway
[b] Department of Electrical and Computer Engineering, Michigan Technological University, Houghton MI 49931, USA

Studies of the depth profile of Porous Silicon (PS) structures etched under a wide span of different formation parameters have been performed using Spectroscopic Ellipsometry (SE) and Transmission Electron Microscopy (TEM). Incorporation of a sharp dip in the porosity profiles close to the sample surface was required for several types of PS films in order to successfully fit ellipsometric data to a Bruggeman Effective Medium Model (BEMA). TEM studies show a corresponding lower porosity region near the sample surface. Investigations have been performed in order to understand the origin of this dip and to explore the parameter space where it is detected. The detected low porosity region is discussed in the context of current knowledge on pore nucleation and growth mechanisms of PS.

Introduction

The simplicity of processing porous silicon (PS) layers is in stark contrast to the complexity of the fundamental questions regarding its formation mechanisms. Although a vast amount of literature is published on the subject, a number of challenging questions still remains, such as the exact dissolution chemistries of silicon and the origin of pore initiation (1, 2).

Ellipsometry is a versatile tool, well suited for detailed characterization of complex structures such as PS. It is well known that the optical properties of mesoporous silicon can be modelled as a mix of Si and air in an effective medium approximation (EMA) (3). From such modelling, a porosity depth profile can be obtained. During the development of multilayer PS antireflection coatings (ARC) for solar cell applications (4), incorporation of a sharp dip in the porosity profile close to the sample surface was required for several types of PS films in order to successfully fit ellipsometric data to a Bruggeman EMA model (5). As the dense PS region is located near the surface, it is natural to investigate whether its origin is in the pore initiation process.

Relatively little literature exists on the field of pore nucleation and early PS growth, but a few models have been proposed. Only early theory assumed pore nucleation to be caused by etching defects at the Si surface. This is now regarded as unlikely due to the difference in scale between etching defect densities and pore density (6). Pore formation due to instability of the semiconductor-electrolyte interface was suggested by Valence (7, 8). However, this theory does not provide a satisfactory explanation of the chemical etching mechanisms of PS (6). Goryachev, et al. (6) presented a model where the H-

terminated Si^{+2} ions at the surface react with each other to produce secondary neutral Si and Si^{+4} ions. The secondary neutral Si atoms will then be adsorbed at the Si surface and form aggregates with resistivities that exceed that of the initial Si.

Without proposing a complete formation model, Brumhead, et al. (9) made an effort to relate the preparation parameters to the pore growth kinetics. They reported a non-linear growth of PS at short anodisation times, before a linear, stable pore growth was reached after about 1 minute. This general growth development is now relatively well established (10-13). According to Brumhead, et al. (9), if the valence of a reaction remains the same, the total mass loss rate will, according to Faraday's law, be constant. Consequently, at low porosity, initial pore growth is fast before a balanced, slower growth with larger porosities take over. Brumhead, et al. (9) proposed three possible explanations for the fast initial pore growth mechanism: (i) each individual pore could be initiated at $t = 0$ with a small cross section, and expand as it grows into the substrate; (ii) the number of pores initiated at $t = 0$ could be small but multiply quickly by branching; and (iii) at $t = 0$ a few pores are generated, and their number increase steadily by further continuous generation at the surface until they are close enough together for carrier depletion to prevent any more pores being formed. By this argumentation, in model (iii) the porosity of the pore initiation region would in time be the same as for the bulk PS layer. Model (i) and (ii) are believed by Brumhead, et al. (9) to inhibit flow of chemicals into the pores, thereby preventing continued growth, and model (iii) was therefore proposed as the most likely mechanism. The formation time necessary to complete the PS nucleation process is proposed to last from a few seconds (14) to 2.5-3 minutes (9,10).

Ronkel and Schultze (14) used highly time resolved voltage transients to study the pore initiation of PS. They performed a detailed analysis of electrochemical conditions and response times related to pore nucleation on substrates and electrochemistries similar to those studied in this work. Their analysis of the initial response during galvanostatic conditions show characteristic regions in the electrochemical dynamics related to double-layer formation in the first 30 μs, space charge region formation in the following 100 ms, pore nucleation in the following 3–10 s, depending on current density and HF concentration, and pore etching following that period. Pascual, et al. (15) argue that nucleation of pores takes place during the first minutes of the anodization, but is less detectable after the first seconds because after that time pore propagation has also started. Pascual, et al. (15) further describe PS growth kinetics with equations similar to those used to describe nucleation and growth of new phases in condensed matter.

The picture of pore nucleation in PS emerging from these theories is incomplete and somewhat contradictory and demonstrates that further work is needed to resolve this complex issue. In the work presented here, we have performed studies of the depth profile of PS structures etched under a wide span of different formation parameters. Structural information has been obtained by spectroscopic ellipsometry and TEM studies. Investigations were performed in order to understand the origin of the observed dense PS region, and place it in the context of the current understanding of pore nucleation.

Experimental

The samples are fabricated using a double cell anodic etching system PSB Plus 4 from Advanced Micromachining Tools (AMMT). The electrolyte consisted of 49 wt.–% HF and ethanol (C_2H_5OH), mixed in volume ratios of 1:4, 3:7, and 2:3. The resulting HF concentrations are stated as 10%, 15%, and 20%, respectively. The wt.–% HF concentrations will be slightly higher than this since the density of HF is larger than that of ethanol. The substrates used were boron doped, 300–350 μm thick, single side polished, monocrystalline silicon with (100) orientation. PS is formed on the polished side of the wafer. The resistivity was determined by four point probe to be 0.012–0.018 Ω·cm. Immediately prior to etching, the wafers were dipped in 5% HF to remove native oxide.

Samples were etched at several different current densities, etching times, and HF concentrations. Ellipsometry measurements were carried out using a Woollam variable angle spectroscopic ellipsometer (VASE) in the wavelength range 300–1100 nm for four different angles of incidence. Depolarization data was also obtained in the measurements. The ellipsometric software WVASE32 from Woollam is used for modelling. Cross-sectional Transmission Electron Microscopy (TEM) samples were prepared by ion-milling using a Gatan precision ion polishing system with 5 kV gun voltage. TEM and Energy Filtered TEM (EFTEM) images were acquired using a 200 keV JEOL 2010F microscope with a Gatan imaging filter and detector. EFTEM images were acquired by placing a 2 eV slit around the plasmon energy of Si (16.8 eV).

Characterization

Ellipsometry

The BEMA gives a good approximation for mesoporous silicon and was used for all ellipsometric modelling in this work (16, 17). TEM images of the PS layer surface show that the PS layers fabricated in this work are indeed mesoporous. The expected porosity profile of a PS film etched on a homogeneous substrate at constant current density would typically be relatively flat, except for a region of gradually decreasing porosity towards the Si interface and a transition region between PS, oxide, and air, towards the surface. We would expect this surface structure to give a lower refractive index than the bulk PS layer.

Instead of adding separate interface layers to model these transition regions, a grading is introduced in the BEMA (17). The best fit models in this work show the anticipated porosity decrease at the PS/Si interface and the porosity increase at the surface. Surprisingly, the best fit models also display a significant lowering of the porosity in a thin region just below the surface. The feature improves the quality of the fit for all measured samples of low and intermediate porosity.

Figure 1.1a, 1.2a, and 1.3a show the porosity profiles obtained from the best fit ellipsometry models for three samples of different porosity. Sample 1.1 is etched at 20 mA/cm^2, corresponding to an average porosity of 45%. Figure 1.2 is etched at 50

mA/cm^2, corresponding to an average porosity of 59%. The sample in Fig. 1.3 is etched at 50 mA/cm^2 at a slightly higher HF concentration than the previous, resulting in a porosity of 53%. The denser PS region appears as a dip in the displayed porosity profiles. The fit of the ellipsometry models is very sensitive to the existence of this porosity dip. However, with respect to the exact shape and position of the porosity dip it should be considered that the porosity is a modelled profile with limited resolution and a fixed number of nodes (points where the porosity is allowed to change). As the total number of nodes and steps are kept constant, models of very thick PS layers will expectedly be less accurate due to poorer resolution.

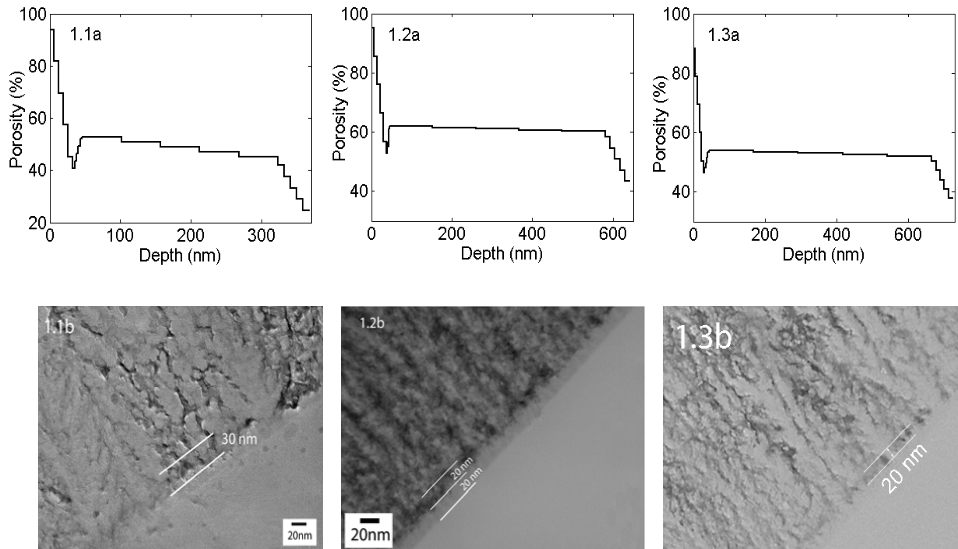

Figure 1. Porosity profile determined from ellipsometry (a) with a corresponding TEM image (b) in an electrolyte containing 20 % HF. The samples are etched at 1.1) 20 mA/cm^2 giving a porosity of 45%, 1.2) 50 mA/cm^2 giving a porosity of 59%, and 1.3) 50 mA/cm^2 at a slightly higher HF concentration, resulting in a porosity of 53 %.

TEM investigations

Figure 1.1b, 1.2b, and 1.3b show the TEM images corresponding to the porosity profiles in Fig. 1.1a, 1.2a, and 1.3.a, respectively. In the TEM images a thin, slightly darker region of the PS layer can be seen towards the PS/air interface. The darker areas correspond to a higher density of Si and hence lowered porosities. It can be seen that the depth of the dense regions roughly corresponds with the depth of the lower porosity regions visible in the ellipsometry porosity profiles. In Fig. 2, the ellipsometry porosity profile is overlaid a TEM image of the same sample. The correlation between the dense region in the TEM and in the ellipsometry profile is fairly good. Small shifts in position can be due to sample inhomogeneities, since TEM and ellipsometry are not performed on the same spot on the sample, or inaccuracies in the ellipsometry model. The dense PS layer is seen to be located at a depth of 20 - 40 nm from the sample surface.

Figure 3 shows a structure where the dense PS region is difficult to see in the regular TEM image, but in the bright field image (b) and EFTEM image filtered at the plasmon energy of Si (16.8 eV) (c), it is clearly visible. The transition between the densified region and the deeper PS layer of constant porosity appears gradual.

TEM images filtered at an energy of 16.8 eV, corresponding to the plasmon peak of Si, show that the topmost region of the PS layer (light grey in the TEM images) is predominantly composed of SiO_2. This layer, typically 20 - 30 nm thick, is likely too thick and uniform in profile to represent ambient oxidation of the surface Si nanocrystallites, leaving the anodic electrochemical oxidation kinetics during the initial pore formation the dominant mechanism for the formation of this layer (14, 18, 19). In the ellipsometric depth porosity profile, the oxide is modelled by the sharp decrease in refractive index near the sample surface. A separate SiO_2 layer may be added, but does not result in a significant improvement in the model.

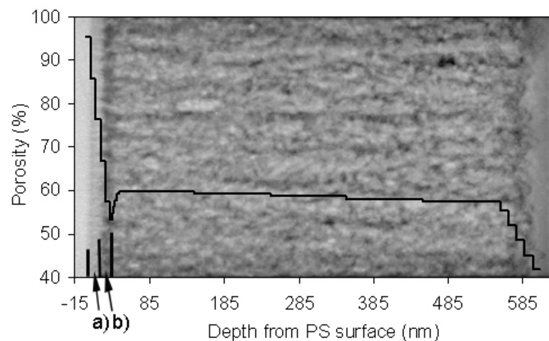

Figure 2. Ellipsometry porosity profile overlaid TEM image of the same sample. A correspondence between the dense PS region in the TEM image and the porosity dip in the ellipsometry porosity profile is seen. The region marked as a) is the oxide, and b) is the dense PS layer.

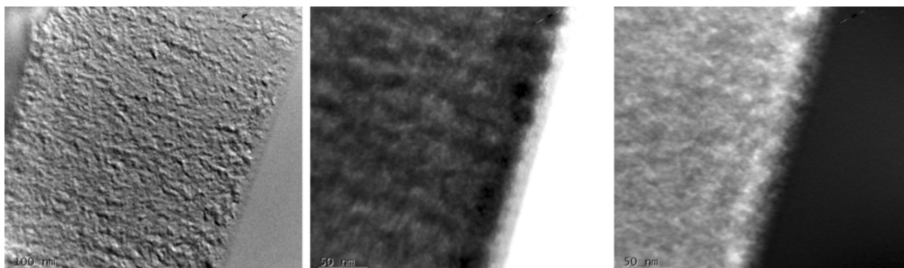

Figure 3. a) TEM image, b) bright field image, c) energy filtered image (16.8 eV).

Dependence of the Porosity Dip on the Parameter Space

Time Dependence

Figure 4 shows the topmost 80 nm of the best fit porosity profiles of four layers etched under nominally identical conditions except for variations in the etching time. The

sample in Fig. 4a is etched for 30 s, 4b is etched for 90 s, 4c is etched for 180 s, and 4d for 300 s. There are small variations between the PS layers but no significant changes in the profile of the porosity dip occur with increasing etching time. A slight increase of a few percent in average porosity of the bulk PS layer can be seen from a) to d). This is likely due to the purely chemical etching of the PS layer. This weak etching takes place simultaneously with the electrochemical etching, but is independent of applied bias.

Since no time dependence of the porosity profiles is found, we regard it as unlikely that pores continue to nucleate at the surface until the surface layer would reach the same porosity as the rest of the layer, at least for p^+ substrates. A possible explanation of the initial fast pore growth could instead be pore widening and/or porosity increase by branching. These models would be compatible with the observed dense PS region which remains even after long etching times. A TEM image of an 18 μm thick PS layer presented by Solanki, et al. (11) displays a clear porosity dip, supporting the view that the dense PS layer does not disappear with increasing etching time.

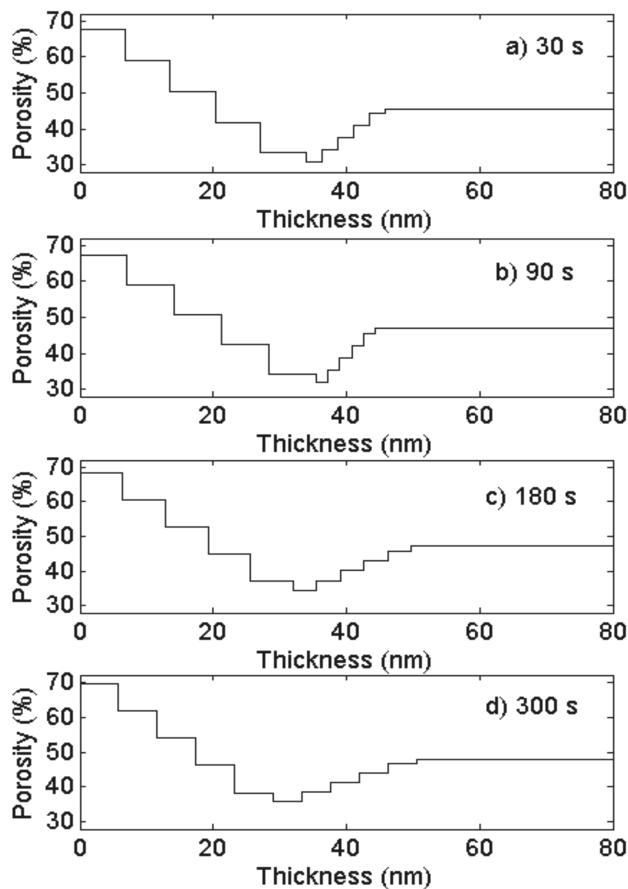

Figure 4. Evolution of the porosity dip in time. Porosity profiles from best fit ellipsometry model on samples etched at 15 mA/cm^2 in 20 wt% HF for different times; a) 30 s, b) 90 s, c) 180 s, and d) 300 s. Note that the full width of the PS layers is not shown. The thickness of the layers is approximately a) 530 nm, b) 1730 nm, c) 3550 nm, and d) 5710 nm.

HF Concentration and Current Density Dependence

Electrolyte with 20% HF. For samples etched in 20% HF at current densities higher than ~100 mA/cm^2, no dip is seen in the ellipsometry models. For lower current densities, a dip is seen both in TEM images and in the ellipsometric profiles. Figure 5 shows how the porosity dip is reduced with increased current density. Three porosity profiles are shown, from samples etched at 10 mA/cm^2, 50 mA/cm^2 and 100 mA/cm^2 corresponding to average porosities of 38%, 55%, and 64% respectively. All samples in Fig. 5 are etched in an electrolyte containing 20% HF.

Electrolyte with 15 wt% HF. At HF concentrations of 15% only ellipsometry measurements have been conducted. A dip is clearly evident in the porosity profile of two samples etched at constant current densities of 1 and 5 mA/cm^2, corresponding to average porosities of 38% and 52 % respectively.

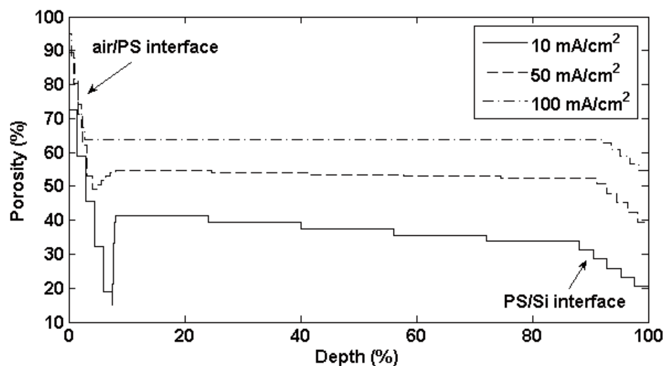

Figure 5. Porosity profile determined from ellipsometry of samples etched at three different current densities for 20 wt.–% HF. Note that the depth is percentual and that these three layers are not of equal thickness; the sample etched at 10 mA/cm^2 is 414 nm thick, the sample etched at 50 mA/cm^2 is 658 nm thick and the sample etched at 100 mA/cm^2 is 977 nm thick.

Electrolyte with 10% HF. For samples etched in an electrolyte containing 10% HF, both TEM studies and ellipsometry have been performed. Fig. 6a shows a TEM image of a sample etched at 7.5 mA/cm^2 (~73% porosity) and a PS thickness of approximately 300 nm. A TEM image of the sample etched at 20 mA/cm^2 (~77% porosity), with a PS thickness of approximately 580 nm, is shown in Fig. 6b. Neither the TEM images nor the ellipsometric characterization show any signs of a dense PS region for these samples.

Porosity. In contrast to the 20% HF electrolyte, all p$^+$ substrates etched in 10% HF electrolytes have very high porosity (>70%). Since the existence of the dense PS region is sensitive both to HF concentration and current density, the common denominator appears to be variation in porosity. Both reduced HF concentration and increased current density lead to high porosity and a PS structure without a densified region close to the surface.

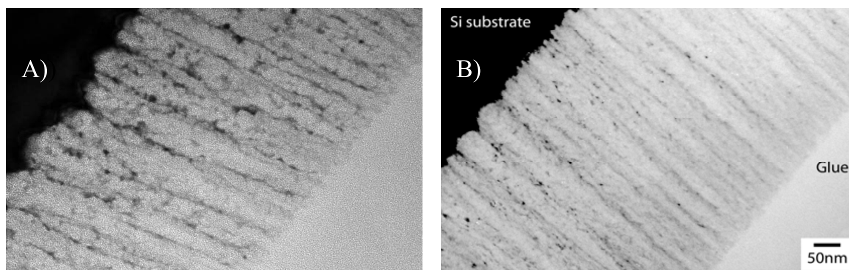

Figure 6. TEM images of PS samples etched at a) 7.5 mA/cm^2 and b) 20 mA/cm^2 in an electrolyte containing 10% HF.

Formation Kinetics

The concentration and current density dependence in the formation of the dense surface PS region and surface oxide likely relate to the electrochemical reaction kinetics during pore growth, as earlier noted. The period of pore nucleation proposed by Ronkel and Schultze (14), 3-10 s, represents an approximate timeframe to produce the 20-30 nm thick dense PS layer found in this work.

Analysis by van den Meerakker and Mellier (18) explored the kinetic and diffusional aspects in silicon etching in HF containing solutions utilizing rotating disk electrodes, and found a mix of kinetic and diffusional control of the dissolution of silicon, as Carstensen, et al. (19) and others have proposed in modelling PS formation mechanisms. We propose that the pore nucleation period described by Ronkel and Schultze (14) may represent a transitional electrochemical condition from a kinetic dominated surface reaction dissolution to a mixed kinetic/diffusional electrochemical dissolution as the concentration of reactive species adjusts to the diffusion limitations imposed by the nanoscaled pore confinement. Both the current density and electrolyte concentration dependence on the formation of the dense PS region demonstrated in this work are reflected in this analysis, since higher current densities and lower electrolyte concentrations will each shift the dynamics of the reaction by modifying the space charge layer formation and thickness and the kinetic/diffusion rate balance.

Conclusions

We have shown that for p^+ type Si wafer etched with a relatively low current density, there exists a surface PS layer of lower porosity than the remaining PS structure. The dense PS region remains present after etching at a current density of 15 mA/cm^2 for 5 minutes. Therefore, the initial pore nucleation in PS either takes longer time than what has been suggested in current formation theories (a few seconds – 2.5-3 minutes) or formation of new pores stops before bulk PS porosity is reached. The pore growth and propagation can therefore not likely be explained by the fast growing model (iii) as suggested by Brumhead, et al. (9). Pore widening and/or porosity increase by branching may instead be the responsible mechanisms. The observed structure of a dense PS layer (and thick SiO_2) layer might be due to a change in formation mechanism, from a kinetic dominated surface reaction dissolution to a mixed kinetic/diffusional electrochemical dissolution.

Acknowledgments

This work has been funded by the Research Council of Norway through the project "Thin and highly efficient silicon-based solar cells incorporating nanostructures," NFR Project No. 181884/S10.

References

1. R. L. Smith and S. Collins, *J. Appl. Phys.*, 7**1** (1992).
2. X. G. Zhang, *J. Electrochem. Soc.* **151** (2004).
3. U. Rossow, U. Frotscher, M. Thonissen, M. G. Berger, S. Frohnhoff, H. Munderb, and W. Richter, *Thin Solid Films,* **255,** 5 (1995).
4. J. H. Selj, A. Thøgersen, S. E. Foss, and E. S. Marstein, *J. Appl. Phys.* **107,** (2010).
5. D. A. G. Bruggeman, *Ann. Phys.* **416,** 665 (1935).
6. D. N Goryachev, L. V. Belyakov, and O. M. Sreseli, *Semiconductors* **34**, 1090 (2000).
7. A. Valence, *Phys. Rev. B*, **52**, 8323 (1995).
8. A. Valence, *Phys. Rev. B*, **55**, 9706 (1997).
9. D. Brumhead, L. T. Canham, D. M. Seekings, and P. J. Tufton, *Electrochimica Acta,* **38**, 191 (1993).
10. A. Pascual, J. F Fernandez, C. R. Sanchez, *J. Appl. Phys*, **92**, 866 (2002).
11. C. S. Solanki, R. R. Bilyalov, J. Poortman, G. Beaucarne, K. Van Nieuwenhuysen, J. Nijs, and R. Mertens. *Thin Solid Films* 451-452, **649** (2004).
12. D. Buttard, D. Bellet, G. Dolino, and T. Baumbach. *J. Appl. Phys.* **92**, 866 (2002).
13. P. Granitzer and K. Rumpf. *Materials* **3**, 943 (2010).
14. F. Ronkel and J. W. Schultze, *J. Por. Mat.* **7**, 11 (2000).
15. A. Pascual, J. F Fernandez, C. R. Sanchez, S. Manotas and F. Agullo-Rueda, *J. Por. Mat.*, **9**, 57 (2002).
16. D. Kovalev et al., *Appl. Phys. Lett.* **78,** 916 (2001).
17. L. A. A. Petterson et al., *Appl. Opt.* **37,** 4130 (1998).
18. J. E. A. M. van der Meerakker and M. R. L. Mellier, *J. Electrochem. Soc.* **148**, G166 (2001).
19. J. Carstensen et al., *J. Electrochem. Soc.* **146**, 1134 (1999).

IV

Ellipsometry, Reflectometry, and XPS Comparative Studies of Oxidation Effects on Graded Porous Silicon Antireflection Coatings

J. H. Selj[a], A. Thøgersen[a], E. S. Marstein[a]

[a] Solar Energy Department, Institute of Energy Technology, 2007 Kjeller, Norway.

Efficient antireflection coatings (ARC) improve the light collection and thereby increase the current output of solar cells. By simple electrochemical etching of the Si wafer, porous silicon (PS) layers with excellent broadband antireflective properties can be fabricated. The close relation between porosity and refractive index, modeled using the Bruggeman effective medium approximation, allows PS multilayers to be tailored to fabricate ARCs optimized for use in solar cells. In this work, the effect of ageing on the reflectance properties of multilayered PS ARCs is studied. The reflectance is correlated to the oxidation of the structures through the use of x-ray photoelectron spectroscopy (XPS) and spectroscopic ellipsometry (SE). It is found that even after extensive oxidation, very small changes in reflectance are measured.

Introduction

It is well known that PS surface layers can drastically reduce the reflectance from Si wafers, by acting as an antireflection coating (ARC). Reduction of optical losses is of principal importance in Si solar cells and cost-efficient processes are particularly sought after. PS can offer both. It is commonly formed by electrochemical etching of Si in an electrolyte containing hydrofluoric acid (HF). The structure is very sensitive to etching parameters such as current density, electrolyte composition, temperature and substrate doping. Variation of current density during etching results in controllable variations in porosity, which again can be related to the refractive index of PS by effective medium approximations (EMA) (1). This gives us a unique opportunity to tailor refractive index profiles and create broadband ARCs applicable to solar cells. We have previously shown that graded PS ARCs with an effective reflection of ~3 % over the solar spectrum can be produced (2).

For PS to become an attractive alternative to today's ARCs, the excellent optical properties must not degrade with ageing of the structures. Due to the very high internal surface area, 200-600 m^2/cm^3 (3), PS is significantly more reactive than bulk Si. Extensive oxidation occurs even in air ambient at room temperature, but very large variations with respect to the porosity, morphology, thickness, and storage of the PS structures are observed (4). During this natural oxidation process, some of the passivating Si-H surface bonds of freshly etched PS are replaced by Si-O bonds. Oxidation also takes place by formation of Si-OH groups which do not affect the original hydrogen passivation (5).

The ageing process changes not only the electrical, but also the optical properties of PS. Reflectance from PS multilayers will be modulated due to changes in the dielectric function caused by oxidation. When the effect of ageing on optical properties of PS has been described, focus has generally been on changes in the photoluminescent properties (6-8). A few notable exceptions are Frotscher et al. (9) and Fried et al. (10), where SE and reflection measurements are used to study refractive index and reflectance. Fried et al. investigated thin, homogeneous PS layers etched in n^+ emitters. Frotscher et al. studied both single PS layers and thick Bragg type multilayers consisting of alternating layers of two different porosities.

Our aim is to study the effect of ageing on reflectance from multilayered PS ARCs applicable to solar cells. The multilayered structures are etched in highly p-doped Si, which is suitable for production of solar cell ARCs in a p^+/n structure. The refractive index of the film varies in a graded manner, but with some sharp features appearing in the optimized coating due to the restrictions placed on porosity range (25 - 75 %) and thickness (~160 nm) (2, 11). Cost efficiency is of great importance in the solar cell industry. Therefore, we use the simplest, most easily implemented form of drying and storage; air at room temperature.

Attention is also given to how ageing of PS is perceived in spectroscopic ellipsometry (SE) measurements. SE is extensively used to characterize PS structures, and oxidation of the inner surface is routinely neglected in the majority of cases found in literature (12-13).

Experimental

The samples are fabricated using a double cell anodic etching system PSB Plus 4 from advanced micromachining tools (AMMT). A special purpose potentiostat, PS2 from AMMT, allowed programming of current density profiles with a time resolution of 50 ms. The electrolyte consisted of 49 wt % HF and ethanol (C_2H_5OH) in a volume ratio 2:3, giving a HF concentration of 20%. The wafers used were boron doped, 300–350 μm thick, one side polished, monocrystalline Si with a (100) orientation. PS is formed on the polished side of the wafer without any additional texturing. The resistivity of the wafers was determined by four point probe to be 0.012–0.018 Ωcm. Prior to etching, the wafers were dipped in 5% HF to remove native oxide.

In order to simplify the identification and quantification of oxidation effects from the SE measurements, homogeneous PS layers were used. Five homogeneous PS samples were etched under galvanostatic conditions, at a current density of 50 mA/cm^2 for 15 s. The etching of the graded PS ARC structure is also performed in galvanostatic mode, by stepwise variation of the current density. Details of the procedure, such as the duration and current density of each step are described elsewhere (2). Only the current density during etching is different for the homogeneous and multilayered samples and the average porosities of the two are similar (in excess of 50%).

The first homogeneous sample ('Day 0') was rinsed in water, dried in N_2 and stored in aluminium foil during transportation to the XPS. This was done in order to achieve a minimally oxidized starting sample. All remaining samples were rinsed in

ethanol, air dried and stored in room temperature and air ambient. Ethanol has a reduced surface tension compared to water and therefore reduces the risk of surface cracking and flaking of the PS films.

Due to destructive sample preparation and ion beam etching for the XPS measurements, one single sample could not be used for all measurements. Five nominally identical PS samples were therefore used for SE and XPS. We have previously shown that the PS layers are reproducible to within an uncertainty of 1.5 % (90 % confidence limit) in thickness and porosity (14).

The ageing of the structures are studied by XPS, SE and spectroscopic reflectometry. Ellipsometry measurements were carried out using a Woollam variable angle spectroscopic ellipsometer (WVASE) in the wavelength range 300–1200 nm and at the angles of incidence 60°, 65°, 70°, 75°, and 80°. Depolarization data is also collected for all samples. XPS was performed in a KRATOS AXIS ULTRA^{DLD} using monochromated Al K_α radiation ($h\nu$ =1486.6 eV) on plane-view samples at zero angle of emission (vertical emission). The x-ray source was operated at 1 mA and 15 kV. The XPS spectra of bulk PS have been obtained after sputtering down to a depth of about 100 nm. Sputtering was performed using a 4 kV ion gun, with a current of 100 μA and a 500s cycle time. The mean free path (λ) of Si-2p electrons in Si is 3.18 nm. This means that the photoelectron escape depth in Si is $3\lambda\cos(\theta)$ = 9.65 nm. However, with a porosity of ~50%, the photoelectron escape depth is calibrated to be ~19 nm. The spectra were peak fitted using Casa XPS (15) after subtraction of a Shirley type background. Finally, reflectance was measured using a Standford Research System setup in the wavelength range 400–1100 nm.

Results and Discussion

Characterization by Spectroscopic Ellipsometric

It is well known that PS can be modelled as a mix of Si and voids in an effective medium approximation (EMA) (1, 16). SE is capable of in depth resolution and accurate determination of the optical constants. In this work, a uniaxially anisotropic, graded Bruggeman effective medium model (BEMA) (17) consisting of crystalline Si (18), polycrystalline Si (19) and air (n=1) is used to fit data obtained from ellipsometric measurements of the homogeneous layers. It has previously been shown that the use of polycrystalline silicon as an EMA component significantly improves the fit quality (12, 20). The component is used to model the enhanced absorption at the boundaries of the nanocrystals.

The grading in the BEMA is introduced to account for roughness in the transitions between air/PS and PS/Si. This allows a higher resolution in depth and possible grading in the main layer can also be accommodated.

Figure 1 shows ellipsometric measurements and corresponding fits for one of the homogeneous layer PS samples. Ellipsometric measurements of all the samples are carried out within 1 day after the etching and then repeated after the samples have aged for 7, 21, and 42 days, respectively. The model fits are very good for all samples.

An initial rapid oxidation is reported to occur already after some tens of minutes (5). Therefore, even the first SE measurements are not performed on completely non-oxidized PS. Figure 2 shows the refractive index with depth in the PS layer at day 1 and day 42. The layers are birefringent, so the refractive indices in both x- and z- (normal to the sample surface) directions are shown. As there is only one axis of anisotropy, the refractive index in the y-direction is identical to the x-direction and is not shown. In both directions, a small reduction in the refractive index is observed from day 1 to day 42.

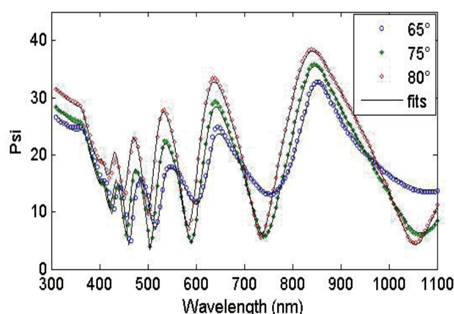

Figure 1. The fit of the ellipsometric model for one of the homogeneous layer PS samples.

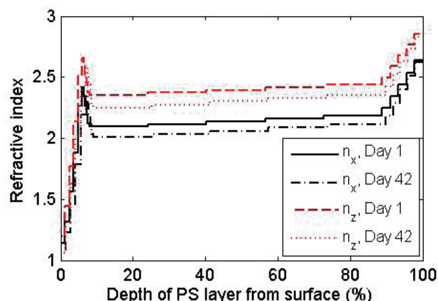

Figure 2. Change in refractive indices from day 1 to day 42.

The average porosity and thickness of the samples determined from ellipsometry are given in Table I. The average porosity appears to increase slightly with increasing ageing, about 2 % absolute after 42 days. The apparent increase in porosity is relatively modest and generates only a small change in the reflectance of these samples. A significant part of the Si is polycrystalline. The remaining part (not shown) is c-Si. An increase in the poly-Si amount also results form ageing. The increase is larger than it first appears, since the total fraction of Si decreases. This might reflect the reduction of the pore wall thickness due to oxidation. Adding SiO_2 in the ellipsometric modeling does not improve the fit of any of the samples.

TABLE I . Values determined from ellipsometry

Sample	Porosity, Day 1	Poly-Si, Day 1	Porosity, Aged	Poly-Si, Aged
Sample 2, aged 1 day	56,8 %	15,4 %	--	--
Sample 3, aged 7 days	56,1 %	13,8 %	56,7 %	14.2 %
Sample 4, aged 21 days	56,5 %	13,6 %	57,6 %	16.1 %
Sample 5, aged 42 days	56,6 %	16,0 %	58,6 %	19.6 %

X-ray Photoelectron Spectroscopy (XPS)

The composition of aged PS is highly complex. A large number of compounds have been detected, including the compounds Si_2O, SiO, Si_2O_3, and SiO_2, also commonly found in oxidized Si samples (5, 21, 22). Additional compounds that have been reported from XPS studies include Si-OH and SiO_2-OH (5), SiH_x (x = 1, 2, 3) groups (23), $(CH_3CH_2)_3SiOH$ (22) and amorphous Si (Si:H) (22). In addition, fluorine (SiF) (24) and carbon (5) impurities have been repeatedly detected. However, it is important to

emphasize that the oxidation effects vary greatly with respect to the porosity, morphology and thickness of the PS structures. Even for nominally very similar samples, the differences can be surprisingly large (4). The large number of possible compounds together with the small binding energy shifts in the Si 2p core level (covering a range of only 4 eV), complicates the task of resolving distinct features by curve-fitting of the XPS spectra (25).

We have performed detailed peak fitting of high resolution XPS Si-2p spectra from the PS surface and PS bulk. The deviation in binding energy measurement is about 0.02 eV, while for the composition the deviation is 0.4 atomic %, determined experimentally. Five samples, aged for 0, 1, 7, 21 and 42 days, respectively, are studied. Figure 3 shows the peak fitted XPS spectrum from the PS bulk of the 'Day 0' sample. All ten spectra are fitted correspondingly and more details of the fitting procedure will be presented in a separate article. Figure 4 shows the evolution of oxidized Si species as determined from the peak fitting, in the bulk of the PS (a) sample and at the surface (b).

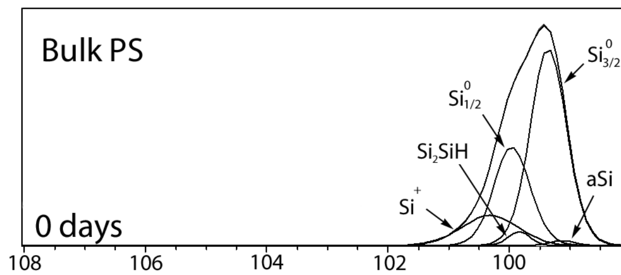

Figure 3. XPS spectra of bulk PS immediately after formation.

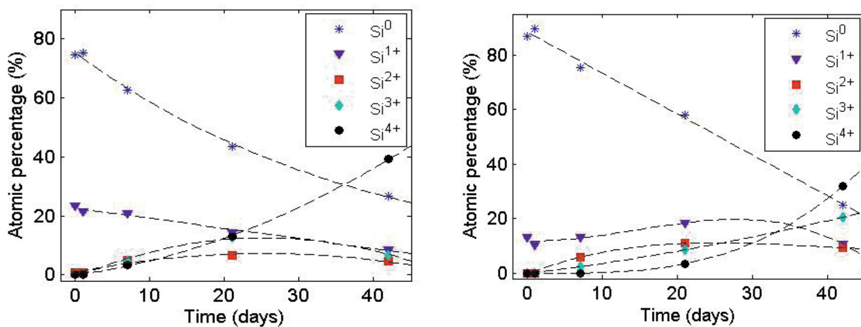

Figure 4. Atomic percentage of pure Si and oxidized Si states as fitted from the (a) surface and (b) bulk XPS spectra. Dashed lines are added as a guide to the eye.

Figure 4a shows that at already at 'Day 0' (day of etching), the surface of the PS sample contains Si_2O (Si^{1+}), and small amounts of SiO (Si^{2+}), in addition to pure Si (Si^0) and Si_2SiH. Although the Si_2SiH and Si concentrations are resolved in the peak fitting, Si_2SiH is included in the Si^0 concentration displayed in Fig. 4, as this corresponds to non-oxidized hydrogen terminated Si. The changes between sample 'Day 0' and sample 'Day 1' are small. After 7 days, the surface PS also contains elements of Si_2O_3 (Si^{3+}) and SiO_2

(Si^{4+}) while the pure Si + Si_2SiH and Si_2O concentration decreases. After 21 days, more oxidation of pure Si occurs at the surface and the concentrations of SiO, Si_2O_3 and SiO_2 increase further. Between 'Day 21' and 'Day 42', the SiO_2 concentration increases significantly, while the concentrations of pure Si and the intermediate oxidation states decrease.

Figure 4b shows that the bulk PS has a similar oxidation process. At the day of etching, bulk PS contains pure Si, Si_2SiH, and Si_2O. No significant change occurs after 1 day in air. After 7 days, additional concentrations of SiO and Si_2O_3 have appeared, whereas the Si_2SiH compound has vanished. SiO_2 first occurs in bulk PS after 21 days. While the Si_2O concentration steadily decreases at the surface of PS, an initial increase is seen in the bulk. Not surprisingly, for all ageing time, the oxidation levels are lower in the bulk than at the surface.

Summarized, we observe that a relatively rapid but partial oxidation, covering a few percent of the inner surface of the PS by oxide, takes place in the early stages of ageing. A gradual increase in oxidation, through the intermediate oxidation states, is observed. Detection of Si^{1+} (Si_2O), is followed by detection of Si^{2+} (SiO) and Si^{3+} (Si_3O_2), before SiO_2 is formed after about one week.

Comparing Results from XPS and SE

For best possible accordance between SE and XPS, each sample is measured by ellipsometry within day one after etching and then again just before XPS measurements. Comparing the information obtained about oxidation of the PS structures, it is clear that SE is rather insensitive to oxidation in the PS structures. Partly, the inclusion of oxide in the ellipsometry model is complicated by the number of different oxidation states; for most of the samples only a small fraction of the oxidized species is SiO_2. It is also possible that an alternative model could give larger deflections with respect to oxygen content. However, when this is said, the marginal difference in Ψ and Δ, and consequently in refractive index between day 1 and day 42 (as showed in Fig. 1) indicates that it is a challenge to determine oxidation of PS with SE. It is also rather common to neglect oxidation when performing ellipsometric characterization of PS (12,13). Whether neglecting SiO_2 is a viable approach or not depends, of course on the amount of oxide, but also on the information sought. Obviously, information about the chemical composition of the material is lost, but, on the other hand, changes in the effective refractive index of the material are small. Considering the densities and molecular weights of Si (d_{Si} = 2330 kg/m^3, Mw_{Si} = 28.0855 g/mol) and SiO_2 (d_{SiO2} = 2200 kg/m^3, Mw_{SiO2} = 60.0843 g/mol) it can be seen that for an oxide of thickness t, the fractional consumption of the Si wall is

$$(Mw_{Si}/d_{Si})/(Mw_{SiO2}/d_{SiO2}) = 0.44t,$$

while the remaining $0.56t$ is expansion into the pores (26). A locally flat surface, i.e. isotropic expansion through the volume (27), and oxidation by SiO_2 only is assumed. The net effect of oxidation can then be thought of as a replacement of a medium consisting of 44% Si and 56% air with a medium consisting of 100% SiO_2. In the BEMA, 44% Si and 56% air have an effective refractive index, N_{eff}, given by the equation

$$0.44\left(\frac{N_{Si}{}^{2}-N_{eff}{}^{2}}{N_{Si}{}^{2}+2N_{eff}{}^{2}}\right)+0.56\left(\frac{N_{Air}{}^{2}-N_{eff}{}^{2}}{N_{Air}{}^{2}+2N_{eff}{}^{2}}\right)=0\,.$$

Inserting the refractive indices N_{Si}(700 nm) = 3.77 and N_{Air}(700 nm) = 1.00, gives an effective refractive index N_{eff} (700 nm) = 2.07. The refractive index of SiO_2 at the same wavelength is 1.45, hence the change in effective refractive index of the oxidized area is relatively small. The small reduction in refractive index gives the observed outcome of increased porosity in the ellipsometric modeling. The apparent increase in porosity with ageing, seen in Table I, is therefore ascribed to an increase in oxide content of the structure.

Time Evolution of Reflection from graded PS ARCs

The evolution of the reflectance from a graded PS ARC with ageing is showed in Fig. 5. The reflectance integrated over the solar spectrum is shown in parenthesis. Reflectance measurements are performed immediately after fabrication and then with intervals of approximately two weeks. A small wavelength shift and amplitude lowering of the reflectance peak is visible. The uncertainty of the measurements is estimated to be ~ 0.15 % absolute, while the measured effective reflectance of the ARC varies by 0.5 % over time. Therefore, it seems that the ARC experiences small variations in the reflectance with time, but the performance is more inclined towards an improvement than a degradation.

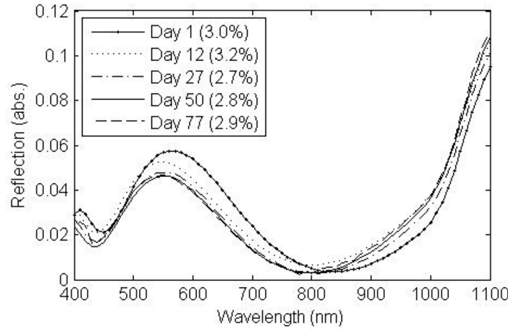

Figure 5. Evolution of the reflection from a PS ARC with time. The integrated reflectance is given in parenthesis.

Conclusions

The induced changes in the spectral reflection of graded layer ARCs due to oxidation in air is quantified by reflection measurements and correlated to ageing (oxidation) by using XPS and SE. PS layers etched at constant current density, with similar average porosity and otherwise identical formation and storage conditions as the multilayers, are used for SE and XPS. This is done to reduce the model complexity in SE so that effects of oxidation can easier be identified. Comparing results from SE and XPS shows that SE has a low sensitivity for detecting oxidation in the PS structures. For

moderately oxidized samples, no improvement in the ellipsometric fit is obtained by adding SiO_2. Finally, a small reduction in reflectivity of the multilayer PS antireflective coatings is measured after the first month of storage. Thereafter the change in reflectance saturates. The reflectance of the multilayer structures is apparently quite robust and not subject to any degradation. If structure and storage conditions are known, the small change in reflectance due to oxidation could be accounted for in the design of the coatings to improve the effective reflectivity further.

Acknowledgments

Thanks to M. F. Sunding at University of Oslo for XPS imaging. This work has been funded by the Research Council of Norway through the project "Thin and highly efficient silicon-based solar cells incorporating nanostructures," NFR Project No. 181884/S10.

References

1. L. A. A. Pettersson, L. Hultman, and H. Arwin, *Appl. Opt.* **37**, 4130 (1998).
2. J. H. Selj, A. Thøgersen, S.E. Foss, and E.S. Marstein., *J. Appl Phys.*, **107,** (2010).
3. R. Herino, G. Bomchil, K. Barla, C. Bertrand, and J. L. Ginoux, *J. Electrochem. Soc.*, **134** (1987).
4. L. Canham in *Properties of Porous Silicon, EMIS Data Reviews Series No 18,* 1997. L. Canham, Editor, p. 44, The institution of Electrical Engineers, London, UK (2006).
5. A. Grosman and C. Ortega in *Properties of Porous Silicon. EMIS Data Reviews Series No 18*. L. Canham, Editor, p. 145, The institution of Electrical Engineers, London, UK (2006).
6. T. Ito and A. Hiraki, *J. Lumin.* **57,** 331 (1993).
7. A.G. Cullis, L. T. Canham and P. D. J. Calcott, *J. Appl. Phys.* **82,** 909 (1997).
8. E.A. Petrova, K.N. Bogoslovskaya, L.A. Balagurov and G.I. Kochoradze. *Mat. Sci. Eng.* **B69-70**, 152 (2000)
9. U. Frotscher, U. Rossow, M. Ebert, C. Pietryga, W. Richter, M.G. Berger, R. Arens-Fischer, and H. Munder. *Thin Solid Films* **276,** 36 (1996).
10. M. Fried, O. Polgar, T. Lohner, S. Strehlke and C. Levy-Clement. *J. Lumin.* **80**, 147 (1999).
11. W. H. Southwell, *Opt. Lett*. **8**, 584 (1983).
12. M. Fried, T. Lohner, O. Polgár, P. Petrik, É. Vázonyi, I. Bársony, J.P. Piel, and J.L. Stehle. *Thin Solid Films* **276**, 233 (1996).
13. C. Wongmanerod, S. Zangooie and H. Arwin. *Appl. Surf. Sci.* **172**, 117 (2001).
14. J. Selj, E.S. Marstein, A. Thøgersen, and S.E. Foss, *Status Physica Solidi (c),* In press.
15. http://www.casaxps.com
16. U. Rossow, U. Frotscher, M. Thonissen, M. G. Berger, S. Frohnhoff, H. Munder, and W. Richter, *Thin Solid Films,* **255**, 5 (1995).
17. D. A. G. Bruggeman, *Ann. Phys.* **416**, 665 (1935).
18. C. M. Herzinger, B. Johs, W. A. McGahan, J. A. Woollam, and W. Paulson, *J. Appl. Phys.* **83**, 3323 (1998).
19. J.A. Woollam Co., WVASE32 software. Optical constants layer name "polysi_p".

20. T. Lohner, M. Fried, P. Petrik, O. Polgar, J. Gyulai, and W. Lehnert. *Mater. Sci. Eng.* **B69–70**, 182 (2000).
21. F.J. Himpsel, F.R. McFeeley, A. Taleb-Ibrahimi, J.A. Yarmoff, and G. Hollinger. *Phys. Rev. B* **38**, 6084 (1988).
22. E.P. Domashevskaya, V.M. Kashkarov, E.Yu. Manukovskii, A.V. Schukarev, and V.A. Terekhov. *J. of. Elec. Spec. Rel. Phenom.* **88-91,** 696 (1998).
23. Y. Kato, T. Ito, and A. Hiraki, *Jap. J. Appl. Phys.* **27,** L1406 (1988).
24. T. Sunada, T. Yasaka, M. Takakura, T. Sugiyama, S. Miyazaki, and M. Hirose *Jpn. J. Appl. Phys.* **29,** L2408 (1990).
25. L-A. O'Hare, B. Parbhoo, and S. R. Leadley *Surf. Interface Anal.* **36,** 1427 (2004).
26. K. Barla, R. Herino, and G. Bomchil, *J. Appl. Phys*. **59**(2), 439 (1986).
27. P. Pirasteh, J. Charrier, A. Soltani, S. Haesaert, L. Haji, C. Godon, and N. Errien, *Appl. Surf. Sci*. **253**, 1999 (2006).

V

Optimization of multilayer porous silicon antireflection coatings for silicon solar cells

J. H. Selj,[1,2,a)] A. Thøgersen,[1] S. E. Foss,[1] and E. S. Marstein[1]
[1]*Department of Solar Energy, Institute for Energy Technology, Instituttveien 18, 2007 Kjeller, Norway*
[2]*Department of Physics, University of Oslo, Pb 1048 Blindern, 0316 Oslo, Norway*

(Received 6 November 2009; accepted 1 February 2010; published online 15 April 2010)

Efficient antireflection coatings (ARC) improve the light collection and thereby increase the current output of solar cells. In this work, multilayered refractive index stacks optimized for antireflection, in bare air and within modules, are modeled. The relation between porous silicon (PS) etching parameters and PS structure is carefully investigated using spectroscopic ellipsometry, gravimetry, x-ray photoelectron spectroscopy, and scanning electron microscopy. The close relation between porosity and refractive index, modeled using the Bruggeman effective medium approximation, allows PS multilayers to be tailored to fabricate the optimized ARCs. Limits imposed by efficient application in photovoltaics, such as thickness restrictions and the angular distribution of incident light, are examined and accounted for. Low reflectance multilayer ARCs are fabricated with integrated reflectances of ~3% in air and 1.4% under glass in the wavelength range 400–1100 nm.
© *2010 American Institute of Physics*. [doi:10.1063/1.3353843]

I. INTRODUCTION

One cardinal goal for photovoltaic power production is to reach grid parity. Two routes exist to reach this goal; higher efficiency and lower production costs. Porous silicon (PS) has several possible applications in photovoltaics and holds potential to contribute to the desired development.[1,2] This paper will focus on using PS for antireflection purposes in solar cells. The most commonly used antireflection coating (ARC) for silicon solar cells is silicon nitride,[3,4] having a reported integrated reflection in the order of 10% for monocrystalline wafers over the spectral range of interest.[5,6] The reflection will, however, be further reduced with standard texturing. For a single layer ARC, the reflection is minimized at one single wavelength given by $\lambda_{min}=4nd$, where n is the refractive index and d is the thickness of the layer.

Excellent broadband ARCs with reflectance less than 3% are obtainable today with a multilayered structure, such as $MgF_2/Al_2O_3/ZnS$, where each layer is seperately deposited.[7] However, multiple depositions increase the cost and in addition, magnesium fluoride, and zinc sulfide are soft and easily damaged.[8] PS offers a simpler one-step production of multilayered stacks. Using electrochemical etching, the refractive index, which is closely related to the porosity, can be tuned. This provides fast and inexpensive manufacture of multilayered ARCs. Excellent broadband reflectivity has been demonstrated for PS.[9] However, the stacks made in this case are too thick (1 μm) for efficient photovoltaic application. Such a large thickness would cause degradation of the electrical characteristics of the solar cell as the typical commercial junction depths are on the order of 350 nm. Deeper diffusions are possible but expensive. In addition, PS shows significant absorption and, therefore, in an optimal coating, reflection must be weighted against absorption. It has been demonstrated that good coatings may be achieved also within these limits but an optimal coating has not been obtained.[10]

This paper presents an optimization of multilayered ARCs for photovoltaic application. A systematic study is carried out to achieve an accurate determination of the effect of etching parameter variations in the PS structure. In particular, it is important to have a broad porosity span to access the maximum refractive index range. It has been discussed that the porosity span accessible by current density variations in thin films is broader than that of thick films because surface and interface roughness increase the porosity span in both directions.[10] However, to our knowledge, systematic experimental studies of the obtainable porosity span for thin films at different concentrations of hydroflouric acid (HF) have not been reported. This will, therefore, be the first step toward an optimized PS ARC.

The optimal ARC is then modeled with constrictions on the available porosity-range and with respect to application in photovoltaics. The optimization is carried out both for operation in air ambient and in encapsulated modules. After formation of the coating, spectral reflectance is measured in the wavelength range 400–1100 nm. An integrated reflection of ~3% is obtained for samples optimized without glass. Within a module, a reflection of 5.6%, including reflections from the air-glass interface, is obtained. This compares favorably with todays commercial single and double layer coatings [SiN_x,[3] MgF_2/ZnS,[7] SiO_2/TiO_2,[11] and MgF_2/CeO_2.[12]

II. EXPERIMENTAL

A double cell electrochemical etching system, PSB Plus 4 from advanced micromaching tools (AMMT), was used to produce the PS layers. The wafers used were boron doped, 300–550 μm thick, one side polished, monocrystalline silicon with a (100) orientation. The nominal resistivities

[a)]Electronic mail: josefine.selj@ife.no.

 © 2010 American Institute of Physics

Author complimentary copy. Redistribution subject to AIP license or copyright, see http://jap.aip.org/jap/copyright.jsp

were 0.01–0.05 Ω cm. However, four point probe measurements were used to determine the resistivity range to 0.012–0.018 Ω cm. The high doping densities are necessary to ease the current flow by reducing the potential barrier for holes between electrolyte and wafer. Alternatively, surface doping of standard solar cell wafers of 1–3 Ω cm could be used for the same purpose. The wafers were dipped in 5% HF to remove native oxide. A mix of 49 wt % HF and ethanol (C_2H_5OH) constituted the electrolyte. HF concentrations were varied from 10% to 20% (volume ratio) to find the optimal porosity span. The special purpose potensiostat, PS^2 from AMMT, allowed programming of current density profiles with a time resolution of 50 ms. After etching, the samples were rinsed in ethanol to avoid cracking due to capillary forces during drying. For samples optimized for use in modules, microscope glass of 1 mm thickness was laminated to the samples, using ethylene vinyl acetate (EVA) as encapsulant.

Ellipsometry measurements were carried out using a Woollam variable angle spectroscopic ellipsometer (WVASE) in the wavelength range 300–1100 nm. To decrease the impact of sample inhomogeneities and depolarization on the measured data, focus probes with a spot diameter of 0.2 mm were applied. On the single layers, variations in the PS layer are evident by visual inspection. This may be due to small variations in resistivity or current density over the sample. For the graded layers no significant inhomogenety can be seen by visual inspection. Gravimetry was used as a control technique to check a selection of the porosities obtained from ellipsometric measurements. The porosities obtained from ellipsometry are, in all cases, confirmed by gravimetry to within 3% absolute. In gravimetry the wafers are weighted before (m_0) and after (m_1) PS formation. The wafer is then etched in 2% KOH to effectively remove the PS layer and subsequently weighted again (m_2). Porosity, P, and thickness, t, of the PS layer, is then calculated from

$$P = \frac{m_0 - m_1}{At\rho},$$

and

$$t = \frac{m_0 - m_2}{A\rho},$$

where $\rho = 2.33$ g/cm^2 is the density of silicon and A is the area where PS is formed. For the samples where scanning electron microscopy (SEM) and transmission electron microscopy (TEM) images are taken, the thickness displayed by these methods are in correspondence with results from ellipsometry and gravimetry. Thickness and layer structure were also investigated using SEM and TEM. Cross-sectional TEM samples were prepared by ion-milling using a Gatan precision ion polishing system with 5 kV gun voltage. The samples were analyzed by high resolution TEM in a 200 keV JEOL 2010F microscope. X-ray photoelectron spectroscopy (XPS) was used to assess the amount of oxide in the samples. XPS was performed in a KRATOS AXIS ULTRA^{DLD} using monochromated Al K_α radiation ($h\nu = 1486.6$ eV) on plane-view samples at zero angle of emission (vertical emission). The x-ray source was operated at 10 mA and 15 kV. The spectra were peak fitted using Casa XPS[13] after subtraction of a Shirley type background. Finally, reflectance was measured using a spectral response unit in the wavelength range 400–1100 nm.

TABLE I. Porosity limits.

Current density J (mA/cm^2)	10% HF	15% HF	20% HF
1	...	38	26
5	76	49	40
Max(18/80/250)	90	80	76

III. FABRICATION AND STRUCTURE

A. PS fabrication

To access a large range of refractive indices in one single etch, the optimal etching parameters must make a broad span in porosities available by varying only the current density. Three different HF concentrations were tested for the purpose of obtaining the widest porosity range, 10%, 15%, and 20%. As expected, in all cases, the porosity increased with current density up until the limit of electropolishing.[14] Table I shows the porosity span available at the various electrolyte compositions. The lowest available porosity is assessed using a current density of 1 mA/cm^2, the highest porosity is assessed using the highest current density which does not give electropolishing. An electrolyte consisting of 20% HF gave the broadest porosity range and was, therefore, used in all further experiments.

Although much is published on the properties of PS and how these vary with current density, resistivity, electrolyte composition, etc,[15–18] the PS layer is so sensitive to etching parameters, wafer-properties, and environment that it is necessary to undertake careful investigations of the relations between these parameters for our specific setup. Especially the relation between current density and porosity and between current density and etch rate must be known in great detail to enable the production of the best performance modeled layer at a later stage. Figure 1 shows porosities and etching rate

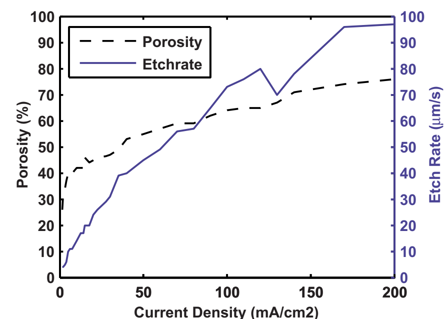

FIG. 1. (Color online) Current density vs porosity and etch rate in a 20% HF solution at room temperature, as determined from ellipsometry and gravimetry.

Author complimentary copy. Redistribution subject to AIP license or copyright, see http://jap.aip.org/jap/copyright.jsp

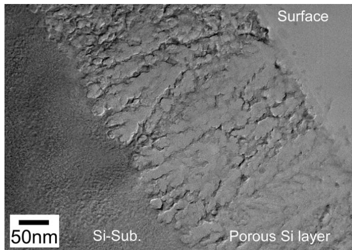

FIG. 2. TEM image of a PS sample, etched for 15 s at a current density of 20 mA/cm^2, shows columnar pores mainly pointing towards the surface. Significant branching is also evident.

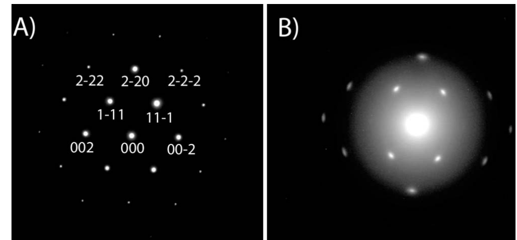

FIG. 3. SAD patterns from the Si substrate to the left and the central area of the porous layer to the right, showing that the crystalline walls in the porous region remain as a single crystal. Only a slight variation in orientation is seen inside the porous region. The diffuse rings in the pattern from the porous region are identical to the rings observed for the epoxy used in the sample preparation.

versus current density during formation, as determined by ellipsometry, gravimetry, and SEM. The curve suggests a nonlinear relationship between current density and porosity, with the steepest gradient at low current densities. Here, the porosity displays a particularly large increase, from 26% at 1 mA/cm^2 to 42% at 14 mA/cm^2. Although a sharp increase at low current densities is not unexpected based on results published by Ref. 19 for similar sets of process parameters, we have increased the sampling frequency and performed ten PS etches within this current density range. All etched samples comply with the low porosity trend.

In this work, heavily doped silicon wafers with a constant doping density are used. In a typical solar cell emitter, the doping density has a certain doping gradient normal to the surface which can affect the porosity profile. Two approaches can be used to address this issue. In one approach, varying resistivities can be compensated for in the final current density profiles used for etching the ARCs. Alternatively, the doping profile can be tailored to give a relatively flat gradient in the resistivity.[20]

TEM images show that the distance between the silicon walls varies between 7–30 nm, indicating that a mesoporous material is formed. The interface between the PS layer and the silicon substrate is rather wavy. This is promising with respect to the light spreading properties of the film. TEM images also reveal that the pores are columnar with significant branching (Fig. 2). The pores point predominantly to the surface, while the branches, or secondary pores, are not restricted to the (100) plane. For (100) wafers, a preferential growth perpendicular to the surface and towards the source of holes is expected. This is due to differences in the passivation speed of the different crystallographic directions.[21] The passivation process works fastest on the ⟨111⟩ surfaces and these surfaces, therefore, show a reduced probability of being etched.[22]

B. Ellipsometric characterization of PS

It is well known that the optical properties of PS can be modeled as a mix of Si and voids in an effective medium approximation (EMA).[23,24] In this work, the Bruggeman EMA (BEMA) (Ref. 25) theory is used. It gives a good approximation for mesoporous silicon, especially when porosities are not too high.[26–28] Amorphous silicon was tested as a constituent of the EMA but with poorer results than crystalline silicon (c-Si). This indicates that the PS layers are crystalline, as expected. This was confirmed by selected area diffraction (SAD) images of the samples, see Fig. 3.

Ellipsometric measurements are used here primarily to obtain the thickness and porosities of the layers. Knowing the thickness of the films, etch rates can easily be calculated. Ellipsometry is based on measuring changes in polarization due to interaction with the sample surface. This change is measured as the ratio of the Fresnel coefficients for parallel (r_p) and perpendicularly (r_s) polarized light. The ratio is usually given in terms of the ellipsometric parameters Ψ and Δ

$$r_p/r_s = \tan \Psi \exp i\Delta.$$

Therefore, physical parameters, i.e., optical and microstructural properties, are not immediately given but must be deduced from the measured data by modeling. Analysis of the optical data is performed using the WVASE software package, WVASE32, which is designed to fit a generated model to a given set of observed data. In the modeling we make use of the tabulated refractive indices of silicon reported by Herzinger *et al.*[29]

For graded layers, the modeling is approached by use of stratified medium theory; ellipsometric data from arbitrary graded index ARCs are reproduced by a variation in $n(z)$ with depth.[30] The best fit $n(z)$ profile can be found by dividing the film into a small number of homogeneous sublayers parametrized by a thickness and complex refractive index. Alternatively, a model function can be used. In this approach the film is again divided into homogeneous layers but the number of layers is so high that the optical properties are identical to those of a continuous medium.[31] In this work, the former procedure is utilized and should be appropriate, as the ARCs indeed are made using a quite limited number of stepwise variations in the current density rather than a continous variation.

Shape anisotropy introduces optical anisotropy in the samples, in principle requiring generalized ellipsometry and a generalized BEMA model. Such a generalized BEMA is previously shown to be a good approximation of birefringent PS.[28,32] However, standard ellipsometry is sufficient if the optical axis of a sample with uniaxial anisotropy is lying perpendicular to, or parallel with, the sample surface. As previously discussed, TEM images showed substantial

Author complimentary copy. Redistribution subject to AIP license or copyright, see http://jap.aip.org/jap/copyright.jsp

branching, secondary pores which are not restricted to the (100) plane. Therefore, both generalized and standard ellipsometry were performed. Generalized ellipsometry did not show any sign of in-plane anisotropy and standard ellipsometry together with a perpendicular uniaxial model was, therefore, adopted in the following work. The columnar shape of the microstructure induces distinct boundary conditions to the electrical and magnetic field in the medium. In the uniaxial BEMA, this charge screening is modeled by the depolarization factor, q_z.

In the single layer models, q_z is allowed to vary giving a best fit between 0.25 and 0.3. Given the columnar shape and significant branching of the pores (Fig. 2), ellipsoids slightly elongated along the pores are a plausible form of the depolarization. As the best fit q_z is relatively consistent in all single layer samples, in the more complex models it is fixed to 0.28 to reduce the number of fitting parameters. The q_x and q_y components are equally split and describe the in-plane symmetry.[33]

TEM images reveal that even for PS layers where the current density during etching has been kept constant, the pores are not uniform along the vertical direction. The fit of the ellipsometry models also improves by adding a small gradient where each sublayer is modeled as a mixture of c-Si and voids. A porosity grading can account for the interface roughness between the substrate and the porous layer and between the porous layer and air.[34,24] In addition, chemical etching may contribute to a further etching of the uppermost part of the PS layer. Numerical algorithms are used to vary the unknown parameters and minimize the difference between simulated and experimental data.

In WVASE, the Levenberg–Marquardt minimization routine is used. The goodness of the fit is measured by the mean squared error (MSE). The models are generally well fitted with MSEs$<$15, except some of the thick and highly depolarizing samples which have somewhat higher MSE. However, almost all models show some deviations from the experimental data in the blue region (300–400 nm). This is likely because the the wavelength approaches the nanostructure size ($\lambda_{air}=300$ nm$\Rightarrow\lambda_{Si}\sim 70$ nm) and therefore approach the end of the applicability range of the static effective medium theory.[28]

Generally, PS has a strong aging process where it oxidizes in air ambient and at room temperature. The presence of SiO_2 is neglected in the ellipsometric fitting for two reasons. First, XPS images show that the oxide content of the PS samples is relatively low, about 9% at a depth of approximately 20 nm, see Fig. 4. PS made from low resistivity p-type material (0.01 Ω cm) has also previously been reported to have little oxide content.[35]

Second, the SiO_2 has a relatively small optical contrast to void, and it is therefore difficult to separate the optical prints of the two. It should be noted, though, that SiO_2 consumes both pores and Si pore walls. Based on the densities and molecular weights of Si(d_{Si}=2330 kg/m^3, Mw_{Si}=28.0855 g/mol) and SiO_2(d_{SiO_2}=2200 kg/m^3, Mw_{SiO_2}=60.0843 g/mol) it can be seen that for an oxide of thickness t, the fractional consumption of the silicon wall is

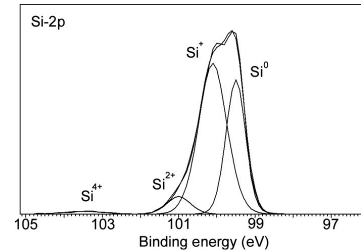

FIG. 4. The XPS Si 2p spectrum of the PS sample. The spectrum was peak fitted with four peaks corresponding to Si^{4+}(SiO_2), Si^{2+}(SiO), Si^{+}(Si_2O), and Si^0 (pure Si).

$$\frac{Mw_{Si}/d_{Si}}{Mw_{SiO_2}/d_{SiO_2}} = 0.44t,$$

while the remaining 0.56t is expansion into the pores. For large oxide contents this could result in an overestimation of the porosity and a more accurate model might have to take a shell-like structure into consideration. However, such a procedure would increase the number of fitting parameters and could result in parameter correlation problems.[36] For the PS samples presented here, oxide content is low and neglecting the SiO_2 does not induce significant error. As a result, the EMA model including solely c-Si and void is a good approximation.

IV. MODELING IDEAL ARCS

To determine the optimal structure of the ARC, simulation is performed in the WVASE32 software. In WVASE32, the best fit structure is constructed within the frame of the generated model by varying a chosen set of parameters. In this optimization, the generated model is a uniaxially anisotropic Bruggeman approximation, i.e., the same type of model that is used to model the ellipsometric data from the real PS layers. We constructed a zero reflection data set which was fed to the program instead of measured data. This zero reflection file was then used as the fitting target. The data file was weighted with respect to the solar spectrum (1.5 AM) and cut-off at 1100 nm, corresponding approximately to the bandgap of silicon. At 1200 nm the absorption coefficient of silicon has decreased by two orders of magnitude. Glass with refractive index of 1.52 at 500 nm is used as ambient for the ARC optimized for use in mudules.

Using Snell's law it can easily be seen that a ray hitting the glass cover at an angle of 10° to the sample surface, will be refracted in the glass and hit the ARC at an angle of 49° to the surface. Therefore, there is no need to accommodate very small incident angles in the modeling. The zero reflection data file, therefore, incorporates relevant incident angles (50°, 60°, 70°, 80°, and 90° to the cell surface). No differentiation has been made between the weighting of the five angles which are accounted for.

The modeling confirms the excellent antireflection properties demonstrated by Uehara *et al.*[9] The models are ideal in the sense that they have the total refractive index range available ($n_{air}-n_{Si}$) and no imposed limits on thickness. Both

Author complimentary copy. Redistribution subject to AIP license or copyright, see http://jap.aip.org/jap/copyright.jsp

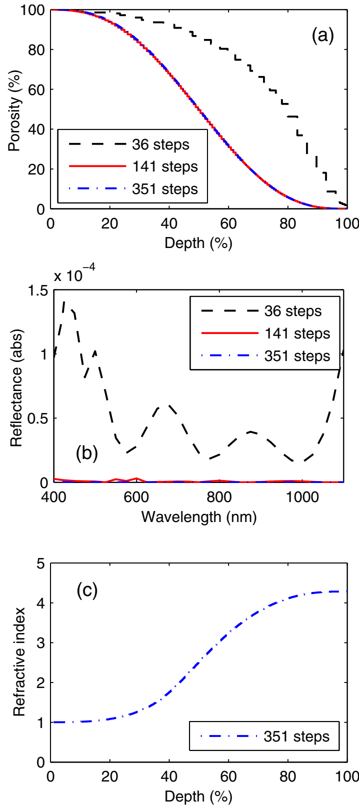

FIG. 5. (Color online) Simulation of an ideal ARC with no limits imposed. The porosity varies smoothly from 0% to 100%. Ambient is set to air, so no module glass is taken into account. The lowest reflections are obtained with thicknesses of 0.7 μm for the 36-step profile, 3.0 μm for the 141-step profile and 5.5 μm for the 351-step profile. (a) Porosity profile. (b) Effect of number of steps on reflection. The reflection of the 141-step and 351-step profiles are in the order of $10^{-4}-10^{-5}$ and is, therefore, difficult to see on the same scale as the 36-step profile. (c) Refractive index at 500 nm vs depth for the porosity profile consisting of 351 steps.

these assumptions are fundamental for the result. The starting parameters are varied in order to find the global minima of reflection. The results of the modeling are displayed in Fig. 5.

In principle, films approaching zero reflection (over a defined broadband wavelength range) can be made by varying the porosity gradually from 0% at the substrate interface to 100% at the air interface.[37] In the approximation that the thickness d is much thicker than the design wavelength, $d \gg \lambda$, the refractive index appears to vary slowly with the layer thickness and the internal reflections within the coating can be neglected. This is also known as the WKBJ approximation.[38] In this case, a lower limit on the reflectance R may be established

$$R \sim [\lambda/(2\pi d)]^{2m}.$$

It is valid when all derivatives up to the mth order are continuous at the boundaries of the graded layer.[38,39] An illustration of a gradually changing refractive index is given in Fig. 5(c). Figure 5(a) shows the corresponding porosity profile of the layer (351 steps). The depth is given in percents of the total PS thickness, with the air interface at 0% and the Si substrate interface at 100%. The only restriction in the model is that it has only eight nodes available to fit. The nodes can, however, have any number of steps within. The models giving the lowest reflection had PS layer thicknesses of 0.7–5.5 μm, depending on the number of steps. The dashed line shows the profile of a model with a total of 36 steps, five steps in the first seven nodes and the last node constituting the final step. The black solid line and the dotted line show porosity profiles of models with a total of 141 (20 steps in each node) and 351 steps (50 steps in each node), respectively.

Figure 5(b) shows the average reflectance of p-polarized and s-polarized light resulting from the three porosity profiles in Fig. 5(a) at normal incidence. The reflectance is extremely low for all incident angles and both polarizations. However, the model with only 36 steps performs significantly poorer than the other two models. It has a higher reflection and different porosity profile. When increasing the number of steps, the optimal porosity curve is a quintic function. The 36 step porosity profile resembles the porosity profile, $p(x) \propto (1-x)^{0.6}$, previously reported as the best performance profile for a 120 nm broadband PS ARC with hypothetical porosities ranging from 20%–90%.[10] In accordance with work by Ref. 40, we find that although these porosity profiles are effective for thick PS layers, better performance profiles exist for thin ARCs. The influence of film thickness on the anti-reflection properties will be further discussed in Sec. VI.

V. MODELING REALISTIC ARCS

As previously discussed, an ideal ARC is not a feasible option for several reasons. In Sec. III the available porosity span was found to be limited to ~25%–75%. In addition, there are restrictions on the thickness of a PS layer with respect to absorption and the junction depth of the cell. Our estimations show that it is absorption which places the strictest limits on thickness. Preliminary results show that an ARC of thickness 150 nm gives a reasonable balance between absorption losses and reflection gains. Ongoing work aim to investigate scattering and absorption in PS films to further optimize the balance between absorption losses and reflection gains.

The modeling of realistic ARCs will be restricted to parameters relevant for fabrication; layers suited for photovoltaic application and porosities experimentally available. The ambient of the profiles shown here (Fig. 6) is set to be EVA+module glass with a refractive index of $n=1.52$ at 500 nm. Optimizations done without module glass follow the same procedure. The total thickness is set to a maximum of 150 nm, the lowest available porosity is limited to 25% and the highest available porosity is limited to 75% (Table I). These restrictions will clearly influence the performance of the ARC.

Author complimentary copy. Redistribution subject to AIP license or copyright, see http://jap.aip.org/jap/copyright.jsp

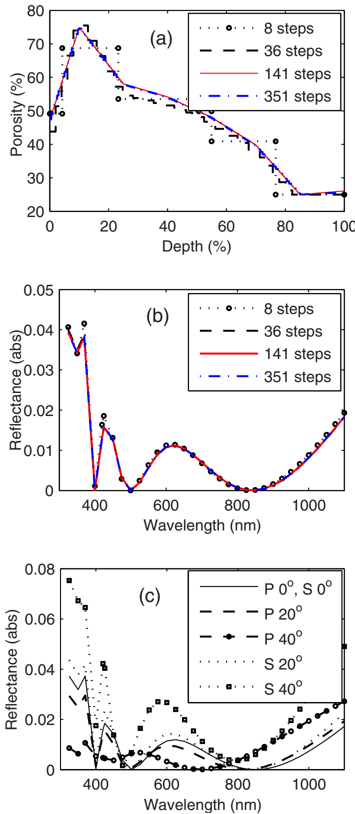

FIG. 6. (Color online) Simulation of the best performance model using realistic limits on porosity (25%–75%) and thickness (150 nm). Module glass is set as ambient in the simulation. (a) The porosity profile. (b) The effect the number of steps has on reflection. (c) The reflectance at both polarizations for relevant angles of incidence.

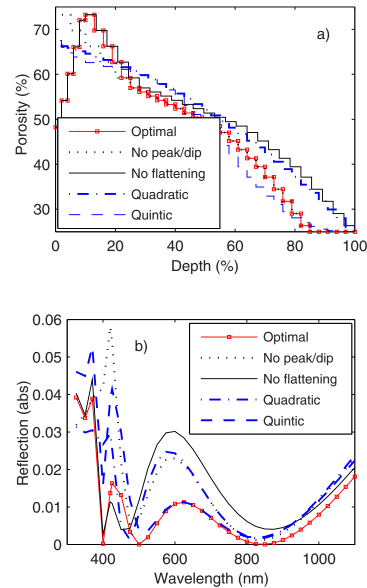

FIG. 7. (Color online) (a) Comparison of the optimal porosity profile with one profile lacking the dip/peak, one lacking the flat part, one quadratic, and one quintic profile. (b) The reflectance resulting form the porosity profiles above.

The optical thickness is the dominating factor in determining the wavelength range of the ARC. It is generally accepted that a minimum optical thickness is required to achieve very low reflectivities. To find this limit, let us follow the reasoning by MacLeod.[37] For a film consisting of n layers, the total optical thickness will be given by $T=n\lambda_0/4$, assuming that each layer has quarter wave optical thickness at the reference wavelength, λ_0. There will exist n minima of reflectance extending from a short wavelength limit

$$\lambda_S = \frac{(n+1)}{n}\frac{\lambda_0}{2} = \frac{2(n+1)}{n^2}T,$$

to a long wavelength limit

$$\lambda_L = (n+1)\frac{\lambda_0}{2} = \frac{2(n+1)}{n}T.$$

If n tends to infinity but T remains finite, λ_S tends to zero, while λ_L tends to $2T$. For all wavelengths between these limits, the reflectance approaches zero. The optical thickness generally required for achieving reflectance approaching zero is therefore $T \sim \lambda_0/2$, although the exact value depends on the refractive index profile. Assuming a linear relation between refractive index and optical thickness, the long wavelength limit of a 150 nm ARC can be estimated. $\lambda_L=2T=2[d(n_{top}+n_{bottom})/2]=150\ \text{nm}(1.5+3.4)=735\ \text{nm}$. A film of thickness 150 nm could, therefore, theoretically give a perfect reflection for $\lambda<735$ nm (Ref. 37). The calculation does not take into account that the optical thickness will vary with reference wavelength and incident angle. We see that even if all refractive indices were available, the porosity profile of a realistic ARC is expected to differ from the profile of the perfect ARC. A more formal derivation in reflectance from films with continuously varying refractive index can be found in Ref. 38.

The profile and reflection of the best performance realistic ARC is shown in Fig. 6, with the ambient/PS interface at 0% and PS/substrate interface at 100%. The thickness of the layer is 150 nm. The profile has a pronounced peak/dip at the high porosity side and flattens out at the low porosity side. This is not surprising for films with optical thickness of one wavelength and less. The index profile of such films often has more structure and may contain index discontinuities and homogeneous layers.[40] To illustrate the effect of these features on reflectivity, Fig. 7 shows a comparison of the optimal porosity profile with one porosity profile lacking the peak/dip and one profile lacking the flat part. Except from an interpolation at these features, the porosity profile is identical to the optimal. The resulting reflections are shown in Fig. 7(b) and a large effect is seen at short and intermediate wavelengths. A quadratic and a quintic porosity profile

Author complimentary copy. Redistribution subject to AIP license or copyright, see http://jap.aip.org/jap/copyright.jsp

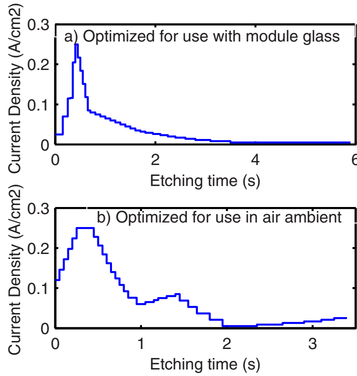

FIG. 8. (Color online) The current density profiles used to make the optimized graded ARCs.

are shown for comparison. The quintic profile is the only one which follows the low reflection of the optimal profile at intermediate wavelengths.

Note from Fig. 6(b) that, in contrast to the perfect ARC model, there is little difference in reflection of the profiles even for the ARC consisting of only one step in each node (eight nodes in total). As the total etching time of a 150 nm thick PS-layer under the current conditions is less than 10 s, there are practical limits on the number of steps which can be implemented in the actual ARC. The smallest time interval permitted by the potensiostat is 50 ms. Therefore, five steps in each node are chosen for modeling and subsequent formation. The simulated reflection of this layer, consisting of a total of 36 steps, is seen in Fig. 6(c). The reflection is low at all angles and both polarizations. The model is very robust and the same optimal profile results independent of the starting point.

The etching parameters used to produce this optimal ARC were extracted from the relations which were established between current density during etching and resulting porosities. The time necessary at each current density was deduced from the etching rates. Figure 8 shows the current densities applied during etching.

VI. RESULTS

We have now established precise relations between PS properties and etching parameters and modeled the optimal design of a PS ARC. Based on this information the current density profiles corresponding to the optimal porosity profiles were estimated and etched.

The graded PS films were characterized by spectroscopic ellipsometry. Gravimetry can be used to find the average porosity of the films but is of no use to assess the porosity profile. TEM images of the graded PS layers (Fig. 9) clearly show a very rough PS/air interface and porosity which decreases with depth.

A. Porosity profiles

Figure 10 shows the porosity profiles of two PS layers, one optimized for use within a module (a) and one optimized for use without module glass (b). The depths are given in percents of the total PS thickness, with the ambient interface at 0% and silicon substrate interface at 100%. The theoretically best porosity profile "designed" is compared with the best fit ellipsometric porosity profile of the corresponding sample "model."

The profiles show that the porosity of the samples roughly follows the original design. However, there are discrepancies in the transition regions between ambient/PS and PS/silicon, in the thickness of the layers and, for (a), in the shape of the porosity profile. Each of these will be discussed in Sec. VI B.

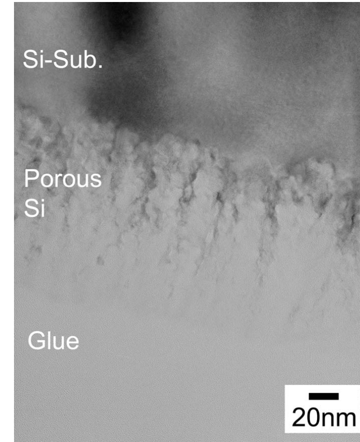

FIG. 9. TEM image of graded PS stack optimized for use in air.

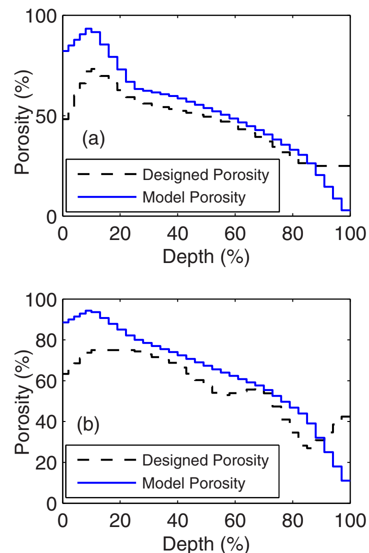

FIG. 10. (Color online) Designed and fitted porosity profile of graded PS ARCs. Interface between PS and air/glass at 0%, interface between PS and Si at 100%. (a) Optimized for operation with module glass. (b) Optimized for operation without module glass.

Author complimentary copy. Redistribution subject to AIP license or copyright, see http://jap.aip.org/jap/copyright.jsp

The discrepancies in the transition region are quite evident and similar in both Figs. 10(a) and 10(b). The modeled porosity profile shows a gradual decrease to almost 0% porosity the last 10 nm before the PS/Si interface rather than a full stop at the designed 25%. The topmost 30–40 nm has a significantly higher porosity than designed. Two mechanisms can be used to explain these deviations. First, characterization of the single layers have shown that some roughness occurs at the two interfaces, this is also reported in previous papers.[10] This effect is not taken into account in the design and will tend to increase the porosity at the ambient/PS interface while it decreases the porosity at the PS/Si interface. This is in accordance with the trends seen in Fig. 10. Second, when PS is exposed to HF, a chemical, unpreferential etching will occur. This effect, however, is much less pronounced than the preferential etch of the pores. The chemical etch would generally tend to increase the pore size of the uppermost part of the PS layer, as this is exposed to HF for the longest period of time. However, as the graded layers are exposed to HF for less than 10 s, we consider this effect to be very small.

Apparently, the etched samples have a more gradual transition between PS and silicon. Intuitively, this would lower the reflectance. However, simulations show that the thickness of the film prevents this outcome, as it is too thin to allow optimized reflectance at all wavelengths. If the low porosity could be incorporated as a dip close to the interface instead of at the interface, this would improve reflectance. However, this does not seem to be the nature of the interface, and as far as we can judge, it will be very difficult to produce. In fact, sharp dips and peaks are in general difficult to manufacture. This is especially noticeable from the profile optimized for use without module glass; the designed profile has a complex shape with distinct dips which are clearly not followed by the ellipsometric model of the actual etched sample. The etch is done in less than 4 s and each step corresponds to approximately 4 nm. It is therefore not surprising that a certain inertia in the etching process prevents an exact match. In addition, pore "seeding" can be a source of discrepancies between design and experimental result. The initial experiments used to determine porosity versus current density and etch rate, are performed in a constant-current configuration from the planar, polished wafer surface. The graded etches, on the other hand, have a varying current density, which leads to constant initiation or seeding of pores from the layers that have already been etched. The optimal porosity profile for a PS layer optimized for use with module glass is smoother with less dips and peaks. The model gives a porosity profile closer to the designed but with the same discrepancies at the interfaces.

The modeled profiles are 20–30 nm thicker than the designed profiles. Judging from TEM images and experience with single layer PS, this is mainly due to the roughness at the PS/silicon interface. In the ellipsometric fitting, this rougness is modeled as part of the PS layer.[34] Time roundings in the etching recipe and inaccuracies in the etch-time calibraton curve may also influence the thickness.

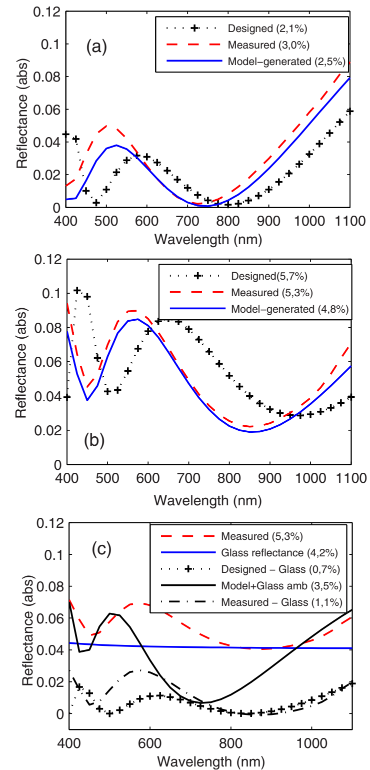

FIG. 11. (Color online) Designed, measured, and modeled reflectance vs wavelength for graded PS ARCs. (a) Optimized for operation without use of module glass. (b) Optimized for operation with use of module glass, reflectance data taken without module glass. (c) Optimized for operation with use of module glass, reflectance data taken with module glass.

B. Reflectance

Figure 11 shows the reflectance of the porosity profiles in Fig. 10. (a) is the PS layer optimized for air, (b) and (c) shows the PS layer optimized for module glass. The curve labeled designed is the reflectance generated by the designed porosity. The curve model is the reflectance generated by the best fit ellipsometric model, corresponding to the model porosity profile in Fig. 10.

The designed PS ARC optimized for air ambient has an integrated reflectance of 2.1%, which is the best obtainable within the given restrictions. Both the model and the actual measurement of the sample "measured" experience a shift, both in absolute values and wavelengths, with respect to the designed values. This is not unexpected, considering that the shifts seen in porosity profiles necessarily will display themselves in the reflectance as well.

In Fig. 11(b) the "designed", "measured", and ellipsometric "model-generated" curves are shown for a PS layer optimized for use within a module but measured and modeled in air. This is done to get a better understanding of where possible discrepancies have their origin. Clearly, a significant shift in wavelengths is visible between the designed

Author complimentary copy. Redistribution subject to AIP license or copyright, see http://jap.aip.org/jap/copyright.jsp

and measured reflectances. The absolute values, however, are similar. The designed curve actually has a higher reflectance than the measured. This is possible because the design is optimized for module operation, while the resulting reflectance is here displayed as it would be in air ambient. Note the excellent fit between the measured and model-generated reflectance. Reflectance data are not utilized during the ellipsometric fitting procedure but generated from the best fit model afterwards. The close fit between measured and modeled values is, therefore, a strong support of the accuracy of the ellipsometric modeling.

In Fig. 11(c), all curves refer to a PS layer optimized for glass and encapsulated in a module. The measurements show a total integrated reflection of 5.3%, included reflections from the glass/air interface but excluded absorption-losses in the glass and EVA. In the designed model, we are not able to include reflectance from the front side of the module glass. Glass may readily be used as ambient, but if used as a separate layer, standing wave interferences arise and complicate the theoretical reflectance spectrum with sharp oscillations. In actual measurements we do, however, not expect to see such oscillations since even the smallest thickness inhomogeneties are enough to effectively destruct them. Therefore, the generated design spectrum will in effect have subtracted the glass reflectance “designed-glass”. For direct comparison we must do the same for the measured spectrum “measured-glass”. This subtraction has the added benefit of clearly displaying the reflectance which actually results from the PS/glass interface. The measured integraded reflectance of the PS ARC is then 1.1%. Note that the integrating sphere setup used for reflectance measurements does not take absorption in the glass and EVA into account. Using transmission data of glass[41] and EVA (Ref. 42) to correct for absorption effects, the actual reflectance of the PS ARC is ~1.4%.

The encapsulated PS sample is too thick to obtain ellipsometric data. Therefore no model-generated curve is shown in Fig. 11(c). Simply using the ellipsometric model obtained without glass and adding a glass ambient in the model will not suffice. The EVA will alter the topmost of the PS layer and an EMA with void as one constituent will no longer be accurate. For simplicity this is not taken into account in the original design.

The refractive indices of the the specific glass used in the modules are found using ellipsometry and transmission data. The reflectance is then calculated from the refractive indices using the WVASE32 software. This is shown in Fig. 11(c) as reference “glass reflectance”. All reflectances are measured and modeled at an incident angle of 10° to the surface normal and integrated reflections are given in the wavelength range 400–1100 nm. The blue part of the terrestrial solar spectrum, 300–400 nm, is not included due to limitations of the spectral response unit used for measurements. However, very few rays in this wavelength range actually reach Earth. Therefore, even if the reflectance in the 300–400 nm range is assumed to be high, it modifies the total reflectance by much less than the standard deviation (0.3) of the reflectance measurements of the laminated PS layer. The uncertainties described by the standard deviation are primarily due to inaccuracies in the spectral response setup and inhomogeneties on the sample surface.

VII. CONCLUSIONS

By varying current density while all other parameters are kept constant, a broad porosity span (25%–75% +roughness) is available for PS. Exploiting the corresponding range of refractive indices, excellent PS ARCs can be designed and fabricated within restrictions applying for application in photovoltaics. Especially when the design incorporates module glass, excellent ARCs with a total reflectance of 5.6%, glass included, can be made inexpensively and in less than 6 s. Without glass, an integrated reflectance of ~3% is obtained. Important questions such as optimal thickness and passivation are still to be addressed before a graded PS ARC can be implemented in efficient Si solar cells.

ACKNOWLEDGMENTS

Thanks to Dr. T. Wagner at Oriel Laser Optik Technologie GmbH and Dr. M. Kildemo at the Norwegian University of Science and Technology for guidance and advice on ellipsometric modeling. Thanks to M. F. Sunding at University of Oslo for XPS imaging. This work has been funded by the Research Council of Norway through the project “Thin and highly efficient silicon-based solar cells incorporating nanostructures,” NFR Project No. 181884/S10.

[1] R. Bilyalov, L. Stalmans, and L. Schirone, IEEE Trans. Electron Devices **46**, 2035 (1999).
[2] R. R. Bilyalov, R. Lüdemann, W. Wettling, L. Staalmans, J. Poortmans, J. Nijs, L. Schirone, G. Sotgiu, S. Strehlke, and C. Levy-Clemet, Sol. Energy Mater. Sol. Cells **60**, 391 (2000).
[3] R. Hezel and R. Schoerner, J. Appl. Phys. **52**, 3076 (1981).
[4] A. G. Aberle, Sol. Energy Mater. Sol. Cells **65**, 239 (2001).
[5] B. Sopori, J. Electron. Mater. **32**, 1034 (2003).
[6] D. N. Wrigth, E. S. Marstein, and A. Holt, *Double Layer Antireflective Coatings for Silicon Solar Cells* (IEEE, New York, 2005).
[7] D. Bouhafs, A. Moussi, A. Chikouche, and J. M. Ruiz, Sol. Energy Mater. Sol. Cells **52**, 79 (1998).
[8] V. M. Aroutiounian, K. Martirosyan, and P. Soukiassian, J. Phys. D **37**, L25 (2004).
[9] S. Uehara, K. Kurose, and T. Matsubara, Phys. Status Solidi A **182**, 461 (2000).
[10] C. C. Striemer and P. M. Fauchet, Phys. Status Solidi **197**, 502 (2003).
[11] K. L. Jiao and W. A. Anderson, Solar Cells **22**, 229 (1987).
[12] S. E. Lee, S. W. Choi, and J. Yi, Thin Solid Films **376**, 208 (2000).
[13] http://www.casaxps.com
[14] H. Lang and P. Steiner, Sens. Actuators, A **51**, 31 (1995).
[15] L. Canham, *Properties of Porous Silicon*, EMIS Datareviews Series No 18, 1997.
[16] B. Hamilton, Semicond. Sci. Technol. **10**, 1187 (1995).
[17] R. L. Smith and S. D. Collins, J. Appl. Phys. **71**, R1 (1992).
[18] X. G. Zhang, J. Electrochem. Soc. **151**, C69 (2004).
[19] St. Frohnhoff, M. G. Berger, M. Thönissen, C. Dieker, L. Vescan, H. Münder, and H. Lüth, Thin Solid Films **255**, 59 (1995).
[20] J. Benick, O. Schultz-Wittmann, J. Schön, and S. W. Glunz, Phys. Status Solidi **2**, 145 (2008).
[21] V. Lehmann, Micro Electro Mechanical Systems, 1996, MEMS ’96, Proceedings, pp. 1–6, February, 1996 (DOE Scientific and Technical Information, Washington, DC, 1996).
[22] J. Carstensen, M. Christophersen, G. Hasse, and H. Föll, Phys. Status Solidi A **182**, 63 (2000).
[23] U. Rossow, U. Frotscher, M. Thonissen, M. G. Berger, S. Frohnhoff, H. Munder, and W. Richter, Thin Solid Films, **255**, 5 (1995).
[24] L. A. A. Pettersson, L. Hultman, and H. Arwin, Appl. Opt. **37**, 4130 (1998).

Author complimentary copy. Redistribution subject to AIP license or copyright, see http://jap.aip.org/jap/copyright.jsp

[25]D. A. G. Bruggeman, Ann. Phys. **416**, 665 (1935).
[26]D. Kovalev, G. Polisski, J. Diener, H. Heckler, N. Künzner, V. Y. Timoshenko, and F. Koch, Appl. Phys. Lett. **78**, 916 (2001).
[27]M. I. Strashnikova, V. L. Voznyi, V. Y. Reznichenko, and V. Y. Gaivoronskii, J. Exp. Theor. Phys. **93**, 363 (2001).
[28]L. A. Golovan', P. K. Kashkarov, and V. Y. Timoshenko, Crystallogr. Rep. **52**, 672 (2007).
[29]C. M. Herzinger, B. Johs, W. A. McGahan, J. A. Woollam, and W. Paulson, J. Appl. Phys. **83**, 3323 (1998).
[30]R. M. A. Azzam, N. M. Bashara, and S. S. Ballard, *Ellipsometry and Polarized Light*, (1978), Vol. 31.
[31]J. Rivory, Thin Solid Films **313-314**, 333 (1998).
[32]S. Zangooie, R. Jansson, and H. Arwin, J. Appl. Phys. **86**, 850 (1999).
[33]K. Kaminska, A. Amassian, L. Martinu, and K. Robbie, J. Appl. Phys. **97**, 013511 (2005).
[34]D. E. Aspnes, J. B. Theeten, and F. Hottier, Phys. Rev. B **20**, 3292 (1979).
[35]C. Pickering, M. I. J. Beale, D. J. Robbins, P. J. Pearson, and R. Greef, J. Phys. C **17**, 6535 (1984).
[36]C. Wongmanerod, S. Zangooie, and H. Arwin, Appl. Surf. Sci. **172**, 117 (2001).
[37]H. A. MacLeod, *Thin-Film Optical Filters*, 2nd ed. (Hilger, Bristol, 1986).
[38]R. Jacobsson, Prog. Opt. **5**, 247 (1966).
[39]D. Poitras and J. A. Dobrowolski, Appl. Opt. **43**, 1286 (2004).
[40]W. H. Southwell, Opt. Lett. **8**, 584 (1983).
[41]Gerhard Menzel GmbH Thermo Fisher Scientific Durchlassigkeit.
[42]Etimex Solar GmbH. Datasheet, December 2008.

Author complimentary copy. Redistribution subject to AIP license or copyright, see http://jap.aip.org/jap/copyright.jsp

VI

Reduction of optical losses in colored solar cells with multilayer antireflection coatings

J. H. Selj[1], R. Søndenå, T. T. Mongstad, E. S. Marstein

Department of Solar Energy, Institute for Energy Technology (IFE), P.O Box 40 NO-2027 Kjeller, Norway

Abstract

Solar modules are becoming an everyday presence in several countries. So far, the installation of such modules has been performed without aesthetic concerns, typical locations being rooftops or solar power plants. Building-integrated photovoltaic (BIPV) systems represent an interesting, alternative approach for increasing the available area for electricity production and potentially for further reducing the cost of solar electricity. In BIPV, the visual impression of a solar module becomes important, including its color. The color of a solar module is to a large extent determined by the color of the cells in the module, which is given by the antireflection coating (ARC). The ARC is a thin film structure that significantly increases the amount of current produced by and, hence, the efficiency of a solar cell. The deposition of silicon nitride single layer ARCs with a dark blue color is the most common process in the industry today and plasma enhanced chemical vapor deposition (PECVD) is mostly used for this purpose. However, access to efficient, but differently colored solar cells are important for the further development of BIPV. In this paper, the impact of varying the color of an ARC upon the optical characteristics and efficiency of a solar cell is investigated. The overall transmission and reflection of a set of differently colored single layer ARCs is compared with multilayered silicon nitride ARCs, all made using PECVD. These are again compared with porous silicon ARCs fabricated using an electrochemical process allowing for the rapid and simple manufacture of ARC structures with many tens of layers. In addition to a comparison of

*Corresponding author e-mail adress: josefine.selj@ife.no, Fax: + 47 63 81 29 05, Tel: + 47 63 80 64 29

the optical characteristics of such solar cells, the effect of using colored ARCs on solar cell efficiency is quantified using the solar cell modeling tool PC1D. This work shows that the use of multilayer ARC structures can allow solar cells with a range of different colors throughout the visual spectrum to retain very high efficiencies.

Keywords: Multilayer antireflection coatings, porous silicon, solar cells, design, building integrated PV (BIPV)

---

1. Introduction

The use of solar cells for electricity production has increased rapidly for more than a full decade. As a result, solar energy systems are becoming an increasingly visible part of everyday life in several countries. Today, the majority of solar cells are currently installed with little regard to aesthetics, in locations such as rooftops or solar power plants. Building-integrated photovoltaic (BIPV) systems represent an interesting, alternative approach for increasing the available area for electricity production and potentially for further reducing the cost of solar electricity [1, Ch. 22]. However, BIPV does not represent a large share of the market today. One factor is that BIPV elements are in part hampered by a limited choice of aesthetic variation. In one survey, more than 85% of architects stated that aesthetic concerns would allow for the installation of solar energy systems with reduced efficiency [2]. One suggested requirement for a 'well integrated' solar energy system is that it results in a good composition of colors and materials [1, Ch. 22]. Clearly, access to efficient solar modules with a range of colors is desirable.

Deposition of antireflection coatings (ARC) at the front of the solar cell is a standard procedure in silicon solar cell fabrication. The ARC improves the photon collection of the cell by reducing the high reflection of a bare Si wafer ($> 30\%$) to around 10%. The reflection is further reduced with standard texturing. The most commonly used ARC in industry today is a thin single layer of amporphous, hydrogenated silicon nitride (a-SiN_x:H, henceforth shortened to SiN_x) deposited by Plasma Enhanced Chemical Vapor Deposition (PECVD). In addition to improving the efficiency, the ARC also determines the color of the solar cell.

In principle, there is much room for modifying the appearance of a solar cell by variation of the ARC. Firstly, by simply varying the thickness of

the silicon nitride ARC covering the solar cell, a range of colors can be obtained [3]. However, in the case of single layer ARCs of today, this leads to a significant reduction in the light transmitted into the solar cell [4]. A second option, therefore, is the use of multilayer ARCs to obtain an increased selection of colors, a benefit which can be combined with reduced optical losses. The deposition of stacks with large numbers of layers is a challenge, at least in a high-throughput, low cost production environment. However, if the relative efficiency gain of differently colored solar cells is sufficiently increased through the use of one slightly more complex processing step, this can potentially justify the use of multilayer coatings in solar cells for BIPV.

In this paper, both single layer SiN_x ARCs and and multilayered ARCs consisting of SiN_x and silicon oxide (SiO_x:H, henceforth shortened to SiO_x) were produced by plasma enhanced chemical vapor deposition (PECVD). For simple processing, only three-layer ARCs requiring relatively short process times are investigated in this paper. The two deposited materials were obtained by using standardized deposition parameters. Modifications of the deposition parameters can give room for further modulations of the optical response.

A third and very promising approach towards the rapid and simple manufacture of multilayer ARCs with very high numbers of layers is electrochemical etching of nanoporous silicon (PS) [5]. By varying the current density during etching the compositional fraction of Si and air can be controlled. The optical properties of PS are closely related to the porosity of the material. This results in a unique opportunity to tailor refractive index profiles and create complex broadband antireflection coatings ARC. In this paper, the obtainable colors and transmission losses resulting from the use of single and multilayer films deposited by PECVD are compared to those of PS ARCs. In addition to a comparison of the optical characteristics of such solar cells, the effect of using colored ARCs on solar cell efficiency is quantified using the solar cell modeling tool PC1D [6].

2. Material and methods

Dielectric films and nanoporous silicon films optimized for antireflection were synthesized and characterized in this work. A PlasmaLab 133 reactor from Oxford Systems was used to deposit single or three-layer ARC stacks. The single layer ARCs were made from conventional amorphous, hydrogenated silicon nitride (SiN_x) with a refractive index (n_{SiN}) of ~ 1.95 and

hydrogenated silicon oxide (SiO_x) with a refractive index (n_{SiO}) of ~ 1.45. The triple-layer ARCs were stacks of SiN_x and SiO_x in the following order: $SiN_x/SiO_x/SiN_x$. SiN_x was deposited at 400° using a gas-mix consisting of N_2, NH_3, and SiH_4, while SiO_2 was deposited at 300° using N_2, N_2O, and SiH_4.

Another set of samples was made by electrochemical synthesis of PS films. For these experiments, a double cell electrochemical etching system, PSB Plus 4, from advanced micromaching tools (AMMT) was used. The substrates used were boron doped monocrystalline silicon wafers, $300 - 350$ μm thick, one side polished, with a (100) orientation. A special purpose potensiostat, PS2 from AMMT, allowed programming of current density profiles with a time resolution of 50 ms.

Selection of colors and modeling of the performance of the structures was performed prior to sample preparation. For the single and triple-layer stacks, the modeling was performed using the software package MacLeod from Thin Films Center Inc. [7]. For the PS layers, the ellispometric software WVASE32 from Woollam was used.

Prior to the deposition of the films of SiN_x and SiO_x, the thickness and deposition rate of the separate films were assessed by ellipsometry. The ellipsometer used was a variable angle spectroscopic ellipsometer (VASE) from Woollam. For PS, careful mapping of the relation between current density, porosity and etch rate was performed on single layers prior to etching complex structures.

After the two different ARC structures were fabricated, their optical and structural properties were characterized using ellipsometry and reflection measurements. Reflection measurements were carried out using an integrated sphere spectral response setup.

In addition to optical characterization, the impact of the resulting transmission variations upon solar cell efficiency was determined by device modeling. The resulting modifications to the short circuit current density, (J_{sc}), and efficiency were obtained by using the software PC1D [6]. The transmission spectra used as input in the PC1D modeling is found by combining absorption spectra obtained from ellipsometry with measured reflection spectra. The main characteristics of the solar cell model are described in Table 1.

It should be mentioned that the ARCs described herein are optimized for use in an air ambient. Practical solar cells will be encapsulated in a polymer (EVA) and protected by glass. However, the methods applied in this work

can also easily be applied to the design ARCs for use in a conventional, laminated solar module configuration.

3. Theory/calculation

3.1. Optics

For the single and triple layer structures fabricated with PECVD, MacLeod was used for determining suitable thicknesses of the layers. For the modeling, layers with a refractive index of 1.95 (SiN_x) and 1.45 (SiO_x) were used. For simplicity, the layers were assumed to be non-absorbing during the modeling. In order to obtain clear colors while maintaining low reflection, a target spectrum with a reflection of 100% for a selected wavelength region and 0% for the remaining, relevant part of the solar spectrum was defined. The layer thicknesses best suited to reproduce the target spectrum is the direct outcome of the fitting procedure.

By using PS, multiple layers with different refractive indices can be etched in one single process-step. Both the thickness and the refractive index can then be varied to obtain the desired reflection. Modeling of the optimal PS structure is complicated by the need of a relation between the porosity and the refractive index. This challenge is met by using the ellipsometric software tool WVASE32 for modeling. The software is usually used to model the physical properties of materials based on information from optical data. Hence, approximations providing the necessary bridge between refractive index and compositional fractions are easily accessible. Effective medium models where the refractive index of the resulting structure is a mix of the refractive indices of air and silicon, are commonly used to model PS [8]. In this work it is the Bruggeman effective medium approximation [9] that is utilized. The optical constants of Si is taken from [10]. The flexibility in the modulation of the reflection spectra generally increase with increasing number of PS layers, but for such thin structures as those presented here, the improvement quickly saturates. Since the total etching time of all PS multilayers prepared in this work is less than 10 s, there are also practical limits on the number of steps which can be implemented in the actual ARC. The smallest time interval permitted by the potensiostat is 50 ms. As a result, a compositional model of PS with 36 layers is chosen to accommodate both practical and optimal considerations. The structure consisting of eight nodes, with five steps in the first seven nodes and the last node constituting the final step. The Levenberg-Marquet minimization routine is used to find the porosity profile

Table 1: Solar cell parameters used during PC1D simulations.

Parameter	Value
Base contact	0.015 Ω
Internal conductor	0.3 S
Internal optical reflection	80 % (specular)
Thickness	270 μm
Diffusion: Sheet res./peak dop./depth factor	50 Ωsq/$1.9 \cdot 10^{20}$ cm^{-3}/0.25
Bulk lifetime	50 μs
Front surface recombination	50000 cm/s
Rear surface recombination	1000 cm/s

which best corresponds to the predefined reflection. Absorption is not taken into account in the optimization procedure, but an upper limit on thickness is set to reduce unwanted absorption in the ARC.

For both types of ARCs, absorption is accounted for in the final evaluation of their performance calculated in PC1D.

3.2. Solar cell modeling using PC1D

Although a comparison of the overall transmission over the relevant wavelength region gives a good first impression of the impact of the different ARCs upon efficiency, the quantum efficiency of a solar cell also depends strongly on the wavelength. In order to enable a better assessment of the effect of introducing colored ARCs on solar cells, PC1D was used as a modeling tool. The basis for the modeling was the solar cell model shown in Table 1. The resulting spectral internal quantum efficiency, IQE(λ), of this solar cell model is shown in Figure 1. The solar cell model results in fairly representative solar cell characteristics, with well-known reductions of IQE(λ) both towards short and long wavelengths. For all of ARC structures, experimentally determined transmission spectra were used as input to the modeling. For simplicity and a more direct comparison with the results from the optical characterization, the cells were assumed to be without any surface texture. Also, shading losses were neglected.

4. Results and discussion

An overview over the fabricated ARC structures is given in Figure 2. The first row shows the thicknesses and colors of the single SiN_x layers,

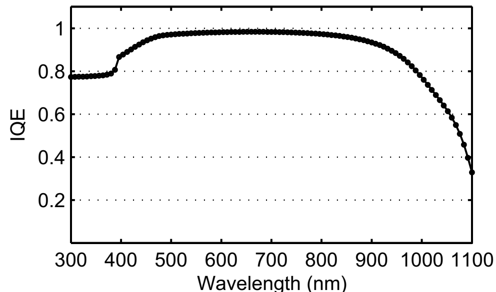

Figure 1: The internal quantum efficiency of the solar cell model used for PC1D simulations.

the second row illustrates the structure and the thicknesses of the three layer dielectric stacks, and the third row shows the thicknesses of the four PS stacks. All thicknesses are determined by spectroscopic ellipsometry. The effective, weighted reflection, absorption and transmission of each of the structures, in the wavelength range $300 - 1100$ nm, is given in Table 2. The solar spectrum used for weighting the number of incoming photons of different wavelengths is the standardized 1.5AM terrestrial reference spectrum [11] adopted by the American Society for Testing and Materials (ASTM). Pictures and reflection spectra of each of these ARCs are shown in section 4.1. An evaluation of the performance of the ARC structures when integrated in a solar cell is performed in PC1D. The efficiencies resulting from each of the ARC structures is summarized in Table 3.

4.1. Reflection

The reflection spectra of the fabricated structures are shown in Figures 3, 4 and 6. The measured reflection is labeled 'measured' and the reflection generated from the best fit ellipsometric model is labeled 'modeled'. Note that it is the thickness and optical constants of the layers that are directly modeled by ellipsometry. The reflection is calculated from the best fit model. The excellent fit between 'measured' and 'modeled' is therefore a strong support of the validity and accuracy of the ellipsometric models employed. The reflection measurements are performed in the wavelength range from $300 - 1000$ nm, due to influence from backside reflection in the wafer in the range $1000 - 1100$ nm. In this wavelength range, modeled data is used in

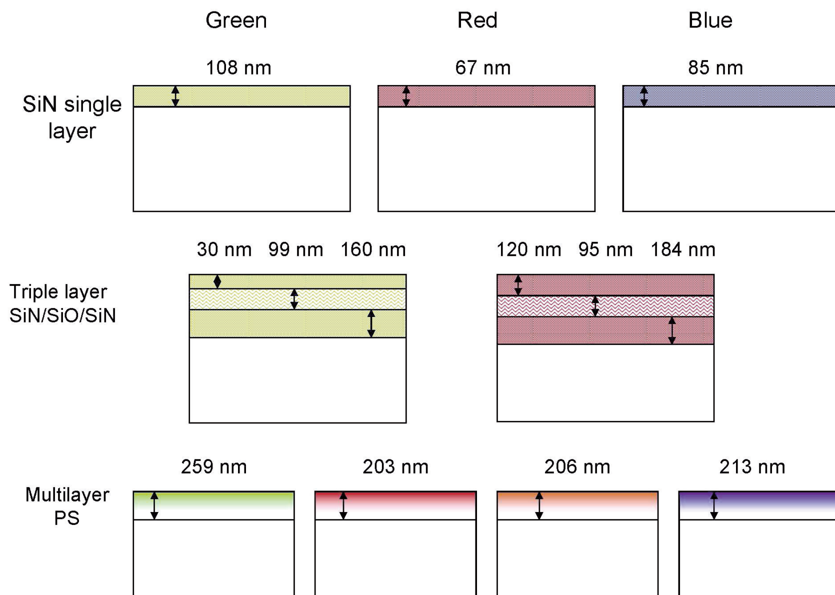

Figure 2: An overview over the fabricated structures. The thicknesses are determined by spectroscopic ellipsometry. The 'red' single layer ARC is only intended to be red, the layer in fact appears closer to blue.

Table 2: Reflection, absorption and transmission through the ARCs, weighted by the a reference solar spectrum [11].

Sample	Reflection	Absorption	Transmission
Single layer SiN - green	0.115	0.035	0.837
Single layer SiN - red	0.094	0.019	0.874
Single layer SiN - blue	0.090	0.028	0.869
Dielectric stack - green	0.175	0.048	0.777
Dielectric stack - red	0.245	0.070	0.685
Dielectric stack - blue	0.143	0.014	0.843
PS multilayer - green	0.074	0.075	0.859
PS multilayer - red	0.042	0.064	0.893
PS multilayer - purple	0.030	0.064	0.907
PS multilayer - orange	0.022	0.059	0.918

calculations of refletion in Table 2. For calculations of absorption in VASE, a wavelength range of $300-1100$ nm is used. The transmitted spectra, used as input for efficiency simulations in PC1D, are obtained from these absorption and reflection spectra.

4.1.1. SiN and dielectric stack ARCs

Figure 3 shows the reflection spectra achieved with single layer SiN_x optimized for green, red and blue reflection spectra, respectively. The integrated reflections are low, but the available color range is limited as the layer thickness is the only variable in these films. The reflection spectra have a single point of zero-reflection. The film intended to be red, is in reality more blue, illustrating the difficulty of achieving different colors with only one SiN_x layer. Ellipsometric modeling of these simple structures is straight forward and the accordance between measured and modeled values is excellent.

Figure 4 shows the reflection spectrum achieved with triple layer dielectric stacks of $SiN_x/SiO_x/SiN_x$ optimized for green, red and blue reflection spectra. The possibility of tailoring the color of the reflection spectra is significantly improved, at the expense of a moderate increase in reflection.

Ellipsometric modeling is carried out by using optical constants obtained from single layer SiN_x made under the same deposition parameters. Optical constants for the SiO_x are approximated by tabulated values for SiO_2 taken from Palik et al. [12]. The thickness of the three layers are fitted. Again the accordance between measured and modeled data is very good. Figure

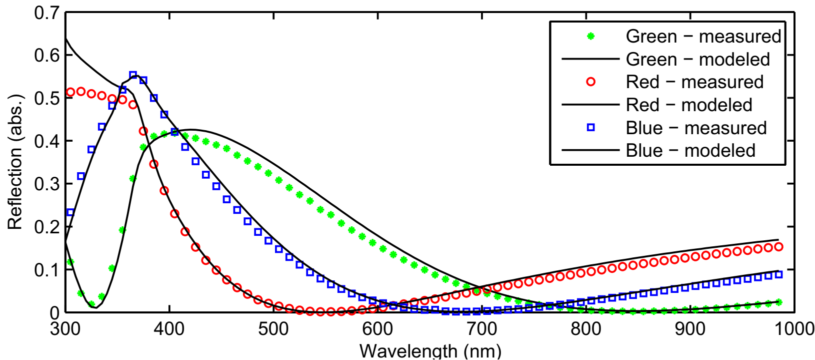

Figure 3: Reflection spectra of green, red, and blue single layer SiN_x. The curve 'measured' refers to the measured spectra and 'modeled' refers to the spectra extracted from the best fit ellipsometric model of the structures.

5 shows the colors of the triple layer $SiN_x/SiO_x/SiN_x$ ARCs corresponding to the reflection spectra in Figure 4. All the SiN_x reflection spectra have a small systematic wavelength shift compared to the designed stack. This is due to a small thickness deviation. Further optimization of the deposition parameters could improve the accuracy with which the designed spectra are reproduced.

4.1.2. Multilayer nanoporous Silicon ARCs

Figure 6 shows the measured ('measured') and ellipsometric model generated ('modeled') reflection spectra of the fabricated colored PS ARCs. Green (6a), red (6b), purple (6c), and orange (6d) PS ARCs are demonstrated. Figure 7 shows pictures of the PS ARCs corresponding to the reflection spectra in Figure 6. Control over both thickness and refractive index results in a large freedom of tailoring the reflection spectra of the films. The layers can then be optimized for low reflection in addition to specific color. As seen in Table 2, the integrated reflection of the PS ARCs are extremely low. Especially as no texturing is performed prior to electrochemical etching.

4.2. Solar cell efficiencies

The efficiency, short circuit current density, and open circuit voltage of the standardized solar cell with the different colored ARCs are shown in

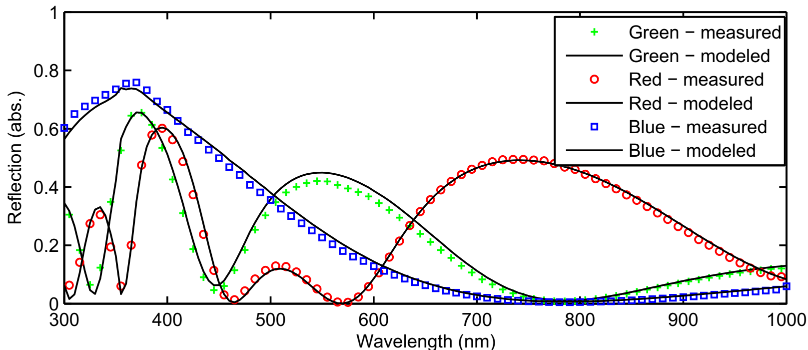

Figure 4: Reflection spectra of the green, red and blue triple layer dielectric stacks. The curve 'measured' refers to the measured spectra and 'modeled' refers to the spectra extracted from the best fit ellipsometric model of the structures.

Table 3. Green, red, blue, purple, and orange colored ARCs are produced that result in simulated efficiencies $> 16.9\%$. PS ARCs provide the highest efficiencies for all colors, but for blue and green ARCs the lead is marginal. For blue ARCs there is no gain in efficiency by going from single layer SiN to a triple layer dielectric stack, but more flexibility is provided with respect to tailoring the tint of the color. For the green ARCs, a modest efficiency improvement is obtained by using a triple layer dielectric stack compared to a single layer SiN_x. In the red part of the spectrum, PS ARCs yield exceptionally low reflection, resulting in significantly higher efficiencies than the triple layer dielectric stacks. It seems to be difficult to produce clear, red colors with a single layer SiN_x ARC.

A selection of colors was performed in order to investigate the potential of these techniques for fabrication of colored ARCs. Optimization with respect to thickness and possible adjustments in the target reflection spectra during modeling may give further improvements in efficiency for both the dielectric stacks and the multilayer PS. For the PS layers, improved control over formation parameters can enhance efficiencies due to closer match between designed and fabricated structures. For SiN_x exciting possiblities to change the refractive index during deposition is emerging. This could increase the flexibility and enhance the efficiencies of colored SiN_x ARCs.

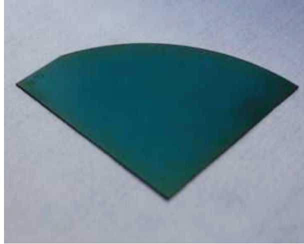

(a) Green dielectric stack

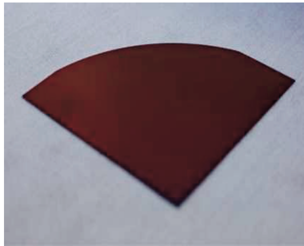

(b) Red dielectric stack

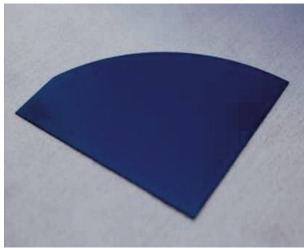

(c) Blue dielectric stack

Figure 5: Appearance of the colored triple layer dielectric stack ARC.

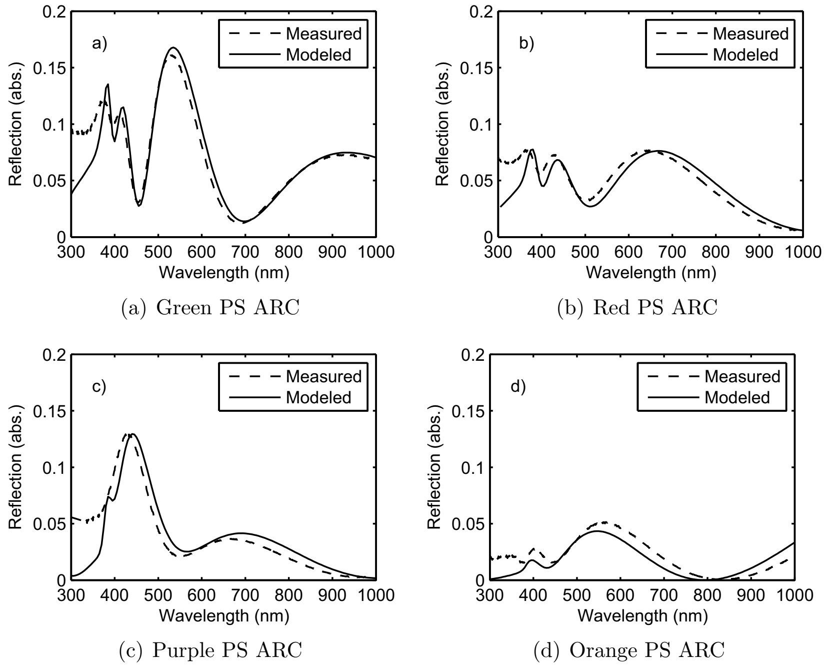

(a) Green PS ARC

(b) Red PS ARC

(c) Purple PS ARC

(d) Orange PS ARC

Figure 6: Reflection from colored PS ARCs. The intended reflection ('design) is shown together with the measured reflection ('measured') and the reflection generated from the optical constants in the best fit ellipsometry model ('modeled').

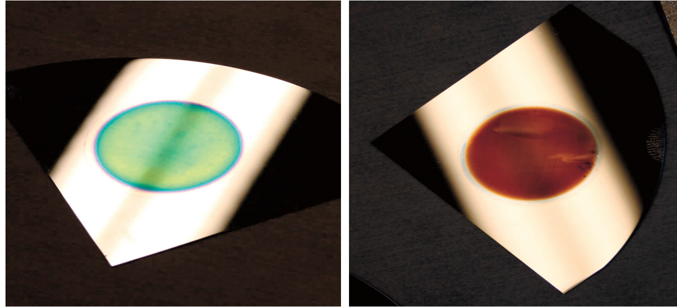

(a) Green PS multilayer stack (b) Red PS multilayer stack

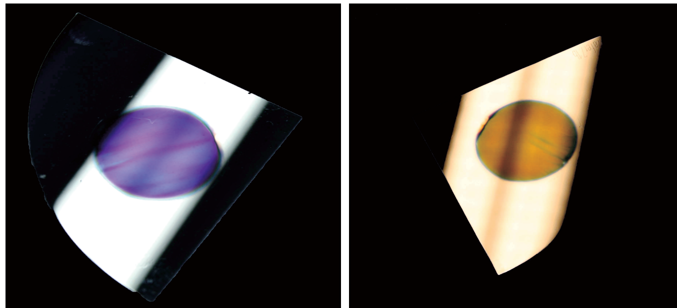

(c) Purple PS multilayer stack (d) Orange PS multilayer stack

Figure 7: Appearance of the colored multilayered PS ARCs.

Table 3: Simulated efficiencies obtained when each ARC is used on a standardized solar cell. Simulated values for short circuit current density (J_{sc}) and open circuit voltage (V_{oc}) are also shown. [1] "Black" referes to perfect transmission through the ARC; no reflection, no absorption.

Sample	Efficiency	J_{sc}	V_{oc}	$J_{sc}/J_{sc}(black)$
"Black"[1]	19.8	38.5	620.1	100.0%
Single layer SiN - green	16.6	32.5	615.8	84.4%
Single layer SiN - red	17.6	34.5	617.4	89.6%
Single layer SiN - blue	17.5	34.1	617.1	88.6%
Dielectric stack - green	15.2	29.8	613.5	77.4%
Dielectric stack - red	13.0	25.7	609.7	66.8%
Dielectric stack - blue	16.6	32.5	615.7	84.4%
PS multilayer - green	16.9	33.0	616.2	85.7%
PS multilayer - red	17.5	34.3	617.2	89.0%
PS multilayer - purple	17.8	34.8	617.7	90.4%
PS multilayer - orange	18.1	35.4	618.0	91.9%

5. Conclusions

We have her showed that the ARC of solar cells can be tailored to give clear colors while retaining high efficiencies. Although the reflection from single layer SiN_x ARCs are generally low, the colors available by simple thickness variations are limited. Using triple layer SiN_x ARCs, a broader range of colors can be achieved, at the expense of a modest increase in reflection. By electrochemical etching of the Si wafer, colored ARCs with lower reflection than conventional, single layer SiN_x ARCs can be produced. Colored solar cells able to absorb in excess of 90% of the incoming light is shown to be accesible with these structures. However, important issues such as passivation and process-integration need further improvement before PS ARCs can be implemented in industrial solar cell production [13].

Acknowledgment

This work has been funded by the Research Council of Norway through the project "Thin and highly efficient silicon-based solar cells incorporating nanostructures," NFR Project No. 181884/S10.

References

[1] T. Reijenga, PV in architecture, in: E. Luque, S. Hegedus (Eds.), Handbook of Photovoltaic Science and Engineering, John Wiley & Sons, 2003, pp. 1005–1042.

[2] W. Weiss, I. Stadler, Faade integration, a new and promising opportunity for thermal solar collectors, in: Proceedings of the Industry Workshop of the IEA Solar Heating and Cooling Programme.

[3] A. MacLeod, Thin Film Optical Filters, Institue of Physics Publishing, 2001.

[4] R. Tölle, R. Bruton, T. Noble, R. Schneider, A. Janka, J.-P. Costard, H. Claus, J. Radike, M. Summhammer, J. Hilcox, D. Aceves, O. Anzizu, O. Koch, W. Tobias, I. Luque, The production of aesthetically pleasing module prototypes within the "bimode" - project, in: Proc. 16th Euro. Conf. Photovoltaic Solar Energy Conversion, pp. 1957–1959.

[5] J. Selj, A. Thøgersen, S. Foss, E. Marstein, Optimization of multilayer porous silicon antireflection coatings for silicon solar cells, J. Appl Phys. 107 (2010).

[6] P. Basore, D. Clugston, PC1D, 2002.

[7] A. MacLeod, The essential macleod, version 8.9.55 (ie), thin film center inc., 2000, 2001, 2002.

[8] L. A. A. Pettersson, L. Hultman, H. Arwin, Porosity Depth Profiling of Thin Porous Silicon Layers by use of Variable-Angle Spectroscopic Ellipsometry: A Porosity Graded-Layer Model, Applied Optics 37 (1998) 4130–4136.

[9] D. Bruggeman, Berechnung verschiedener physikalischer Konstanten von heterogenen Substanzen. I. Dielektrizitätskonstanten und Leitfähigkeiten der Mischkörper aus isotropen Substanzen, Annalen der Physik 416 (1935) 665–679.

[10] C. Herzinger, B. Johs, W. McGahan, J. Woollam, W. Paulson, Ellipsometric determination of optical constants for silicon and thermally grown silicon dioxide via a multi-sample, multi-wavelength, multi-angle investigation, Journal of Applied Physics 83 (1998) 3323–3336.

[11] C. Gueymard, D. Myers, K. Emery, Proposed reference irradiance spectra for solar energy systems testing, Solar Energy 73 (2002) 443–467.

[12] E. Palik, Handbook of Optical Constants of Solids, volume 1, Elsevier, 1998.

[13] R. Bilyalov, R. Ludemann, W. Wettling, L. Staalmans, J. Poortmans, J. Nijs, L. Schirone, G. Sotgiu, S. S., C. Levy-Clemet, Multicrystalline silicon solar cells with porous silicon emitter, Solar Energy Materials and Solar Cells 60 (1 February 2000) 391–420(30).